

Search for Supersymmetry in Trilepton Final States with the DØ Experiment

Dissertation

zur Erlangung des mathematisch-naturwissenschaftlichen Doktorgrades

“Doctor rerum naturalium”

der Georg-August-Universität Göttingen

im Promotionsprogramm ProPhys

der Georg-August University School of Science (GAUSS)

Vorgelegt von

Jason Dhia Mansour

aus

Washington, D.C.

Göttingen, 2014

Search for Supersymmetry in Trilepton Final States with the DØ Experiment

Dissertation

zur Erlangung des mathematisch-naturwissenschaftlichen Doktorgrades

“Doctor rerum naturalium”

der Georg-August-Universität Göttingen

im Promotionsprogramm ProPhys

der Georg-August University School of Science (GAUSS)

Vorgelegt von

Jason Dhia Mansour

aus

Washington, D.C.

Göttingen, 2014

Betreuungsausschuss:

Prof. Dr. Arnulf Quadt
Prof. Dr. Carsten Hensel

Mitglieder der Prüfungskommission:

Referent: Prof. Dr. Arnulf Quadt
II. Physikalisches Institut, Georg-August-Universität Göttingen
Korreferent: PD Dr. Jörn Grosse-Knetter
II. Physikalisches Institut, Georg-August-Universität Göttingen

Weitere Mitglieder der Prüfungskommission:

Prof. Dr. Ariane Frey
II. Physikalisches Institut, Georg-August-Universität Göttingen
Prof. Dr. Carsten Hensel
Centro Brasileiro de Pesquisas Fisicas, Rio de Janeiro, Brasilien
Prof. Dr. Wolfram Kollatschny
Institut für Astrophysik, Georg-August-Universität Göttingen
Jun.-Prof. Dr. Steffen Schumann
II. Physikalisches Institut, Georg-August-Universität Göttingen

Tag der mündlichen Prüfung: 19.11.2014

Referenz: II.Physik-UniGö-Diss-2014/04

GEORG-AUGUST-UNIVERSITÄT GÖTTINGEN

II. Physikalisches Institut

Search for Supersymmetry in Trilepton Final States with the DØ Experiment

von

Jason Dhia Mansour

A search for supersymmetry in the trilepton final state is performed using the full dataset of the DØ experiment. The analyzed data amounts to $\int \mathcal{L} = 9.7 \text{ fb}^{-1}$ of $p\bar{p}$ collisions, produced at $\sqrt{s} = 1.96 \text{ TeV}$ at the Fermilab Tevatron collider. The studied process is the coproduction of charginos $\tilde{\chi}_1^\pm$ and neutralinos $\tilde{\chi}_2^0$, decaying into a final state of three leptons and missing transverse energy. To increase efficiency, only two identified leptons (e, μ) and one additional isolated track are required per event. The QCD multijet background is estimated from data, while other backgrounds are modeled via Monte Carlo. After a series of background-reduction cuts, a multivariate analysis is performed using boosted decision trees (BDT). In the distribution of the BDT output, no excess of data over background is seen. Limits on the cross section are set for the mSUGRA (CMSSM) model, as well as for a scenario with non-universal gaugino masses.



Post address:
Friedrich-Hund-Platz 1
37077 Göttingen
Germany

II.Physik-UniGö-Diss-2014/04
II. Physikalisches Institut
Georg-August-Universität Göttingen
October 2014

Contents

1. Introduction	3
2. Theory	5
2.1. The Standard Model of Particle Physics	5
2.1.1. Gauge invariance	5
2.1.2. Electroweak unification	7
2.1.3. Higgs mechanism	7
2.1.4. Renormalization	9
2.2. Physics beyond the Standard Model	11
2.2.1. Hierarchy Problem	11
2.2.2. Grand Unification	11
2.2.3. Dark matter	13
2.3. Supersymmetry	13
2.3.1. R Parity	14
2.3.2. The Minimal Supersymmetric Standard Model (MSSM)	15
2.3.3. Fine-Tuning and Hierarchy Problems	18
2.4. Non-Universal Models	19
2.4.1. Non-Universal Gaugino Masses from $SU(5)$	19
2.4.2. Exploration of Parameter Space	20
2.5. Review of present constraints on SUSY	27
2.5.1. SUSY searches with colliders	27
2.5.2. Precision Measurements	30
3. Experiment	35
3.1. The Tevatron	35
3.2. The DØ Experiment	35
3.2.1. Tracking system	37
3.2.2. Central Fiber Tracker	39
3.2.3. Solenoid Magnet	39
3.2.4. Calorimeter	39
3.2.5. Muon System	43
3.2.6. Luminosity Monitor	45
3.2.7. Triggers	46
4. Event reconstruction	49
4.1. Tracks	49
4.1.1. Track reconstruction	49
4.1.2. Momentum measurement	52
4.2. Vertex Reconstruction	53
4.3. Electron ID	53

4.4.	Muon ID	55
4.4.1.	Muon isolation	56
4.4.2.	Cosmic Veto	57
4.5.	Jets	57
4.5.1.	Jet Energy Scale	59
4.6.	Missing Transverse Energy	59
5.	Samples and Event Selection	61
5.1.	Monte Carlo	61
5.2.	Signal MC Generation	62
5.3.	Software versions	65
5.4.	Event Selection	66
5.4.1.	eel Preselection	67
5.4.2.	$e\mu\ell$ Preselection	67
5.4.3.	$\mu\mu\ell$ Preselection	67
5.5.	MC normalization	68
5.6.	MC corrections	68
5.6.1.	Luminosity Reweighting	69
5.6.2.	Beam Reweighting	69
5.6.3.	$Z p_T$ Reweighting	69
5.6.4.	$Z p_T / \cos \beta_1$ Reweighting	70
5.6.5.	$W p_T$ Reweighting	70
5.6.6.	Electron p_T Reweighting	72
5.6.7.	Unclustered Energy Reweighting	72
5.6.8.	3D electron likelihood reweighting	73
5.7.	QCD Multijet	77
5.7.1.	Selection of the fake-enriched sample (eel channel)	77
5.7.2.	Selection of the fake-enriched sample ($e\mu\ell$ channel)	77
5.7.3.	Selection of the fake-enriched sample ($\mu\mu\ell$ channel)	77
5.7.4.	Multijet reweighting	78
5.8.	Cutflow	79
6.	Multivariate Analysis	95
6.1.	Boosted Decision Trees (BDTs)	96
6.1.1.	Training	97
6.1.2.	Forests and Boosting	98
6.2.	Input variables	99
7.	Limit Setting & Results	107
7.1.	Statistical methods	107
7.1.1.	Two-dimensional limits	109
7.2.	Systematics	110
7.2.1.	Trigger	111
7.2.2.	Object ID	111
7.2.3.	Cross Sections	111
7.2.4.	Multijet Estimation	111
7.2.5.	Jets	111
7.2.6.	$Z p_T / \cos \beta_1$ Reweighting	111

7.2.7.	EM Smearing and Scaling	111
7.3.	mSUGRA Limits	112
7.4.	NUGM Limits	115
8.	Summary & Outlook	119
8.1.	Further improvements	119
8.2.	Outlook	120
A.	Appendix	121
A.1.	Samples and Event Selection	121
A.1.1.	RunII Skims	121
A.1.2.	Luminosity Reweighting	122
A.1.3.	Beam Reweighting	123
A.1.4.	$Z p_T$ Reweighting	124
A.1.5.	QCD Multijet reweighting functions	127
A.2.	BDT inputs	131
A.2.1.	$ee\ell$ channel	131
A.2.2.	$e\mu\ell$ channel	132
A.2.3.	$\mu\mu\ell$ channel	133
A.3.	BDT Outputs	135
A.4.	BDT Plots	137
A.5.	Limits	137
A.5.1.	$\tan\beta$ scan	137
	List of Figures	147
	Bibliography	153

“The only way of discovering the limits of the possible is to venture a little way past them into the impossible”.

– ARTHUR C. CLARKE

1. Introduction

With physics being arguably the most fundamental of the natural sciences, the study of elementary particles is in turn the most fundamental area of physics. As such, it has a special role at the foundation of our scientific knowledge, allowing us to approach big questions like “What is matter made of?” or “Why is there something and not nothing?”.

While the idea that matter is made of indivisible particles goes back to the ancient Greeks, modern particle physics begins roughly with the discovery of the electron by Thompson in 1897. Soon afterwards, Planck discovered the quantized nature of light while studying blackbody radiation. The early twentieth century saw a flurry of development when physicists tried to understand the behavior of photons and electrons, and to formulate quantum theory. The next milestone was the discovery of antiparticles. A consequence of Dirac’s relativistic theory of the electron, the prediction was met with skepticism, until the positron was actually discovered in cosmic rays by Anderson in 1932. With growing experimental sophistication, notably the introduction of particle accelerators and colliders, more and more particles were discovered over time.

A formative phase of modern particle physics were the 1960s and 1970s, starting with the postulation of quarks by Gell-Mann in 1964. By then, a large “zoo” of hadrons and mesons had been discovered, that could be finally understood and systematized by the new theory. Then, electroweak theory was developed by Abdus Salam, Sheldon Glashow and Steven Weinberg, which was confirmed by the discovery of weak neutral currents in 1973 at CERN. This new collection of theories, called the standard model of particle physics, has been incredibly successful in explaining all phenomena of strong, weak, and electromagnetic forces to date.

With the advent of the Large Hadron Collider, another exciting new chapter in particle physics has begun. The final missing part of the standard model, the Higgs boson, has finally been found, completing the success story. At the same time, conceptional questions remain as we are probing the limits of the standard model harder than ever before. The standard model with the Higgs boson, but no further physics beyond, raises the question of the hierarchy problem, essentially: why is the Higgs boson so improbably “light” compared to the fundamental Planck scale?

A promising theory beyond the standard model designed to deal with the hierarchy problem is supersymmetry. Like in the history of antimatter, supersymmetry comes with the price of doubling the number of predicted particles. However, it elegantly solves the hierarchy problem, and might provide an explanation for the phenomenon of dark matter. At present, we do not know whether supersymmetry is realized as a fundamental symmetry in nature, or not. The search for supersymmetry, in final states containing three leptons and missing transverse energy, is the topic of this thesis.

Another open question surrounding the standard model is grand unification. While electroweak theory and QCD stand next to each other in the standard model, the question arises whether a unifying, more symmetrical description can be found. Multiple such grand unified theories have been proposed. One interesting effect of bringing together grand unification and supersymmetry is considered in this thesis, namely gaugino mass non-universality. In models with non-universal gaugino masses (NUGM), strongly and only electroweakly interacting supersymmetric particles may have larger mass differences than in models with gaugino mass universality. A consequence is that such a model might have evaded detection in previous analyses, thus it seems worthwhile to consider such a scenario.

In chapter 2 of this thesis, an overview of our theoretical framework, the standard model, will be

given, followed by an introduction to the beyond-standard-model theories of grand unification and supersymmetry. The consequences of uniting grand unification and supersymmetry are considered, and the parameter space of a resulting model is explored. Finally, an overview of the current state of experimental searches for supersymmetry is presented. In the following chapter 3, the Tevatron particle accelerator and the DØ experiment are described in detail. Chapter 4 describes object identification and event reconstruction, i.e. how detector measurements are combined to reconstruct properties of produced particles, jets, and other objects. Chapter 5 contains a description of the data samples used in the analysis, the background modeling by Monte Carlo samples, and various corrections applied to those samples. A series of cuts is applied in order to improve the signal-over-background ratio. In chapter 6, the basics of multivariate analysis and boosted decision trees (BDTs) are introduced. Various candidate variables are presented and considered, and a selection with good power of separation between background and signal is chosen. BDTs are trained on a subset of the background and signal samples, and the BDT output distribution is determined for signal, background and data. Finally, in chapter 7, we derive limits on the cross section times branching ratio for various signal hypotheses. A short summary and an outlook to possible future research, especially at the LHC, is given in chapter 8.

2. Theory

In this chapter, the theoretical foundation of this work will be presented. A short overview of the standard model of particle physics will be given, with focus on its core ideas (such as gauge invariance and spontaneous symmetry breaking), as well as the problems that hint towards physics beyond the standard model (BSM). As examples of such physics, two kinds of BSM theories will be introduced: grand unified theories and supersymmetry. A short review of current experimental constraints on supersymmetric models will be given. The combination of certain grand unified theories with supersymmetry leads to the prediction of non-universal gaugino masses (NUGM). This allows a greater variety in the masses of supersymmetric particles, and notably lets the mass scales of weakly and strongly interacting supersymmetric particles (charginos/neutralinos and gluinos, respectively) differ. In this way, NUGM allows sub-TeV scale supersymmetry, while explaining why supersymmetry has evaded previous searches.

2.1. The Standard Model of Particle Physics

The theoretical basis of this analysis is the standard model of particle physics. The standard model is one of the most successful and accurately tested theories in modern physics. It describes the elementary constituents of matter, as well as the electromagnetic, and weak and strong nuclear forces. As a quantum field theory, it combines quantum physics and special relativity. Some important guiding principles in the construction of the standard model are local gauge invariance (Section 2.1.1) and renormalizability (Section 2.1.4).

All particles fall into one of two categories. Fermions or “matter particles” have spin 1/2. Examples for fermions are quarks and electrons. Table 2.1 shows all fermions of the standard model. Bosons in contrast have integer spin, and elementary forces are mediated by the exchange of gauge bosons (listed in Table 2.2). Additionally, the standard model contains a spin zero Higgs boson. The Higgs boson, which was only recently discovered in 2012 [1], is responsible for the masses of the fundamental particles (Section 2.1.3).

1 st generation		2 nd generation		3 rd generation		Charge	QCD	Electr.	Weak force
up	u	charm	c	top	t	$+2/3$			
down	d	strange	s	bottom	b	$-1/3$			
electron	e^-	muon	μ^-	tau	τ^-	-1			
e -neutrino	ν_e	μ -neutrino	ν_μ	τ -neutrino	ν_τ	0			

Table 2.1. Fermions of the standard model, and the interactions they are subject to. The upper two rows show quarks, the lower two rows show leptons. Each fermion is accompanied by an antiparticle with opposite charges, and each quark can have one of three colors.

2.1.1. Gauge invariance

A powerful principle leading to the construction of the standard model is local gauge invariance. The idea of gauge invariance (in its global form) is familiar from classical electrodynamics: One is free to add a constant term to the electric potential Φ , since only differences in potential result in a measurable

	Carrier	Carrier Mass
Electromagnetic force	Photon (γ)	-
Weak force	W^\pm boson	80.385 GeV
	Z boson	91.1876 GeV
Strong force	Gluons (g)	-

Table 2.2. Forces of the standard model and their associated bosons.

electric field. Similarly, since the magnetic field is given by $\vec{B} = \text{rot}\vec{A}$, the magnetic vector potential \vec{A} is only determined up to a divergence of a scalar field, $\vec{A} \rightarrow \vec{A} + \vec{\nabla}\lambda(\vec{x}, t)$. Taken together, the following transformation of the relativistic four-potential $A_\mu = (\Phi/c, \vec{A})$ leaves physics unchanged:

$$A_\mu \rightarrow A_\mu + \frac{1}{e} \partial_\mu \chi(\vec{x}, t) \quad (2.1)$$

By demanding that the Lagrangian of classical electromagnetics remains invariant under this transformation, one obtains the continuity equation $\partial_\mu J^\mu = 0$, where $J^\mu = (c\rho, \vec{j})$ is the electric four-current, and its components are electric charge density and current density. It follows easily from the continuity equation that charge is conserved.

In quantum field theory, spin- $1/2$ particles such as electrons are described by spinors ψ . The interaction of electrons with the electromagnetic field is given by the Dirac equation, which is equivalent to the Lagrangian

$$\mathcal{L}_{\text{Dirac}} = \bar{\psi}(i\hbar\gamma^\mu\partial_\mu - m)\psi. \quad (2.2)$$

A simple phase change $\psi \rightarrow e^{i\theta}\psi$ should leave all probabilities unchanged, and also preserve the form of the Lagrangian. However, if we demand that $\theta = \theta(\vec{x}, t)$ is a local gauge freedom, the transformed Lagrangian no longer has the same form as the untransformed [2]. This is because $\partial_\mu\psi$ does not transform in a simple way:

$$(\partial_\mu\psi)' = e^{i\theta(x)}(i\partial_\mu\theta(x) + \partial_\mu)\psi$$

The solution to this is to add an expression to the partial derivative ∂_μ that, upon transformation, gives a new term which cancels the extra $i\partial_\mu\theta(x)$. The expression must transform by adding the gradient of a scalar field, so a natural choice is the four-potential A_μ . Note that A_μ is now a quantized field. We define:

$$D_\mu := \partial_\mu - ieA_\mu$$

leading to

$$\begin{aligned} (D_\mu\psi)' &= (\partial_\mu - ieA_\mu\psi)' \\ &= e^{i\theta(x)}(\partial_\mu - ieA_\mu + i\partial_\mu\theta(x) - i\partial_\mu\chi(x))\psi \\ &= e^{i\theta(x)}D_\mu\psi, \quad \text{with } \theta = \chi \end{aligned}$$

Since this new object D_μ transforms in a covariant fashion, it is called the covariant derivative. By doing this identification, we have related the gauge transformation of the electromagnetic field (2.1) to a change of phase of the matter field ψ . This implies a coupling of the matter (Dirac) field and the electromagnetic field, also known as minimal substitution. For a momentum operator $p_\mu = -\frac{i}{\hbar}\partial_\mu$, minimal substitution is given by $p_\mu \rightsquigarrow p_\mu + ieA_\mu$, which corresponds to the replacement of $\partial_\mu \rightsquigarrow D_\mu$. Finally, this means that the relativistic four-potential A_μ is a gauge field, related to the local $U(1)$ symmetry.

The standard model contains two other gauge symmetries: $SU(2)$ corresponding to the weak force, with the W^\pm and Z bosons as force carriers, and $SU(3)$ corresponding to the strong force, mediated by gluons. In the standard model, the weak $SU(2)$ and the electromagnetic $U(1)$ are intertwined by a mechanism called electroweak unification.

2.1.2. Electroweak unification

The theory of electroweak unification was formulated by Glashow, Salam and Weinberg in the 1960s. It provides a unified description of quantum electrodynamics and weak interactions by the gauge group $SU(2)_L \times U(1)_Y$. The $SU(2)$ and $U(1)$ gauge fields of the standard model do not directly correspond to observable particles. $SU(2)_L$, which is associated with three massless gauge fields W_μ^i ($i = 0 \dots 2$), is generated by weak isospin $T_i = \sigma_i/2$. The group $U(1)_Y$ has a single gauge field B_μ , and its generator is the hypercharge Y .

The index L on $SU(2)_L$ refers to left-handedness, since the weak force only couples to fermions of left-handed chirality. In the electroweak theory this is accomplished by the fact that left-handed fermions (and right-handed antifermions) are $SU(2)$ doublets, while right-handed fermions are singlets. Since mass terms for Dirac fermions contain a combination of left- and right-handed fermions ($e_L e_R$), only the charged leptons are massive in the Standard Model. Before the discovery of neutrino oscillations, neutrinos were thought to be massless, which is reflected in the SM:

$$\text{doublet } (T = 1/2): \begin{pmatrix} \nu_e \\ e \end{pmatrix}_L \quad \text{singlet } (T = 0): e_R$$

The physically observable bosons are superpositions of the gauge fields W_μ^i and B_μ . The neutral bosons γ and Z are built from B and W^0 , rotated by the weak mixing angle, or Weinberg angle θ_W :

$$\begin{pmatrix} \gamma \\ Z \end{pmatrix} = \begin{pmatrix} \cos \theta_W & \sin \theta_W \\ -\sin \theta_W & \cos \theta_W \end{pmatrix} \begin{pmatrix} B \\ W^0 \end{pmatrix}$$

The Weinberg angle also relates the coupling constants of $SU(2)_L$ and $SU(1)_Y$, g and g' respectively, as well as the W and Z boson masses to each other:

$$\cos \theta_W = \frac{g}{\sqrt{g^2 + g'^2}} = \frac{M_W}{M_Z}$$

Similarly, W^\pm bosons of definite charge are created by mixing the W^1 and W^2 fields:

$$\begin{pmatrix} W^+ \\ W^- \end{pmatrix} = \frac{1}{\sqrt{2}} \begin{pmatrix} 1 & i \\ 1 & -i \end{pmatrix} \begin{pmatrix} W^1 \\ W^2 \end{pmatrix}$$

Up to this point, all bosons are massless. Explicitly adding mass terms to the Lagrangian would break local gauge invariance, as well as renormalizability. The way masses are generated in the SM while preserving gauge invariance is via the Higgs mechanism.

2.1.3. Higgs mechanism

Instead of explicitly inserting masses into the Lagrangian, the idea behind the Higgs mechanism is to add a scalar field, which gives mass to the gauge bosons by coupling to them. The Higgs field in the standard

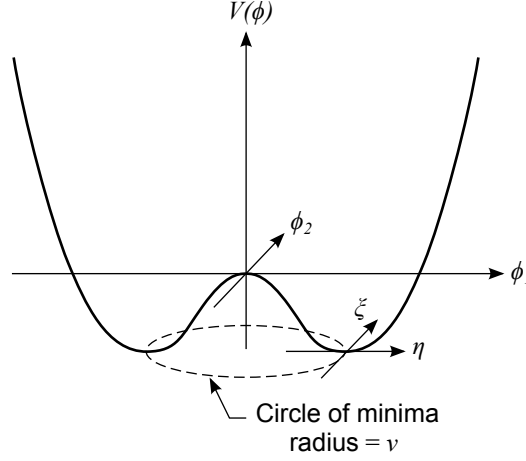


Figure 2.1. Sketch of the Higgs potential showing spontaneous symmetry breaking. The dimensions ϕ_3 and ϕ_4 have been omitted. From [3].

model is a complex doublet, meaning it has four real components:

$$\phi = \frac{1}{\sqrt{2}} \begin{pmatrix} \phi_1 + i\phi_2 \\ \phi_3 + i\phi_4 \end{pmatrix}$$

The Lagrangian of the Higgs field is given by

$$\mathcal{L}_{\text{Higgs}} = (\partial_\mu \phi)^\dagger (\partial^\mu \phi) + \mu^2 \phi^\dagger \phi - \lambda (\phi^\dagger \phi)^2, \quad (2.3)$$

where the last two terms can be thought of as a potential $V(\phi^\dagger \phi)$. The constant in front of the quartic term must be positive ($\lambda > 0$) in order for a stable minimum to exist. μ^2 could be either positive or negative, but the interesting case is when $\mu^2 < 0$. In this case, the potential resembles a “Mexican hat” (Figure 2.1). There is no longer one unique ground state around which the system is rotationally symmetric, but many possible ground states satisfying

$$\phi_1^2 + \phi_2^2 = v^2 \quad \text{with} \quad v^2 = -\frac{\mu^2}{\lambda},$$

which do not share the symmetry of the Lagrangian. This situation where a symmetry of the theory is not reflected in the ground state is called spontaneous symmetry breaking. It is now possible to expand the field ψ around the new minimum:

$$\phi(x) = \frac{1}{\sqrt{2}} (v + \eta(x) + i\xi(x)) \quad (2.4)$$

The effective degrees of freedom have now changed. Rotations around the bottom of the potential, in direction of ξ , correspond to a massless Goldstone boson. This degree of freedom is unphysical and can be removed by an appropriate gauge transformation. Oscillations in direction of η correspond to a new massive scalar, which is the Higgs boson.

After inserting the expansion of ϕ (2.4) into the Lagrangian and transforming away the Goldstone boson, one finds that the new Lagrangian contains terms like $\frac{1}{2} e^2 v^2 A_\mu^2$ which give the gauge boson associated with A_μ^2 a mass. In the full electroweak theory, one obtains

$$m_{W^\pm} = \frac{1}{2} g v, \quad m_Z = \frac{1}{2} v \sqrt{g^2 + g'^2}, \quad \text{and} \quad m_\gamma = 0.$$

Not only has the Higgs mechanism given the gauge boson masses (while preserving gauge invariance), but it is also possible to introduce masses for fermions, via Yukawa couplings to the Higgs field:

$$\mathcal{L}_{\text{Fermion}} = \bar{\psi} \gamma^\mu D_\mu \psi + G_f \bar{\psi} \phi \psi.$$

Here, the mass of a fermion is determined by the Higgs vacuum expectation value v , and its coupling to the Higgs field G_f :

$$m_f = \frac{1}{\sqrt{2}} G_f v.$$

2.1.4. Renormalization

In calculations in quantum field theory, infinities occur that have to be dealt with by regularization and renormalization. Consider a simple scalar field. The case where the particle propagates freely from A to B cannot be distinguished from cases where intermediate particles are created, so the amplitudes must be summed up (Figure 2.2). The amplitude for a particle going from A to B , neglecting mass, is in position space:

$$\langle 0 | \phi(B) \phi(A) | 0 \rangle \propto \frac{1}{(A - B)^2}, \quad (2.5)$$

where $(A - B)^2$ is the squared distance between points A and B . It is clear that the amplitude for detecting a particle at a point is higher the closer the point is to where it was emitted. However, if the distance goes to zero, (2.5) diverges. This divergency in the propagator is the source of most infinities in QFT.

Now consider the second diagram on the right hand side of Figure 2.2, where an intermediate particle is emitted and absorbed at the same point. The propagator for the loop is not well-defined, since its denominator would be zero. However, we can temporarily ignore processes below a certain length scale δ (or equivalently above a certain energy scale), assuming they should not be relevant for the result. In this case, the amplitude for this diagram is proportional to the quartic coupling λ , and to $1/\delta^2$. This process of replacing a divergency with a finite quantity is an example of regularization, in this case cut-off regularization.

The physically measurable quantities should not depend on the regularization parameter, and it is desirable to remove the parameter δ from the expression for the particle's mass. However one cannot just take the limit of $\delta \rightarrow 0$, as the term $1/\delta^2$ is divergent. The key to removing this quadratic divergency is the realization that the bare mass m_0 is not observed directly, but is a free parameter in the theory. It is possible to redefine m_0 and include a counterterm proportional to the divergency but with opposite sign. The “absorption” of the divergency removes the dependency on the cutoff and keeps the measurable mass m finite (Figure 2.2). This procedure is called renormalization.

Many quantities in QFT besides mass undergo renormalization, including the electric charge. An effect of renormalization is that the renormalized parameter is scale dependent. In case of the electric charge, this can be intuitively understood as a screening effect. A bare charged particle induces a polarization of the vacuum, which surrounds it by pairs of virtual particles that screen the bare particle's charge. When scattering with a low-energy probe, the probe will only “see” a reduced effective charge. As the energy of the probe (and thus the momentum exchange) increases, so will the measured charge and coupling constant (Figure 2.3). The coupling of the electromagnetic interaction is $\alpha \approx 1/137$ in the limit of low energies, but $\alpha(m_Z) \approx 1/128$ at the scale of the Z boson mass [4]. The running of parameters is governed by the renormalization group equations (RGE), which for example also determine the masses of supersymmetric particles from fundamental parameters at highest energies (Section 2.3).

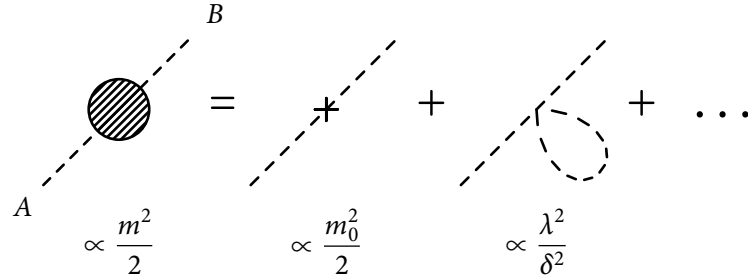


Figure 2.2. Renormalization of the scalar mass. Processes below the length scale δ are “blurred out” by the regulator. The first order loop is quadratically divergent, but this divergency is canceled by a counterterm in m_0 , such that the physical mass m is finite.

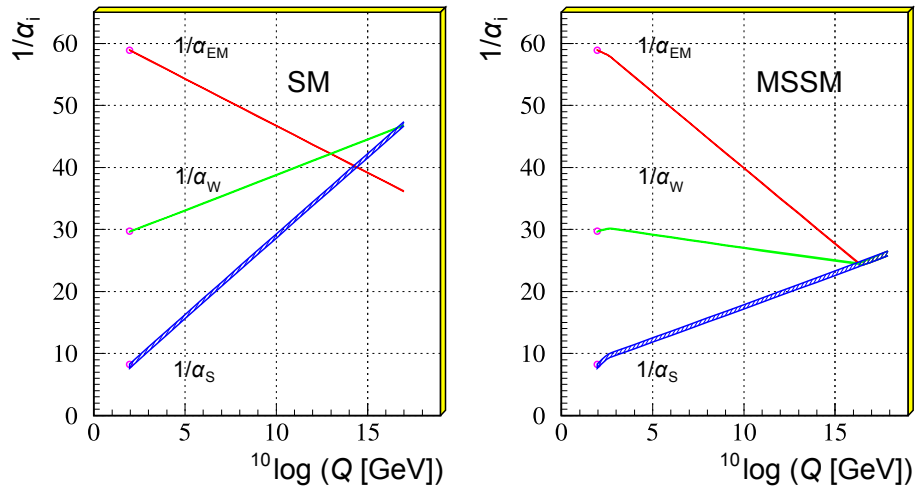


Figure 2.3. Running couplings in the standard model and the MSSM. The couplings of electromagnetic, weak, and strong force grow closer at higher energies, but do not unify at a single point. In the MSSM, new particles at the TeV scale modify the running of couplings such that they can unify at the GUT scale $Q \approx 10^{16}$ GeV. Adapted from [5].

2.2. Physics beyond the Standard Model

While the Standard Model has been extremely successful, there are several hints of theoretical and experimental nature that point out the need for an extension.

2.2.1. Hierarchy Problem

As described above, a scalar particle such as the Higgs boson receives large mass corrections proportional to the cutoff scale Λ squared. Assuming there is no “new physics” above the standard model, the latest point where we could set the cutoff is at the Planck scale, $\Lambda_P \approx 10^{16}$ GeV, since this is where quantum gravity effects are expected to become strong. These huge corrections to the scalar mass have to be balanced by a bare mass of similar magnitude but opposite sign to achieve a small, but finite observed mass. Since there is no general principle known that fixes the Higgs mass to $m_H \approx 126$ GeV, the bare mass could have any value a priori. It is considered very implausible that the bare mass is accidentally “fine tuned” to result in a small, but finite Higgs mass. This is called the “hierarchy problem”, since it is related to the large hierarchy between the Planck and the electroweak scale. The hierarchy problem is a strong indication that one of the assumptions is wrong, namely that there is no new physics at scales above the standard model. Supersymmetry is an interesting candidate for such new physics that elegantly resolves the hierarchy problem (Section 2.3).

It shall be mentioned that other solutions for the hierarchy problem have been proposed. One type of theory attempts to bring down the Planck scale closer to the electroweak scale. In the Randall-Sundrum-Model [6] this is done by assuming that gravity actually propagates in more than 3+1 dimensions, and is thus weak at macroscopic scales, while it is comparable to the other fundamental forces at microscopic scales. As a consequence, the actual Planck scale is only a few orders of magnitude above the electroweak scale, and there is no large hierarchy. Another kind of solution assumes that the Higgs boson is composite, thus avoiding the quadratic divergencies of fundamental scalars. The most prominent kind of composite Higgs theories are Technicolor models [7], where the Higgs is a bound state of quark like particles. So far however, all searches at the LHC for extra spatial dimensions [8] or composite scalars have turned out negative.

2.2.2. Grand Unification

At the large energy scale of $\Lambda_{\text{GUT}} \approx 10^{16}$ GeV, the running couplings of the electromagnetic, weak and strong forces seem to converge in the SM, but they do not actually meet in a point. It is an appealing idea that in an extension of the standard model, these couplings might meet, and that above a certain energy scale the three fundamental forces might have a simple unified description. This grand unification is thought of as analogous to the electroweak unification, or the unification of electric and magnetic forces to electromagnetism.

The first grand unified theory (GUT) proposed, and one of the simplest, is the $SU(5)$ GUT of Georgi and Glashow [9]. One can ask whether there is a simple gauge group G that contains the standard model gauge groups:

$$G \supset SU(3) \times SU(2) \times U(1).$$

Georgi and Glashow have shown that the simplest choice for such a unification group is $SU(5)$. This group has a five dimensional representation that can accommodate for the standard model fermions of one generation [10]. Since there are $16 + 16 = 2^5$ fermions per generation (if right-handed neutrinos are included), each Fermion can be described by five pieces of information (each 0 or 1), and thus be indexed by a five-component vector

$$(u, d, r, g, b).$$

Fermion	Condition	Particle	Q	T_3	Y
Left-handed quark	Y = even integer + 1/3	u_L	+2/3	+1/2	+1/3
		d_L'	-1/3	-1/2	+1/3
Left-handed lepton	Y = odd integer	ν_L	0	+1/2	-1
		e_L^-	-1	-1/2	-1
Right-handed quark	Y = odd integer + 1/3	u_R	+2/3	0	+4/3
		d_R	-1/3	0	+2/3
Right-handed lepton	Y = even integer	(ν_R)	0	0	0)
		e_R^-	-1	0	-2

Table 2.3. Hypercharge conditions for fermions from $SU(5)$ GUT. Hypercharge Y , electric charge Q and the third component of weak isospin are related by $Y = 2(Q - T_3)$. Right-handed neutrinos ν_R are conventionally not part of the Standard Model, yet included here.

Here u and d refer to the weak isospin up and down states, and r, g, b to the colors of QCD. An antiparticle is represented by flipping 0s and 1s, and leptons are given by $r = g = b = 0$. For example, the vector $(0, 1, 0, 1, 0)$ refers to a particle with isospin down, carrying green color charge: the green left-handed down quark d_L^g .

The symmetry transformations that make up $SU(5)$ can simply be described by certain 5×5 matrices which transform fermions into each other. These matrices have an obvious subset, which are the block diagonal matrices built from unitary 2×2 and 3×3 matrices:

$$M = \begin{pmatrix} \begin{pmatrix} U(2) \end{pmatrix} & 0 \\ 0 & \begin{pmatrix} U(3) \end{pmatrix} \end{pmatrix} \quad \text{where} \quad \det M = 1 \quad (2.6)$$

These transformations can be described as $S(U(2) \times U(3))$. This subclass of $SU(5)$ transformations does not mix particles with and without color charge. For the grand unified theory to contain the standard model, this group must be isomorphic to the standard model group, modulo some subgroup that acts trivially on the SM fermions. One finds that

$$S(U(2) \times U(3)) \cong G_{\text{SM}}/\mathbb{Z}_6.$$

The breaking of the $SU(5)$ symmetry down to the SM is accomplished physically by a scalar field ϕ in a fashion similar to the Higgs mechanism. ϕ transforms as a **5** representation of $SU(5)$. The role of the SM Higgs, breaking G_{SM} down to $SU(3)_C \times U(1)_{\text{EM}}$ and generating mass, is fulfilled by a second Higgs-like field Φ that transforms as **24**.

The $SU(5)$ theory makes it necessary that certain relations for the weak hypercharge Y are satisfied, which are listed in Table 2.3. These are a consequence of the requirement that \mathbb{Z}_6 acts trivially on all fermions, so that what remains after symmetry breaking, $G_{\text{SM}}/\mathbb{Z}_6$, is equivalent to the Standard Model. The hypercharge conditions are indeed valid for all SM fermions, and this requirement can explain the hypercharge formula, or the fractional charges of quarks.

Looking again at Equation (2.6), one can ask what elements of $SU(5)$ with off-diagonal entries mean. These do not belong to any standard model group, but represent new gauge bosons, called X and Y [11].

These new bosons can convert leptons and quarks into each other, and thus allow for baryon and lepton number violation, and in consequence, proton decay. Since the proton is stable (with a lower bound on its mean lifetime $\tau > 21 \cdot 10^{28}$ years [12]), one must find a way to suppress these processes. One way to ensure this is that the masses of the X and Y bosons are sufficiently high (of the order of 10^{15} GeV). On the positive side, the violation of baryon and lepton numbers via X and Y bosons might explain baryogenesis, or the question why there is more matter than antimatter in the universe. Another difficulty of the Georgi-Glashow model is the doublet-triplet splitting problem: The Higgs doublets come from a representation of the gauge group that also contains color triplet states, so there should be additional Higgs-like bosons carrying color charge. These would mediate proton decay as well, if sufficiently light. The doublet-triplet splitting problem is the question why the doublets are so light compared to the triplets.

While $SU(5)$ has been ruled out in its incarnation of the Georgi-Glashow model due to the non-observed proton decay, in general GUTs remain viable theories. Most of the shortcomings of $SU(5)$ can be solved in extensions of the theory, such as $SO(10)$ grand unification. In the following, we are only interested in general features of GUTs containing a $SU(5)$ or $SO(10)$ gauge group, and the consequences for supersymmetry.

2.2.3. Dark matter

In 1933, by analyzing the redshift of stars in galaxies, the astronomer Fritz Zwicky discovered that their motion apparently does not agree with the distribution of visible matter. In rotational curves, plots of stars' rotational velocity over distance from the galaxy center, a decline towards higher radii is expected according to Kepler's laws. However, almost universally, galaxies show a rotational curve that remains flat up to the visible edge of the galaxy (Figure 2.4). This motion suggests that there is much more matter in typical galaxies than currently accounted for. The current best estimate of the amount of this "dark" matter in the universe comes from the WMAP (Wilkinson Microwave Anisotropy Probe) experiment [13], which analyzed the cosmic microwave background. The contribution of conventional (baryonic) matter to the total energy density of the universe turns out to be only 4.6%, while dark matter accounts for 23% of the energy density. The remaining energy density is attributed to dark energy, which is the driving force in the accelerated expansion of the universe.

There have been many attempts to explain the nature of dark matter. It can be ruled out that it consists completely of dust, undiscovered planets or other dark bodies made of baryonic matter (massive compact halo objects, or MACHOs), since the necessary amount would obstruct the light of objects behind it. It is possible that a fraction of dark matter consists of neutrinos. However, since neutrinos are nearly massless, they would be highly relativistic, and thus would be "hot" dark matter. The amount of hot dark matter allowed is limited by observations of the cosmic microwave background. The nature of the remaining cold dark matter (CDM) remains a mystery, but one possibility is that it is made up of stable supersymmetric particles (Section 2.3).

2.3. Supersymmetry

Supersymmetry (SUSY) is a new proposed symmetry which relates bosons and fermions. The supersymmetry transformation Q takes a bosonic state to a fermionic state and vice-versa. The operator Q is fermionic, or spinor-valued, and thus anticommutes with itself, and with the momentum operator P_μ :

$$\begin{aligned}\{Q_\alpha, Q_\beta\} &= \{\bar{Q}_{\dot{\alpha}}, \bar{Q}_{\dot{\beta}}\} = 0 \\ \{Q_\alpha, P_\mu\} &= \{\bar{Q}_{\dot{\alpha}}, P_\mu\} = 0 \\ \{Q_\alpha, \bar{Q}_{\dot{\beta}}\} &= 2\sigma_{\alpha\dot{\beta}}^\mu P_\mu\end{aligned}$$

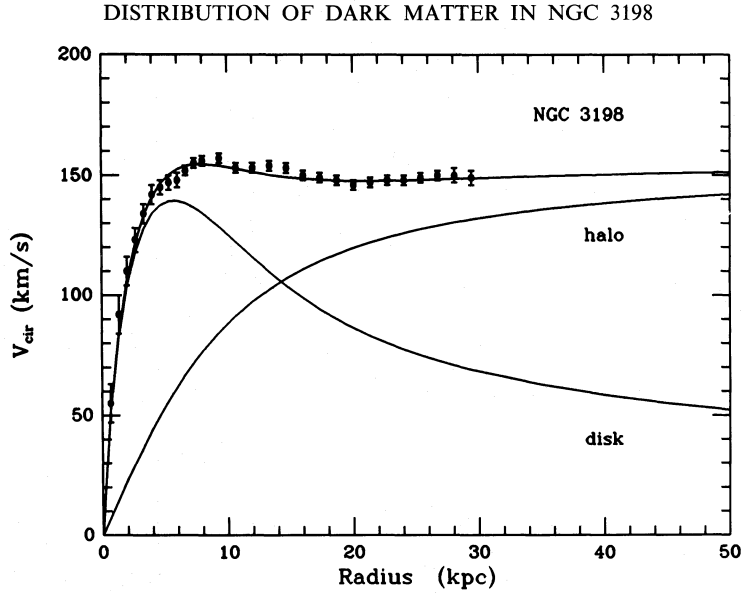


Figure 2.4. Rotation curve of the NGC3198 galaxy, from Doppler shift measurements of the 21.1 cm hydrogen line [14]. The “disk” graph is the rotation curve expected from the visible mass alone. The “halo” graph is the rotation curve of a hypothetical dark matter halo, fitted to give the observed total rotation curve. There is some uncertainty in the total observed mass, and other possible fits are presented in the publication, however the dark matter halo is dominant in each case, especially at high radii.

The interpretation of the last equation is that two successive supersymmetry transformations lead to a state with the original spin, but translated by an infinitesimal amount. In this sense, a SUSY transformation can be thought of as the square root of an infinitesimal translation. Thus, supersymmetry can be seen as an extension of space-time (Poincaré) symmetry.

Several possible supersymmetric extensions of the Standard Model are possible. In this case, we will only consider $N = 1$ SUSY, meaning there is only one set of supersymmetric operators Q, \bar{Q} . In the supersymmetric version of the standard model, each SM particle acquires one supersymmetric partner. Superpartners of fermions are named by prefixing “s-” to the SM particle’s name, reminding that they are scalars (spin 0), whereas partners of bosons are named by adding “-ino”.

It is clear that supersymmetry must be broken in nature, since superpartners of standard model particles have not yet been observed. For example, since selectrons are bosons, and do not obey Pauli’s exclusion principle, selectrons with the same mass as electrons would accumulate in the ground state of atomic shells, disturbing the structure of the periodic table.

A supersymmetry breaking mechanism that does not introduce new quadratic divergencies to scalar masses is called “soft” SUSY breaking. This was first proposed by Georgi and Dimopoulos [15]. The symmetry breaking is thought to arise in a “hidden sector” of particles and is then mediated to the standard model sector. Different breaking scenarios are possible and lead to different sets of parameters in the theory. On specific breaking scenario, minimal supergravity, is considered below.

2.3.1. R Parity

A general supersymmetric theory contains processes that allow for baryon or lepton number violation, which would lead to proton decay (similarly as in the $SU(5)$ theory). One way to prevent this is to introduce a new conserved quantum number called R parity. R parity is multiplicative, and standard model particles

have $R = +1$, while all superpartners have $R = -1$. It can be formally defined by

$$R = (-1)^{3(B-L)+2S},$$

where B and L are baryon and lepton numbers, and S is the particle's spin. It is possible to consider both R parity conserving (RPC) and violating (RPV) theories, where RPV theories must suppress proton decay by other means. In the following, R parity conservation shall be assumed. If R is conserved, SUSY particles can only be produced in pairs. Furthermore, SUSY particles can only decay into other SUSY particles. An important consequence of this is that the lightest supersymmetric particle (LSP) would be stable. A stable LSP would be a good candidate for cold dark matter, provided it has no color or electromagnetic charge, and only interacts via the weak force or gravity. Charged LSPs at the EW scale can be ruled out by a combination of direct searches and cosmological bounds [16]. If the LSP was charged, it would be able to form hydrogen-like atoms, leading to super-heavy water molecules. The abundance of LSPs in our galaxy needed to explain dark matter would imply that a significant amount of super-heavy water could be found on earth. However, all searches for such molecules have been negative. In fact, bounds from direct searches have excluded charged LSP densities far less than what would be required to explain dark matter. Furthermore, charged LSPs would likely be visible since they interact with the electromagnetic field, and thus would not be “dark” matter. Similarly, LSPs with color charge can also be ruled out as a source of dark matter [17].

2.3.2. The Minimal Supersymmetric Standard Model (MSSM)

The MSSM is the supersymmetric extension of the standard model with the lowest number of new particles. It includes one set of SUSY operators, so each standard model particle acquires one superpartner. As opposed to the standard model, the MSSM has not one but two Higgs doublets H_u and H_d , to generate mass for the up- and down- type fermions, respectively. In the SM, down-type quarks couple to the single Higgs field, and up-type quarks to its complex conjugate, but this is not possible in a supersymmetric theory since the superpotential must be analytic to preserve the symmetry. Another reason is that the Higgsino as a new Fermion introduces a new anomaly to the theory, and to cancel this the other Higgs doublet, which has opposite hypercharge, is necessary. Since two complex scalar doublets have eight degrees of freedom, and three are “eaten” by the W and Z bosons, five physical Higgs bosons remain. Two are neutral scalars, h_0 and H_0 , one is a pseudoscalar A_0 , and two are charged scalars H^+ and H^- . As in the electroweak theory, fields with the same quantum numbers mix to yield mass eigenstates. There are four neutral spin-1/2 particles after mixing, and two charged ones. These neutralinos $\tilde{\chi}_{1,2,3,4}^0$ and charginos $\tilde{\chi}_{1,2}^\pm$ are simply numbered by ascending mass. A list of all particles in the MSSM is given in Table 2.4.

In the MSSM, supersymmetry is softly broken, and the most general parametrization of soft SUSY breaking adds about 115 new parameters to the model. By looking at concrete breaking mechanisms, or making simplifying assumptions, one can greatly reduce this number of parameters. One such breaking scenario is minimal supergravity (mSUGRA), which predicts a unification of certain parameters at the GUT scale, simplifying the MSSM to five parameters. The MSSM constrained by these assumptions is also called the CMSSM (constrained MSSM)¹. The five parameters are:

- Unified scalar mass m_0 at the GUT scale, $m_0^2 = M_{Q,u,d,L,e}^2$
- Unified gaugino mass $m_{1/2}$ at the GUT scale, $m_{1/2} = M_1 = M_2 = M_3$

¹Conventionally, the terms mSUGRA and CMSSM are often used interchangeably to refer to the five-parameter theory resulting from unification assumptions. Here, CMSSM refers to the parametrization, while mSUGRA refers to the concrete breaking scenario leading to this parametrization. It should be noted that strictly speaking, minimal supergravity imposes two additional constraints on parameters beyond the CMSSM, that are not considered here [18]. These are $B_0 = A_0 - m_0$ for the common bilinear coupling, and $m_{3/2} = m_0$ for the gravitino mass.


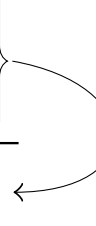
Particle	Symbol	Spin	Particle	Symbol	Spin
quark	q_R, q_L	$1/2$	squark	\tilde{q}_R, \tilde{q}_L	0
charged lepton	ℓ_R, ℓ_L	$1/2$	slepton	$\tilde{\ell}_R, \tilde{\ell}_L$	0
neutrino	ν_L	$1/2$	sneutrino	$\tilde{\nu}$	0
SU(3) gluon	g	1	gluino	\tilde{g}	$1/2$
SU(2) W	W_i	1	wino	\tilde{W}_i	$1/2$
SU(1) B	B	1	bino	\tilde{B}	$1/2$
Higgs bosons	h_0, H_0	0	Higgsinos	\tilde{h}_0, \tilde{H}_0	$1/2$
	h^\pm, A			\tilde{h}^\pm, \tilde{A}	
					
W^\pm and Z bosons photon γ			2 charginos $\tilde{\chi}_i^\pm$ 4 neutralinos $\tilde{\chi}_i^0$		

Table 2.4. Particles of the minimal supersymmetric standard model (MSSM). The particles in grey mix to create the electroweak gauge bosons, and the charginos and neutralinos.

- Common trilinear coupling $A_0 = A_u = A_d = A_e$
- Ratio of the Higgs vacuum expectation values, $\tan \beta = v_u/v_d$
- Sign of the Higgsino mass parameter, $\text{sgn } \mu$

The Higgs mass parameter μ relates the Higgsino masses at the unification scale to the unified scalar mass, by $m_{H_{u,d}}^2 = m_0^2 + \mu^2$ (Figure 2.5). The requirement of electroweak symmetry breaking gives the conditions $\partial V / \partial H_{u,d} = 0$, where V is the Higgs potential (2.3), and this fixes the absolute value of μ :

$$|\mu|^2 = \frac{1}{2} \left(\frac{|m_{H_d}^2 - m_{H_u}^2|}{\cos 2\beta} + m_{H_u}^2 - m_{H_d}^2 - m_Z^2 \right) \quad (2.7)$$

Depending on m_0 and $m_{1/2}$, the CMSSM parameter space can be split into four different regions. Each region has a different dominant mechanism by which the charginos and neutralinos produced in the early universe are annihilated to achieve the correct present-day dark matter density.

- The bulk region at low m_0 and $m_{1/2}$. This is the most well-studied region, where also this search will take place. The bulk region has no accidental degeneracies of superpartner masses, and typically a lightest neutralino mass of $m(\tilde{\chi}_1^0) < 200$ GeV.
- The focus point region at high $m_0 \gg m_{1/2}$. In this region, the neutralino $\tilde{\chi}_1^0$ is mostly Higgsino-like. The production (and annihilation) cross section of charginos and neutralinos is greatly amplified. Sleptons are very heavy, and most likely out of reach of current collider experiments.
- The rapid annihilation funnel, extending to high m_0 and $m_{1/2}$, where the cross section is enhanced by intermediate heavy Higgs bosons A .
- The co-annihilation region at low m_0 and high $m_{1/2}$, near the disallowed region where the charged slepton would be the LSP. Here, the LSP is only slightly lighter than the slepton, leading to an enhanced LSP annihilation rate.

A search for the production of charginos and neutralinos, especially at the lower center-of-mass energy of the Tevatron compared to the LHC, is sensitive in the low $m_{1/2}$ area of the CMSSM, which corresponds

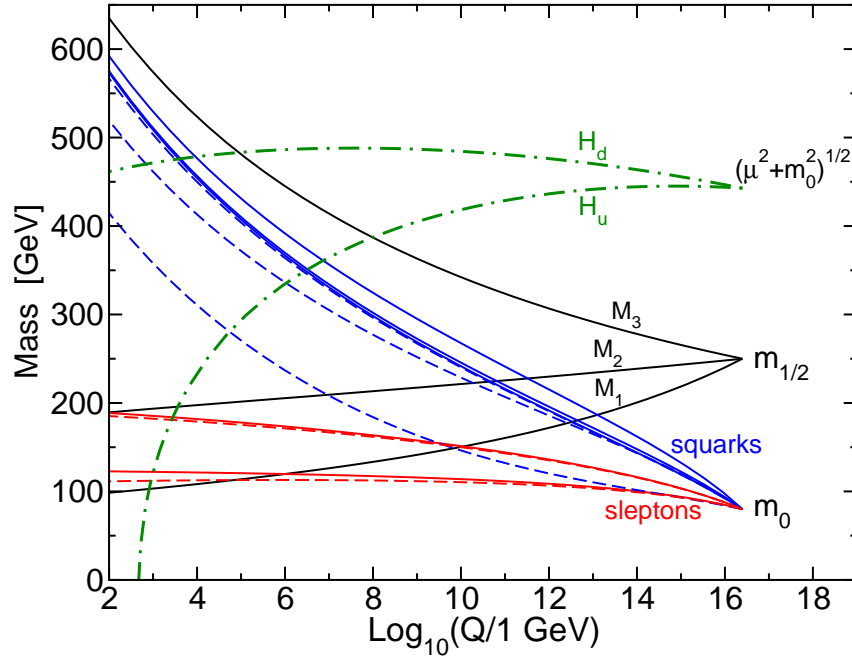


Figure 2.5. Running of the SUSY parameters in the CMSSM, from [19].

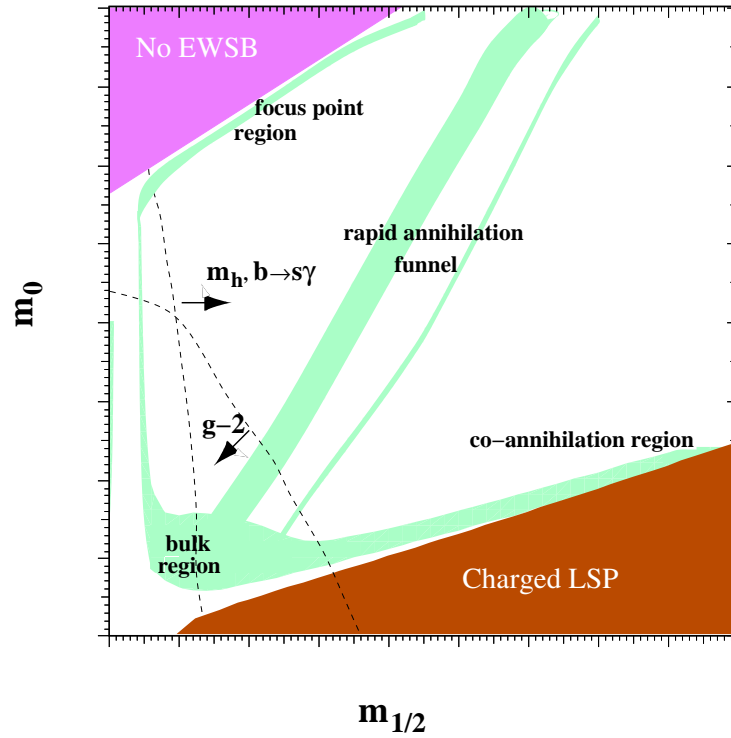


Figure 2.6. Schematic plot of different regions in the (c)MSSM, from [20].

to the bulk and the focus point region. However, while parameter points near the focus point region have beneficial low masses and high-cross sections, they are often not viable due to lack of electroweak symmetry breaking. For this reason, the search will be restricted to the bulk region.

2.3.3. Fine-Tuning and Hierarchy Problems

As noted before, supersymmetry provides an elegant solution to the hierarchy problem. The mass of the Higgs boson receives large corrections from loop diagrams involving standard model particles, which are proportional to the square of the cutoff scale Λ . By adding a partner to each standard model particle, new corrections are introduced. If supersymmetry is unbroken, these have the same magnitude as the original corrections, but opposite sign (since they have different spin), and thus cancel out exactly and naturally (Figure 2.7). With broken supersymmetry, the cancellation is approximate, but still good enough to provide a solution to the hierarchy problem, as long as the superpartners are not too heavy.

While supersymmetry can solve the hierarchy problem, a second, smaller source of fine-tuning remains, concerning the mass of the Z boson. In the MSSM, it is related to the Higgs mass parameters by (see also (2.7))

$$m_Z^2 = -2(|\mu|^2 + m_{H_u}^2) + \dots \quad (2.8)$$

Here, $|\mu|$ and $|m_{H_u}|$ are unnaturally much larger than m_Z (note that $m_{H_u}^2$ can be negative). This is called the little hierarchy problem, or the μ problem. The absolute values of $|\mu|^2$ and $m_{H_u}^2$ can serve as a measure of fine tuning. The value of $m_{H_u}^2$ at the TeV scale can be calculated from high-scale parameters. Assuming a unification scale of $M_U = 2 \cdot 10^{16}$ GeV and $\tan \beta = 10$ one has at two-loop level [21]:

$$\begin{aligned} -m_{H_u}^2 \approx & \underline{1.82M_3^2} - 0.21M_2^2 + 0.16M_3M_2 + 0.023M_1M_3 + 0.006M_1M_2 \\ & - 0.006M_1^2 - 0.32A_0M_3 - 0.07A_0M_2 - 0.022m_0^2. \end{aligned} \quad (2.9)$$

Here, the largest contribution is typically from the term including M_3 , which is related to the gluino mass. High lower limits on the gluino mass tend to imply large fine tuning, especially in the CMSSM where gaugino masses are unified ($M_i = m_{1/2}$). This was one major motivation behind considering non-universal gaugino masses, as described in Section 2.4.1. In areas of the parameter space where the ratio M_3/M_2 is small, fine-tuning can be reduced significantly.

A more sophisticated measure of fine-tuning was introduced by Barbieri and Giudice [22], in an attempt to put an upper limit on possible superpartner masses. Their approach was to note that a variable at one scale, in this case the Z boson mass, should not depend too much on a parameter a at a more fundamental (higher energy) scale. They introduced the measure

$$c(m_Z^2, a) = \left| \frac{\partial \ln m_Z^2}{\partial \ln a} \right| = \left| \frac{a}{m_Z^2} \frac{\partial m_Z^2}{\partial a} \right| \quad (2.10)$$

Here, the logarithms of m_Z^2 and a enter, so that $c(m_Z^2, a)$ depends on their orders of magnitude, roughly how many orders of magnitude the Z mass changes when a is changed by a certain amount. In case of multiple parameters, the maximum $c = \max\{c_a\}$ can be used. Barbieri and Giudice chose to put the threshold of naturalness at $c(m_Z^2, a) \lesssim 10$. Models with a larger value of $c(m_Z^2, a)$ are fine-tuned according to this criterion. However, since there is no distinguished or objective measure in the parameter space, it is difficult to quantify fine-tuning and to pick an exact cutoff. Naturalness considerations cannot be used to strictly falsify a certain hypothesis, but they are valuable for motivation and guidance.

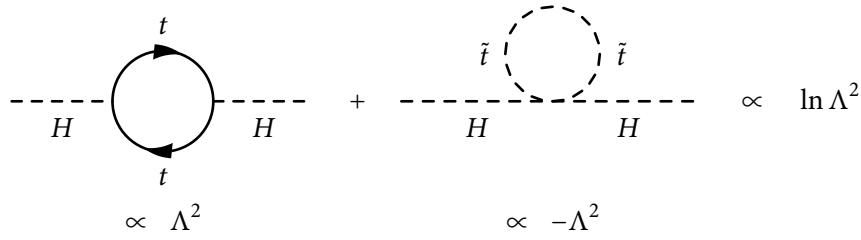


Figure 2.7. Resolution of the hierarchy problem by supersymmetry. As a scalar particle, the Higgs boson receives quadratically divergent corrections to its mass through loops. Supersymmetry adds superpartners with the same properties, but different spin. The contributions of the superpartners to the Higgs mass have the same magnitude, but different sign, which leads to a natural cancellation.

2.4. Non-Universal Models

While most often models with high-scale universalities such as mSUGRA are studied, universality is not a necessity. The general MSSM permits for example to choose the scalar masses M_1 , M_2 and M_3 at the GUT scale independently from each other, instead of having a unified $m_{1/2}$ like in the CMSSM.

This additional freedom has interesting consequences for SUSY searches. Given a certain model, for example mSUGRA, different search channels are linked. A search for gluinos that has excluded a certain parameter point $(m_0, m_{1/2}, \dots)$ also excludes the existence of charginos with properties predicted for this point. *Assuming the validity of the model*, the additional search would be unnecessary. This does not mean the charginos of these masses cannot exist, but observing them after excluding their co-predicted gluinos will be at odds with the assumption of the mSUGRA scenario. A scenario will make multiple predictions per parameter point – some easier, some harder to evaluate. By choosing the right channel, one can quickly exclude large areas of the parameter space. For example, the current ATLAS limits on mSUGRA are largely driven by zero-lepton channel searches (Figure 2.21).

If the underlying assumption of a certain scenario is softened, channels are not necessarily linked anymore. A gluino of a given mass does not imply charginos with certain properties, and not finding gluinos in a certain mass range does not make it unnecessary to search for other particles, since the masses of both particles can be adjusted independently.

The mass parameters do not have to be chosen completely arbitrarily however. Just like the mSUGRA breaking scenario implies a unified scalar mass m_0 , other assumptions about GUT-scale physics may imply other relations between parameters of the MSSM. In the following, the consequence of $SU(5)$ grand unification for the high-scale SUSY parameters will be explored.

2.4.1. Non-Universal Gaugino Masses from $SU(5)$

In supersymmetric versions of grand unified theories, the masses of gauginos at the unification scale may become non-universal [23]. The $SU(5)$ group containing the standard model has a 24-dimensional representation (24), which gives rise to F -terms that contribute to the gaugino masses². The mass ratio at the GUT scale imposed by the F -terms is

$$M_1 : M_2 : M_3 = 1 : 3 : -2.$$

²This not only occurs in the supersymmetric $SU(5)$ GUT, but also in other models. For instance, in $SO(10)$, the 54 representation of the $SO(10)$ that contains the GUT $SU(5)$ allows the same terms.

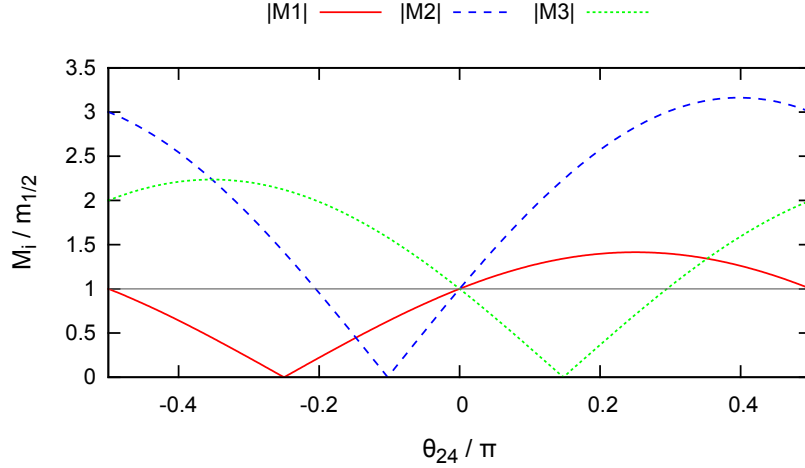


Figure 2.8. Dependence of the absolute gaugino mass parameters $|M_i|$ on θ_{24} , shown in units of the unified gaugino mass $m_{1/2}$. Since the magnitude of M_i is taken, the functions have a period of π .

In this scenario, any linear combination of this mass ratio and the universal ratio, $1 : 1 : 1$, may be realized. We can parametrize the mixing of both contributions by the angle θ_{24} , which is defined such that $\theta_{24} = 0$ results in universal masses (as in mSUGRA), and $\theta_{24} = \pm\pi/2$ results in a maximal contribution of the F -terms. A transformation of $\theta_{24} \rightarrow \theta_{24} + \pi$ leaves the magnitudes of M_i constant but flips the signs, which effectively is the same point with the signs of μ and the scalar cubic couplings flipped. Given a common gaugino mass parameter $m_{1/2}$, and θ_{24} , the individual gaugino masses at the unification scale are given by:

$$\begin{aligned} M_1 &= m_{1/2} (\cos \theta_{24} + \sin \theta_{24}) , \\ M_2 &= m_{1/2} (\cos \theta_{24} + 3 \sin \theta_{24}) , \\ M_3 &= m_{1/2} (\cos \theta_{24} - 2 \sin \theta_{24}) . \end{aligned}$$

2.4.2. Exploration of Parameter Space

In this analysis, we are interested in the co-production of charginos $\tilde{\chi}_1^\pm$ and neutralinos $\tilde{\chi}_2^0$ (Figure 2.9), which then decay leptonically into three leptons, a neutrino, and LSPs (Figures 2.10 and 2.11). To understand how the various observables, such as sparticle masses, branching ratios, and cross sections depend on the model's parameters, we perform an exploration of the parameter space. As a starting point, we choose the parameters

$$m_0 = 160 \text{ GeV}, \quad m_{1/2} = 160 \text{ GeV}, \quad A_0 = 0 \text{ GeV}, \quad \text{sgn } \mu = +1, \quad \tan \beta = 10, \quad \theta_{24} = -0.15\pi. \quad (2.11)$$

This point was selected since it is within reach of the DØ experiment, and parameter values are similar to previously studied mSUGRA points. It should be noted that this specific point is ruled out by other experiments, and particularly has too low a Higgs mass of $m_h < 126 \text{ GeV}$. In the following, individual parameters will be varied, while studying the behavior of chargino and neutralino masses, the Higgs mass (m_{h_0}), and the branching ratios into leptons.

m_0 By varying the scalar mass m_0 , the masses of interest for this analysis, $m(\chi_{1,2}^0)$ and $m(\chi_1^\pm)$ do not change notably. The branching ratio of the chargino/neutralino pair into trileptons has its maximum around 160 GeV (Figure 2.12).

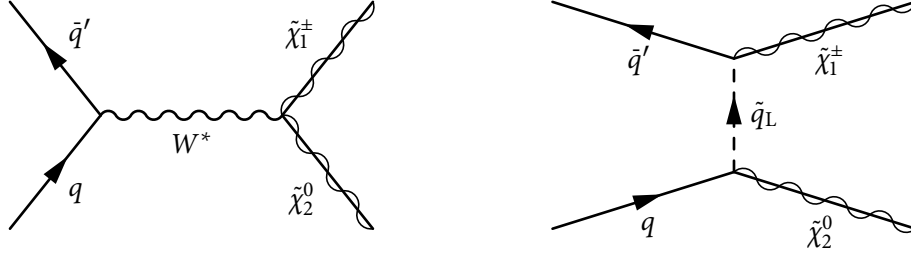


Figure 2.9. Co-production of charginos $\tilde{\chi}_1^\pm$ and neutralinos $\tilde{\chi}_2^0$ can occur via an off-shell W boson (left), or by exchange of a squark \tilde{q}_L (right).

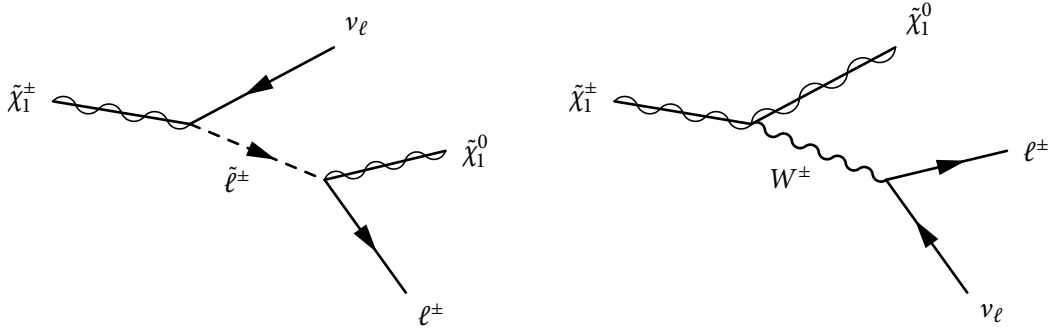


Figure 2.10. Leptonic decays of the chargino $\tilde{\chi}_1^\pm$. The chargino can decay via slepton or W boson, with the prevalent mode depending on the sparticle masses. The final state includes a charged lepton, a neutralino $\tilde{\chi}_1^0$, and a neutrino.

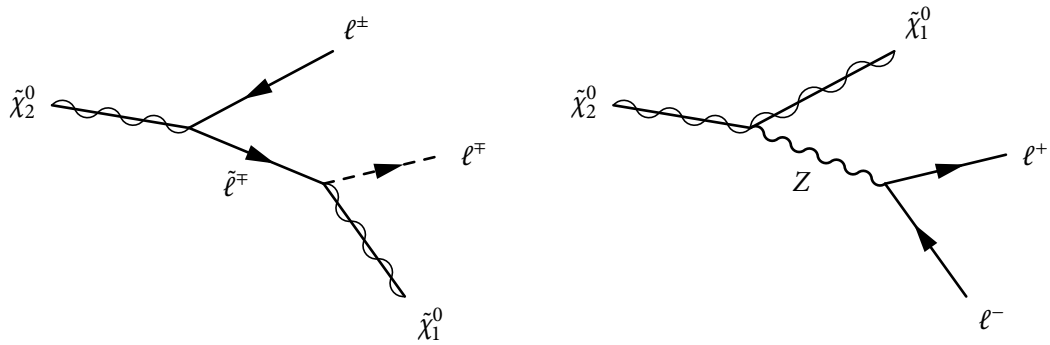
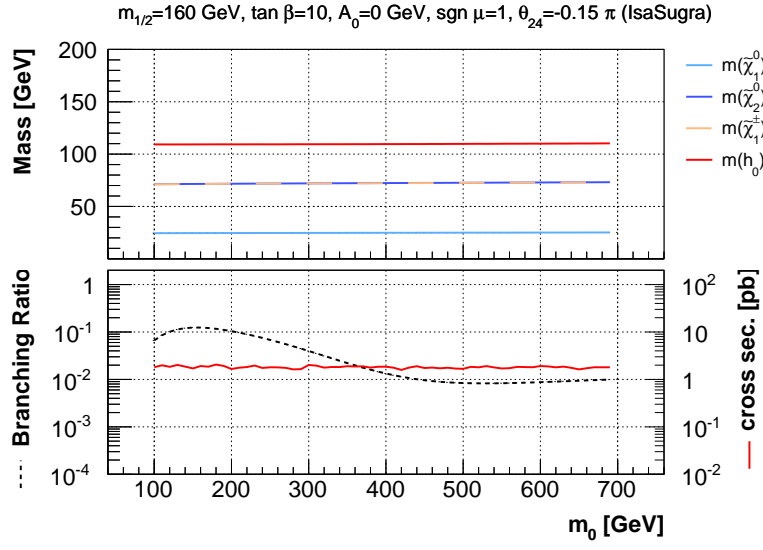
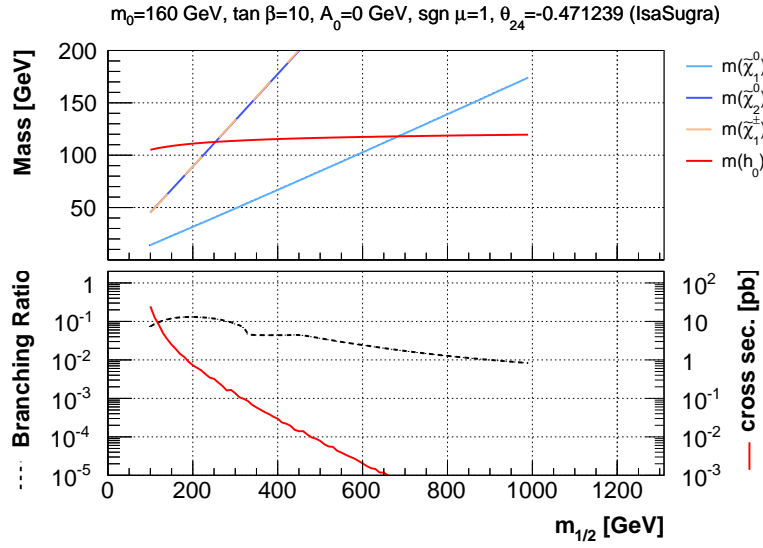


Figure 2.11. Leptonic decays of the second-lightest neutralino $\tilde{\chi}_2^0$. The decay can proceed via slepton or Z boson, and the final state includes a same-flavor opposite-sign lepton pair, and a neutralino $\tilde{\chi}_1^0$.

- $m_{1/2}$** The gaugino mass parameter $m_{1/2}$ determines the gaugino masses M_i at the unification scale. The masses of charginos and neutralinos are proportional to $m_{1/2}$, and the mass of the lightest Higgs boson h_0 increases with m_0 , but reaches a plateau at around the TeV scale. The branching ratio into trileptons declines with increasing $m_{1/2}$ (Figure 2.13).
- $\tan \beta$** With growing $\tan \beta$, the masses of the lightest Higgs and the LSP increase, while the masses of $\tilde{\chi}_1^\pm$ and $\tilde{\chi}_2^0$ decrease. The dependency is strongest at low $\tan \beta$ ($\tan \beta \lesssim 10$), with the masses reaching a plateau afterwards. Since the mass difference and the branching ratio into trileptons go down, the reach of the analysis decreases with $\tan \beta$. At higher values, the decay modes into taus become dominant (Figure 2.14).
- θ_{24}** Going from the mSUGRA value of $\theta_{24} = 0$ to lower values, the cross section increases strongly, while the chargino and neutralino masses decrease. In the area around $\theta_{24} \approx -0.1\pi$, the cross section diverges, and the spectrum generation failed to consistently converge. This area is experimentally excluded due to too low chargino masses, and has been omitted. Around $\theta_{24} = -0.15\pi$, there is a plateau in the branching ratio, and the cross section is comparable to the mSUGRA case (Figure 2.15).
- A_0** The masses of charginos and neutralinos are fairly constant wrt. variation of the trilinear coupling A_0 . Towards low A_0 ($A_0 = -2m_0$) the Higgs boson mass is increased, at the expense of the trilepton branching ratio (Figure 2.16).
- m_{top}** The mass of the top quark has a strong influence on the Higgs boson mass, since it contributes loop corrections to it. In this analysis, a conventional top mass of $m_t = 172.5$ GeV is used for background and signal MC, since the official background MC samples are generated and certified with this value, and to remain comparable to previous analyses. The current best measurement of the top quark mass, 174.34 ± 0.64 GeV from a combination of DØ and CDF results [24], increases the predicted Higgs mass by the order of 3 GeV (Figure 2.17). The LHC and Tevatron combination [25], including results from ATLAS and CMS, gives a slightly smaller value of 173.34 ± 0.76 GeV, resulting in a Higgs mass increase of approximately 2 GeV (Figure 2.17).

Next, the $(m_0, m_{1/2})$ plane is explored. In order to estimate the reach of the analysis, the previous DØ search for charginos and neutralinos is taken as a reference (Figure 2.18). This is compared with the cross section times branching ratio into trileptons in the plane (Figure 2.19). The reach of the old analysis is conservatively estimated to be up to $\sigma \times BR < 0.03$ pb, which is the value at $m_0 = 100$ GeV and $m_{1/2} = 230$ GeV. Note, however, that this estimate does not take the signal efficiency into account, which is the third factor next to cross section and branching ratio which determines the sensitivity for a given signal point. Especially the “dip” around the line of $m(\tilde{\ell}) = m(\tilde{\chi}_2^0)$ is not considered. In this area, the lightest slepton and the neutralino-2 have very similar masses, and leptons emitted from the $\tilde{\chi}_2^0$ will have low p_T and might evade detection. Above and below the dip are regions of two- and three-body-decay of the $\tilde{\chi}_2^0$, respectively, which have different kinematics. A search will have a different reach with respect to $\sigma \times BR$ in both regions.

The case of NUGM with $\theta_{24} = -0.15\pi$ and $\tan \beta = 10$ is shown in Figure 2.20. Important differences are that the cross section is increased for a given scalar mass m_{12} compared to Figure 2.19, and that the sensitive area is shifted towards higher gaugino masses m_0 .

**Figure 2.12.** Varying the value of m_0 .**Figure 2.13.** Varying the value of $m_{1/2}$.

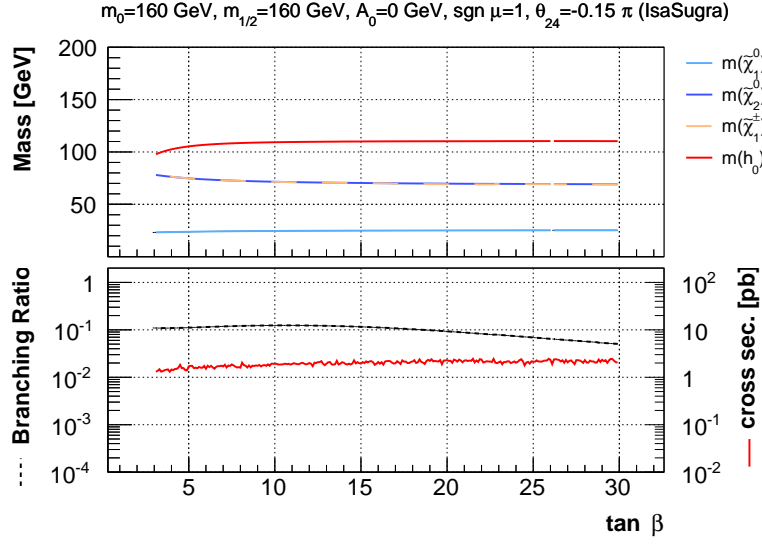


Figure 2.14. Varying the value of $\tan \beta$. Showing the masses of charginos, neutralinos and lightest Higgs, as well as the branching ratio into electrons and muons, including leptonically decaying taus, and the production cross section of charginos and neutralinos.

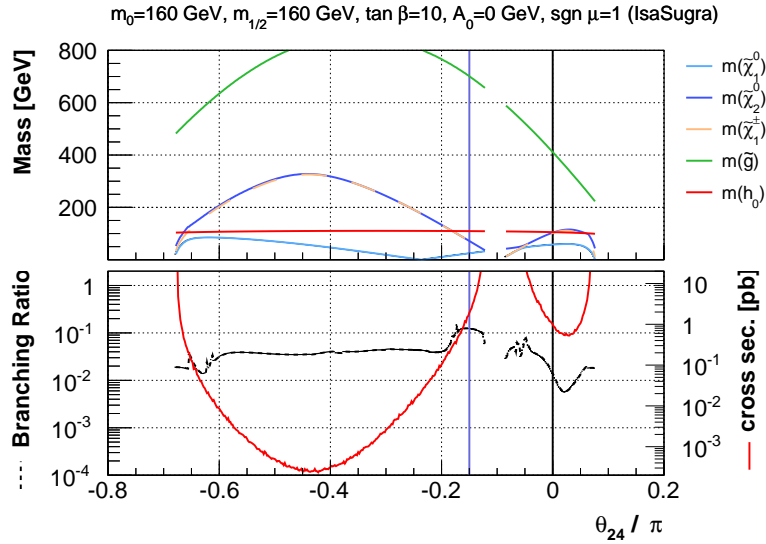


Figure 2.15. Varying the value of θ_{24} . At $\theta_{24} = 0$, the model corresponds to the CMSSM. Around $\theta_{24} = -0.1\pi$, the chargino masses approach zero while the cross section diverges. The vertical line at $\theta_{24} = -0.15\pi$ indicates the value chosen for study in the $m_0, m_{1/2}$ plane.

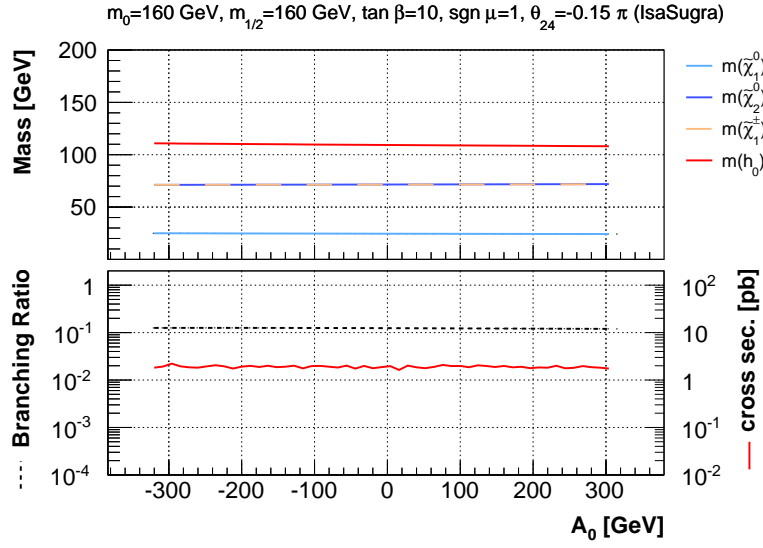


Figure 2.16. Varying the value of A_0 .

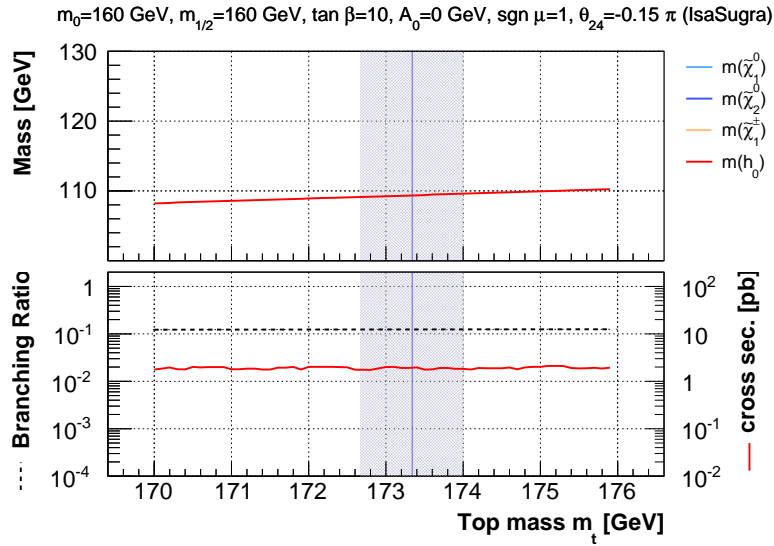


Figure 2.17. Varying the value of the top quark mass. The vertical line and shaded area indicate the current best value and total uncertainty, $173.34 \pm 0.76 \text{ GeV}$, from [25]. In this analysis, a conventional value of $m_t = 172.5 \text{ GeV}$ is used for signal and top background MC.

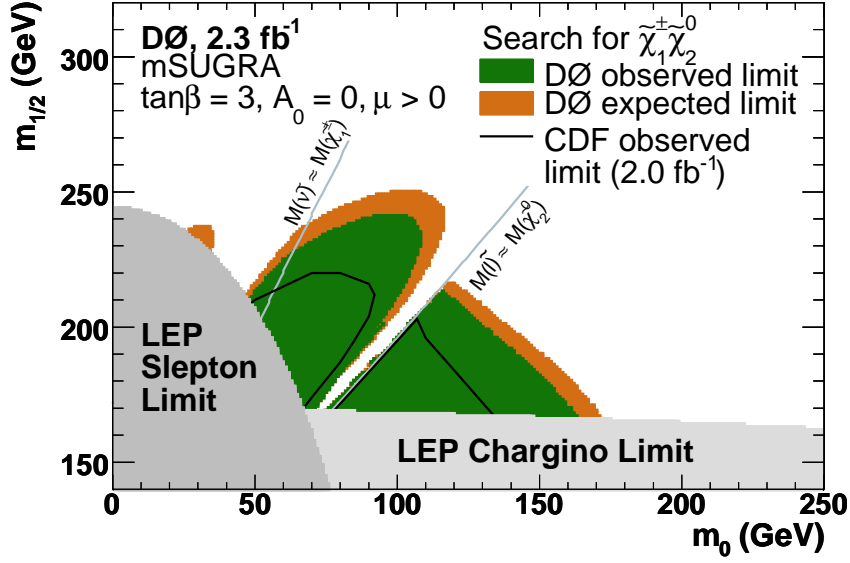


Figure 2.18. For comparison, mSUGRA limits set by a previous DØ search for charginos and neutralinos with 2.7 fb^{-1} [26].

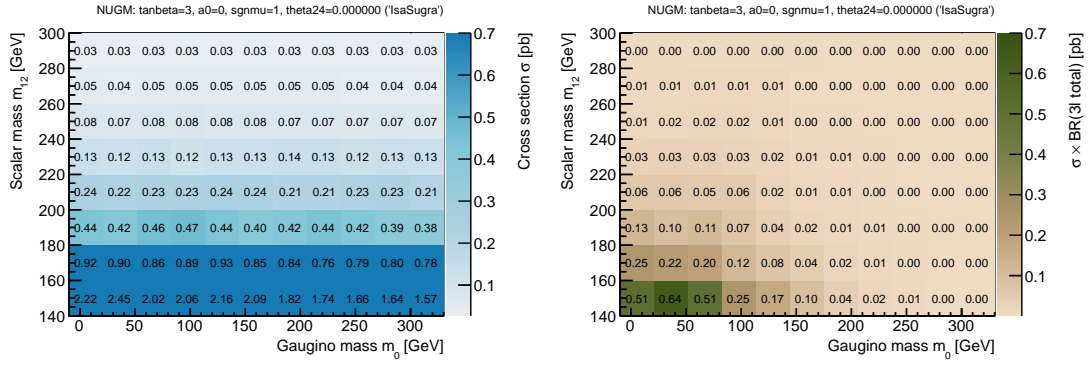


Figure 2.19. Exploration of the mSUGRA $(m_0, m_{1/2})$ plane, as explored in a previously published DØ search. Here, $\tan\beta = 3$, $A_0 = 0 \text{ GeV}$ and $\text{sgn}\mu = +1$. Left is cross section, right is cross section times branching ratio into three light leptons (including intermediate τ decays into light leptons). The old analysis was sensitive up to $m_0, m_{1/2} = 100, 250 \text{ GeV}$ or $\sigma \times BR(3\ell) \approx 0.03$.

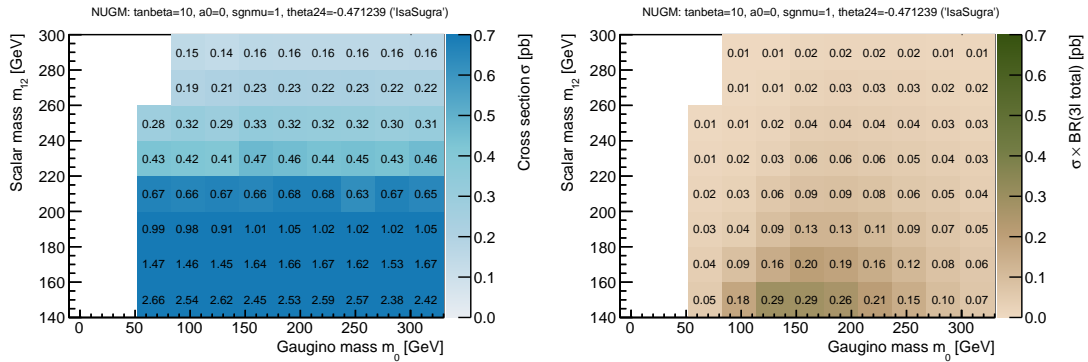


Figure 2.20. Same as above but with $\tan\beta = 10$ and $\theta_{24} = -0.15\pi$ (non-universal gaugino masses).

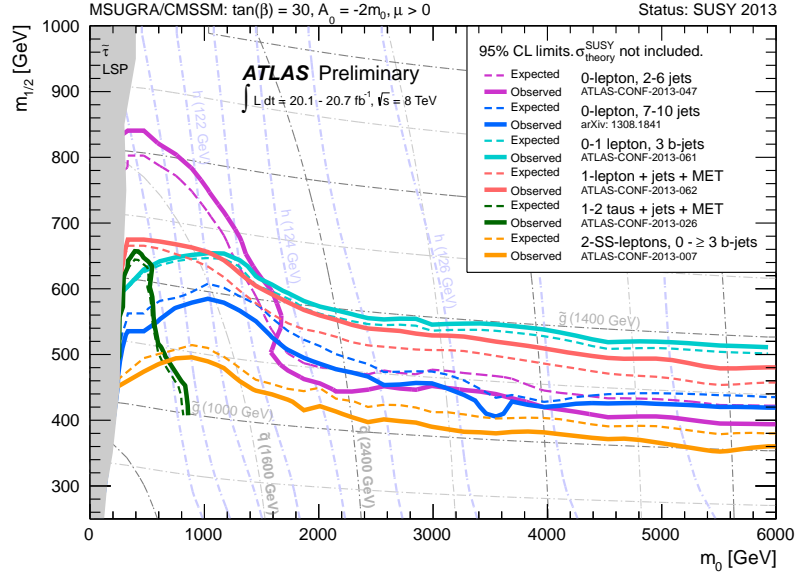


Figure 2.21. Summary of ATLAS searches in the $(m_0, m_{1/2})$ plane of the mSUGRA/CMSSM model, showing exclusion limits at 95% CL for the 8 TeV data set. In this plot, $\tan \beta = 30$, $A_0 = -2m_0$ and $\mu > 0$. From the ATLAS Supersymmetry physics group [27].

2.5. Review of present constraints on SUSY

Before we discuss the details of this analysis, a brief review of the present constraints on supersymmetric models shall be given. These constraints come from several areas: direct searches for the production of SUSY particles with colliders, indirect searches through precision measurements, direct searches for dark matter, and finally constraints from theoretical considerations.

2.5.1. SUSY searches with colliders

By far the most stringent constraints come from searches at the LHC. In the following, some relevant results will be described. For simplicity, this will focus on results from the ATLAS experiment, while it should be noted that the CMS experiment has published very comparable limits. An overview of many searches in the mSUGRA/CMSSM model showing the reach of the ATLAS experiment in the $(m_0, m_{1/2})$ plane is given in Figure 2.21.

Gtt simplified model

In this model, gluino pair production is considered. The gluinos are heavy enough to decay into a $t\bar{t}$ pair and a lightest neutralino $\tilde{\chi}_1^0$. This analysis, performed on $\sqrt{s} = 8$ TeV data, is split into four channels (Figure 2.22):

- Zero leptons, with 7–10 jets at $\int \mathcal{L} = 20.3 \text{ fb}^{-1}$ [28]. This analysis covers the largest area in the low m_0 , high $m_{1/2}$ region.
- Zero or one lepton, at least 3 b -tagged jets, $\int \mathcal{L} = 20.1 \text{ fb}^{-1}$ [29]. This analysis has the highest reach especially in the high m_0 region, and in the limit of low $\tilde{\chi}_1^0$ mass, excludes gluino masses up to 1.4 TeV.

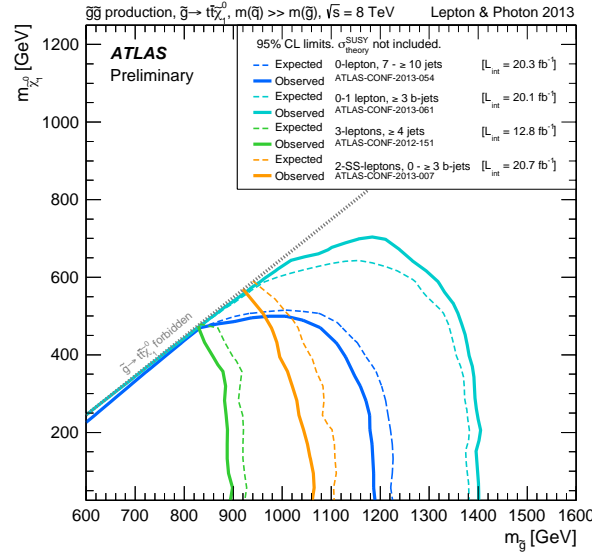


Figure 2.22. Summary of ATLAS limits in searches for gluino pair production (Gtt simplified models). From the ATLAS Supersymmetry physics group [27].

- Three leptons and at least four jets, $\int \mathcal{L} = 12.8 \text{ fb}^{-1}$ [30]
- Two same-sign leptons, 0–3 b -jets, $\int \mathcal{L} = 20.7 \text{ fb}^{-1}$ [31]

Direct stop pair production

In case gluinos are heavy, stops are predominantly directly produced in pairs, and then decay into top or bottom quarks. The search for this process puts limits on the stop mass, especially if the \tilde{t} is allowed to decay into $t + \tilde{\chi}_1^0$. In the limit of low neutralino-1 masses, stop masses of $320 \text{ GeV} < m(\tilde{t}) < 660 \text{ GeV}$ are excluded at 95% CL [32] (Figure 2.23).

Direct gaugino production

In this case, similar to our analysis, charginos and neutralinos are produced together, and decay into a final state consisting of three leptons and missing transverse energy [33]. Depending on the particles' masses, the decay can either happen via intermediate sleptons (charged sleptons or sneutrinos):

$$\tilde{\chi}_1^\pm \tilde{\chi}_2^0 \rightarrow \tilde{\ell}^\pm \nu \tilde{\ell}^\mp \ell^\pm$$

or via intermediate off-shell gauge bosons:

$$\tilde{\chi}_1^\pm \tilde{\chi}_2^0 \rightarrow W^* \tilde{\chi}_1^0 Z^* \tilde{\chi}_1^0.$$

Heavy neutralinos $\tilde{\chi}_{2,3,4}^0$ might also decay via a Higgs boson, and combinations of the above decays are also possible (with one particle decaying via a gauge boson, and one particle via slepton). Searches for the decays involving intermediate sleptons achieve further reaching limits in the chargino-1 / neutralino-1 mass plane, or the $(m_0, m_{1/2})$ plane, however these limits depend on the slepton masses in the given model. Assuming that the sleptons are sufficiently heavy that they are not a possible decay mode of the charginos and neutralinos, the gauge boson decay mode becomes relevant. Limits set under this assumption are independent of the slepton masses, given these are sufficiently high.

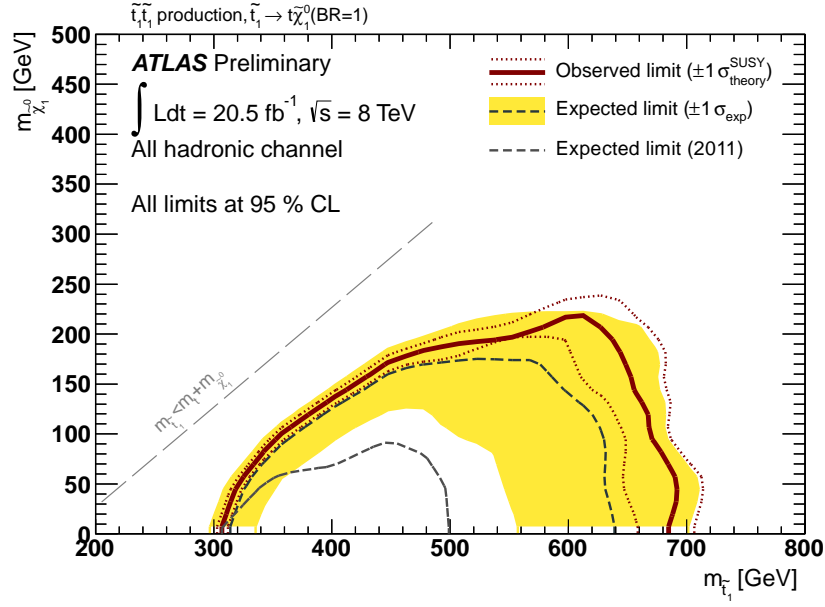


Figure 2.23. Limits depending on the mass of the lightest stop \tilde{t}_1 and the lightest neutralino $\tilde{\chi}_1^0$, from a search for stop pair production, assuming the stops decay exclusively $\tilde{t} \rightarrow t \tilde{\chi}_1^0$. The search was performed using $\int \mathcal{L} = 20.5 \text{ fb}^{-1}$ of 8 TeV data in the all-hadronic channel by the ATLAS collaboration [32].

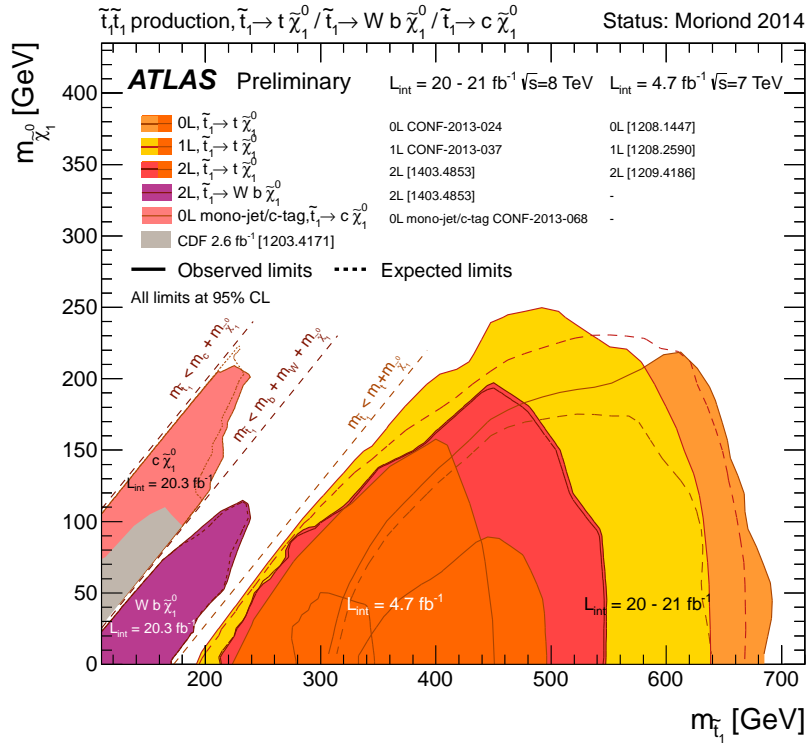


Figure 2.24. Overview of limits ATLAS limits from searches for stop pair production, in the plane of $(m(\tilde{t}), m(\tilde{\chi}_1^0))$. From the ATLAS Supersymmetry physics group [27].

For the case of intermediate slepton decay, degenerate $\tilde{\chi}_2^0, \tilde{\chi}_1^\pm$ masses are excluded up to 600 GeV in the limit of large mass difference to the lightest neutralino. Assuming only intermediate gauge boson decay, the limit becomes $m(\tilde{\chi}_2^0, \tilde{\chi}_1^\pm) < 315$ GeV.

2.5.2. Precision Measurements

Muon anomalous magnetic dipole moment ($g - 2$)

A very interesting measurement that is somewhat in tension with the standard model is the measurement of the muon anomalous magnetic dipole moment ($g - 2$). Charged fermions have a magnetic moment μ_S resulting from their spin S . It is given by

$$\mu_S = \frac{g\mu_B}{\hbar} S$$

where μ_B is the Bohr magneton. The factor g can be calculated by relativistic quantum mechanics, using the Dirac equation, giving $g = 2$. However, this is just a tree-level result, corresponding to the left diagram in Figure 2.25. To get a more accurate result, one has to consider higher orders in perturbation theory. The simplest of these vertex corrections can be seen in the right diagram in Figure 2.25. This diagram yields a slight deviation of g from 2. Defining the anomaly as $a = (g - 2)/2$, the one-loop vertex correction gives an anomaly for the electron of

$$a_{1\text{-loop}} = \frac{\alpha}{2\pi} \approx 0.0011614.$$

Corrections have been calculated up to α^4 , and the resulting magnetic dipole moment of the electron agrees with the experiment to ten significant digits, making this one of the most accurate predictions in physics.

A similar calculation can be done for the muon. However, due to the higher mass of the muon, much more massive intermediate particles are possible. The calculation is thus also sensitive to potential new physics, as shown in Figure 2.26. The anomalous magnetic moment of the muon has been measured by the E821 experiment at Brookhaven National Laboratory (BNL) using a muon storage ring, by studying the precession of muons in a constant magnetic field [34]. When comparing the theoretical value of a_μ^{SM} with the measured value, one indeed finds a discrepancy at 3.6σ level. At this point, it is unclear if this is due to a statistical fluctuation, an incorrect understanding of systematic uncertainties of the predicted or measured value, or if it is actual evidence of new physics. The prediction for the muon's dipole moment can be split into three parts:

$$a_\mu^{\text{SM}} = a_\mu^{\text{QED}} + a_\mu^{\text{EW}} + a_\mu^{\text{Had}}.$$

The first part contains contributions from QED only, and is analogous to the calculation for the electron. The second part contains terms from electroweak processes, such as intermediate Z bosons. The final part sums up the contributions from hadronic processes, which cannot be calculated just from theory. It can be estimated from the ratio of hadronic to $\mu^+\mu^-$ production cross sections in e^+e^- beams. This is one of the largest sources of uncertainty of the theoretical prediction [4].

Currently, an experiment is in preparation at Fermilab to improve the measurement of the muon g factor [35]. It is hoped that this experiment will either confirm the discrepancy, or reconcile the measured value with the standard model. Since the current measurement seems to “rule out” even the standard model, its power in excluding possible BSM models is limited, although it certainly can serve as a guide when constructing such models.

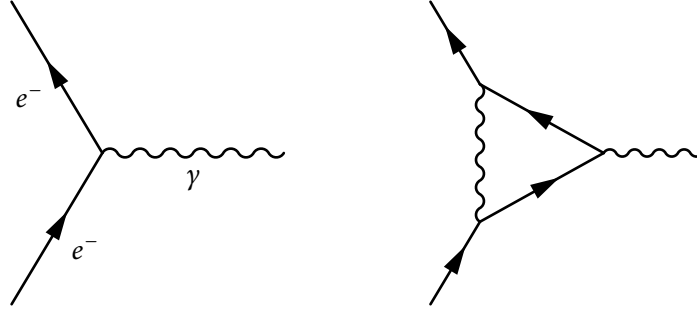


Figure 2.25. Electron / photon vertex diagram, and a first-order vertex correction involving a virtual photon. The vertex correction contributes to a_μ^{SM} .

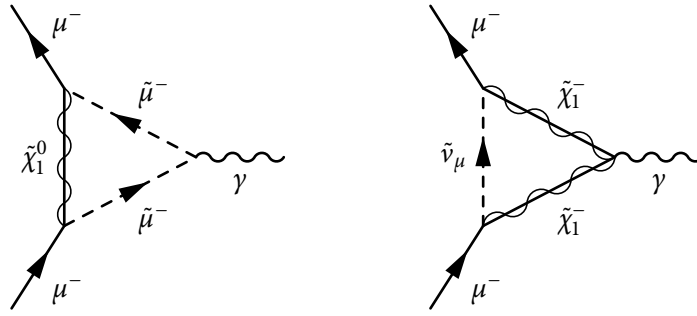


Figure 2.26. Possible corrections to the muon's magnetic moment from supersymmetric particles. Left: One-loop vertex correction from smuons $\tilde{\mu}$ and neutralinos $\tilde{\chi}_1^0$. Right: Correction from loop including a sneutrino $\tilde{\nu}_\mu$ and charginos $\tilde{\chi}_1^\pm$.

$B_s \rightarrow \mu\mu$ decay

Constraints on SUSY can be set by studying processes that are rare in the standard model, but become much more frequent in new physics models. The prime example of this is the decay of the B_s into two muons. The B_s meson consists of a \bar{b} -quark and an s -quark. Its decay into dimuons is doubly suppressed in the standard model. First, it requires a flavor changing neutral current (FCNC), a process which converts the s into a b quark, and results in an electrically neutral final state. FCNCs do not exist at tree level in the standard model. Second, the process is helicity suppressed. The B_s in the initial state is a pseudoscalar meson with spin 0 ($J^P = 0^-$), while the final state has a total spin of 1. Together, this makes the decay $B_s \rightarrow \mu\mu$ extremely rare in the standard model. In 2013, the LHCb experiment measured [36] a value of

$$BR(B_S^0 \rightarrow \mu\mu) = 3.2^{+1.4}_{-1.2}(\text{stat})^{+0.5}_{-0.3}(\text{syst}) \times 10^{-9},$$

which is in excellent agreement with the predicted value [4] of

$$BR(B_S^0 \rightarrow \mu\mu) = 3.23 \pm 0.27 \times 10^{-9}.$$

While rare in the SM, this decay mode might be considerably enhanced in BSM scenarios, which would be constrained by this measurement. An example in the MSSM is shown in Figure 2.28. The s quark is converted via a stop/chargino loop into a b quark, which annihilates with the incoming \bar{b} quark into a CP-odd Higgs A^0 . This diagram may become very relevant in certain areas of the parameter space, where

the coupling of the A^0 to bottom quarks or muons is enhanced. The interaction term has the following form:

$$L_{\text{int}}^{f\bar{f}} = -\tan\beta \frac{m_f}{v} A^0 \bar{d}(i\gamma_5)d \quad \text{where } d = d, s, b, e, \mu, \tau$$

For high values of $\tan\beta$, this leads to a strong enhancement of the A^0 - b and A^0 - μ couplings. For up-type quarks and neutrinos, \tan is replaced by \cot , resulting in a suppression of the interaction.

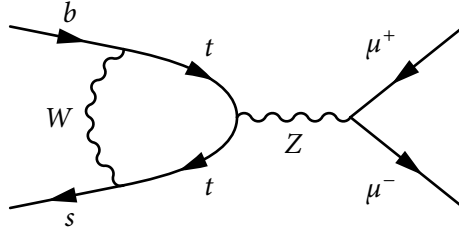


Figure 2.27. Decay of a B_s meson into two muons via a standard model process (“penguin” diagram). This decay mode is suppressed in the SM.

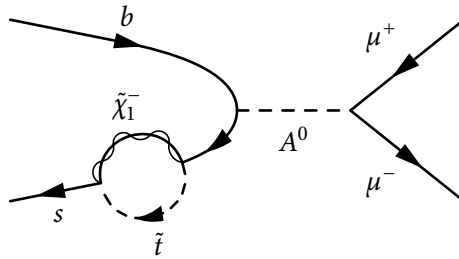


Figure 2.28. Possible decay of a B_s meson into two muons via SUSY particles (chargino $\tilde{\chi}_1^-$, stop \tilde{t} , pseudoscalar Higgs A^0). The addition of SUSY particles can greatly enhance the branching ratio into two muons.

3. Experiment

The events studied in this thesis were produced by the Tevatron, a proton-antiproton collider at the Fermi National Accelerator Laboratory in Batavia, USA. In the period called Run I, from 1992 to 1996, it ran at a center of mass energy of 1.8 TeV, and produced an integrated luminosity $\int \mathcal{L}$ of 125 pb⁻¹. One major achievement in this period was the discovery of the top quark in 1995. After 1996, the Tevatron was upgraded to a higher energy of 1.96 TeV and a higher luminosity. In this Run II from 2001 to 2011, $\int \mathcal{L} = 11.7 \text{ fb}^{-1}$ of collisions were produced in total.

There were two general-purpose particle detectors at the Tevatron, DØ and CDF. The basis of this thesis are the 10.7 fb⁻¹ of data that have been recorded by the DØ experiment during the Run II period. In the following, the Tevatron accelerator complex and the DØ experiment shall be described.

3.1. The Tevatron

The accelerator sequence begins with H⁻ ions which are brought to 750 keV (3.7 % of the speed of light c) with a Cockroft-Walton accelerator. The ions are then fed into a linear accelerator (LINAC), where their energy is increased to 400 MeV (71% of c). In the LINAC, the ions pass a thin graphite window which strips off their electrons. This change of charge allows one to use the same potential difference twice for acceleration. The protons emerging from the LINAC reach the booster synchrotron, where they are brought to an energy of 8 GeV. The protons from the booster are then passed into the main injector (MI). The MI not only increases the particles' average energy to 150 GeV, but also groups them into bunches. The time between the passing of two bunches is 396 ns. Twelve such bunches form one superbunch. There are three superbunches in the MI at a given time, each separated by 2 μ s. This time structure is chosen such that one full cycle fits inside the circumference of the Tevatron. While the protons are now ready for the final stage of acceleration in the Tevatron, a part of the beam is diverted from the MI to create antiprotons.

For this process, protons are injected into the antiproton source. The bunch structure is removed, and the beam energy is reduced from 150 GeV to 120 GeV in the debuncher. Next, the beam hits a copper-nickel target, with which a fraction of the protons react to create antiprotons. In 2–4 seconds, 7×10^{12} protons hit the target, while approximately 10^8 antiprotons with a mean energy of 8 GeV are created. The antiprotons are separated from the proton beam and focused with a lithium solenoid coil, using a current of 650 kA. The antiprotons are passed into the accumulator in a process called “stacking”, until the order of 10^{12} are collected.

Once this is done, the antiprotons are moved back into the main injector, and finally into the Tevatron, where they together with the protons are accelerated to 960 GeV per beam.

3.2. The DØ Experiment

The DØ detector is a general purpose particle detector located at the interaction point of same name. It provides nearly 4π coverage and is well suited for the investigation of particles with high masses and final states with large missing transverse momenta. From the inside out it is composed of a tracking system for charged particles, surrounded by a 2 T solenoid. Outside of the solenoid is the liquid argon / uranium based compensating calorimeter. The calorimeter is surrounded by a 2 T toroidal magnet system. Around the

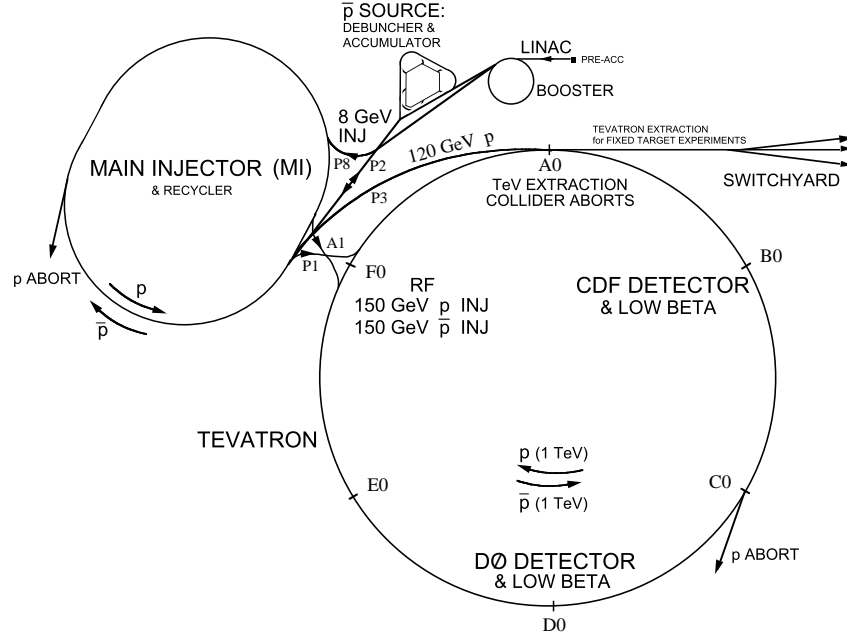


Figure 3.1. Plan of the Fermilab accelerator complex during Run II of the Tevatron. Originally from [37].

calorimeter, the muon spectrometer is located. In this chapter, each individual subsystem will be described in detail.

In the following, a right handed coordinate system will be used, as is convention for the DØ experiment. The x direction points away from the center of the collider, the y axis points upwards. The z axis points in the direction of the proton beam, which is westwards, or counter-clockwise around the ring.

It is convenient to also use polar coordinates r , φ and θ , where r is the radial distance to the z axis, and φ and θ are the azimuthal angle and inclination, respectively. Both φ and θ go from 0 to 2π . The following relations hold for the polar and Cartesian coordinates:

$$r = \sqrt{x^2 + y^2} \quad \varphi = \arctan \frac{y}{x} \quad \theta = \arctan \frac{r}{z}.$$

Often, instead of θ , the pseudorapidity η is used.

$$\eta = -\ln \tan \frac{\theta}{2}.$$

Pseudorapidity is closely related to the rapidity in z direction ϑ_z , which is a very useful quantity in relativistic kinematics. As opposed to velocities, rapidities are additive even in the relativistic regime. Rapidity differences $\Delta\vartheta_z$, and rapidity distributions $dN/d\vartheta_z$ are invariant under boosts along the z axis. Also, in inclusive QCD scattering, the rapidity distribution of the final state particles is flat on average (neglecting the acceptance of the detector). In the limit where the particle's mass is negligible compared to its energy, or $E \approx pc$, rapidity becomes equivalent to pseudorapidity, since:

$$\vartheta_z = \frac{1}{2} \ln \frac{E + p_z c}{E - p_z c} \quad \text{and} \quad \eta = \frac{1}{2} \ln \frac{p + p_z}{p - p_z}.$$

For the choice of origin, there are two options. In detector coordinates, the origin is chosen to be in the center of the detector. One example of such coordinates is η_{det} , which will be used to describe the coverage of detector parts wrt. the azimuthal angle. Alternatively, in physics coordinates, the origin is chosen to be

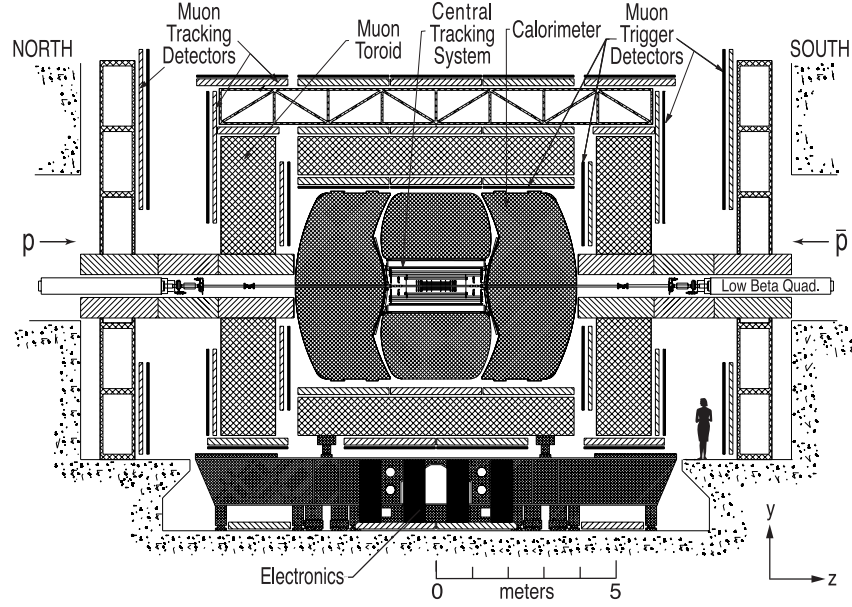


Figure 3.2. Schematic overview of the DØ detector, from [38].

at the primary vertex, i.e. the reconstructed location of the hard interaction. For the rest of this chapter, detector coordinates are assumed.

3.2.1. Tracking system

At the core of the detector, the purpose of the tracking system is to trace tracks of charged particles and to locate interaction vertices with high precision. From the tracks' radius of curvature their transverse momentum p_T can be determined (see section 4.1.2), a precise measurement of which is important for this analysis. A schematic of the tracking system can be found in Figure 3.3.

Silicon Microstrip Tracker (SMT)

The SMT, which uses semiconductor strips to detect particle passages with high precision, is separated into barrel and disc parts. This allows it to have surfaces crossed by particle tracks over its whole range of acceptance in η_{det} . The six barrels are located in the central region, with the silicon modules, called ladders, aligned axially, such that the strips are along the z -direction. Thus, when a particle hits the module, its r and ϕ coordinates are known with precision. The barrels are made up of four layers; the inner two layers each contain 12 ladders per barrel, while the outer two contain 24 per barrel, making a total of 432 ladders.

The discs are located further in forward direction. Between barrels and at their ends are the F discs. Each disc is made of 12 double-sided wedges. The strips are arranged on opposing sides of the F disc wedges in stereo configuration. Furthest from the center are the larger H discs, which are made up of 24 single-sided wedges. The strips on the discs are arranged to provide an accurate z , r measurement, and thus determine the inclination of the track (see Section 4.1).

During the shutdown in 2006, an additional layer of silicon strips was inserted, the so called layer 0. Layer 0 consists of 48 strips spread over 6 facets. Built on a carbon fiber support structure, it is 1.68 m long and only 3.2 cm in diameter. The new layer greatly improves tracking accuracy. By adding a further point to tracks close to the beam, the lever arm is increased, leading to a better p_T resolution and a reduced fake rate. Layer 0 doubles the impact parameter resolution (see Section 4.1). Furthermore it compensates for

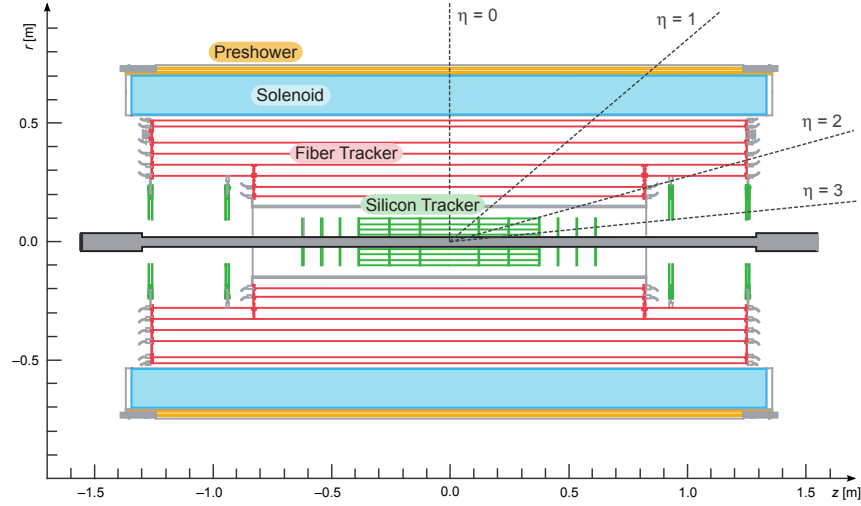


Figure 3.3. Schematics of the tracking system (including SMT and CFT), the solenoid, and the central preshower detector. From [38].

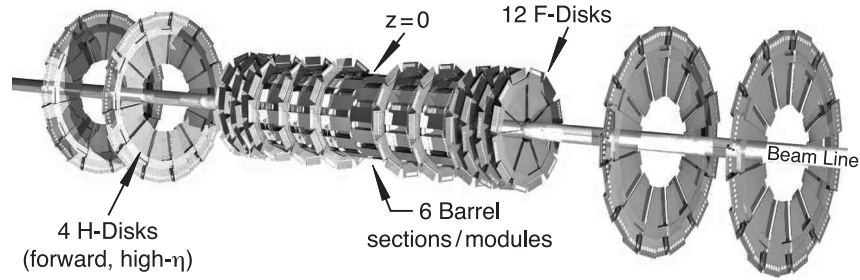


Figure 3.4. Rendering of the silicon microstrip tracker, showing barrels and discs. From [38].

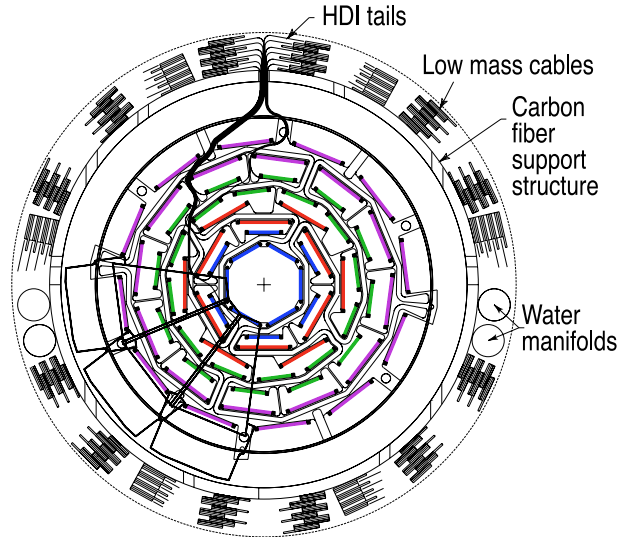


Figure 3.5. Cross sectional view of an SMT barrel. The SMT consists of four layers, the inner layers (blue and red) each contain 12 silicon modules, while the outer layers (green and violet) both have 24. Each layer is made of two sublayers, which are rotated with respect to each other to avoid acceptance gaps. Adapted from [38].

radiation damage to the SMT and successfully helped the detector to maintain performance throughout the rest of Run II.

3.2.2. Central Fiber Tracker

The Central Fiber Tracker (CFT) uses visible-light scintillating fibers for particle detection. A total of 76800 fibers are mounted on eight support cylinders. The CFT spans a radial region of $r = 20 \dots 50$ cm and the pseudorapidity interval $|\eta_{\text{det}}| < 1.6$. The innermost two cylinders fit between the H Discs of the SMT and are 1.66 m long, the outer cylinders are 2.52 m long.

The fibers are arranged in two double layers per cylinder, making a total of 32 individual layers. On the first half of a double layer the fibers are aligned axially, on the second half they are arranged in a stereo configuration, rotated alternately by $+3^\circ$ or -3° . This makes it possible to determine the z coordinate of hits. The spatial resolution of a double layer is of the order of 100 μm .

The diameter of a scintillating fiber is 935 μm . The emitted light has a wavelength of 530 nm, which corresponds to a yellow-green color in the visible spectrum. Photons are led through clear fiber guides of 8-12 m length to the visible light photon counters (VLPC) below the detector. The waveguides at $\varphi = \pi/2$ coming from the top of the detector are longer than those at $\varphi = 3\pi/2$, which leads to a φ dependency in tracking efficiency.

The VLPCs used have a very high quantum efficiency of 75%. A minimum ionising particle will produce an average yield of 8.5 detected photoelectrons per single layer [39].

3.2.3. Solenoid Magnet

To curve the tracks of charged particles in the tracking system, the DØ detector uses a 2 T solenoidal magnet. Since the magnet was only installed for Run II, its design was subject to space constraints. The solenoid has a length of 2.73 m, and a diameter of 1.42 m. The superconducting magnet is placed in a cryostat and cooled to a temperature of 10 K. In the central region, at $\eta_{\text{det}} = 0$, magnet and cryostat account for 0.87 radiation lengths (X_0) of material. The solenoid was designed for a magnetic field of 2.0 T, which is created by a current of $I = 4.75$ kA. The stored energy in the magnetic field at design parameters is 5.3 MJ. However, since the shutdown in fall 2004, the magnet could not be ramped to full current due to a defective solder joint. From then, till the end of the run, it has been operating at $I = 4.55$ A, corresponding to a magnetic field of $B = 1.92$ T. The polarity of the solenoid (and the toroid, section 3.2.5) is reversed regularly to compensate for possible asymmetries in the detector.

3.2.4. Calorimeter

The calorimeter in DØ is divided into an electromagnetic and a hadronic part. It is complemented by the preshower detector and the intercryostat detector (ICD). The calorimeter measures the deposited energy of particles and jets, and is able to distinguish between different types of particles.

There are several different processes for energy deposition of particles. The energy deposition of **electrons** is shown in Figure 3.7. At low energies, the main loss is due to ionization of target atoms. A smaller contribution comes from Møller scattering. At higher energies, the energy deposition is largely due to bremsstrahlung where electrons emit photons on deceleration. Photons above the energy threshold of $2m_e c^2$ may in turn produce an $e^+ e^-$ pair (with a nucleus absorbing momentum). In this way, a shower is produced, and the energy of the incoming particle (electron or photon) is distributed over a large number of secondary particles. The distance over which the fraction $1/e$ ($\approx 37\%$) of the energy is deposited is given by the radiation length X_0 .

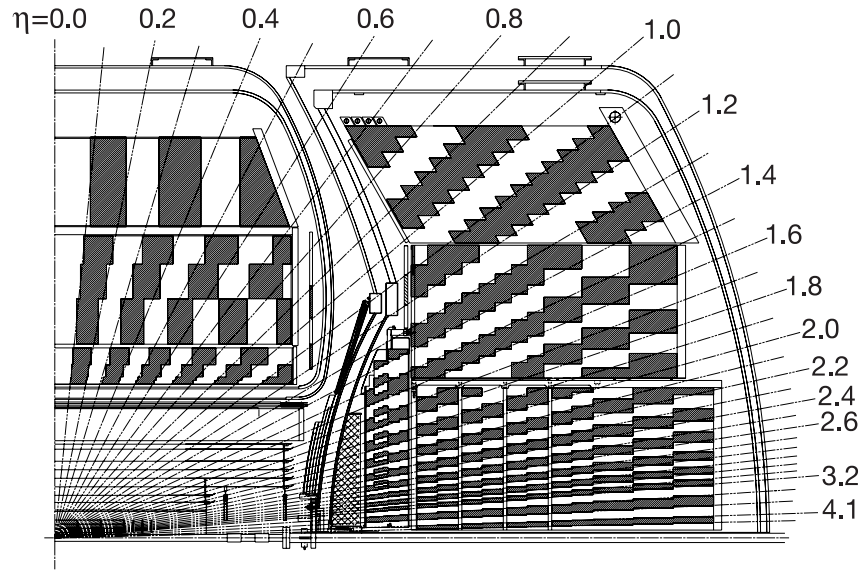


Figure 3.6. Side view of one quadrant of the DØ calorimeter, showing the central and endcap regions. The shading illustrates the grouping of calorimeter cells into towers, each covering $\Delta\eta_{\text{det}} \times \Delta\phi \approx 0.2 \times 0.2$ in most parts of the calorimeter. From [38].

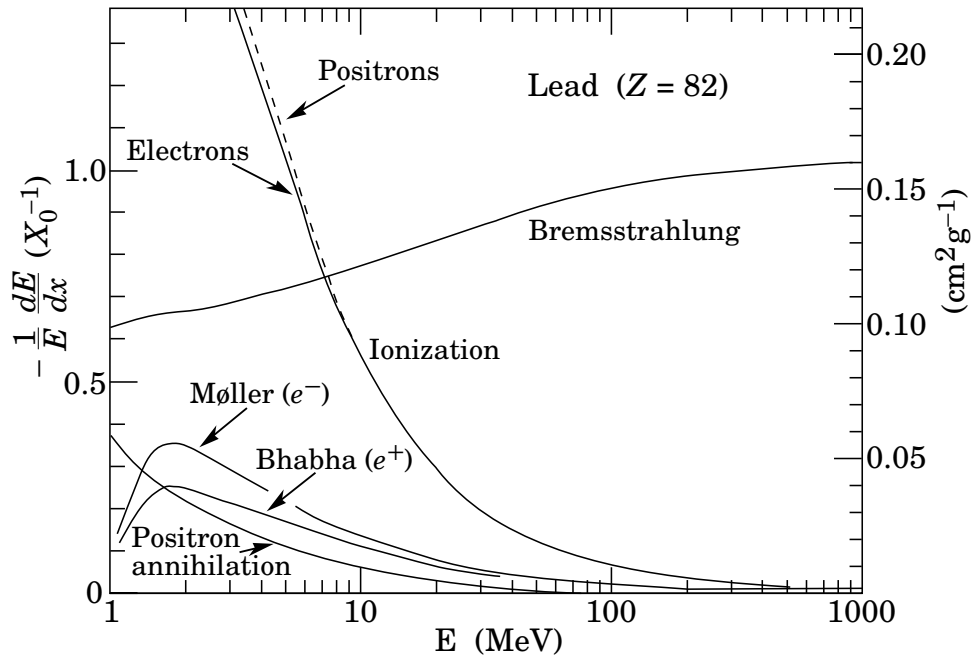


Figure 3.7. The various contributions to the energy loss of electrons and positrons in matter, here lead. From [40].

Hadrons deposit energy by scattering inelastically with nuclei, producing pions and nucleons. These in turn scatter again, producing a hadronic shower. In analogy to the radiation length, the distance over which $1/e$ of a hadron's energy is deposited is defined as the nuclear interaction length λ_I .

Neutrinos (and possible LSPs) are special, since they do not take part in the electromagnetic and strong interactions, and leave no energy in the calorimeter. Their presence can still be detected through the momentum imbalance of the event: While the total momentum of the initial state in beam direction is not known, its component in the transverse plane p_T is zero. Thus the sum of all final state momenta in the transverse plane is zero. Undetected particles appear as missing transverse momentum $\vec{p}_T = -\sum \vec{p}_T$. Since for high energy particles $E \approx p$, an equivalent quantity is missing transverse energy, which is defined as $\cancel{E}_T = |\sum \vec{E}_T|$.

Finally, **muons** created in high energy collisions are minimal ionizing particles (MIPs), meaning that they only deposit a minimal amount of energy, around 3 GeV, regardless of their momentum. For this reason, the energy measured in a part of the calorimeter has to be corrected when a muon is detected in that area.

Preshower Detector

The purpose of the preshower detector is to restore the energy resolution of the electromagnetic calorimeter after the addition of the solenoid with the start of Run II. It provides an improved detection of showers that begin before the calorimeter, which helps with the identification of electrons, and improves the measurement of shower energies. The preshower detector is divided into two regions:

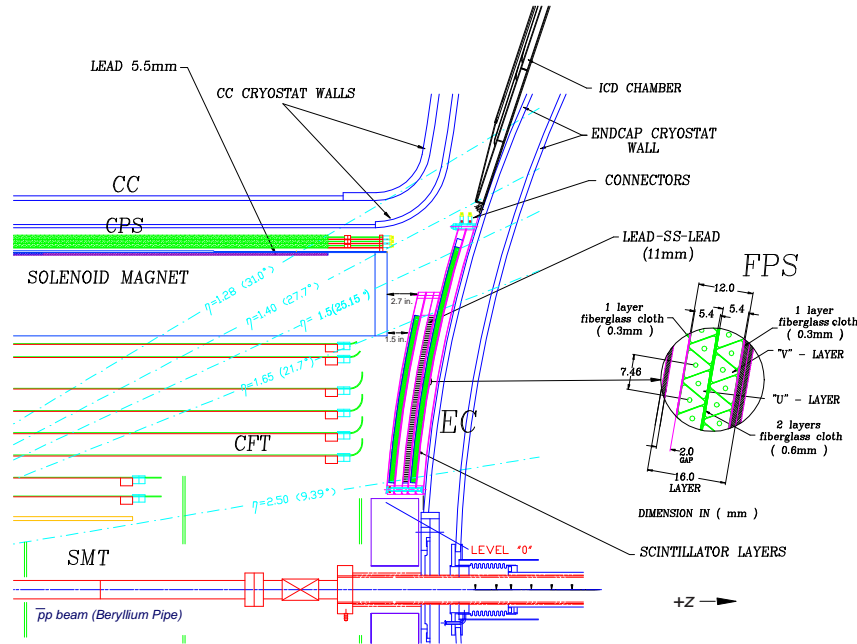


Figure 3.8. Location of the central (CPS) and forward preshower detectors (FPS) and the intercryostat detector (ICD). From [38].

The central preshower detector (CPS) forms a cylinder around the solenoid, and extends in the radial direction from 71.8 to 74.2 cm. It covers pseudorapidities up to $|\eta_{\text{det}}| < 1.3$. The CPS contains three layers of triangular scintillator stripes, connected via optical fibers to VLPCs. The strips of the inner layer are laid out axially, whereas the two outer layers are in stereo configuration. In front of the CPS is a lead radiator with a thickness of 0.56 cm ($\approx 1 X_0$), which is meant to initiate showers from electrons and photons, helping

distinguishing them from pions. Together with the solenoid, the radiator amounts to (depending on η_{det}) $2 \dots 4 X_0$ of material.

The forward preshower detectors (FPS) are each constructed of two layers of scintillators, one on each side of a stainless steel absorber plate of $2 X_0$ thickness. Each layer consists of two planes of scintillating fibers, connected to VLPCs. The inner layer is called the “MIP” layer. Charged particles leave a minimal ionization signal here, photons do not. On the other hand, both electrons and photons create showers in the absorber, which leads to a signal in the outer “shower” layer. By comparing both layers, electrons and photons can be distinguished. The extent of the MIP layer is $|\eta_{\text{det}}| = 1.65 \dots 2.5$, the shower layer covers $|\eta_{\text{det}}| = 1.5 \dots 2.5$.

Calorimeter

DØ’s calorimeter is built in three parts: The central calorimeter (CC) covers the region $|\eta_{\text{det}}| < 1.0$, while the two endcaps (EC) cover $|\eta_{\text{det}}| \approx 0.7 \dots 4$ (see Figure 3.6). The CC and the ECs are housed in separate cryostats, filled with liquid argon (LAr) at 90 K. The LAr serves as active material for the calorimeter. The calorimeter is further separated into an electromagnetic calorimeter (ECal), and fine and coarse hadronic calorimeters (HCal). The HCal is placed further away from the interaction point, since the maximal depositions of hadronic showers occur at larger depths.

The smallest unit of the calorimeter is called a cell. Each cell contains an absorber plate, a gap filled with LAr, and a pad (Figure 3.9). Showering occurs in the absorber plate, and the deposited energy causes ionization in the gap. The produced charges are then collected by a 2 kV voltage between the absorber and the pad. Since pseudorapidity intervals become increasingly smaller in the forward region, but same η_{det} intervals receive the same rate of particles, the calorimeter must have a finer granularity in the forward region, as can be seen in Figure 3.6.

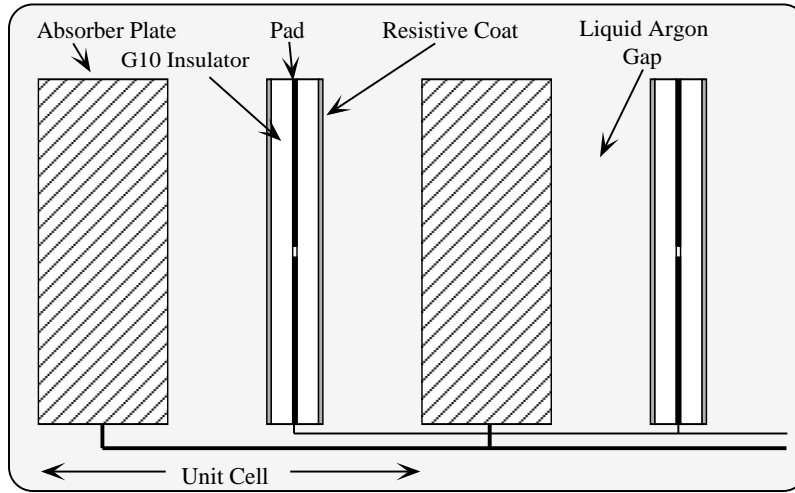


Figure 3.9. Schematic drawing of two calorimeter unit cells. From [38].

The ECal uses 3 and 4 mm thick absorbers made of depleted uranium. The fine HCal uses 6 mm absorbers made of a uranium alloy with 2% niobium, while the coarse HCal uses 46.5 mm plates, made of copper in the CC, and stainless steel in the EC. The cells of the ECal are arranged in four layers. In the central region, they have a thickness of 1.4, 2.0, 6.8 and $9.8 X_0$, in the endcaps they are 1.6, 2.6, 7.9 and $9.3 X_0$ thick. The granularity of the electromagnetic calorimeter is $\Delta\eta \times \Delta\phi \approx 0.1 \times 2\pi/64 \approx 0.1 \times 0.1$, except in the third layer, where showers have their maximum on average. There, the granularity is 0.05×0.05 .

Particle	A	B	C
e	$0.0115^{+0.0027}_{-0.0036}$	$0.135 \pm 0.005 \sqrt{\text{GeV}}$	0.43 GeV
π	0.032 ± 0.004	$0.45 \pm 0.004 \sqrt{\text{GeV}}$	0.975 GeV

Table 3.1. Resolution of the calorimeter for electrons and pions, as measured in a test beam. A , B and C refer to the corresponding terms in equation (3.1). From [41].

Generally, the response of a hadronic calorimeter is different for different particles, and also depends on the shower composition. Calorimeter response is defined as the average signal divided by the energy of the incoming particle. While a hadronic shower has non-electromagnetic as well as electromagnetic components, without additional measures the response to the non-electromagnetic part h will be smaller than the electromagnetic response e , or $e/h > 1$. One cause is the inelastic scattering of shower particles with nuclei. The energy used to break nuclear bonds and release nuclei is largely invisible in the calorimeter. Another cause is the production of muons, which may escape the calorimeter, and neutrinos.

A calorimeter in which $e/h \approx 1$ is called a compensating calorimeter. One way to achieve compensation is to boost the hadronic response, by using uranium as an absorber material. Neutrons, which accompany reactions leading to invisible energy, cause fission reactions in the uranium, thus increasing the response again. For DØ, the response ratio e/h is between $1.02 \dots 1.09$, making it an almost compensating calorimeter.

Since the deposited energy is proportional to the number of collected charges, it must carry a Poissonian uncertainty $\Delta E \propto \sqrt{E}$. There is an additional term linear in E from calibration errors, and a constant term due to noise. The full uncertainty can be parametrized as follows:

$$\Delta E = \sqrt{(A \cdot E)^2 + (B \cdot \sqrt{E})^2 + (C)^2} \quad (3.1)$$

Nominal values for the parameters in equation (3.1), determined with a test beam, are given in table 3.1.

Intercryostat Detector

Gaps between the CC and the ECs result in a reduced calorimeter acceptance around $|\eta_{\text{det}}| = 0.8 \dots 1.4$. To correct for this, DØ has the intercryostat detector (ICD). The ICD is attached to the endcaps and is made of layers of scintillating tiles.

3.2.5. Muon System

The muon system in DØ uses two different types of detectors: drift tubes and scintillators. In addition, it includes a toroidal magnet system to curve the muon tracks. The muon system is divided into a central and forward region, and A, B and C layers.

Drift tubes (or wire chambers) are gas filled rectangular boxes, in which wires are strung. A high voltage is applied between the wires and the walls. When a charged particle passes the chamber, it ionizes the gas, and the created charges drift towards the wires and walls. The position of a hit along the wire can roughly be determined by using the timing difference between signals at both ends of the tube. To allow a more precise measurement, veneer cathode pads are installed at the top and bottom of each tube, which allow the localization of the hit within 3 mm.

Scintillators, which have a faster response time, but do not measure the muon position precisely, are used for triggering.

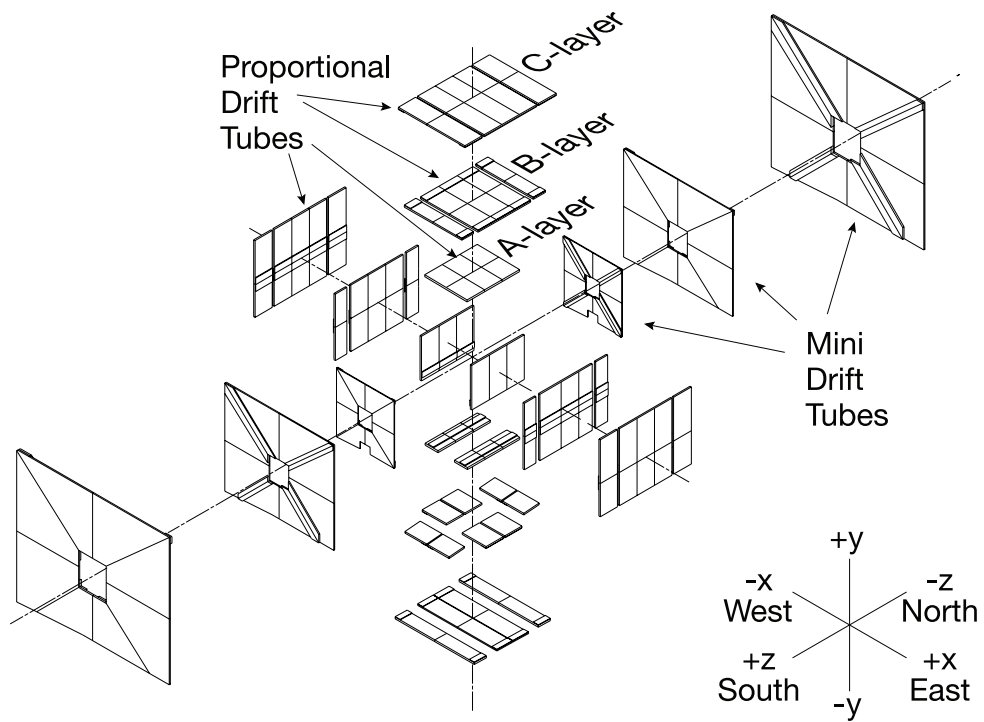


Figure 3.10. Overview of the drift tubes in the muon system. From [38].

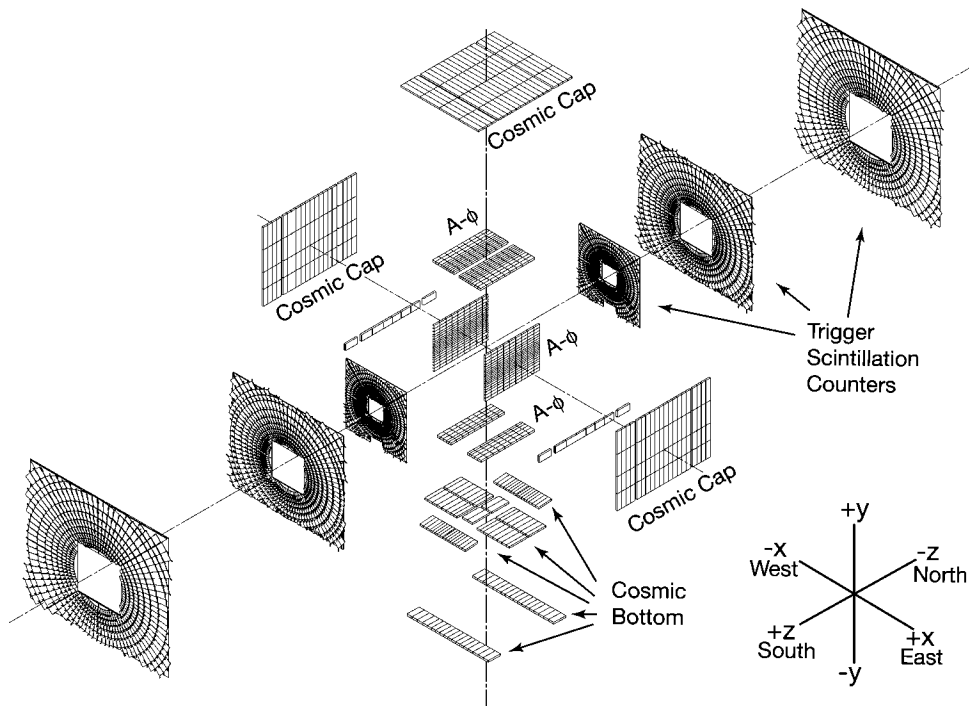


Figure 3.11. Overview of the scintillators in the muon system. From [38].

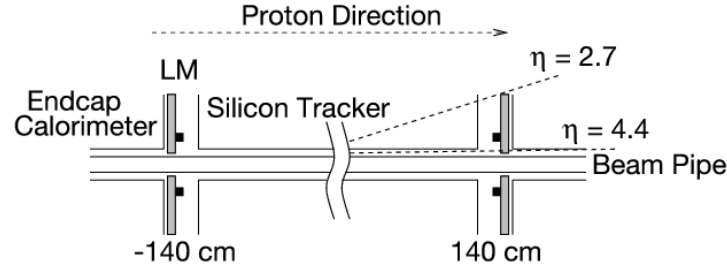


Figure 3.12. Sketch of the DØ luminosity monitor, from [38]

Central Muon Detector

The central muon detector covers the region up to $|\eta_{\text{det}}| < 1.0$, and has an area of $2.8 \times 5.6 \text{ m}^2$ facing the center of the detector. Its drift tubes are called proportional drift tubes (PDT), and are divided into cells with an individual area of $11.01 \times 5.5 \text{ cm}^2$. Each cell contains a single wire which is parallel to the toroid's magnetic field. The PDTs are filled with 84% Argon, 8% Methane, and 8% CF_4 . The drift velocity of electrons and ions is 10 cm/ms, and the maximum drift time is 500 ns.

The central region contains two layers of scintillators: Inside of the magnet, in the A layer, are the A – ϕ scintillation counters. The scintillators of the C layer on the top and at the sides are called “cosmic caps”, while those on the bottom are named “cosmic bottom”.

Forward Muon Detector

The forward muon detector was added with Run II. It provides coverage for $|\eta_{\text{det}}| \approx 1.0 \dots 2.0$. The forward muon detector utilizes smaller chambers, called mini drift tubes (MDTs), each made of eight cells of $9.4 \times 9.4 \text{ mm}^2$ area. The MDTs are filled with a mixture of 90% CF_4 and 10% Methane. The maximal drift time of 60 ns is much shorter than that of the PDTs, allowing a faster response. The accuracy of hit measurements of the PDTs is 0.7 mm.

Toroid Magnet

The toroidal magnets are positioned between the A and B layers of the muon system. Unlike the solenoid, they were part of the detector since the beginning of Run I. The toroids generate a magnetic field of $B = 1.8 \text{ T}$, and are operated with a current of $I = 1500 \text{ A}$. The total weight of the toroids is 1973 tons. The magnet system is separated into a central and two endcap parts. The central part forms a large square ring, with the yoke occupying $x, y \approx \pm 318 \dots 427 \text{ cm}$. The endcap parts are at $z \approx \pm 454 \dots 610 \text{ cm}$, with openings for the beam pipe. The magnetic field lines circle around the beam axis, and go along the x direction on the top and bottom, and along the y direction on the sides. Deflection from the toroids occurs in the r, z planes. A particle originating from the center of the detector, moving outwards, describes a path curved towards or away from the beam.

3.2.6. Luminosity Monitor

It is necessary to accurately measure the instantaneous luminosity \mathcal{L} to model the expected backgrounds, since event characteristics depend on it. With increasing \mathcal{L} , pile-up and detector occupancy also increase. DØ includes a dedicated luminosity monitor for this task (Figure 3.12).

The luminosity monitor determines \mathcal{L} by detecting inelastic $p\bar{p}$ collisions. It also provides beam monitoring data, such as a measurement of the beam halo, and can quickly determine the z -coordinate of

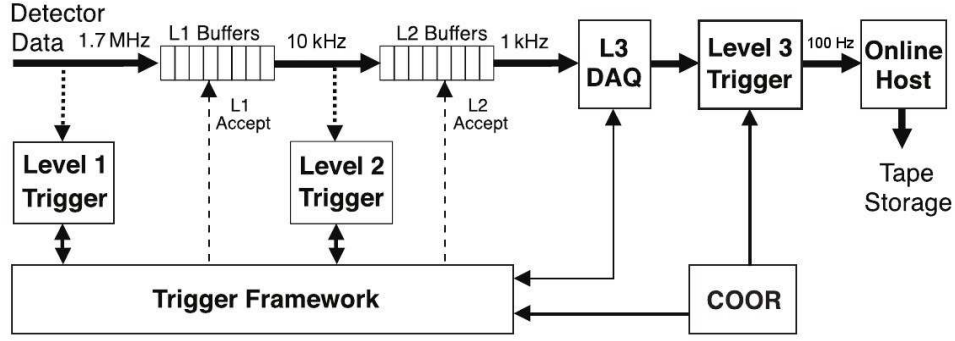


Figure 3.13. Overview of the three level trigger system, from [38].

the interaction point. It is made of two parts (north and south), located before the EC at $z = \pm 140$ cm. The luminosity monitor is situated very close to the beam, and thus covers the extreme forward region of $|\eta_{\text{det}}| \approx 2.7 \dots 4.4$

To determine the instantaneous luminosity, the rate of inelastic $p\bar{p}$ events is measured. Given the efficiency ε and acceptance A of the luminosity monitor, and the inelastic $p\bar{p}$ cross section $\sigma_{p\bar{p}}$, the luminosity can be calculated as follows:

$$\mathcal{L} = \frac{1}{\varepsilon \cdot A \cdot \sigma_{p\bar{p}}} \cdot \frac{dN}{dt}$$

All data collected with the DØ detector is divided into “lumi blocks”. Lumi blocks, which are indexed by lumi block number (LBN), are changed at least once every minute, so that one can assume that \mathcal{L} is approximately constant for each LBN.

3.2.7. Triggers

With a bunch crossing every 396 ns, the rate of incoming data is about 2.5 MHz. However, it is only possible to store about 100 events per second to disc. Thus, a trigger system is necessary, which suppresses backgrounds, selects events for analysis, and reduces the event rate. In DØ, a three level trigger system is used (Figure 3.13).

Level 1

The level 1 trigger (L1) needs to operate at a very high speed to reduce the data rate from 1.7 MHz to 10 kHz. It must make a decision whether to keep an event or not in 3.5 μ s. To achieve this, the L1 trigger is implemented completely in hardware. It operates on a simple representation of the detector, and uses a very basic reconstruction. For example, a L1 trigger may fire if the energy in a calorimeter tower is above a certain threshold. Tracks can be reconstructed from the CFT, the preshower detector, and the muon system, and may fire a trigger if they pass a certain p_T threshold. Electrons can fire a trigger up to $|\eta_{\text{det}}| = 2.5$ by having hits in the preshower detector. Muons can be triggered on up to $|\eta_{\text{det}}| = 2.0$ which corresponds to the coverage of the muon system.

Level 2

Level 2 (L2) is subdivided into two stages. In the “preprocessor” stage, simple aggregate objects such as tracks or calorimeter energy clusters are constructed. For this, information from SMT, CFT, preshower detector, calorimeter, and muon system is used. In the “global-processor” stage, these aggregates are

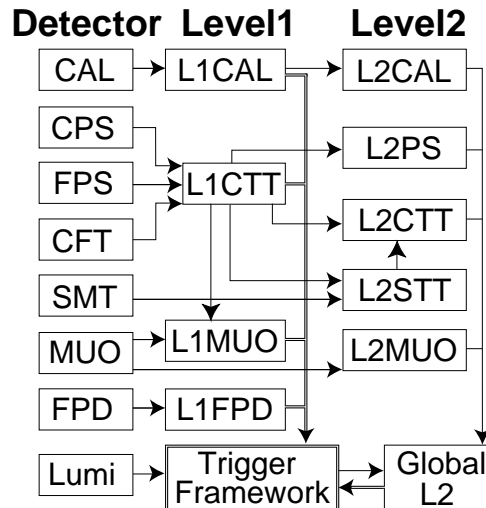


Figure 3.14. Schematics showing which detector systems are considered in the level 1 and level 2 triggers. From [38].

combined into candidates for physical objects, such as muons. Trigger decisions are issued based on properties of these objects, in less than 100 μ s. This allows a reduction of the rate to 1 kHz. At the highest rates (e.g. at the beginning of a store), L2 has typically less than 5% dead time.

Level 3

In contrast to level 2, level 3 works on whole events. The collected detector data of an event is passed to one of many farm nodes, which use generic PC hardware. A simplified version of the offline reconstruction algorithm is then run. The level 3 trigger reduces the rate to approximately 100 Hz. At this point the data can be written to disc, with one event having a size of about 250 kB.

4. Event reconstruction

4.1. Tracks

Charged particles are detected at various points in the tracking system (and in the case of muons also in the muon system). These hits are combined to reconstruct the particles' tracks. Due to the detector's magnetic fields, tracks of charged particles (in the following simply "tracks") take the form of helices.

To describe a general helical path going through a point, six real parameters are necessary: Three describe the location of the point, two the angle and direction of the track in the point, and one specifies the radius of curvature¹. If we do not single out one point along the track, five parameters are enough:

- d_0 describes the distance of closest approach (dca) of the track to the z -axis.
- φ is the track's angle in the transverse plane, at the point of closest approach on the track (PCA).
- z is the z coordinate of the point of closest approach.
- $\tan \lambda$ is the inclination of the track, given by dz/ds_T , and describes how fast a particle progresses in z direction while moving along a circular path in the transverse plane (Figure 4.1).
- ρ is the radius of curvature in the transverse plane.

These parameters are called the TRF parameter set, after the track reconstruction program of same name. In TRF parameters, the movement in the transverse projection is completely given by the three parameters d_0 , φ and ρ (Figure 4.2).

The point of closest approach is fixed to a circle around the z axis of radius d_0 . The angle φ gives the direction tangential to the track and to the circle, which fixes PCA to one of two opposite points. These can be distinguished by the sign of d_0 . Another ambiguity is in the orientation of the track, which can be clockwise or counter-clockwise, and can be specified by the sign of ρ .

Additional parametrizations are used in the GTR algorithm. If the track crosses a known surface, the tracks path as well as the crossing point can be given in five parameters. Examples of such parametrizations are shown in Figure 4.3. For instance, surfaces of the CFT are described by cylinders aligned along the z axis. Errors due to deviations from the ideal geometry are negligible, when the geometry is only used for parametrization.

4.1.1. Track reconstruction

Track reconstruction is the task of taking individual hits, and inferring from those the original path of the charged particle. One challenge is the possibility of misreconstruction due to ambiguities, or missing hits. Furthermore, it is desirable that a track reconstruction algorithm is fast. At DØ, two algorithms are used: The histogramming track finder (HTF), and the alternative algorithm (AA).

The HTF is based on the Hough transform, which was already employed to find tracks in photographs from bubble chamber experiments. Its benefit is that it works efficiently even for a very large number of

¹It would seem that an additional parameter is necessary to describe how much the track advances with each revolution. However, since the magnetic field is known, this information is included in the track direction.

Figure 4.1 Illustration of the $\tan \lambda$ parameter. s is the length along the track, s_T its transverse projection. $\tan \lambda = \partial z / \partial s_T$ describes how fast the track advances in z direction while describing a circle in the transverse plane.

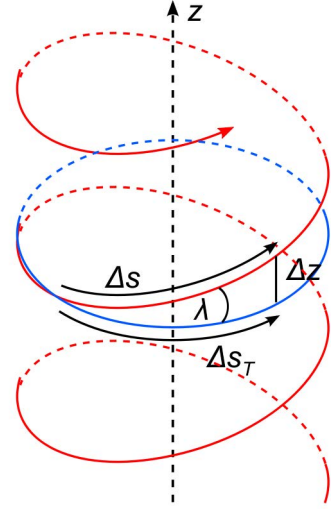


Figure 4.2 Transverse projection of a track. In the transverse plane, a track is described by impact parameter d_0 , radius of curvature ρ , and angle φ .

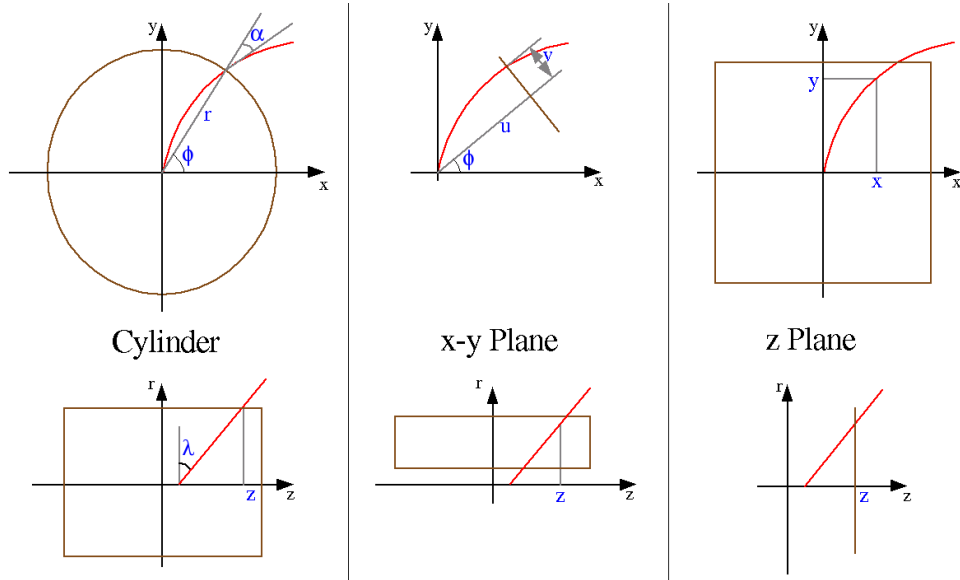
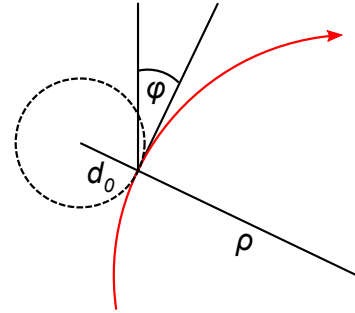


Figure 4.3. Parametrization of tracks using intersections with geometric surfaces, from [42]. The track is red and the surface is shown in brown.

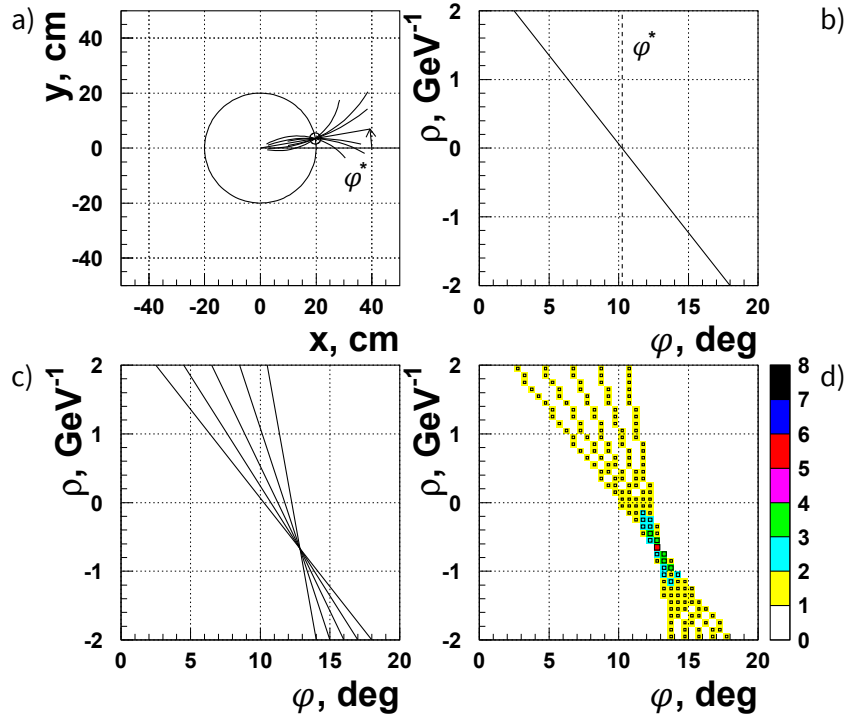


Figure 4.4. Illustration of the Histogramming Track Finder. a) Shows one hit in the detector, in Cartesian coordinates. The hit is indicated by the small circle, curved lines through the hit show possible tracks. φ^* is the angle of the track with $\rho = 0$. b) All possible tracks in ρ, φ space. Each track becomes one point after the Hough transform. c) Four further hits are added, consistent with a track of $\varphi = 13^\circ$ and $\rho = -0.6 \text{ GeV}^{-1}$. d) In the histogram, the found track is visible as a peak. Adapted from [43].

hits. Limitations of HTF include that it works solely in the transverse plane and assumes that the impact parameter d_0 is negligible compared to the track dimensions. In this case, a track can be represented by φ and ρ alone.

To understand the HTF algorithm, it is instructive to first consider a naive histogramming algorithm. For each pair of hits, one can create a candidate track which goes through both hits and the origin ($d_0 \approx 0$ assumption). This candidate track represents a segment of a full track. Since neighboring segments have similar values of φ and ρ , tracks result in clusters in a 2D histogram. While this algorithm would work, it is not very efficient for a large number of hits N_{hits} . Since all pairs of tracks have to be considered, it has a run time of $\mathcal{O}(N_{\text{hits}}^2)$.

The actual HTF algorithm improves on this by using the Hough transform. While a path segment corresponds to a pair (φ, ρ) , a single hit can match multiple (φ, ρ) -combinations, which form a line $\varphi(\rho)$ in the angle-radius plane (Figure 4.4 a) and b)). The Hough transform is the mapping of hits to lines in the (φ, ρ) plane. If these lines are superimposed for all hits, tracks are again visible as concentrations (Figure 4.4 c) and d)). The HFT algorithm works as follows: The possible radii are partitioned in N_ρ bins. For each hit, and for each possible ρ , the value of $\varphi(\rho)$ is calculated, and the bin for φ, ρ is incremented. Finally, tracks are identified in the histogram. This algorithm only has a complexity of $\mathcal{O}(N_{\text{hits}} \times N_\rho)$, and the run time is thus linear in the number of tracks.

In addition to the HFT, the alternative algorithm (AA) is also used. It begins with seeds of three hits in the SMT, and tries to add further hits compatible with the track, such that the χ^2 of the track remains under a given threshold. This is continued until there has been no hit for three detector layers, or the track leaves the tracking system.

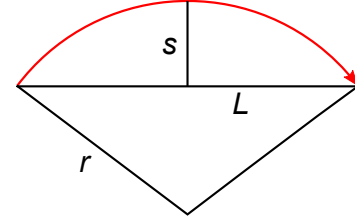


Figure 4.5 Illustration of the chord length L and the sagitta s . The red curve is a track with a radius of curvature of r .

The Global Track Reconstruction algorithm (GTR) is the most complex algorithm used, and takes inputs from both HTF & AA. It starts with candidate tracks, extending these outwards step by step taking the magnetic field and interactions with the detector into account. Hits are modeled as intersections of tracks with simple geometric surfaces, as described above. The GTR algorithm is modular and is built upon the following components:

- **Propagators** take a track and pass it through the detector to a new surface. It takes the particle's interaction with the detector material and the magnetic field into account. The track's parameters and error matrix (including the parameter's uncertainties and covariances) are updated accordingly.
- The **fitter** is used to add new hits to existing tracks. It calculates the χ^2 for each hit cluster, and accepts the cluster if it is below a certain threshold. In that case, the track parameters are updated. Else, it is assumed that the hit was missed due to inefficiencies, and the track probability is adjusted to reflect this.
- **Filters** finally remove track candidates that do not pass certain criteria. Tracks are rejected that have too high a χ^2 , or improbably many missed surfaces. If a track shares more than three clusters with other tracks, only the one with the least χ^2 is kept.

4.1.2. Momentum measurement

Tracks of charged particles in a magnetic field B are curved according to their momentum p with a radius of curvature r :

$$p(B, r) \approx 0.3 r B \frac{\text{GeV}/c}{\text{T} \cdot \text{m}}$$

Inserting the radius of curvature in the transverse projection, ρ , gives the transverse momentum p_T . The uncertainty on the transverse momentum σ_{p_T} depends on the hit positions' uncertainty $\sigma(x)$, the number of hits used to fit the track N_{hits} , and the chord length L (Figure 4.5). It can be calculated by the Glückstern formula [44]:

$$\frac{\sigma_{p_T}}{p_T} = \frac{\sigma_x \cdot p_T}{0.3 B L^2} \cdot \sqrt{\frac{720}{N + 4}}$$

Using the sagitta s , the transverse momentum can be expressed alternatively as:

$$p_T(B, L, s) = \frac{0.3 B L^2}{8 s} \frac{\text{GeV}/c}{\text{T} \cdot \text{m}}$$

with the benefit that the relative uncertainty reduces to that of the sagitta ($\sigma_s^2 = 3/2 \sigma_x^2$):

$$\frac{\sigma_{p_T}}{p_T} = \frac{\sigma_s}{s} = \frac{\sqrt{96}}{0.3} \frac{\sigma_x p_T}{B L^2}$$

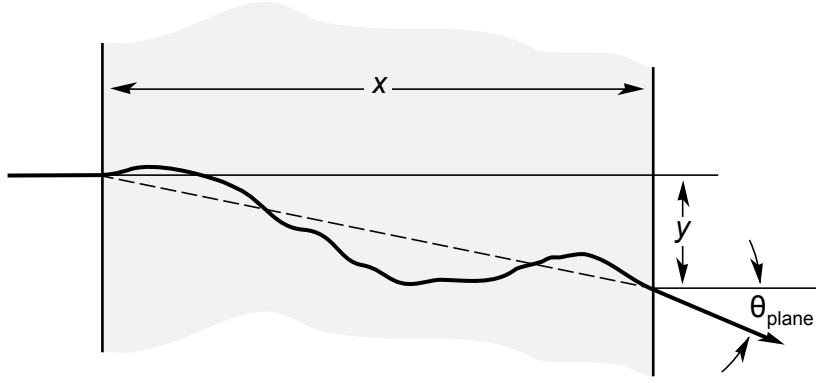


Figure 4.6. Track momentum uncertainty due to multiple scattering, adapted from [42]. A particle is deflected while passing through a material of thickness x . The angular deflection is θ_{plane} , while the transverse deflection is y .

There is also a component of the momentum's uncertainty due to multiple scattering of the particle, depending on the interaction length X_0 of the material [45] (see also Figure 4.6):

$$\left(\frac{\sigma_{p_T}}{p_T} \right)_{\text{M.S.}} = \frac{0.05}{B} \sqrt{\frac{1.43}{L \cdot X_0}}.$$

4.2. Vertex Reconstruction

Tracks can be traced back to their mutual origin to find the location of interaction, or vertex. Events have multiple vertices due to multiple interactions per event, or decays of secondary particles. Typically there are multiple soft interactions of low momentum transfer, and one hard interaction that contains the “interesting” physics which triggered the event. The vertex of the hard interaction is called the primary vertex (PV).

To determine the PV, the adaptive primary vertex algorithm (APV) is used [46]. For this, tracks with a transverse momentum $p_T > 0.5$ GeV are considered. Tracks in the acceptance region of the SMT must additionally have at least two SMT hits. First, groups of tracks are identified by choosing tracks within $\Delta z < 2$ cm of each other (z -clustering). Then, it is attempted to fit the tracks in a cluster to a common vertex, using a Kalman fitter. A preselection of tracks is made using the χ^2 of this fit, and the distance of closest approach (dca) of the tracks. For each step of the algorithm, the track with the worst match (highest χ^2) to the vertex is removed. This is repeated until the fit χ^2 is below a certain threshold, or there are only two tracks left. Matched tracks are removed from the list, and the algorithm is repeated until no more vertices are found.

To determine the primary vertex, the probability for each vertex to result from soft scattering (“minimum bias probability”) is calculated from the $\log(p_T)$ distribution of the vertex's tracks. The vertex with the lowest minimum bias probability is selected as primary vertex. Additionally, the PV is required to have at least three associated tracks, and an z position of $|z| < 50$ cm.

4.3. Electron ID

Electrons and photons interact with the calorimeter material to form showers (see Section 3.2.4). Due to the equal behavior in showering, both are treated together as EM objects. They can be distinguished by

the presence of a charged track. If a track can be matched to the EM object, it is most probably due to an electron and not a photon. In certain detector regions, the identification can come from the preshower detector: in $|\eta_{\text{det}}| < 1.1$ using the central, in $1.5 < |\eta_{\text{det}}| < 2.5$ the forward preshower detector.

Jets can be misidentified as electrons, in case a $\pi^0 \rightarrow \gamma\gamma$ decay falls together with a charged track. While this process has a low probability, the high hadronic production rate makes these electron fakes a sizable background. Real electrons can be distinguished from fakes by looking at several shower and track properties:

- Electromagnetic (EM) showers peak in the EM calorimeter, while jet showers peak in the hadronic calorimeter. The fraction of the total cluster energy deposited in the EM part of the calorimeter is given by `EMFraction`. For electrons, `EMFraction` ≈ 1 , while for jets `EMFraction` < 1 is expected.
- The H-Matrix algorithm combines information on the longitudinal and lateral shape of depositions in the ECal into the `HMx7` and `HMx8` variables, which are constructed from seven or eight input variables, respectively.
- Clusters from jets tend to be less isolated than real EM clusters. Thus the calorimeter isolation can be used to distinguish them:

$$\text{isolation} = \mathcal{I}_{\text{cal}} = \frac{E_T^{\text{tot}}(0.4) - E_T^{\text{EM}}(0.2)}{E_T^{\text{EM}}(0.2)}$$

$E_T^{\text{tot}}(\Delta R)$ is the transverse energy deposited in a cone of ΔR . E_T^{tot} only counts the energy deposited in the ECal. A smaller value of \mathcal{I}_{cal} means that the cluster is more isolated, and thus less likely to be from a jet.

- An alternative measure of isolation is track isolation (`IsoHC4`). It is defined as the scalar sum of transverse momenta of all tracks in a hollow cone from $\Delta R = 0.05 \dots 0.4$. The lower limit on ΔR is chosen to exclude the candidate track itself.
- When an electron hits the calorimeter, it deposits almost its entire energy in the ECal. Since its mass is small compared to its energy, $p \approx E$, meaning the fraction $E_{\text{cal}}^{\text{EM}}/p$ is approximately 1. This variable is called EOP (energy over p). Charged hadrons on the other hand, leave only a fraction of their energy in the ECal and are expected to have a smaller EOP. It can be also used to suppress $\pi^0 \rightarrow \gamma\gamma$ with an accidentally matched track, since a randomly picked track tends to have a lower momentum compared to the energy deposition, resulting in a high value of EOP.
- A neural network is used, taking four or seven input variables, to distinguish real electrons from fakes. The output of the neural net is called `NNout4` or `NNout7` depending on the number of inputs used.
- A likelihood function, `Lhood8`, is constructed using eight input variables, and allows further discrimination of electrons and fakes.
- Since an EM shower will reach its maximum width earlier than a hadronic one, the width of the EM cluster in the third layer, where the shower is expected to peak, is used as a distinguishing variable called `sigphi`.

In this analysis, different electron quality requirements are applied in the central calorimeter (CC, $|\eta_{\text{det}}| < 1.1$) and endcap (EC, $1.5 < |\eta_{\text{det}}| < 2.5$) regions. The cuts are displayed in table 4.1, and correspond to the `Point05` working point for CC electrons, and `Point1` for EC electrons.

Variable	CC	EC
isolation	< 0.15	< 0.1
EMfraction	> 0.9	< 0.9
HMx7	-	-
HMx8	-	< 40
IsoHC4	< 3.5	< 100
NNout7	> 0.3	-
NNout4	-	> 0.05
Sigphi	-	> 100
Lhood8	> 0.05	> 0.05
EOP	< 8.0	-

Table 4.1. Quality cuts applied to electrons in the CC ($|\eta_{\text{det}}| < 1.1$) and EC ($1.5 < |\eta_{\text{det}}| < 2.5$) regions.

4.4. Muon ID

Muons are the only particles that can leave the calorimeter and reach the muon system with noticeable probability. The reconstruction of muons involves not only the muon system, but also the tracker, and in certain cases the calorimeter.

Hits in the three layers of the muon system are combined to segments. Hits in the A layer form A segments, the B and C layers are treated together, where hits form BC segments. These segments are combined into muon candidates, or *local muons*.

Local muons are matched to central tracks, as these provide a better measurement of the muon p_T and charge, and provide an independent confirmation of the muon. Even if no local muon can be constructed, tracks can be matched to individual segments, hits in the muon system, or muon signatures in the calorimeter. This method, call muon tracking in the calorimeter (MTC), works by looking for a MIP signal (with a typical energy deposition of 3 GeV). Due to the fine granularity of the calorimeter, it is possible to reconstruct muon tracks out of calorimeter cells. The MTC method only has an efficiency of about 50%, but provides a higher angular acceptance, and a further independent confirmation of muons.

Reconstructed muons are classified according to their muon type (nseg) and quality, which will be described in the following.

Muon Type

The muon type nseg (originally: number of segments) specifies from which kind of segments a muon was reconstructed, and whether it was matched to a central track or not. A muon of type nseg = 3 is a local muon with A and BC segments, matched to a central track. Alternatively, it can be a central track matched to both A and BC segments (in the case a local muon was not reconstructed). A muon with nseg = 2 (1) is reconstructed from a track matched to an A (BC) segment. If nseg = 0, a central track was matched to no segment, but individual hits in the muon system, or a muon signature in the calorimeter (MTC). The muon type can also be negative, in which case there is no matched central track, but the signature is otherwise the same as for |nseg|. A summary of all possible values is given in Table 4.2.

Muon quality

Reconstructed muons can be classified beyond nseg by detailing in which parts of the muon system its hits were. The muon quality variable takes this information into account. There are two possible values of muon quality, “loose” and “medium”, although a muon may also fail the loose criteria and have no quality.

$ nseg $	Muon identification	Track matching (if $nseg \geq 0$)	
3	A and BC segments	local \rightarrow central	(if muon fit converged)
		central \rightarrow segments	(otherwise)
2	BC segment only	central \rightarrow segment	
1	A segment only	central \rightarrow segment	
0	muon hits / MTC	central \rightarrow hits / calo track	

Table 4.2. Possible values of muon type ($nseg$). A negative value indicates that no central track has been matched.

The formerly used “tight” quality has been discontinued in p20. The definition of muon quality varies with $nseg$:

$nseg = \pm 3$

A muon with $nseg = \pm 3$ is **medium** if it fulfills the following criteria:

- Two or more A layer wire hits, and at least one A layer scintillator hit
- Two or more BC layer wire hits
- One or more BC layer scintillator hits (unless the muon is in the central region, and there are less than 4 BC wire hits)

A muon is considered **loose** if it fails only one of the three tests, but has at least one scintillator hit.

$nseg = +2$

Muons with $nseg < 3$ must be matched to a central track to be loose or medium. An $nseg = +2$ muon is **loose** if it has two or more BC layer wire hits and at least one BC layer scintillator hit. It is **medium** if it is additionally in the central bottom region of the detector ($|\eta_{det}| < 1.6$ and fifth or sixth octant in φ).

$nseg = +1$

Like $nseg = +2$, but with the A layer instead of the BC layers. In addition, there is an exception for low p_T muons which were unlikely to have reached the BC layers. If the probability for a muon to reach the BC layers is less than 0.7, it is considered to be **medium**. The probability function has been determined in dependence of muon p_T and η using a GEANT simulation of the detector.

4.4.1. Muon isolation

Isolation serves to distinguish muons from different physical processes. A “prompt” muon, e.g. coming from a $Z \rightarrow \mu\mu$ will be isolated, save for coincidental particles in the same area, whereas a “secondary” muon emitted from a jet will not. There are two commonly used definitions for muon isolation at DØ:

$$etTrkCone5 = \sum_{\Delta R < 0.5} p_T \quad \text{and} \quad etHalo = \sum_{0.1 < \Delta R < 0.4} E_T$$

The track isolation $etTrkCone5$ is the scalar sum of all track p_T in a cone of $\Delta R < 0.5$ around the muon. Only tracks whose point of closest approach to the z -Axis is within 2 cm of that of the muon’s matched track are included. The calorimeter isolation $etHalo$ is the sum of all energy depositions in the calorimeter in a hollow cone of $\Delta R = 0.1 \dots 0.4$ centered around the muon. The lower bound on ΔR is to exclude depositions by the muon itself. Contributions from coarse HCal cells are not included in the sum.

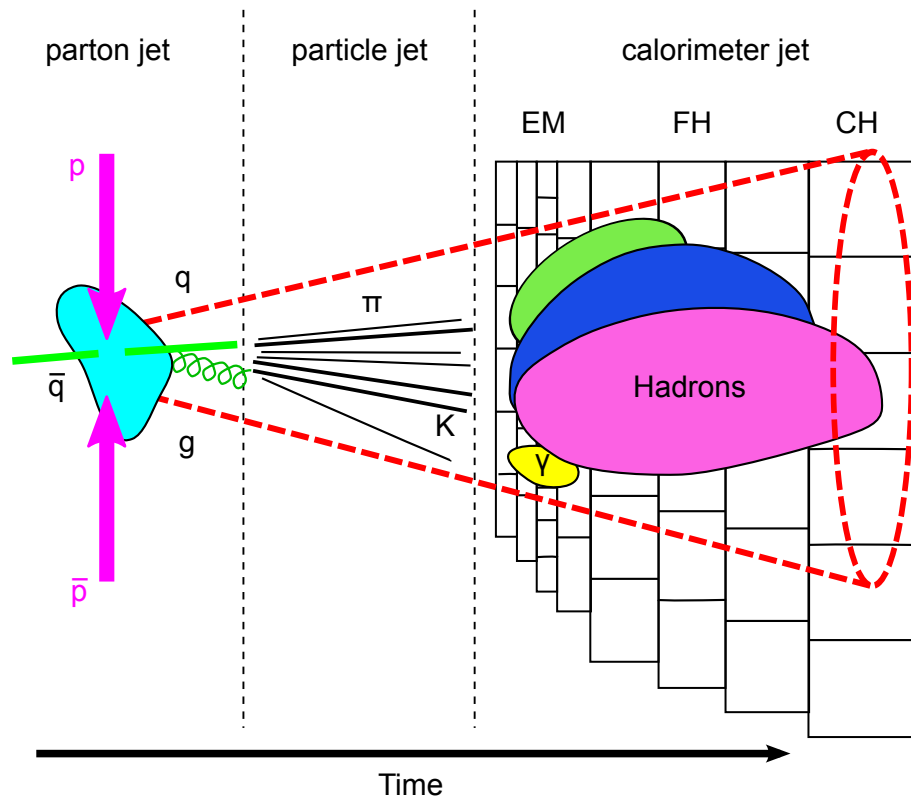


Figure 4.7. Schematic of jet evolution in a detector. Partons from the hard collision undergo hadronization and form particle jets, including hadrons and mesons. Particle jets hit the calorimeter, where they start showers. Electrons and photons shower predominantly in the electromagnetic calorimeter. Hadrons also shower in the fine and coarse hadronic calorimeter. Calorimeter jets are then identified by a jet algorithm.

4.4.2. Cosmic Veto

Since muons can penetrate the whole of the detector, cosmic muons can enter from the outside, and form a source of background. These muons are suppressed by a cosmic veto. Assuming that good muons come from the center of the detector and move outwards, all hits of the muon in the A and BC layers must be within ± 10 ns of the expected hit times for the muon to pass.

4.5. Jets

Quarks and gluons hadronize upon production, producing jets of hadronic particles, which create showers in the calorimeter. The task of a jet algorithm is to recognize jets in the calorimeter depositions. What is considered a jet is a matter of definition, and depends on the details of the algorithm used. Two features are generally desired in a jet algorithm:

- **Infrared safety:** The infrared divergence of QCD means that infinitely many soft (low momentum) gluons are emitted. The results of a jet algorithm should not change drastically in the presence of small depositions from these soft gluons (figure 4.8(a)).
- **Collinear safety:** The jet detection should not be affected if the jet's energy is split over adjacent cells, instead of deposited into one (figure 4.8(b)).

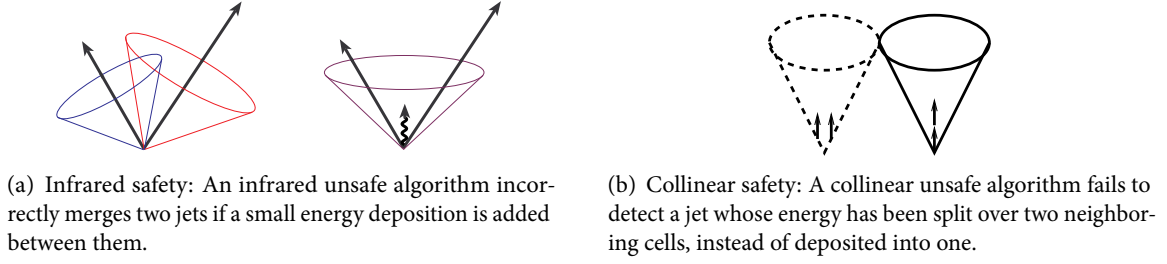


Figure 4.8. Infrared and collinear safety of jet algorithms. Images from [47].

The algorithm used in the following fulfills both criteria, and is called the Run II improved legacy cone algorithm (ILCA). It works by building a candidate list of jets using a cone algorithm, and refining the list using jet splitting and merging, and a set of filters.

- First, a set of **preclusters** is found using the “simple cone” algorithm. It starts with the tower with the highest E_T reading, but at least $E_T > 0.5$ GeV. Then, all towers with $E_T > 1$ MeV within $\Delta R < 0.3$ are added to the precluster. The algorithm continues with the next highest E_T tower, until no towers above the threshold are remaining.
- The preclusters and midpoints between preclusters are used as seeds for the construction of **proto-jets**.
- Proto-jets are constructed within cones of $\Delta R = 0.5$. The proto-jets may overlap.
- A jet splitting and merging procedure is applied to remove overlap and overcounting of energy deposits. All jet candidates with $E_T > 6$ GeV are kept.

Now, this list of candidates is cleaned from fakes due to noise, and misidentified electrons and photons.

- Individual calorimeter cells which have a high noise level and dominate a jet are called hot cells. To remove jets with hot cells, a cut on the hot fraction is applied:

$$\text{HotF} = \frac{E_T(\text{leading cell})}{E_T(\text{second cell})} < 10$$

- Similarly, if more than 90% of a jet’s energy is from a single tower, the jet is removed.
- Since the coarse HCal is very noisy, the fraction of a jet’s energy which comes from that part of the calorimeter is limited to $f_{\text{CH}} < 0.4$. Depending on $|\eta_{\text{det}}|$, the allowed fraction may be higher.
- Like in the case of EM objects, the fraction of energy deposited in the ECal is used to distinguish jets from electrons and photons. Jets are required to have $f_{\text{EM}} < 0.95$. A minimal value of $f_{\text{EM}} > 0.05$ is also required in order to suppress fakes due to calorimeter noise. These limits are also dependent of $|\eta_{\text{det}}|$.
- The energy of the reconstructed jet must be comparable with the energy given in the L1 trigger readout. This is specified by a cut on L1ratio:

$$\text{L1ratio} = \frac{E_T(\text{L1 readout})}{E_T(\text{jet})} > 0.5$$

This cut may be weaker depending on the $|\eta_{\text{det}}|$ region of the detector.

4.5.1. Jet Energy Scale

The energy of a calorimeter jet as reconstructed above does not necessarily reflect the energy of the original parton, or the sum of all particle's energies in the particle jet. There are multiple reasons for this:

- Acceptance gaps, and inaccessible material in front of the calorimeter cause energy depositions to be missed.
- Electronic noise in the calorimeter can cause a systematic mismeasurement.
- The response of the calorimeter is not necessarily linear over the whole energy range.
- Out-of-cone showering, where the jet algorithm cannot register part of the particle shower, causes the jet energy to be underestimated
- Neutrinos and minimal ionizing particles, such as muons, can carry away a part of the original parton's energy.

To account for these effects, a correction called jet energy scale (JES) is applied to the measured jet energies:

$$E_{\text{jet}} = \frac{E_{\text{jet}}^{\text{uc}} - O}{F(\eta_{\text{det}}) \cdot R(E) \cdot S}$$

Here, $E_{\text{jet}}^{\text{uc}}$ is the uncorrected jet energy before JES, O is a constant energy offset, $F(\eta_{\text{det}})$ is a η_{det} dependent correction. $R(E)$ is a energy dependent response function, e.g. to remedy nonlinearities in the response, and S is a factor for shower development. Not taken into account in this correction is the emission of hard gluons, which can divert energy at early stages of particle jet evolution to large angles.

4.6. Missing Transverse Energy

Uncharged particles, such as neutrinos or supersymmetric neutralinos, leave no direct signal in the detector. Their presence can inferred however from missing transverse energy.

The proton-antiproton collision is balanced on average, i.e. the center of mass of the $p\bar{p}$ system is at rest. However, in the actual hard collision, partons (quarks or gluons) are involved, which carry a fraction of the (anti-)protons' longitudinal momentum, depending on the parton density functions. The remaining momentum is carried away by the remnants of the (anti-)protons. This means that the initial momentum of the hard collision in z -direction is not known.

In contrast, the transverse component of the initial momentum is known to be zero. Thus, the total transverse momentum of all final state particles should be zero, too ($\sum \vec{p}_T = 0$). Any imbalance is a sign of undetected particles, or of a mismeasurement.

Instead of looking for missing transverse momentum, it is useful to use missing transverse energy (MET), which is a similar quantity measured mainly by the calorimeter. Missing energy is defined as the negative vectorial sum of energy depositions in the calorimeter. For a calorimeter cell at the position \vec{r}^i with an energy reading of E^i , an vectorial energy is defined by

$$\vec{E}^i = \frac{\vec{r}^i}{|\vec{r}^i|} E^i.$$

Its transverse components are given by the expressions [48]:

$$E_x^i = E^i \sin(\theta) \cos(\varphi) \quad \text{and} \quad E_y^i = E^i \sin(\theta) \sin(\varphi).$$

The visible energy can be defined as the vectorial sum of all energies, here its x and y -components:

$$E_{x,y}^{\text{vis}} = \sum_{i \in \text{cells}} \vec{E}_{x,y}^i.$$

From the sum all coarse HCal cells are excluded unless they are part of a recognized jet, since these cells have a high noise level. Also cells with an energy of less than 100 MeV are not included. The magnitude of missing transverse energy is of course equal to that of visible energy:

$$\cancel{E}_T = \sqrt{(E_x^{\text{vis}})^2 + (E_y^{\text{vis}})^2}$$

This value of \cancel{E}_T receives corrections for various objects in the event, since the energy from the reconstructed object is usually more accurate than the calorimeter reading alone. Cells associated with the object are removed from the sum and replaced by the object's energy. A special case are muons, which are minimal ionizing particles and deposit about 3 GeV in the calorimeter, essentially independent of their actual energy. A correction is applied to account for the full energy of the muons.

5. Samples and Event Selection

In this analysis, the full Run II dataset of the DØ experiment is analyzed, amounting to 10.4 fb^{-1} of recorded data. The data is split into three parts (Table 5.1) that differ in the software version used for event reconstruction. The first period, p17 or RunIIa, is also different because the detector had no SMT layer 0 yet (Section 3.2.1). A small fraction of the recorded data could not be used due to parts of the detector being offline while recording and other data quality issues. Runs with problems in SMT, CFT, calorimeter or muon system, or with invalid luminosity information, are flagged as bad. Affected runs have been omitted from the analyzed data, leaving a total of 9.749 fb^{-1} passing data quality (DQ) checks.

Part	Epoch	Recorded	$\int \mathcal{L} [\text{fb}^{-1}]$
p17	RunIIa	Apr. 20, 2002 – Feb. 22, 2006	1.079
p20	RunIIb-1	June 9, 2006 – Aug. 4, 2007	1.217
p20_2	RunIIb-2	Oct. 28, 2007 – June 13, 2009	3.061
	RunIIb-3	Sep. 15, 2009 – July 18, 2010	1.942
	RunIIb-4	Sep. 15, 2010 – Sep. 30, 2011	2.407

Table 5.1. Overview of the RunII data. The given integrated luminosity is the recorded luminosity after application of data quality (DQ) selection. The total delivered luminosity for all of RunII is 11.074 fb^{-1} (recorded: 10.448 fb^{-1} , after DQ: 9.749 fb^{-1}).

The analysis is divided into three different channels, $e\bar{e}l$, $e\mu l$ and $\mu\mu l$. To maximize the event yield, datasets of events satisfying any electron ($e\bar{e}l$ and $e\mu l$ channels) or muon triggers ($e\mu l$ and $\mu\mu l$) were combined via logical OR. Table 5.2 shows the preselected datasets (skims) used. For the $e\bar{e}l$ channel, the EMinclusive skim is used, for $e\mu l$, the EMMU skim is used, and for $\mu\mu l$, it is 2MUhighpt. The skims differ in which event tags are required. The precise requirements are listed in the appendix in Tables A.1 – A.3.

5.1. Monte Carlo

All background processes, with exception of QCD multijet (Section 5.7), as well as the signal, are modeled in this analysis using Monte Carlo (MC) samples. The production of a MC sample involves several steps. First, generator level-MC is created using an event generator such as PYTHIA. This is processed through a GEANT based model of the detector (DØGSTAR) to simulate interactions of particles with detector material. The next step is digitization, in which hits of particles in the simulated detector are detected. This is performed by the program DØSIM, which also simulates pile-up. The digitized MC is then overlaid with minimum-bias events to emulate underlying events. Finally, this is processed through the same reconstruction as the recorded data, using DØRECO.

The background MC used in this analysis are standard samples generated for the collaboration by the Common Samples Group (CSG). We consider four classes of background MC: $Z + \text{jets}$ and $W + \text{jets}$ is generated with ALPGEN, interfaced to PYTHIA 6.319 [49]. Diboson MC, including WW , WZ and ZZ , and top pair MC is generated with PYTHIA.

The $W/Z + \text{jets}$ samples include events with one W or Z boson and possibly jets, where we distinguish between light parton jets (u, d, s quarks and gluons), and b and c jets. The samples are generated at leading

Epoch	SAM dataset definition
RunIIa	CSG_CAF_<SKIM>_PASS3_p18.14.00
RunIIb-1	CSG_CAF_<SKIM>_PASS2_p21.10.00
RunIIb-2	CSG_CAF_<SKIM>_PASS4_p21.10.00_p20.12.00
	CSG_CAF_<SKIM>_PASS4_p21.10.00_p20.12.01
	CSG_CAF_<SKIM>_PASS4_p21.10.00_p20.12.02
	CSG_CAF_<SKIM>_PASS4_p21.10.00_p20.12.04
	CSG_CAF_<SKIM>_PASS4_p21.12.00_p20.12.05_allfix
RunIIb-3	CSG_CAF_<SKIM>_PASS5_p21.18.00_p20.16.07_fix
	CSG_CAF_<SKIM>_PASS5_p21.18.00_p20.16.07_reduced2
	CSG_CAF_<SKIM>_PASS5_p21.18.00_p20.16.08
RunIIb-4	CSG_CAF_<SKIM>_PASS6_p21.20.00_p20.18.02b
	CSG_CAF_<SKIM>_PASS6_p21.20.00_p20.18.02b_fix
	CSG_CAF_<SKIM>_PASS6_p21.21.00_p20.18.03
	CSG_CAF_<SKIM>_PASS6_p21.22.00_p20.18.04
	CSG_CAF_<SKIM>_PASS6_p21.22.00_p20.18.05

Table 5.2. Skims used in the analysis. Here, <SKIM> is either EMinclusive ($e\bar{e}l$ channel), 2MUhighpt ($\mu\mu l$), or EMMU ($e\mu l$).

MC Sample	k -factor
$Z + \text{lp jets}$	1.30
$Z + c\bar{c} + \text{lp jets}$	1.67
$Z + b\bar{b} + \text{lp jets}$	1.52
$W + \text{lp jets}$	1.30
$W + c\bar{c}/b\bar{b} + \text{lp jets}$	1.47

Table 5.3. k -factors for LO \rightarrow NLO scaling of $W/Z + \text{jets}$ samples.

order, and scaled to next-to-leading (NLO) order cross sections. The NLO scale factor is known as k -factor, and it differs in events containing only light parton jets compared to events with b or c jets. The k -factors for different samples are given in Table 5.3.

5.2. Signal MC Generation

There are three groups of signal Monte Carlo: mSUGRA points with $\tan\beta = 3$, mSUGRA points with $\tan\beta > 3$, and points with non-universal gaugino masses (NUGM). The spectra for the mSUGRA points have been generated using SUSY-HIT version 1.3 (including SDECAY 1.3b and HDECAY 3.4), the NLO cross sections were determined using PROSPINO2. The NUGM spectra have been generated with IsaSUGRA 7.83, and the cross sections were calculated with PYTHIA 8.170. For all signal points, event generation was performed using PYTHIA 6.319 and the standard DØ Monte Carlo toolchain, as described above. In the following, when no specific signal point is named in a figure, the mSUGRA point $m_0 = 100$ GeV, $m_{1/2} = 240$ GeV, $\tan\beta = 3$, $A_0 = 0$ and $\text{sgn}\mu = +1$ shall be implied.

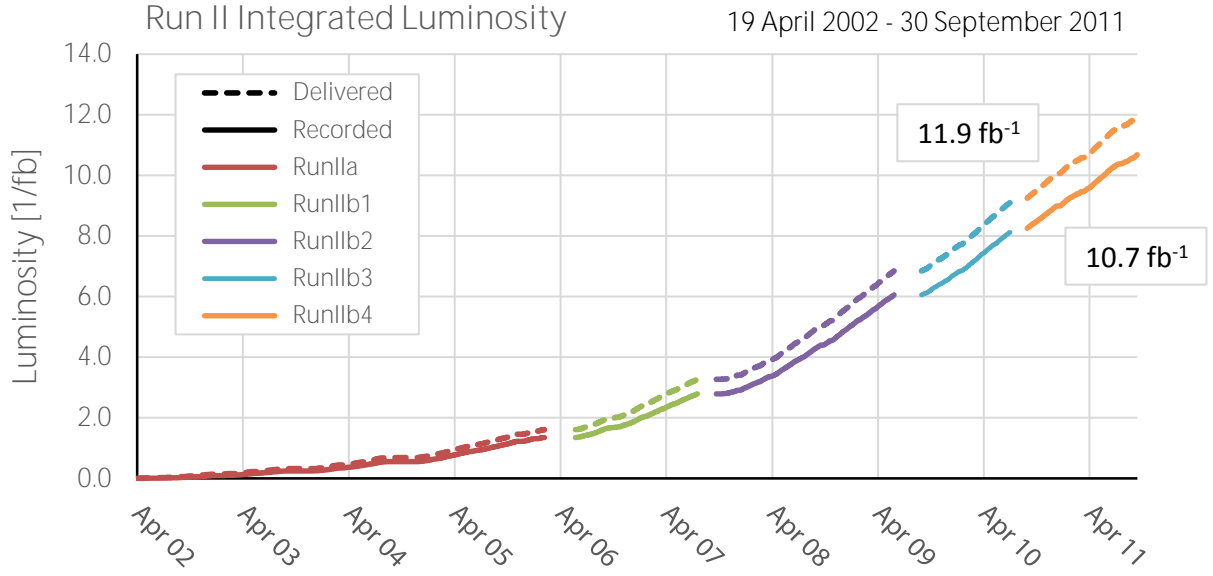


Figure 5.1. Integrated luminosity of the five epochs of RunII.

m_0 [GeV]	$m_{1/2}$ [GeV]	Points	Comment
60	70, 80, ..., 300	24	3l-max scenario
170	90, 100, ..., 300	16	heavy sleptons scenario
40, 50, ..., 200	180	17 (15)	
40, ..., 200	170, ..., 260	73 (38)	Along boundary of old $D\bar{D}$ result

Table 5.4. List of mSUGRA signal points for $\tan \beta = 3$, $A_0 = 0$ and $\mu > 0$. There are a total of 93 points in this list. Since there is some overlap between rows, the number of points unique to a row is given in parentheses.

m_0 [GeV]	$m_{1/2}$ [GeV]	$\tan \beta$	Points
50	350	10, 15, ..., 40	7
170	230		7
230	230		7
170	230	5, 7, 9, 11, 12, 13	6

Table 5.5. List of mSUGRA signal points for $\tan \beta > 3$, $A_0 = 0$ and $\mu > 0$. There are a total of 27 points in this list.

m_0 [GeV]	$m_{1/2}$ [GeV]	Points
140, 160, ..., 220	160, 180, 200	15
160	220, 240, ..., 320	6
300	160, 180, ..., 320	9
140, 160, ..., 320	260	10 (8)

Table 5.6. List of NUGM signal points for $\tan \beta = 10$, $\theta_{24} = -0.15\pi$, $A_0 = 0$ and $\mu > 0$. The points are illustrated in Figure 5.3.

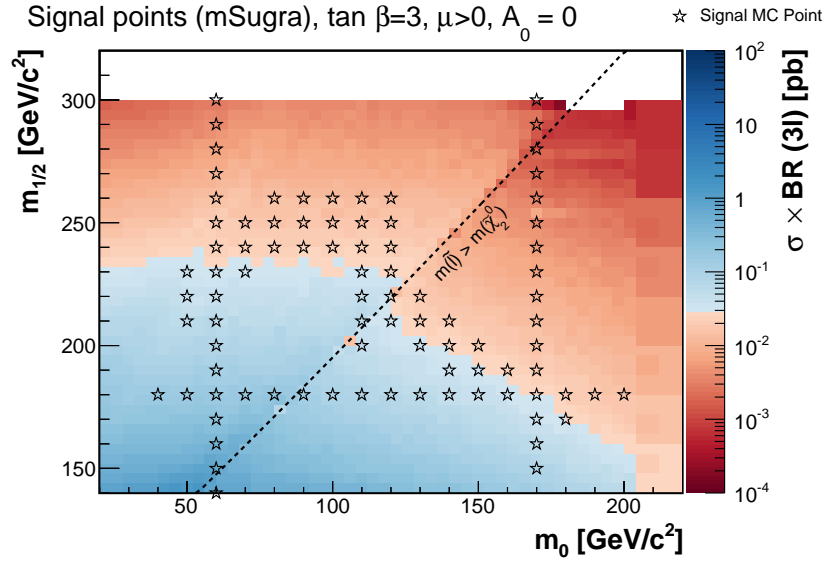


Figure 5.2. Signal MC points for the mSUGRA scenario, in the $(m_0, m_{1/2})$ plane. For these points, $\tan \beta = 3$, $A_0 = 0$ and $\mu > 0$. The color indicates cross section times branching ratio into three light leptons (e, μ), the transition between red and blue shows the estimated reach of the analysis, $\sigma \times BR \lesssim 0.03$ pb.

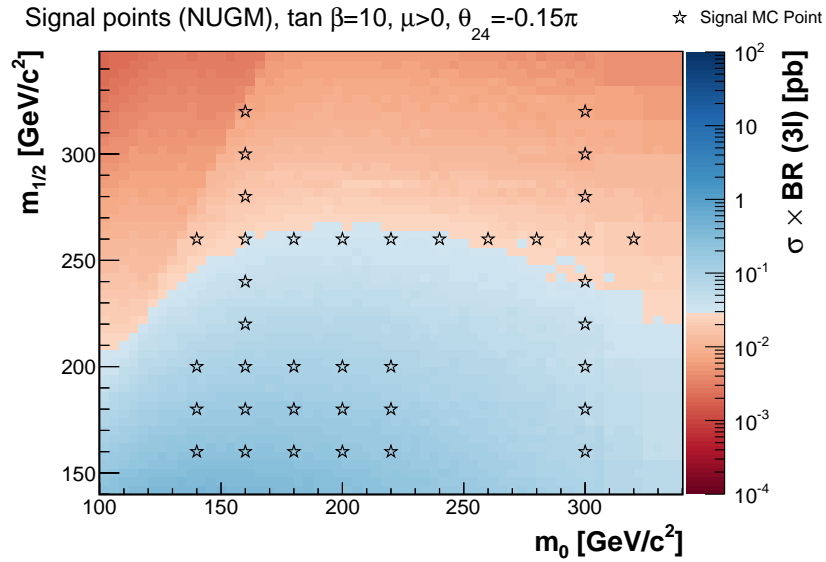


Figure 5.3. Signal MC points generated with non-universal gaugino masses (NUGM), in the $(m_0, m_{1/2})$ plane. For all these points, $\tan \beta = 10$, $\theta_{24} = -0.15\pi$, $A_0 = 0$ and $\mu > 0$. The color indicates cross section times branching ratio into three light leptons (e, μ), the transition between red and blue shows the estimated reach of the analysis, $\sigma \times BR \lesssim 0.03$ pb.

m_0 [GeV]	$m_{1/2}$ [GeV]	θ_{24}/π					Points
160	160	-0.674,	-0.65,	-0.6,	-0.5,	-0.4,	19
		-0.3,	-0.2,	-0.18,	-0.165,	-0.135,	
		-0.045,	-0.03,	-0.015,	0.0,	0.015	
		0.03,	0.045,	0.06,	0.075		

Table 5.7. List of NUGM signal points for $\tan\beta = 10$, $m_0 = m_{1/2} = 160$ GeV, $A_0 = 0$ and $\mu > 0$.

5.3. Software versions

The analysis is based on a modified version v5.6.18 of the `VJETS_CAFE` package, which depends on several other software packages, listed in Table 5.8. In order to process RunIIb4 data, `VJETS_CAFE` v5.7.23 was used for the p20_2 epoch. Physics treatment is identical in both versions, but the newer version contains updated data quality information necessary for the last data period.

Package	Version	Package	Version
beamposition	v2011-10-26	dq_util	p21-br-05
caf_dq	p21-br-04	eff_utils	p21-br-32
caf_eff_utils	p21-br-51	emid_cuts	p21-br-29
caf_mc_info	v2011-10-19	emid_eff	v09-00-11
caf_mc_util	p21-br-192	EMresolution_cafe	v00-07-07
caf_trigger	p21-br-136	jetid_eff	v05-00-00
caf_util	p21-br-157	lumi_profiles	v2011-11-08
cafe	p21-br-44	muid_eff	v05-05-01
cafe_sam	p21-br-07	tmb_tree	p21-br-94
dq_defs	v2011-09-30	vjets_cafe	v05-06-18

Table 5.8. Selection of common analysis framework (cafe) packages used for this analysis.

5.4. Event Selection

The leptonic final state of chargino-neutralino coproduction is characterized by three charged leptons, two of which are of same flavor, and missing transverse momentum. To increase the acceptance of the analysis, only two identified leptons (electrons or muons) are demanded, plus an additional third track. The possible combinations of identified leptons give three channels: electron+electron ($ee\ell$), electron+muon ($e\mu\ell$), and muon+muon ($\mu\mu\ell$). The selection criteria for individual electrons, muons, unmatched tracks, and jets are identical for all three channels:

- Electrons must pass quality requirements as given in Table 4.1, which is `Point05` in the CC region, and `Point1` in the EC region, and they must have at least $p_T > 15$ GeV. The electron track must have at least one hit in the SMT.
- Muons must fulfill the following requirements:
 - Transverse momentum $p_T > 15$ GeV
 - The muon has `loose` quality and `TopScaledMedium` isolation
 - A cosmic veto is applied to reject cosmic muons
 - The muon is matched to a central track of `tracknewmedium` quality
 - The muon has a pseudorapidity of $|\eta_{\text{det}}| < 2.0$
 - The central track matched to the muon must have at least one hit in the SMT
- Third tracks must have at least $p_T > 4$ GeV, and fulfill certain track quality and isolation requirements:
 - `tight` track quality
 - ΔR between a track and the next jet is greater than 0.5
 - ΔR between a track and muons or electrons is greater than 0.5
 - The track's distance of closest approach to the beamline `dca` is less than 0.2 cm. For `p17` and `p20_2`, in events with SMT hits, the cut is $|\text{dca}| < 0.1$ cm (Table 5.9)
 - The track's z coordinate (at closest approach to the beam line) is within 2 cm of that of the identified leptons
 - There must be at least one hit in the CFT
 - The track fit must have $\chi^2 < 4$
 - Tracker isolation `etTrkCone5` < 4 GeV
 - Calorimeter isolation `etHalo` < 10 GeV
- Jets used in this analysis are identified by the JCCB algorithm, with a cone size of $\Delta R < 0.5$. Jets must have the following properties:
 - Jet transverse momentum after corrections: $p_T > 20$ GeV
 - Jet transverse momentum before corrections: $p_T > 6$ GeV
 - Jet pseudorapidity $|\eta| < 2.4$
 - Energy fraction in the coarse hadronic calorimeter is less than 0.4
 - EM fraction is between 0.05 and 0.95
 - Level 1 confirmation (Jet energy as determined by level 1 trigger divided by final jet energy) is greater than 0.5

- In RunIIb (p20 and p20_2): Jet is vertex confirmed and shares a vertex with the two leptons.

Jet energy scale (JES) is applied using `jet_id_eff` version v05-00-00, and jet smearing, shifting and removal (JSSR) is applied by `caf_mc_util` version p21-br-192.

5.4.1. $ee\ell$ Preselection

From the skimmed data, a set of dilepton+track events is selected, which is called the preselection. The preselection criteria for the $ee\ell$ channel are as follows:

- Leading electron $p_T > 20 \text{ GeV}/c$
- Second electron $p_T > 15 \text{ GeV}/c$
- Dielectron invariant mass $M_{ee} > 15 \text{ GeV}$
- At least one electron is in the central calorimeter ($|\eta_{\text{det}}| < 1.1$)
- Both electrons are less than 2 cm apart in z direction (at point of closest approach to the beamline).

5.4.2. $e\mu\ell$ Preselection

The preselection is defined in the $e\mu\ell$ channel as:

- Electron $p_T > 15 \text{ GeV}/c$
- Muon $p_T > 10 \text{ GeV}/c$
- Electron and muon are less than 2 cm apart in z direction.

5.4.3. $\mu\mu\ell$ Preselection

The preselection for the $\mu\mu\ell$ channel is:

- Leading muon $p_T > 20 \text{ GeV}/c$
- Second muon $p_T > 15 \text{ GeV}/c$
- Both muons are less than 2 cm apart in z direction
- At least one of the muons must be in the central region ($|\eta_{\text{det}}| < 1.6$)
- For the matching of each muon to its central track, $\chi^2 < 100$ to remove erroneous matchings.
- For both muons, `etHalo` $< 10 \text{ GeV}$.
- The muons must have opposite charge. Events with like-sign muon pairs are used to determine the QCD multijet background (Section 5.7).

Part	SMT hits present	no SMT hits
p17 (RunIIa)	$ \text{dca} < 0.1 \text{ cm}$	$ \text{dca} < 0.2 \text{ cm}$
p20 (RunIIb-1)	$ \text{dca} < 0.2 \text{ cm}$	
p20_2 (RunIIb-2-4)	$ \text{dca} < 0.1 \text{ cm}$	$ \text{dca} < 0.2 \text{ cm}$

Table 5.9. Cuts on the tracks distance of closest approach (dca) variable.

Channel	RunIIa	RunIIb-1	RunIIb-234
$ee\ell$	1.04	1.00	0.95
$\mu\mu\ell$	1.08	1.03	1.05
$e\mu\ell$	0.96	1.06	1.02

Table 5.10. Scale factors from surface normalization for each channel and period.

5.5. MC normalization

The absolute number of expected background events is given by $N_{\text{exp}} = \int \mathcal{L} \cdot \sigma_{\text{BG}} \cdot \varepsilon$, where σ_{BG} is the cross section of a given background process, and ε is the combined efficiency of object and event selection, including the trigger efficiency. The number of MC events generated does not correspond to the recorded luminosity, instead many more events N_{MC} are generated and given weights, to achieve smoother distributions. The normalization of MC is given by

$$N_{\text{MC}}^{\text{norm}} = N_{\text{MC}} \frac{\int \mathcal{L} \cdot \sigma_{\text{BG}}}{N_{\text{MC}}}$$

so that the number of expected events is

$$N_{\text{exp}} = N_{\text{MC}} \frac{\int \mathcal{L} \cdot \sigma_{\text{BG}}}{N_{\text{MC}}} \cdot \varepsilon.$$

The number of events in data is likewise $N_{\text{data}} = N_{\text{data}}^0 \varepsilon_{\text{data}}$. These efficiencies are not individually known, and can in principle be different for data and background, since the background model is not perfect. For this reason, the background must be individually normalized by comparing the background prediction with data in a well-understood background region. This scale factor will be around one if the original normalization is correct. If applied selection criteria have a different efficiency in MC as compared to data, this will reflect in a value differing from one.

The normalization is derived for the $ee\ell$ and $\mu\mu\ell$ channels around the Z boson peak. For this, the preselection is applied and events in the invariant mass region $M_{\ell\ell} = 80 \dots 100 \text{ GeV}$ are selected. The normalization scale factor is then computed as $S = N_{\text{data}}/N_{\text{exp}}$. The scale factor is computed separately for each epoch, RunIIa, RunIIb-1 and RunIIb-234. In the $e\mu\ell$ channel, the normalization is derived in the dilepton mass window $M_{e\mu} = 35 \dots 70 \text{ GeV}$ instead. The results of the normalization are given in Table 5.10.

5.6. MC corrections

Since the MC samples as-is do not describe the backgrounds completely, additional corrections are applied. The applied corrections are summarized in Table 5.11.

Correction	Samples	Channels
Inst. luminosity (VJets)	all	all
Beam z -position (VJets)	all	all
$W p_T$ N -jets-dep. (VJets)	$W + \text{jets}$	all
$Z p_T$ N -jets-dep. (VJets)	$Z/\gamma^* + \text{jets}$	all
$Z p_T / \cos \beta_1$	$Z/\gamma^* + \text{jets}$	all
Electron p_T	all	$ee\ell, e\mu\ell$
Unclustered Energy	all	all
3D electron likelihood	all	$ee\ell$

Table 5.11. List of reweightings applied to the different samples and channels.

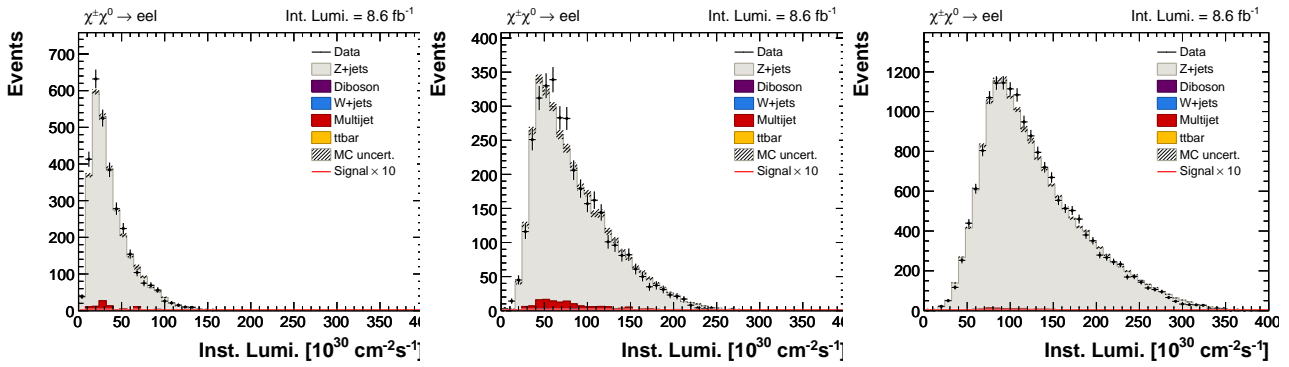


Figure 5.4. Instantaneous luminosity \mathcal{L} after application of all corrections, $ee\ell$ channel, for RunIIa, RunIIb-1, and RunIIb-234. For the other channels, see Figures A.1 and A.2 of the appendix.

5.6.1. Luminosity Reweighting

All samples, all channels

The luminosity profile of the minimum bias events that have been used to emulate underlying events in MC does not match that of the data sample. Since events have different characteristics at higher instantaneous luminosity \mathcal{L} – higher occupancy and pile-up, objects tend to be less isolated, reconstruction efficiency tends to be lower – it is important that the luminosity profiles in data and MC match. To achieve this, a reweighting is applied to correct the luminosity profile of the simulation. Distributions of the instantaneous luminosity for data and MC after reweighting can be seen for the $ee\ell$ channel in Figure 5.4, and for other channels in the appendix (Figures A.1 and A.2). The luminosity reweighting is part of the `VJETS_CAFE` suite.

5.6.2. Beam Reweighting

All samples, all channels

The distribution of the z position of the primary vertex does not initially agree in data and MC. To correct this, a standard reweighting (“Beam Reweighting”) is applied to the simulation. The corrected z distribution is shown in Figure 5.5 for RunIIb1 data for the $ee\ell$ channel.

5.6.3. $Z p_T$ Reweighting

$Z + \text{jets}$, all channels

The distribution of the Z boson p_T is not satisfactorily modeled in the $Z + \text{jets}$ MC. It is obvious that this variable is sensitive to discrepancies regarding jet emissions which cause a boost of the Z boson. A reweighting is applied to the ALPGEN + PYTHIA Monte Carlo to correct for this. This correction is derived according to [50]: The differential Z cross section in dependence of p_T is considered in $Z \rightarrow \ell\ell$ ($\ell = e, \mu$)

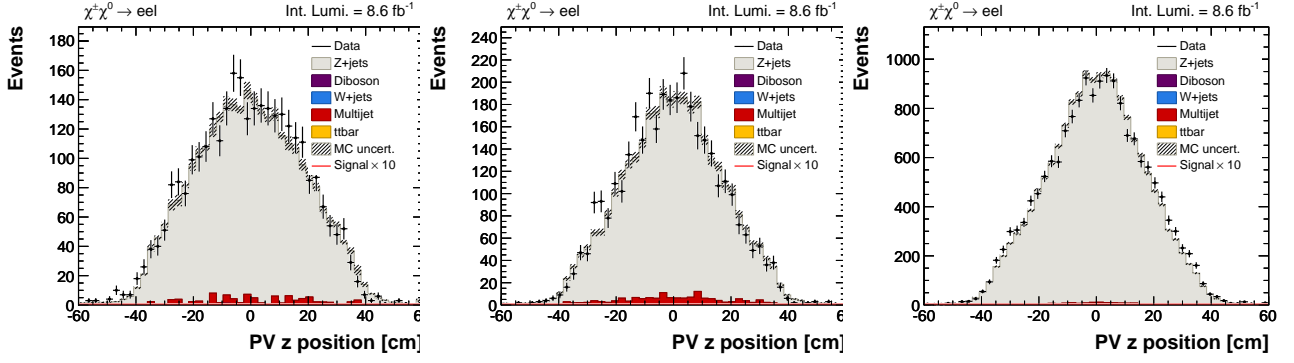


Figure 5.5. z coordinate of the primary vertex for the $ee\ell$ channel. After application of all corrections, for RunIIa, RunIIb-1, and RunIIb-234. For the other channels, see Figures A.3 and A.4 of the appendix.

events for regular and tuned MC, and the ratio is fitted with a modified Fermi function. This is used as an event-wise reweighting function, depending on the p_T of the Z boson. This reweighting, as available in the standard VJets package, is jet-inclusive, i.e. it does not depend on the number of jets in the event. An additional correction dependent on the number of jets in an event is applied, which is described in [51]. This N -jets-dependent correction has since been introduced into the official VJETS_CAFE package.

5.6.4. $Z p_T / \cos \beta_1$ Reweighting

$Z + \text{jets}$, all channels

After application of the preselection, including the third track requirement, it was found that there was a remaining mismodeling of the Z boson p_T . This is especially pronounced in the RunIIa MC. To improve modeling, another correction was derived as a function of the $Z p_T$ and $\cos \beta_1$, the angle between the Z boson transverse momentum vector \vec{p}_T and the first lepton (5.1):

$$\cos \beta_1 = \frac{\vec{p}_T(\ell_1) \cdot \vec{p}_T(Z)}{|\vec{p}_T(\ell_1)| |\vec{p}_T(Z)|} \quad (5.1)$$

Two-dimensional histograms of $Z p_T$ and $\cos \beta_1$ are created for data and for all backgrounds, and all backgrounds except $Z + \text{jets}$ (multijet, $t\bar{t}$, diboson and $W + \text{jets}$) are subtracted from the data histogram. Bins containing too low statistics (less than 15 events) are merged with neighboring bins. Then, the ratio of data minus non- Z backgrounds, and $Z + \text{jets}$ is calculated bin-by-bin and applied as a reweighting to the $Z + \text{jets}$ sample. The correction, for the $ee\ell$ channel and the RunIIa period, can be seen in Figure 5.8. Events at low $Z p_T$ (around 5 GeV) and $\cos \beta_1 \approx 1$ receive an enhancement, while events at higher $Z p_T$ receive a lower weight, shifting the distribution slightly towards lower p_T . Plots of $Z p_T$ and $\cos \beta_1$ distributions before application of this reweighting are shown in Figures 5.6 and 5.7 and after application in Figures 5.9 and 5.10.

5.6.5. $W p_T$ Reweighting

$W + \text{jets}$, all channels

A reweighting similar to the $Z p_T$ reweighting is applied to $W + \text{jets}$ events, depending on the transverse momentum of the W boson. The correction, which is described in [52], is derived from the ratio of $W p_T$ and $Z p_T$ calculation in NNLO and the inclusive $Z p_T$ reweighting as described above. This correction is part of VJets, and applied before the preselection stage.

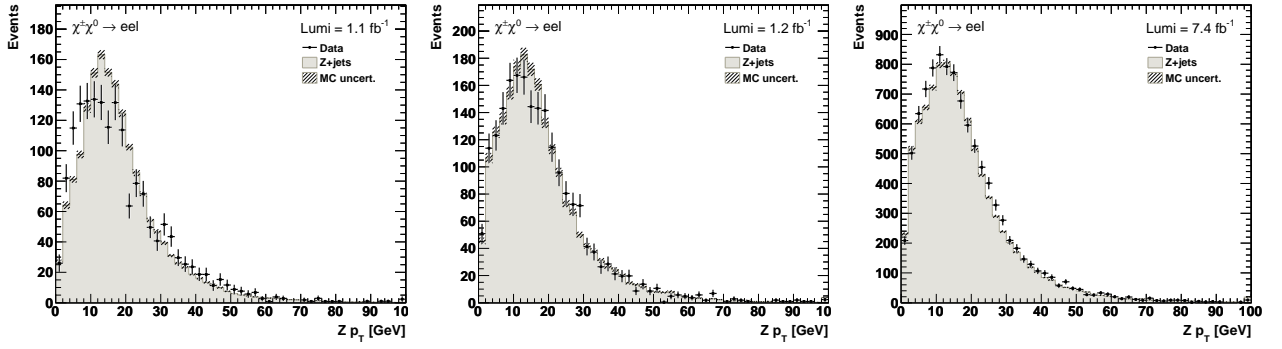


Figure 5.6. Reconstructed Z boson p_T , before application of the additional $Z p_T / \cos \beta_1$ reweighting (but after application of the electron p_T correction). From the data distribution, $t\bar{t}$, multijet, diboson and W + jets backgrounds have been subtracted. Shown for the $ee\ell$ channel, for RunIIa, RunIIb-1 and RunIIb-234.

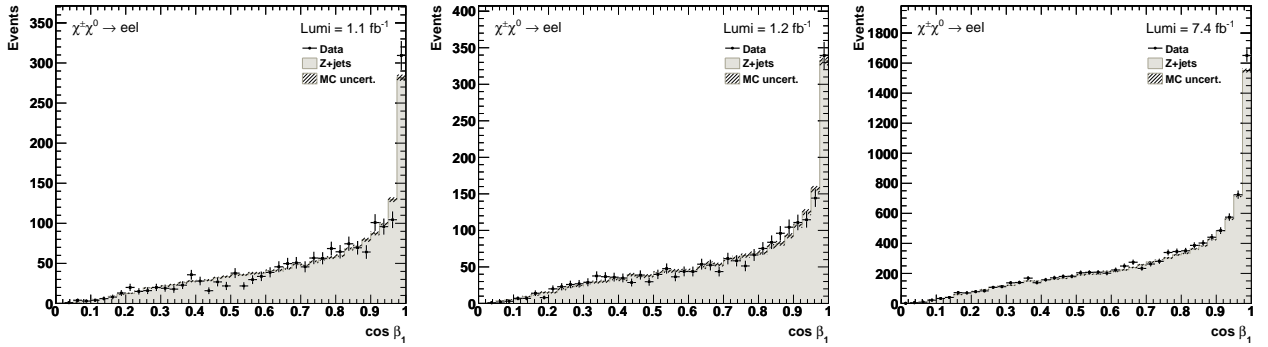


Figure 5.7. Distribution of $\cos \beta_1$, before application of the additional $Z p_T / \cos \beta_1$ reweighting (but after application of the electron p_T correction). From the data distribution, $t\bar{t}$, multijet, diboson and W + jets backgrounds have been subtracted. Shown for the $ee\ell$ channel, for RunIIa, RunIIb-1 and RunIIb-234.

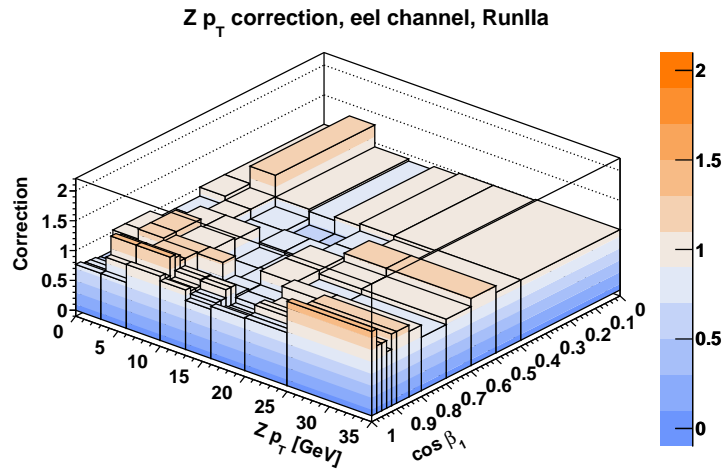


Figure 5.8. Scale factors for the additional $Z p_T / \cos \beta_1$ reweighting, for the ee channel, RunIIa period. Plots for the other epochs can be found in Figure A.5 of the appendix.

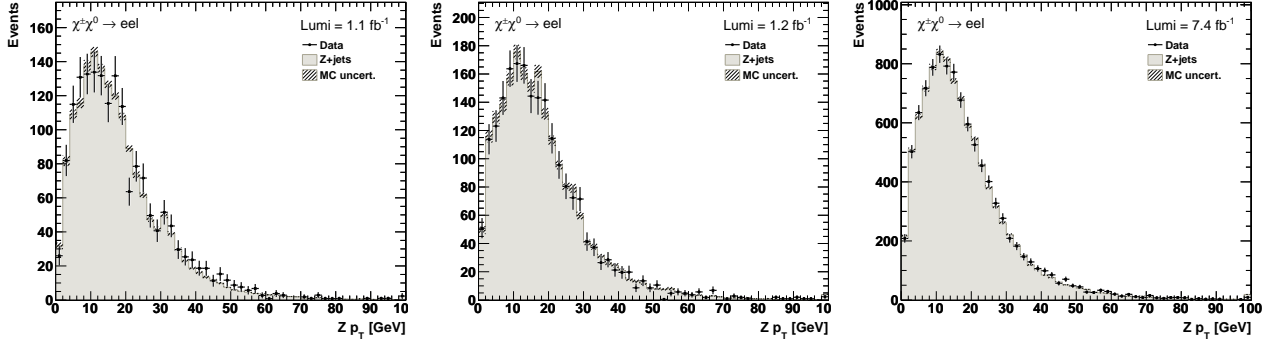


Figure 5.9. Reconstructed Z boson p_T , after application of the additional $Z p_T / \cos \beta_1$ reweighting. From the data distribution, $t\bar{t}$, multijet, diboson and W + jets backgrounds have been subtracted. Shown for the $ee\ell$ channel, for epochs RunIIa, RunIIb-1 and RunIIb-234.

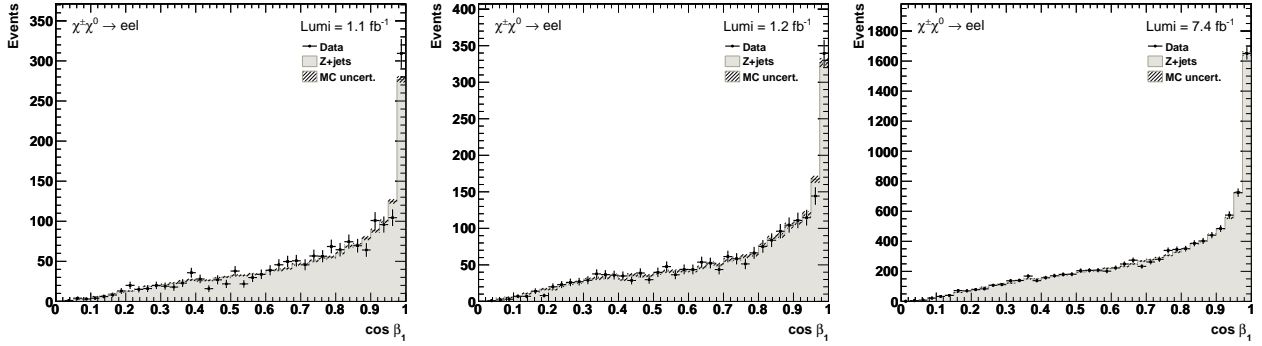


Figure 5.10. Distribution of $\cos \beta_1$, after application of the additional $Z p_T / \cos \beta_1$ reweighting. From the data distribution, $t\bar{t}$, multijet, diboson and W + jets backgrounds have been subtracted. Shown for the $ee\ell$ channel, for epochs RunIIa, RunIIb-1 and RunIIb-234.

5.6.6. Electron p_T Reweighting

All samples, $ee\ell$ channel

In addition to the standard electron ID corrections, which are parametrized in η_{det} , φ and instantaneous luminosity \mathcal{L} , a further electron p_T dependent correction is applied [53]. Using the tag and probe method described in [54], separate corrections for CC and EC electrons have been calculated. The scale factors are fitted with an error function (5.2):

$$f(x) = a + d \cdot \text{erf}\left(\frac{x - b}{c}\right) \quad \text{where} \quad \text{erf}(x) = \frac{2}{\sqrt{\pi}} \int_0^x e^{-\tau^2} d\tau \quad (5.2)$$

Then the correction is applied on top of the standard corrections as an event weight in dependence of the electron p_T , once for the first and once for the second electron in the event. Figure 5.11 and 5.12 show the weights for RunIIb1 and RunIIb2,3,4, respectively.

5.6.7. Unclustered Energy Reweighting

All samples, all channels

The unclustered energy (UE) of an event is the sum of all energy depositions in the calorimeter and the ICD which are not clustered into jets or EM objects (as described in chapter 4). A major source of UE is the underlying event. Since the calculation of missing transverse energy involves almost all calorimeter cells,

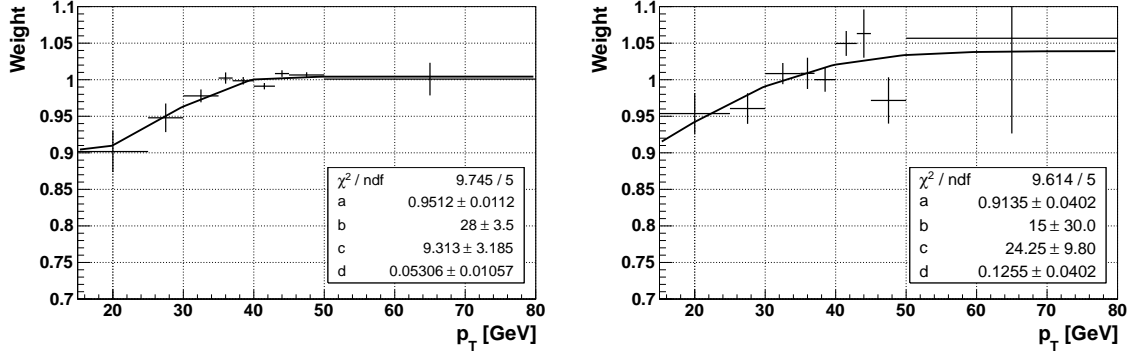


Figure 5.11. p_T dependent electron scale factors for RunIIb-1 (p20), CC region (left) and EC region (right). The scale factor is fitted with the function $f(x) = a + d \operatorname{erf}((x - b)/c)$.

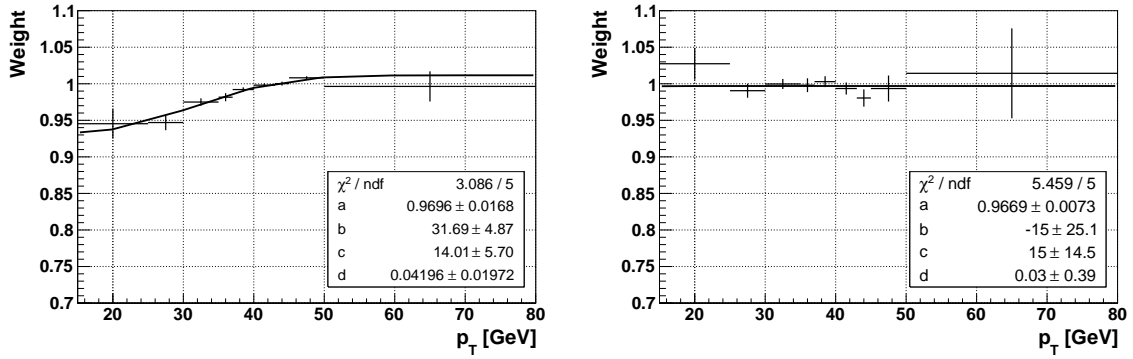


Figure 5.12. p_T dependent electron scale factors for RunIIb-2,3,4 (p20_2)

including the unclustered ones, it is closely related to UE. Thus a good modeling of unclustered energy improves the description of \cancel{E}_T .

An event-by-event reweighting is applied to the preselection samples that has the effect of making the UE distributions agree with data. The UE distribution is not further used in the analysis, since in it the background model agrees with the data by construction. The general improvement in data/MC agreement is especially strong in the $ee\ell$ and $\mu\mu\ell$ channels, but for consistency the correction is also applied in $e\mu\ell$. Figures 5.13–5.18 show the \cancel{E}_T and UE distributions before and after reweighting for the $ee\ell$ channel.

5.6.8. 3D electron likelihood reweighting

All samples, $ee\ell$ channel

A final reweighting is applied to the $ee\ell$ channel, intending to correct the electron ID likelihood distributions. This reweighting depends on the `minqual` variable, which is defined as the lowest EM likelihood of both identified electrons:

$$\text{minqual} := \min(\text{Lhood8}(e_1), \text{Lhood8}(e_2)).$$

The reweighting is performed in bins of p_T and η_{det} , always using the values of the lowest likelihood electron. A 3D histogram is filled for each background and data. Bins with insufficient statistics are merged, and the ratio of both histograms is used as the reweighting. The scale factors are plotted in Figures 5.19–5.21.

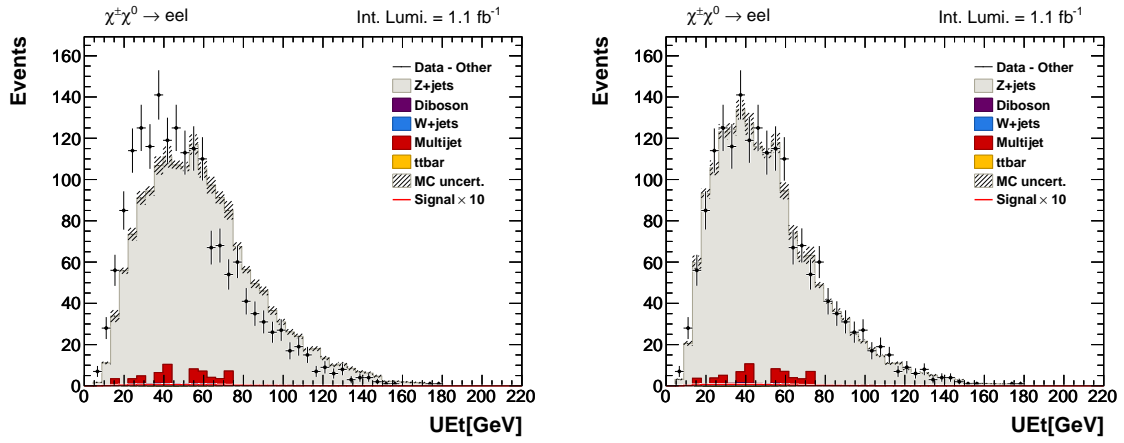


Figure 5.13. Unclustered energy before and after unclustered energy reweighting, $e\bar{e}l$ channel, p17 period.

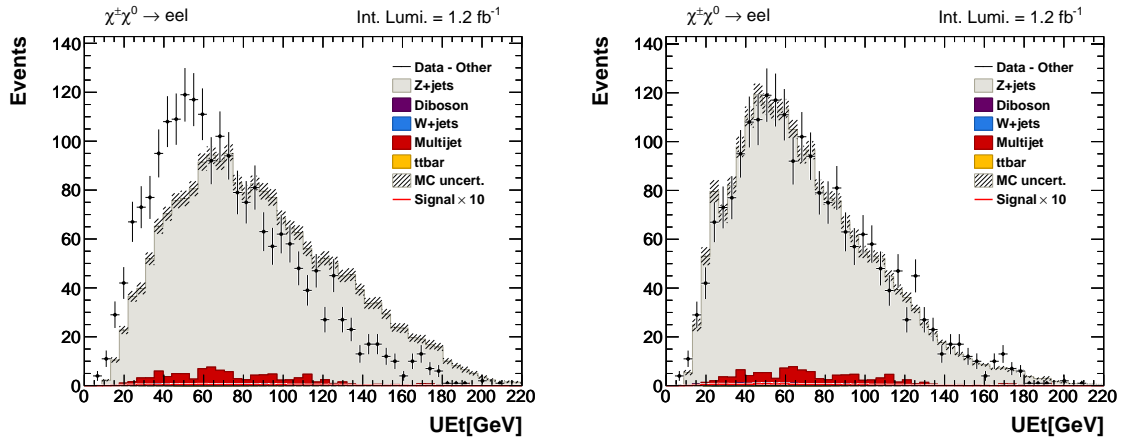


Figure 5.14. Unclustered energy before and after unclustered energy reweighting, $e\bar{e}l$ channel, p20 period.

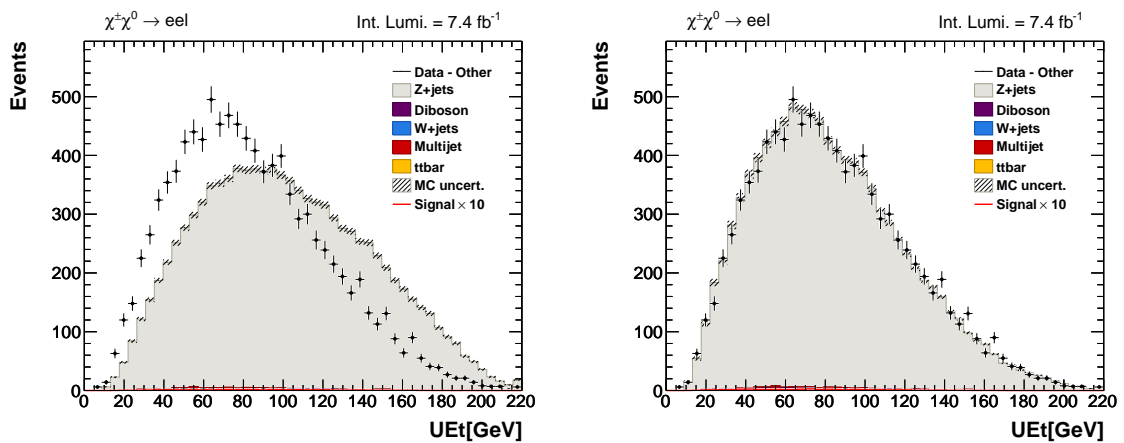


Figure 5.15. Unclustered energy before and after unclustered energy reweighting, $e\bar{e}l$ channel, p20_2 period.

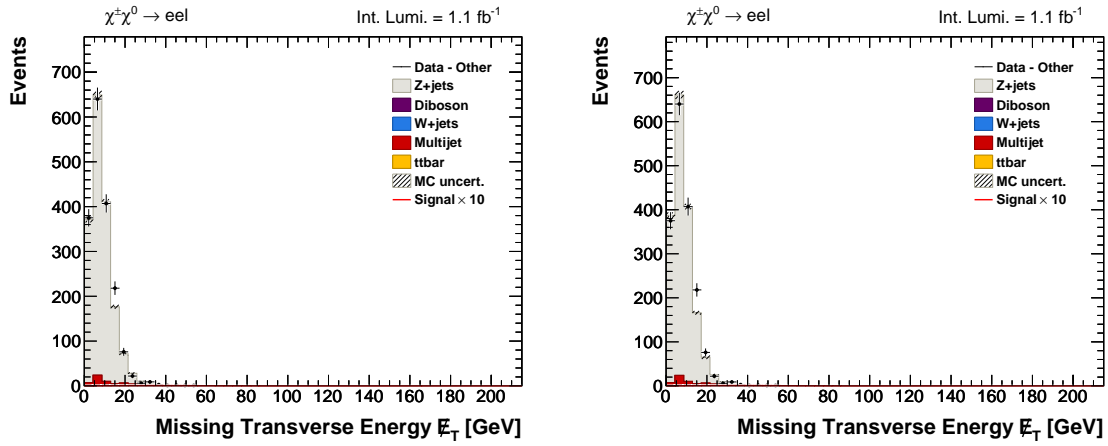


Figure 5.16. MET before and after unclustered energy reweighting, $ee\ell$ channel, p17 period.

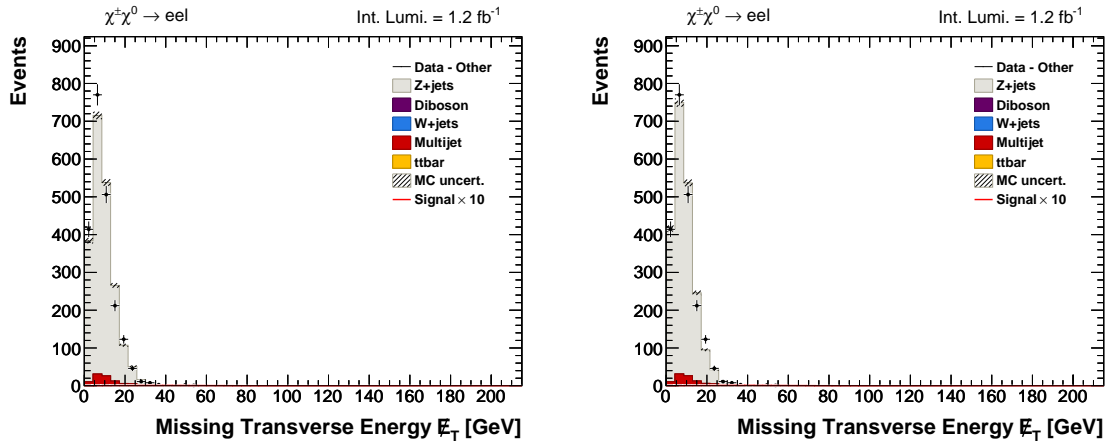


Figure 5.17. MET before and after unclustered energy reweighting, $ee\ell$ channel, p20 period.

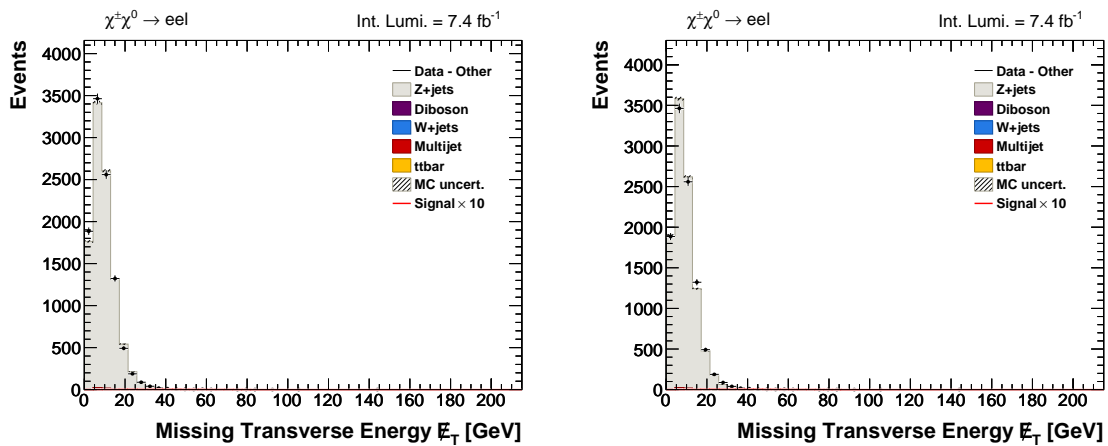


Figure 5.18. MET before and after unclustered energy reweighting, $ee\ell$ channel, p20_2 period.

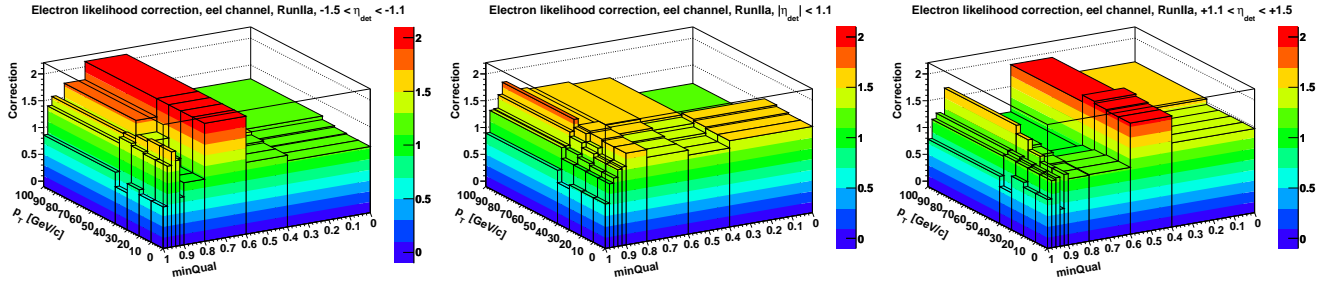


Figure 5.19. 3D electron likelihood reweighting, for the $ee\ell$ channel, p17 period. From left to right: $\eta_{\text{det}} = -1.5 \dots -1.1$, $\eta_{\text{det}} = -1.1 \dots 1.1$, and $\eta_{\text{det}} = 1.1 \dots 1.5$.

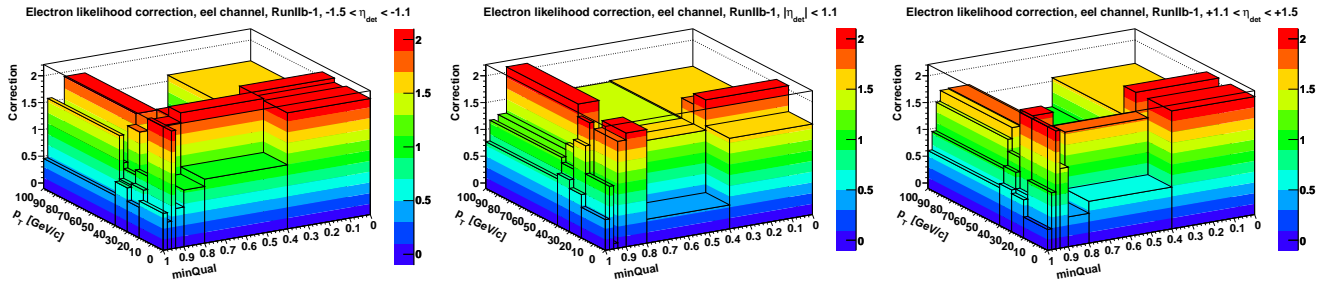


Figure 5.20. 3D electron likelihood reweighting, for the $ee\ell$ channel, p20 period. From left to right: $\eta_{\text{det}} = -1.5 \dots -1.1$, $\eta_{\text{det}} = -1.1 \dots 1.1$, and $\eta_{\text{det}} = 1.1 \dots 1.5$.

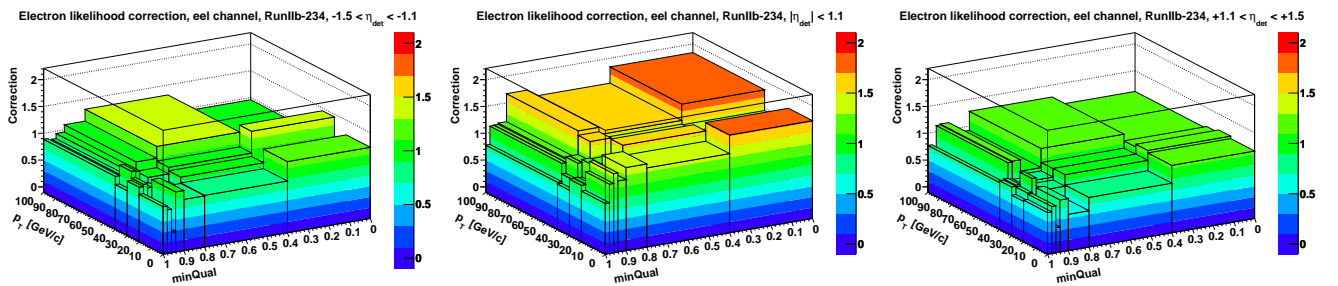


Figure 5.21. 3D electron likelihood reweighting, for the $ee\ell$ channel, p20_2 period. From left to right: $\eta_{\text{det}} = -1.5 \dots -1.1$, $\eta_{\text{det}} = -1.1 \dots 1.1$, and $\eta_{\text{det}} = 1.1 \dots 1.5$.

5.7. QCD Multijet

The QCD multijet background mainly consists of $b\bar{b}$ and $c\bar{c}$ events, but also contains all background processes that are not covered otherwise by Monte Carlo. This includes events with multiple jets from the underlying event and initial/final state radiation, when these are not contained in other samples.

The modeling of the QCD multijet background is done by a data driven process, which is slightly different in the three channels. First, a data sample is selected which is enriched in QCD multijet events (“fakes”) and has no overlap with the main selection sample. Then, a reweighting function depending on the leading lepton p_T is determined. The function is applied on an event-by-event basis to the fake enriched sample to make it a suitable estimation of the QCD background in the main selection.

5.7.1. Selection of the fake-enriched sample ($ee\ell$ channel)

The fake-enriched sample is selected by starting with the preselection criteria (see Section 5.4) and reversing cuts on the electron identification neural net output. Specifically, central electrons ($\eta_{\text{det}} < 1.1$) must fulfill $\text{NNout7_CC} < 0.3$, while for endcap electrons the cut is $\text{NNout7_CC} < 0.05$. This ensures the orthogonality of the fake-enriched sample to the main sample. To increase statistics, the cut on the electron likelihood variable LHood8 is relaxed from 0.05 to $\text{LHood8} > 0.001$.

For the calculation of the QCD reweighting, the selection criteria are loosened in order to improve overall statistics and to reach a higher fraction of QCD events in the sample. Instead of 20 GeV and 15 GeV, the leading and second electron p_T must be higher than 15 GeV and 10 GeV. The track’s transverse momentum cut is reduced to $p_T(\text{trk}) > 2$ GeV (4 GeV) and the requirement that the electrons have SMT hits is removed.

5.7.2. Selection of the fake-enriched sample ($e\mu\ell$ channel)

To select the fake-enriched sample in the $e\mu\ell$ channel, the electron ID neural net cuts are reversed like in the $ee\ell$ channel (for central electrons ($\eta_{\text{det}} < 1.1$) the cut is $\text{NNout7_CC} < 0.3$ and for endcap electrons it is $\text{NNout7_CC} < 0.05$). Additionally, the muon must fail one of either the calorimeter or the track isolation criteria, which are $\text{etHalo}/p_T < 0.5$ and $\text{etTrkCone5}/p_T < 0.2$. To increase statistics, the `tracknewmedium` quality requirement of the matched track is dropped.

When determining the QCD reweighting, the preselection criteria are loosened as follows: The dimuon invariant mass cut is reduced to $M > 5$ GeV (instead of $M > 15$ GeV), the minimum track transverse momentum is $p_T(\text{trk}) > 2$ GeV (instead of $p_T(\text{trk}) > 4$ GeV). Also, the requirement of SMT hits for the identified leptons is dropped.

5.7.3. Selection of the fake-enriched sample ($\mu\mu\ell$ channel)

The selection criteria of the fake-enriched sample in the $\mu\mu\ell$ channel is the same as the preselection, but the two muons must have the same sign. To achieve orthogonality, the same sign events are omitted from the preselection.

Again, for the determination of the reweighting, the cuts are loosened. The invariant mass of the two muons must be greater than 15 GeV and 10 GeV (instead of 20 GeV and 15 GeV), and the track must have $p_T(\text{trk}) > 2$ GeV (rather than $p_T(\text{trk}) > 4$ GeV). Also, the tracks matched to muons do not require SMT hits.

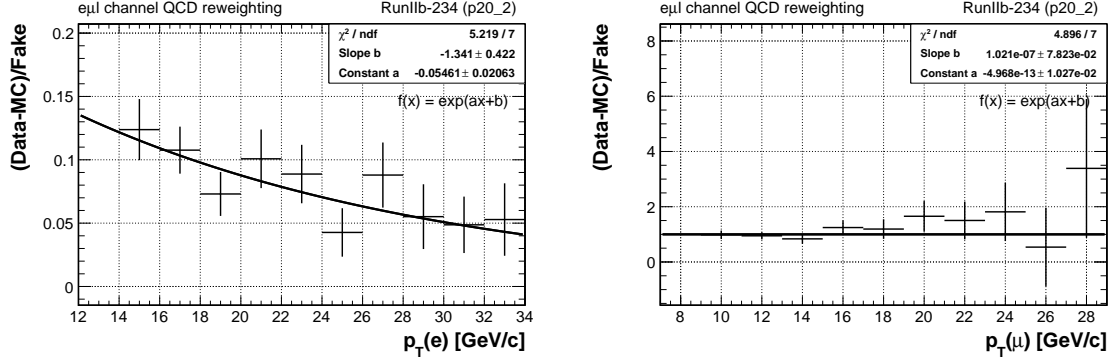


Figure 5.22. QCD multijet reweighting functions, $e\mu\ell$ channel, p20_2 period. The first reweighting (left) is dependent on the electron p_T , the second on the muon p_T . For other channels and epochs, see the appendix (Section A.1.5).

5.7.4. Multijet reweighting

The reweighting function that is applied to the fake-enriched sample is determined in the subset of events where the two identified leptons have the same charge, to suppress Drell-Yan events ($Z \rightarrow \ell\ell$). A histogram of the leading lepton p_T in same-sign events is created, including data events from the main sample, data events from the fake-enriched sample, and MC events. The fake-enriched sample is to be reweighted so that it forms a good description of the total background together with the MC. Thus, the fake-enriched distribution has to be scaled binwise by the difference between the data and MC event counts, divided by the fake event count:

$$f = \frac{N_{\text{data}}^{SS} - N_{\text{MC}}^{SS}}{N_{\text{fake}}^{SS}} \quad (5.3)$$

The quantity f is determined bin-by-bin. It is expected to roughly follow a falling exponential function in dependence of p_T , since QCD events are exponentially more prevalent at low p_T . To determine the reweighting function $f(p_T)$, an exponential function is fitted to the bin-by-bin ratio:

$$f(p_T) = \exp(ap_T + b) \quad (5.4)$$

The resulting fit can be seen for the $e\mu\ell$ channel, p20_2 epoch, in Figure 5.22. The reweighting function depending on the leading lepton p_T is determined as described above and applied to the fake-enriched sample. The procedure is then repeated with the second lepton p_T , using the reweighted fake-enriched sample. The whole QCD estimation procedure can be summarized as follows:

$$\begin{aligned} f_1(p_{T1}) &= \frac{N_{\text{data}}^{SS} - N_{\text{MC}}^{SS}}{N_{\text{fake}}^{SS}} \Rightarrow N_{\text{fake},1}^{SS} = f_1 \otimes N_{\text{fake}}^{SS} \Rightarrow \\ f_2(p_{T2}) &= \frac{N_{\text{data}}^{SS} - N_{\text{MC}}^{SS}}{N_{\text{fake},1}^{SS}} \Rightarrow N_{\text{QCD}} = f_2 \otimes f_1 \otimes N_{\text{fake}}, \end{aligned}$$

where $f_1(p_{T1})$ is the reweighting function determined in the leading lepton p_T distributions and $f_2(p_{T2})$ for the second lepton respectively. The various samples, and their binwise event count, are given by N : N_{data}^{SS} and N_{MC}^{SS} are data and MC samples with preselection, N_{QCD}^{SS} is the fake-enriched sample and \otimes stands for event-by-event application of the reweighting. The final sample which estimates the QCD multijet

background for the data sample is N_{QCD} . The reweighting functions are determined and applied separately for each epoch (RunIIa, RunIIb1 and RunIIb2-4).

5.8. Cutflow

Now that the modeling of all backgrounds is complete and all corrections are applied, we perform a series of cuts to improve the signal/background ratio before input to the multivariate analysis.

- Cut 1: $\Delta\varphi(\ell_1, \ell_2) < 2.5$

The angle between both identified leptons must be less than 2.5 radians. This is mainly to reduce $Z \rightarrow \ell\ell + \text{jets}$ events, in which the leptons tend to be back-to-back.

- Cut 2: Missing transverse energy $\cancel{E}_T > 15 \text{ GeV}$

A certain amount of missing transverse energy is characteristic for the signal, since the final state contains LSPs and neutrinos.

- Cut 3: Transverse momentum balance $\text{ptBalance} < 5.0$

Assuming that the identified leptons, the undetected particles in form of \cancel{E}_T and the selected track originate from the same interaction (with possible intermediate states), their transverse momentum should be balanced. Specifically, the sum of three components' p_T should have the same magnitude as the fourth component. This leads to the definition of ptBalance :

$$\text{ptBalance} = \frac{|\vec{p}_{T1} + \vec{p}_{T2} + \vec{\cancel{E}}_T|}{p_{T3}} \quad (5.5)$$

The ptBalance variable is expected to peak around 1 for the signal, with the background distributions more smeared out.

- Cut 4: Z mass veto, $M(\ell_1, \ell_2) \neq 80 \dots 100 \text{ GeV}$.

By removing events with a dilepton invariant mass around the Z mass, events from $Z \rightarrow \ell^+ \ell^-$ are suppressed. This cut is only applied in the $e\ell\ell$ and $\mu\mu\ell$ channels.

In the following tables, the event yield at preselection and after each cut is presented. Table 5.12 is for the $e\ell\ell$ channel, 5.13 for $e\mu\ell$ and 5.14 for $\mu\mu\ell$. Data from all three epochs is considered together in the tables. The signal point used is the mSUGRA point with $m_0 = 100 \text{ GeV}$, $m_{1/2} = 240 \text{ GeV}$, $\tan\beta = 3$, $A_0 = 0$ and $\text{sgn}\mu = +1$.

5. Samples and Event Selection

Sample	Preselection	Cut 1	Cut 2	Cut 3	Cut 4
Data	23245.00 \pm 152.47	2799.00 \pm 52.90	615.00 \pm 24.80	419.00 \pm 20.47	171.00 \pm 13.07
Signal	17.40 \pm 4.17	14.09 \pm 3.76	13.56 \pm 3.68	12.71 \pm 3.57	12.41 \pm 3.52
Tot. bkg.	23116.66 \pm 152.04	2786.56 \pm 52.79	566.67 \pm 23.81	404.21 \pm 20.11	151.79 \pm 12.32
$Z \rightarrow ee$	22592.99 \pm 150.31	2650.58 \pm 51.48	484.57 \pm 22.01	337.65 \pm 18.37	107.06 \pm 10.35
$Z \rightarrow \tau\tau$	117.26 \pm 10.83	11.06 \pm 3.33	7.00 \pm 2.65	4.28 \pm 2.07	4.02 \pm 2.01
Ttbar	4.56 \pm 2.13	3.01 \pm 1.73	2.85 \pm 1.69	1.63 \pm 1.28	1.36 \pm 1.16
W+jets	32.21 \pm 5.67	21.78 \pm 4.67	20.65 \pm 4.54	18.82 \pm 4.34	17.00 \pm 4.12
WW	14.13 \pm 3.76	8.45 \pm 2.91	8.27 \pm 2.87	7.20 \pm 2.68	6.39 \pm 2.52
WZ	54.06 \pm 7.36	31.08 \pm 5.57	26.53 \pm 5.15	24.43 \pm 4.95	9.95 \pm 3.15
ZZ	21.59 \pm 4.64	10.64 \pm 3.27	5.73 \pm 2.39	4.87 \pm 2.21	1.38 \pm 1.18
Multijets	279.88 \pm 16.72	49.96 \pm 7.07	11.08 \pm 3.33	5.34 \pm 2.31	4.63 \pm 2.15

Table 5.12. Cutflow for the $ee\ell$ channel, for all epochs combined. The signal is the mSUGRA point $m_0 = 100$ GeV, $m_{1/2} = 240$ GeV, $\tan\beta = 3$, $A_0 = 0$ and $\text{sgn}\mu = +1$.

Sample	Preselection	Cut 1	Cut 2	Cut 3
Data	1105.00 \pm 33.24	336.00 \pm 18.33	214.00 \pm 14.63	147.00 \pm 12.13
Signal	7.50 \pm 2.74	4.70 \pm 2.16	4.30 \pm 2.08	4.08 \pm 2.01
Tot. bkg.	1081.15 \pm 32.88	315.59 \pm 17.76	201.83 \pm 14.21	156.78 \pm 12.52
$Z \rightarrow ee$	33.89 \pm 5.83	19.77 \pm 4.44	5.01 \pm 2.24	4.07 \pm 2.02
$Z \rightarrow \mu\mu$	210.03 \pm 14.50	74.83 \pm 8.65	42.37 \pm 6.51	38.45 \pm 6.20
$Z \rightarrow \tau\tau$	378.40 \pm 19.45	50.90 \pm 7.13	32.18 \pm 5.67	17.30 \pm 4.16
Ttbar	10.91 \pm 3.31	7.11 \pm 2.67	6.74 \pm 2.60	3.65 \pm 1.91
W+jets	59.13 \pm 7.69	40.56 \pm 6.37	38.90 \pm 6.24	32.61 \pm 5.72
WW	32.35 \pm 5.69	19.86 \pm 4.46	19.02 \pm 4.36	14.95 \pm 3.87
WZ	29.34 \pm 5.42	19.37 \pm 4.40	18.23 \pm 4.27	16.98 \pm 4.12
ZZ	6.73 \pm 2.59	4.07 \pm 2.01	3.14 \pm 1.78	2.90 \pm 1.70
Multijets	320.36 \pm 17.90	79.12 \pm 8.89	36.24 \pm 6.02	25.86 \pm 5.09

Table 5.13. Cutflow for the $e\mu\ell$ channel, for all epochs combined.

Sample	Preselection	Cut 1	Cut 2	Cut 3	Cut 4
Data	29837.00 \pm 172.73	3419.00 \pm 58.47	1022.00 \pm 31.97	599.00 \pm 24.48	301.00 \pm 17.35
Signal	18.96 \pm 4.36	15.21 \pm 3.90	14.57 \pm 3.82	13.48 \pm 3.67	13.17 \pm 3.63
Tot. bkg.	29461.04 \pm 171.64	3259.94 \pm 57.10	977.75 \pm 31.27	630.04 \pm 25.10	314.09 \pm 17.72
$Z \rightarrow \mu\mu$	29078.86 \pm 170.52	3132.74 \pm 55.97	865.65 \pm 29.42	540.83 \pm 23.26	246.04 \pm 15.68
$Z \rightarrow \tau\tau$	131.17 \pm 11.45	11.20 \pm 3.35	7.92 \pm 2.81	3.88 \pm 1.97	3.84 \pm 1.96
Ttbar	6.21 \pm 2.49	4.22 \pm 2.06	4.06 \pm 2.02	2.37 \pm 1.54	1.89 \pm 1.37
W+jets	35.38 \pm 5.95	22.52 \pm 4.75	22.25 \pm 4.72	15.14 \pm 3.89	14.02 \pm 3.74
WW	19.34 \pm 4.40	11.24 \pm 3.35	10.95 \pm 3.31	9.59 \pm 3.09	8.31 \pm 2.89
WZ	63.38 \pm 7.96	35.99 \pm 6.00	31.46 \pm 5.61	28.72 \pm 5.36	15.55 \pm 3.94
ZZ	27.36 \pm 5.23	12.93 \pm 3.60	9.04 \pm 3.01	7.57 \pm 2.75	4.17 \pm 2.04
Multijets	99.34 \pm 9.97	29.10 \pm 5.39	26.41 \pm 5.14	21.95 \pm 4.69	20.28 \pm 4.50

Table 5.14. Cutflow for the $\mu\mu\ell$ channel, for all epochs combined.

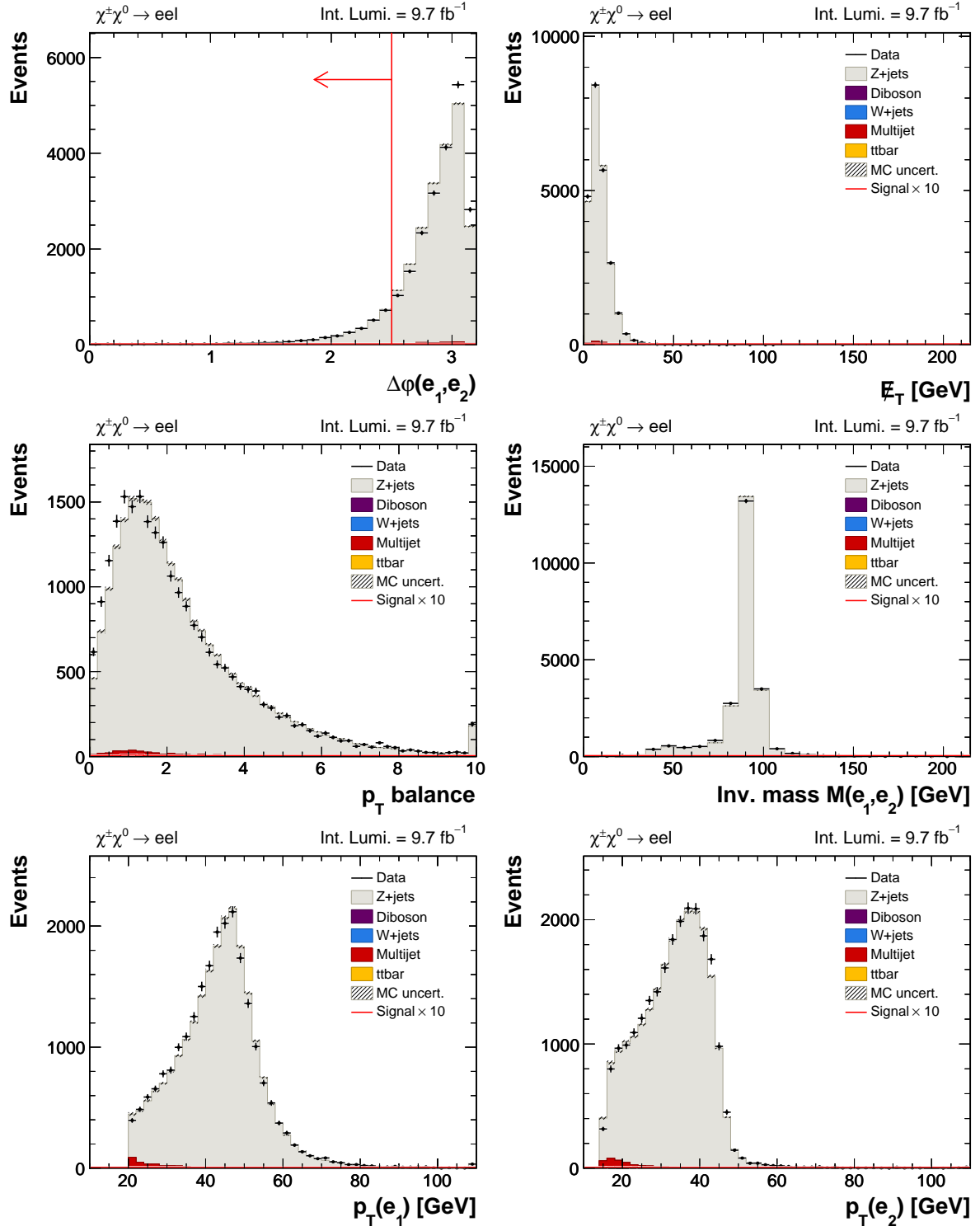
Figure 5.23. $e\bar{e}\ell$ channel, preselection

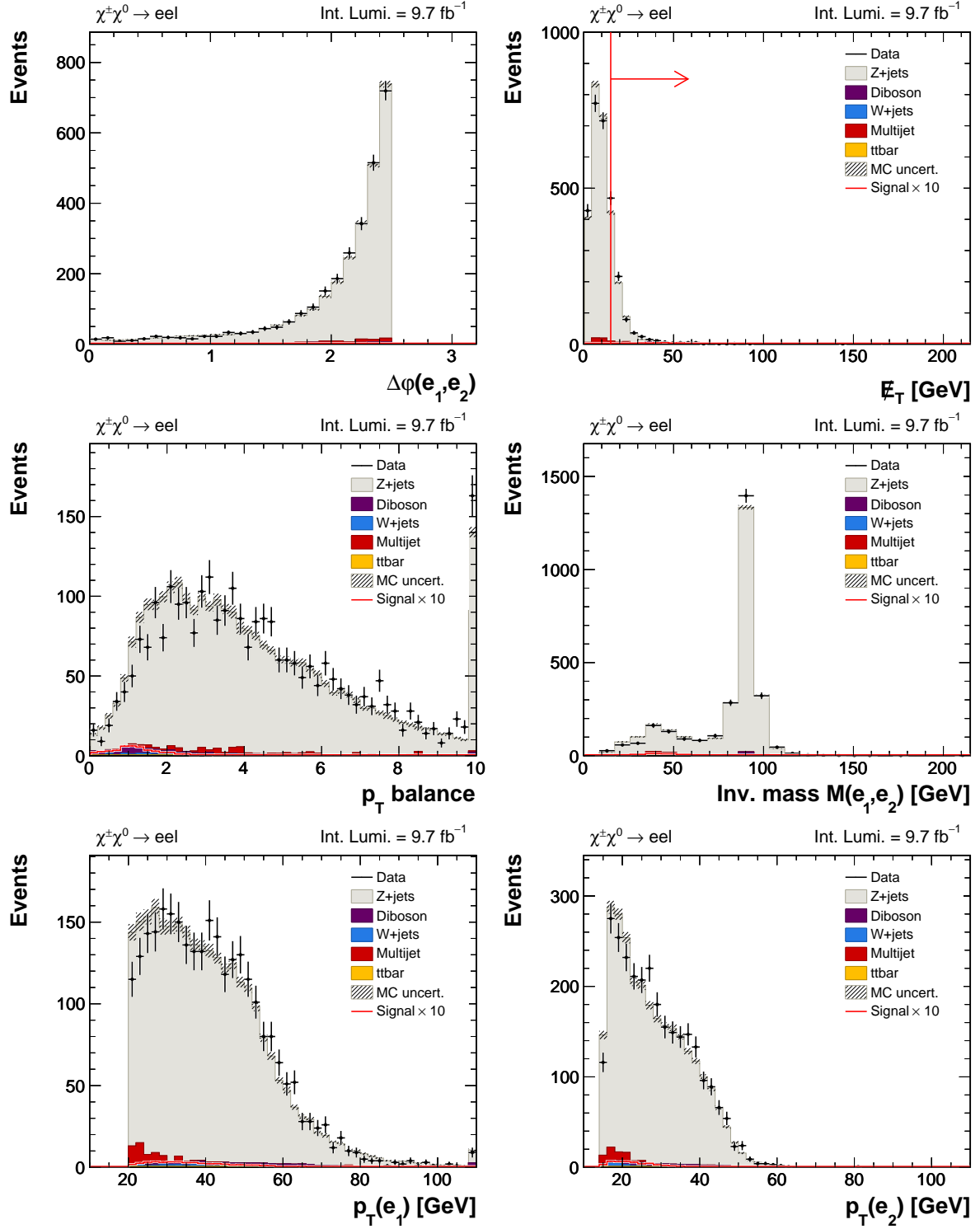
Figure 5.24. $e\ell$ channel, after cut 1: $\Delta\phi(e, \mu) < 2.5$ 

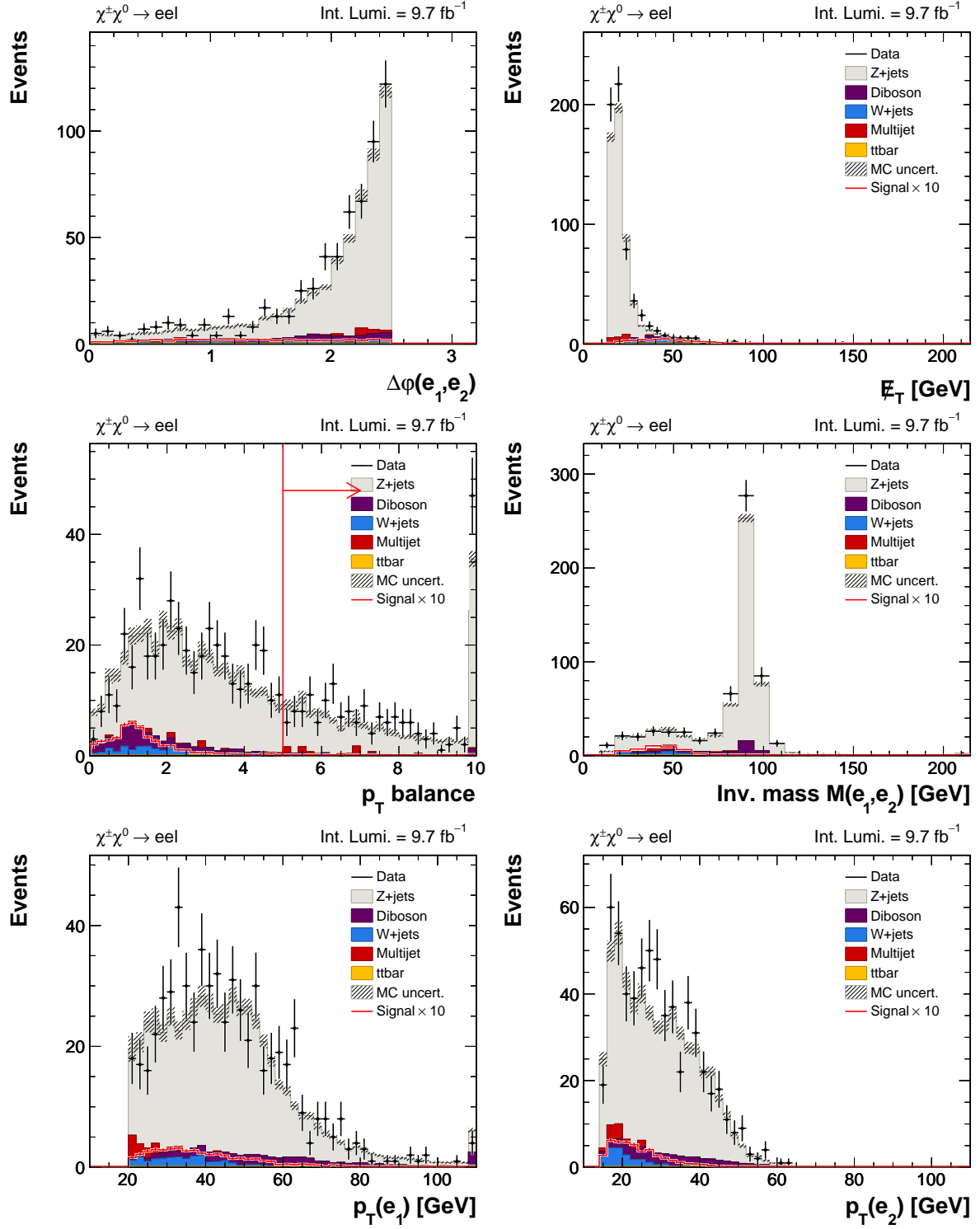
Figure 5.25. $e\bar{e}\ell$ channel, after cut 2: $\cancel{E}_T > 15$ GeV

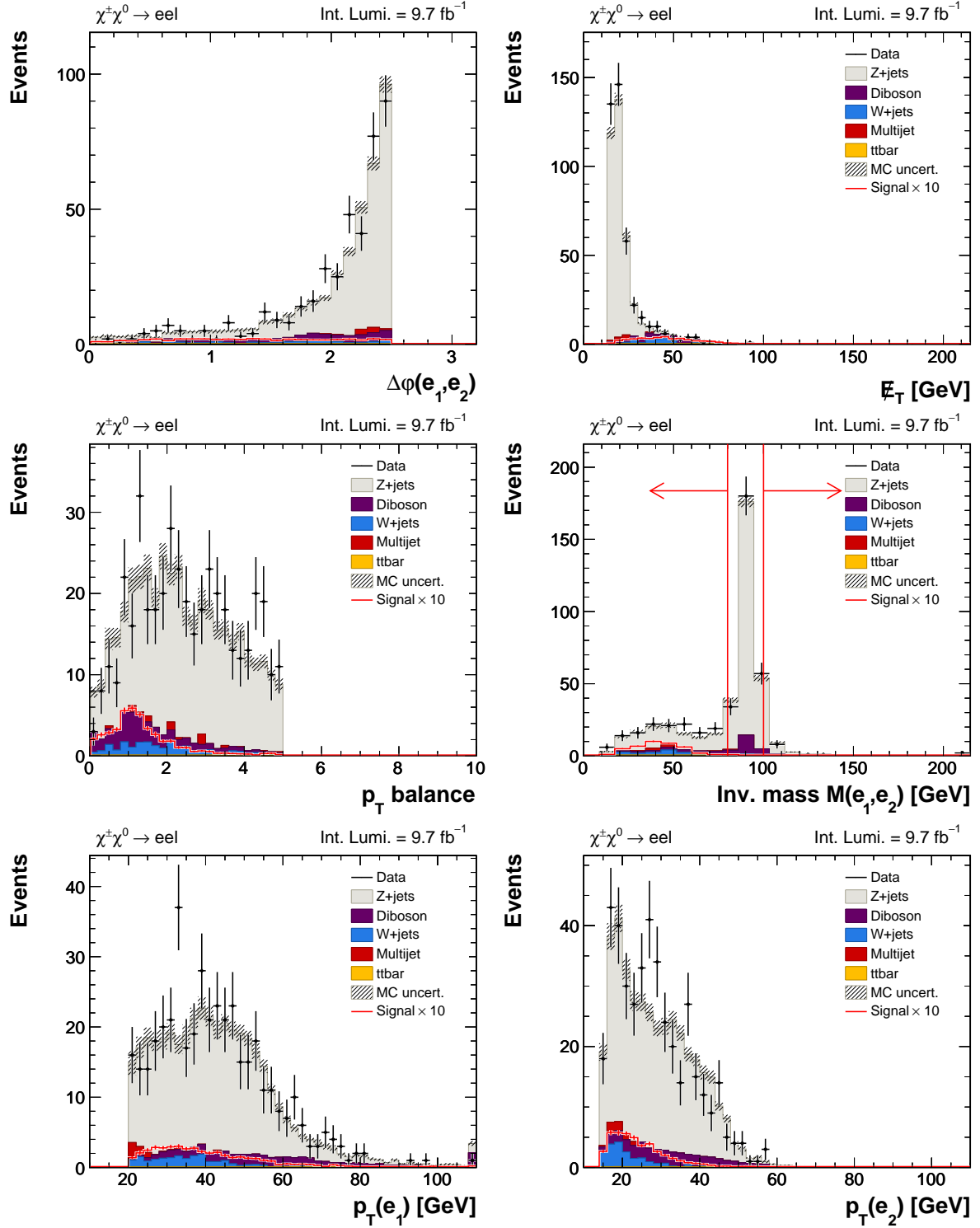
Figure 5.26. eel channel, after cut 3: $ptBalance < 5.0$ 

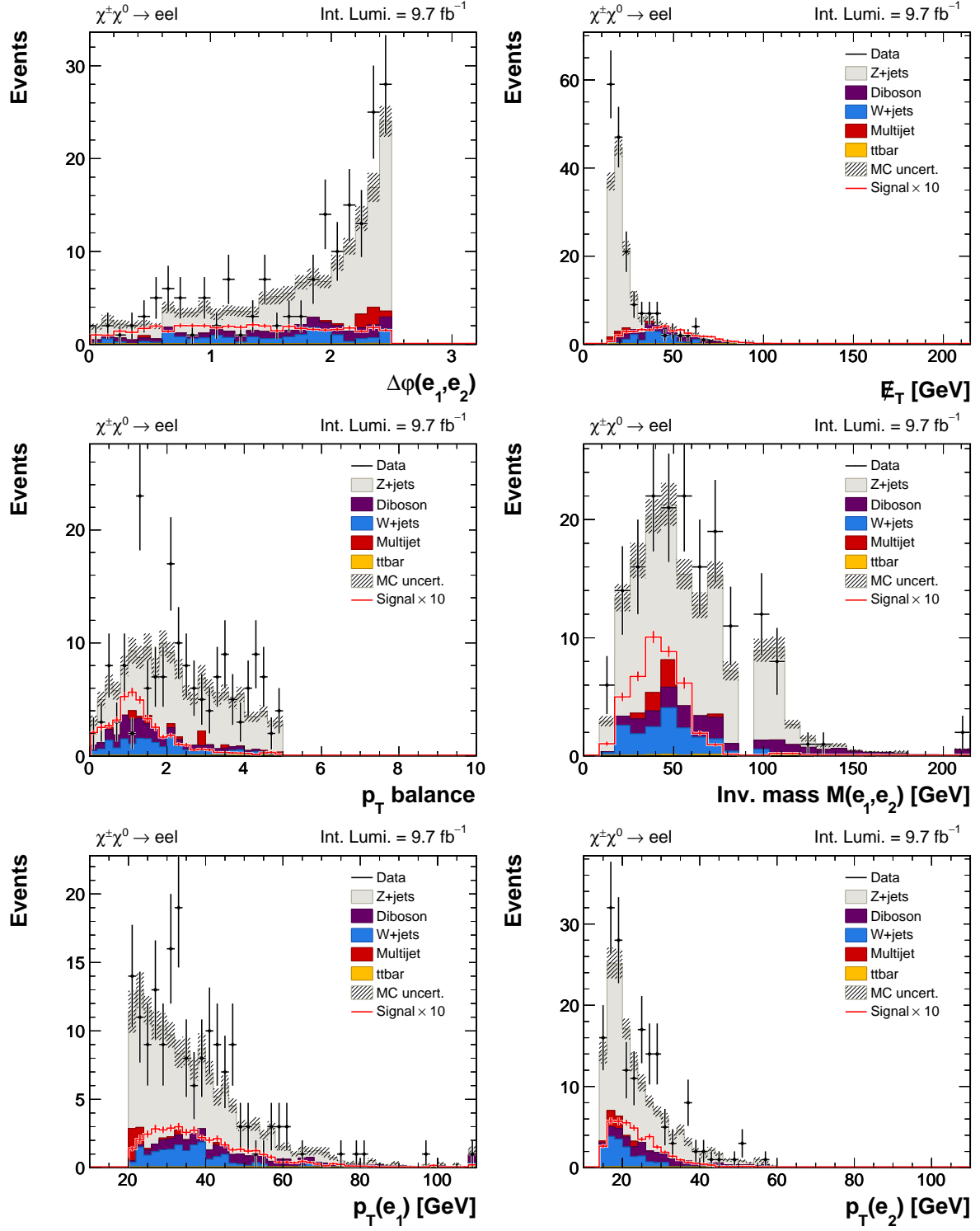
Figure 5.27. $e\ell$ channel, after cut 4: $80 \text{ GeV} < M_{\ell\ell} < 100 \text{ GeV}$ 

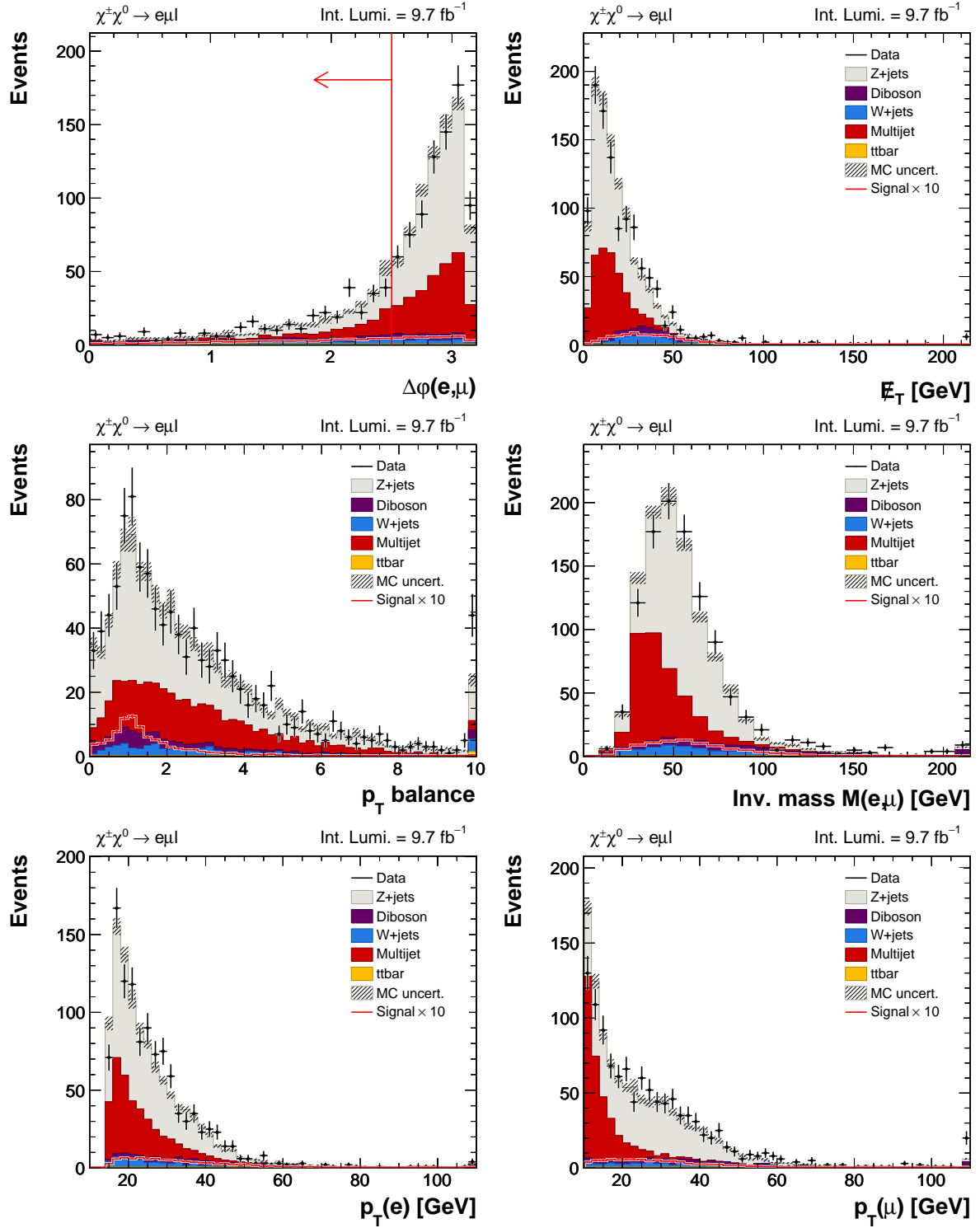
Figure 5.28. $e\mu\ell$ channel, preselection

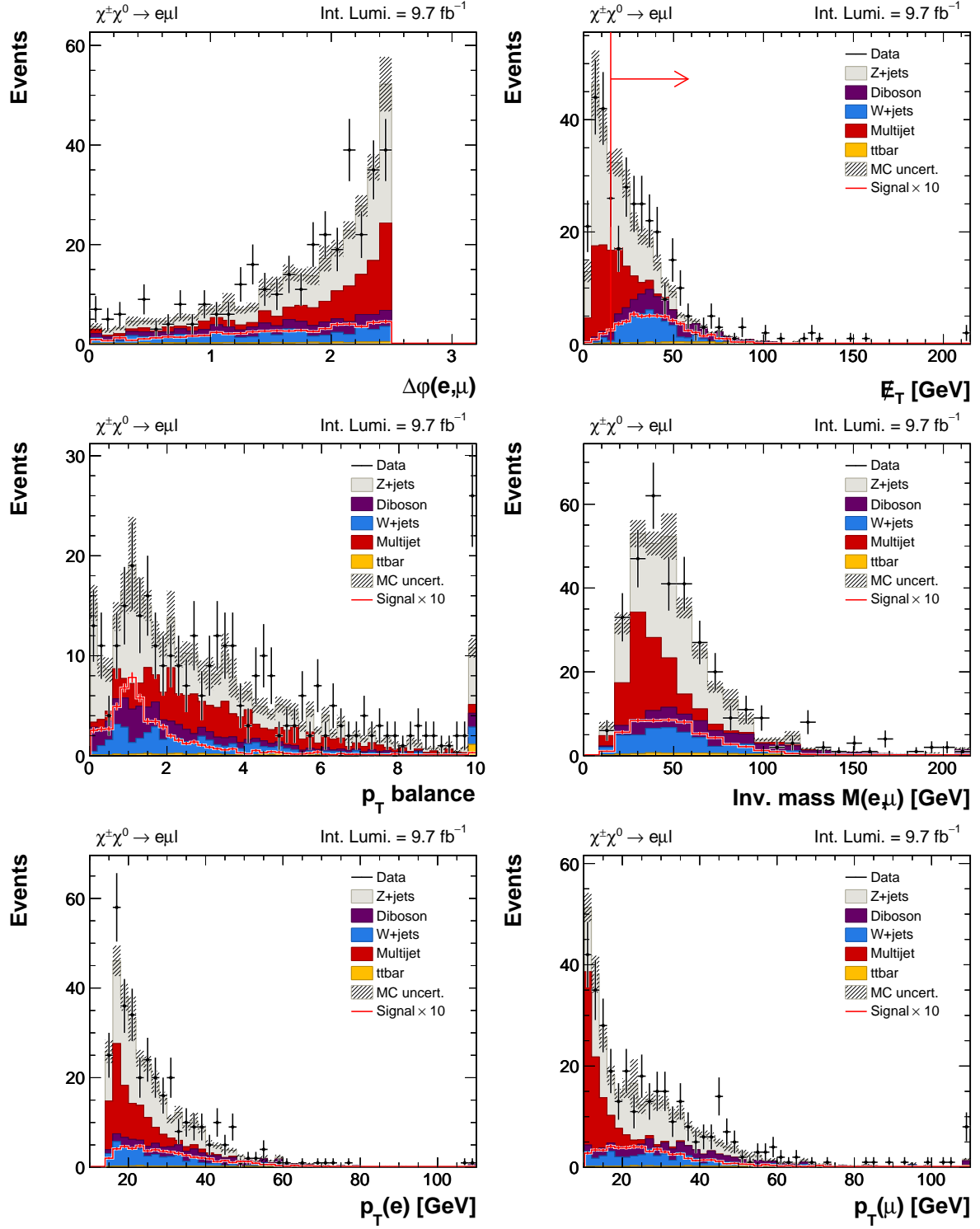
Figure 5.29. $e\mu\ell$ channel, after cut 1: $\Delta\phi(e, \mu) < 2.5$ 

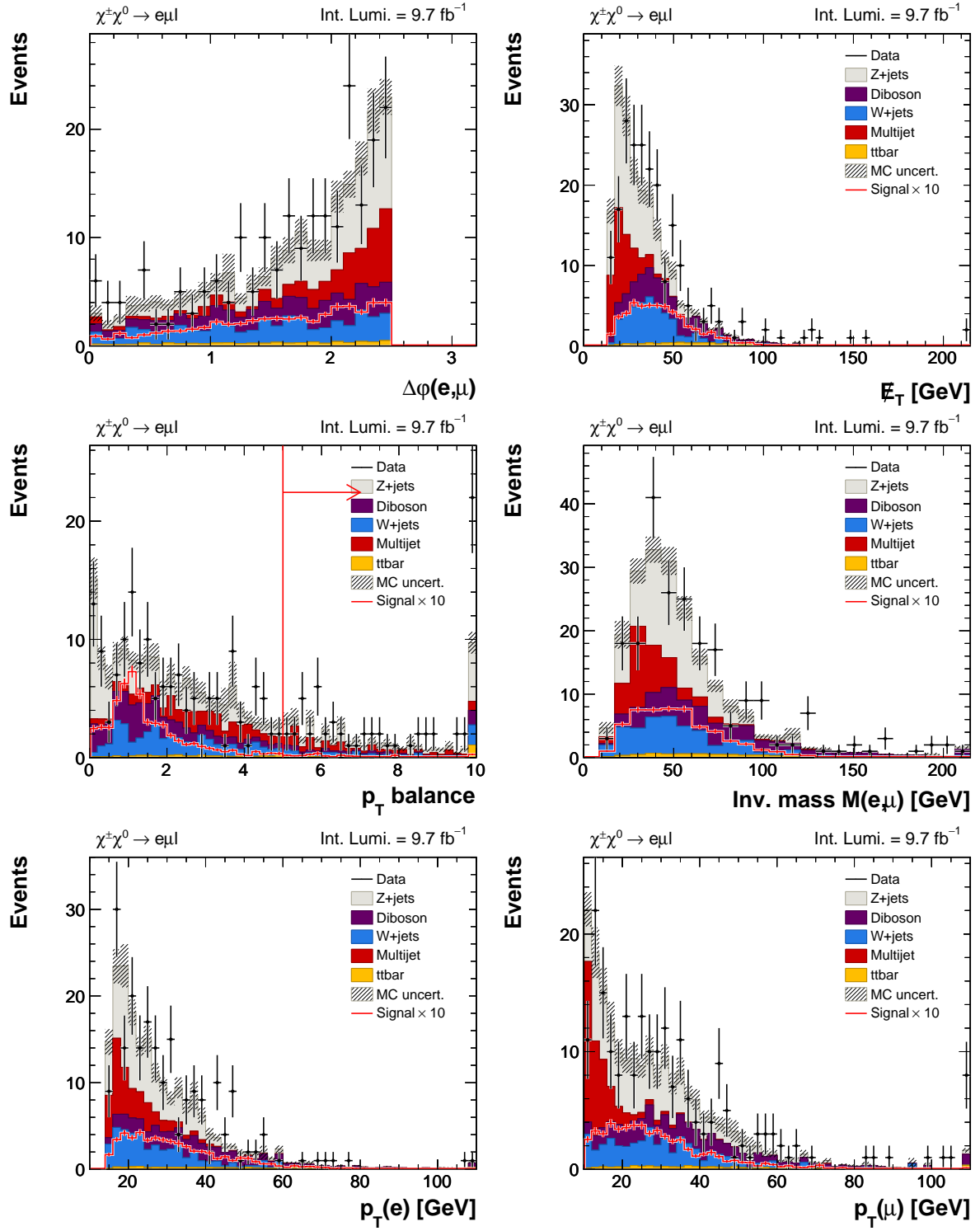
Figure 5.30. $e\mu\ell$ channel, after cut 2: $\cancel{E}_T > 15$ GeV

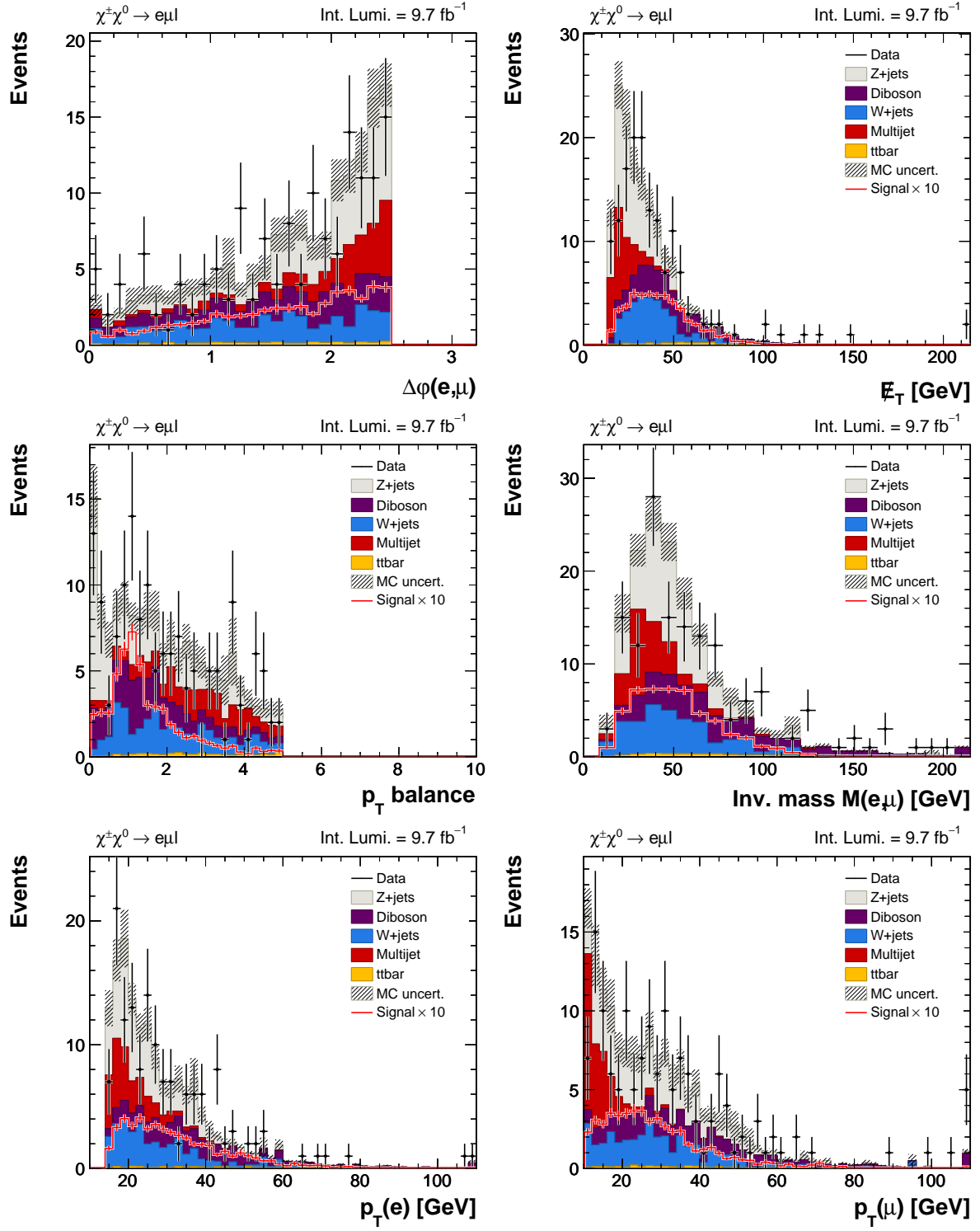
Figure 5.31. $e\mu\ell$ channel, after cut 3: $p_{\text{T}}\text{Balance} < 5.0$ 

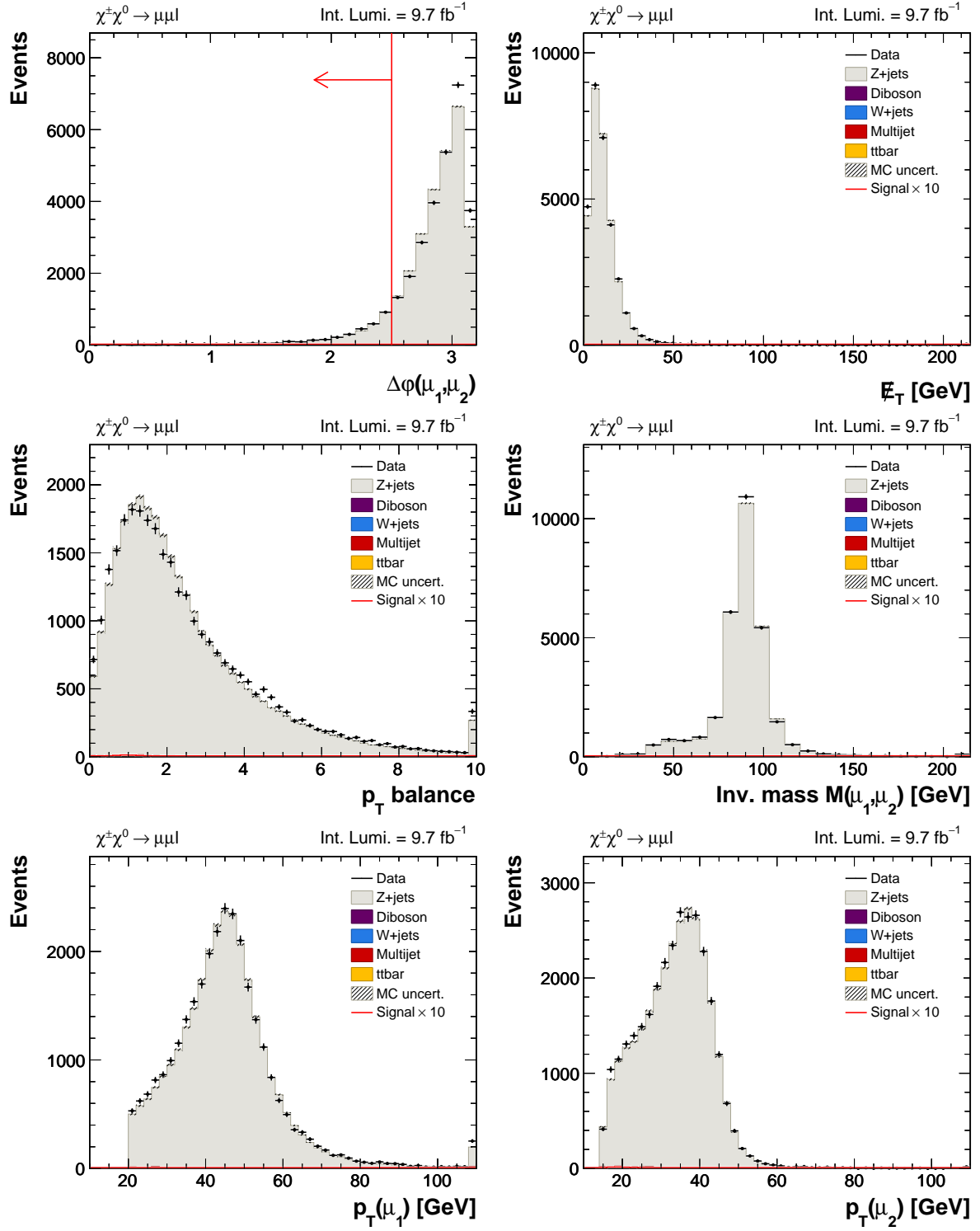
Figure 5.32. $\mu\mu\ell$ channel, preselection

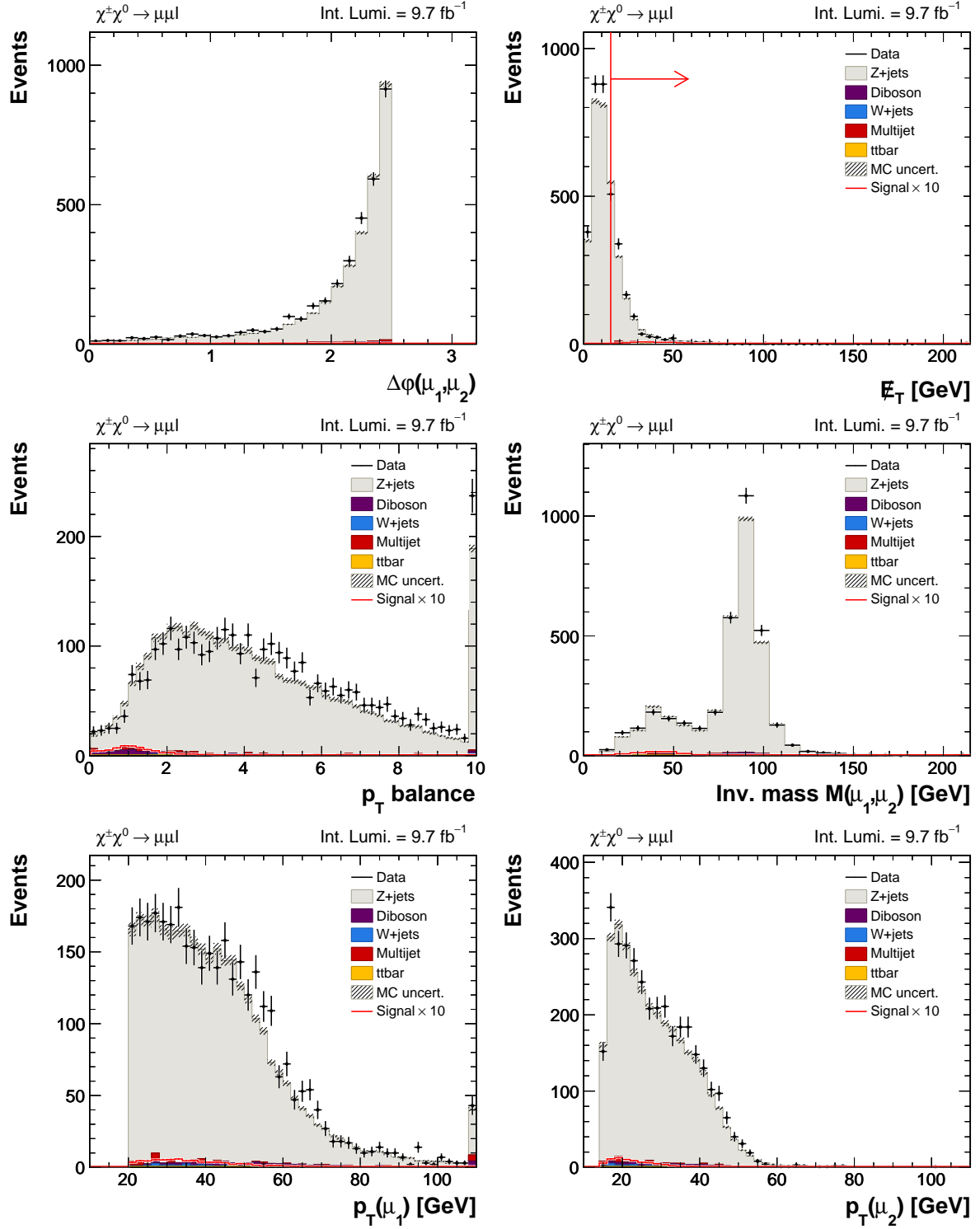
Figure 5.33. $\mu\mu\ell$ channel, after cut 1: $\Delta\phi(e, \mu) < 2.5$ 

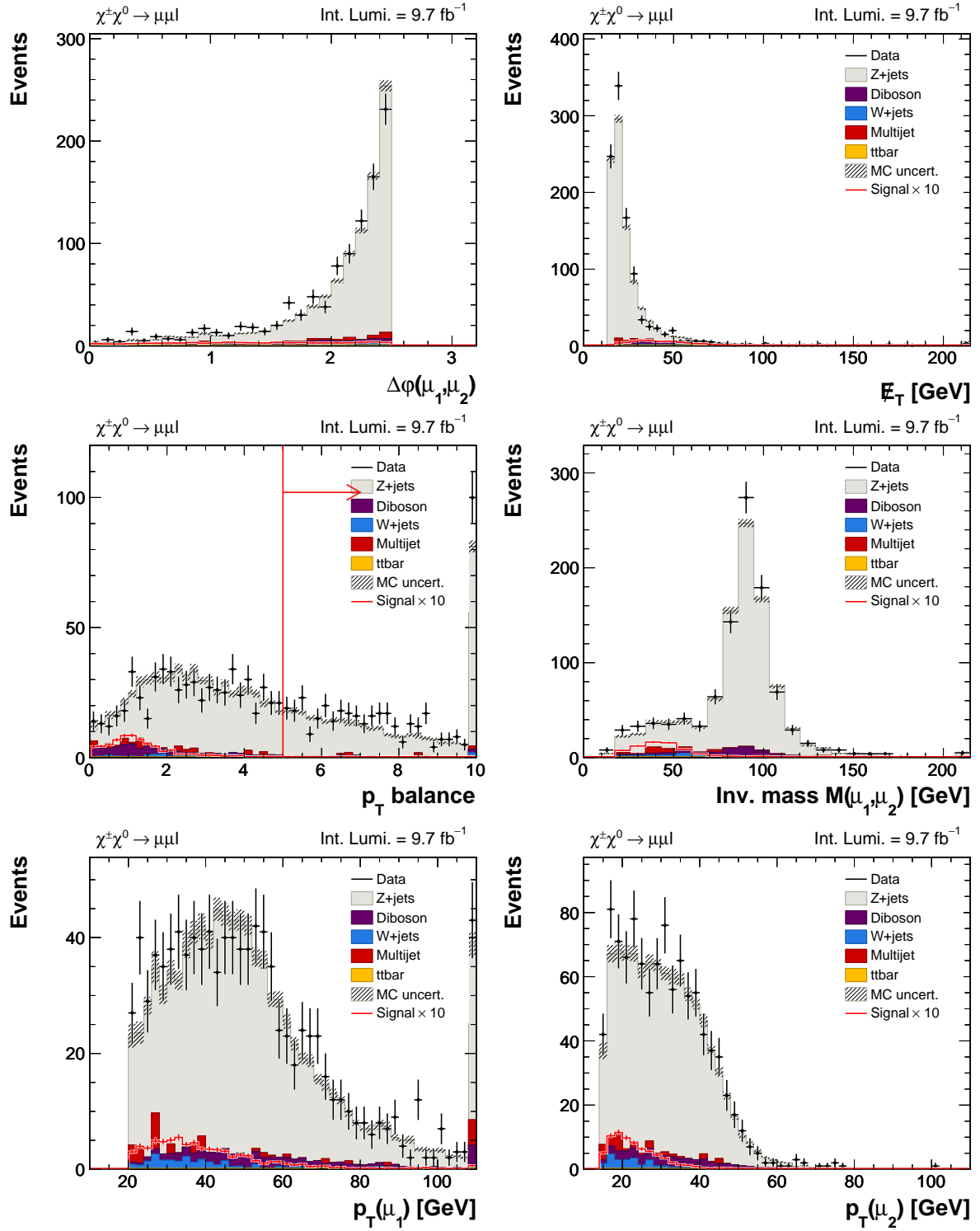
Figure 5.34. $\mu\mu\ell$ channel, after cut 2: $\cancel{E}_T > 15$ GeV

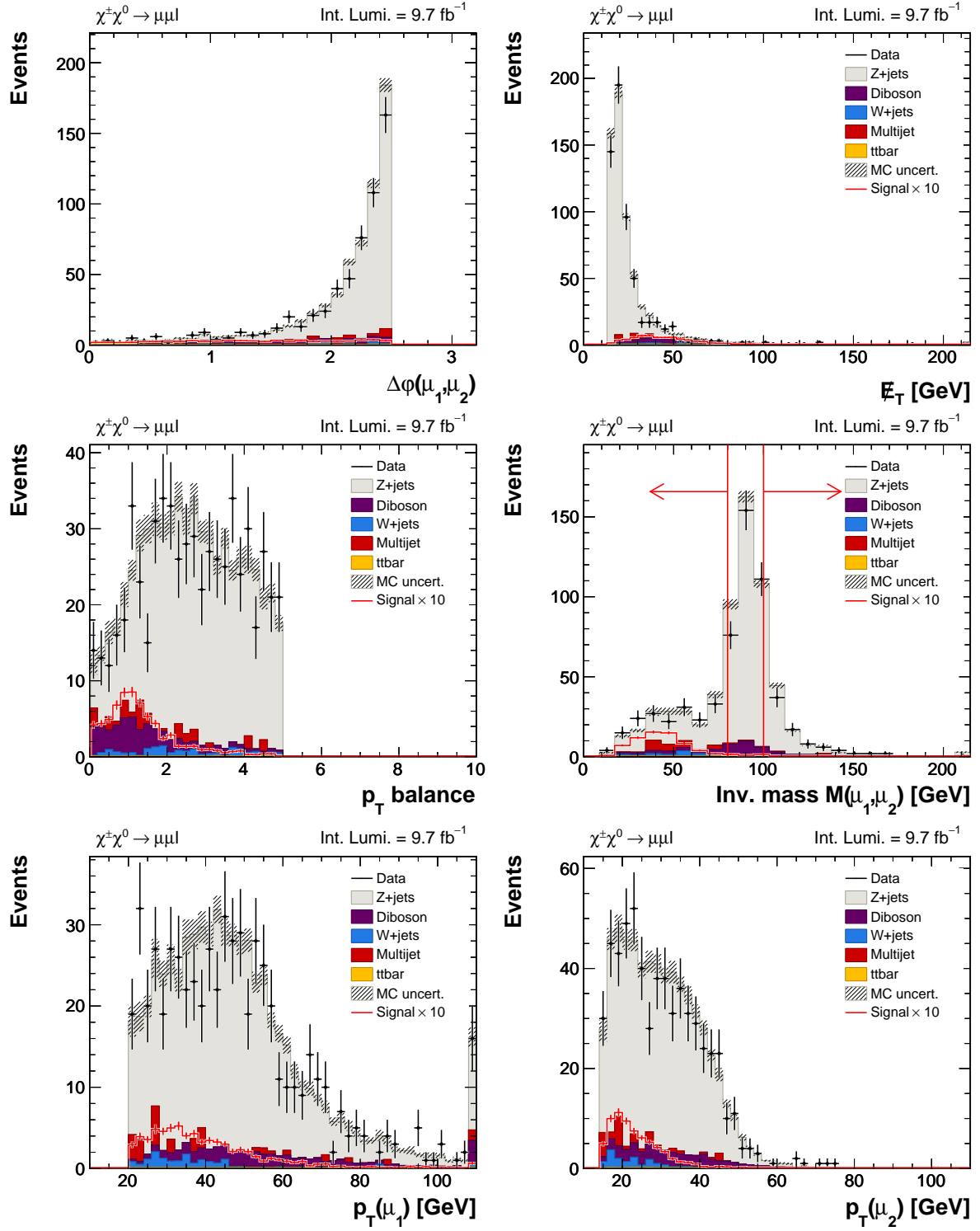
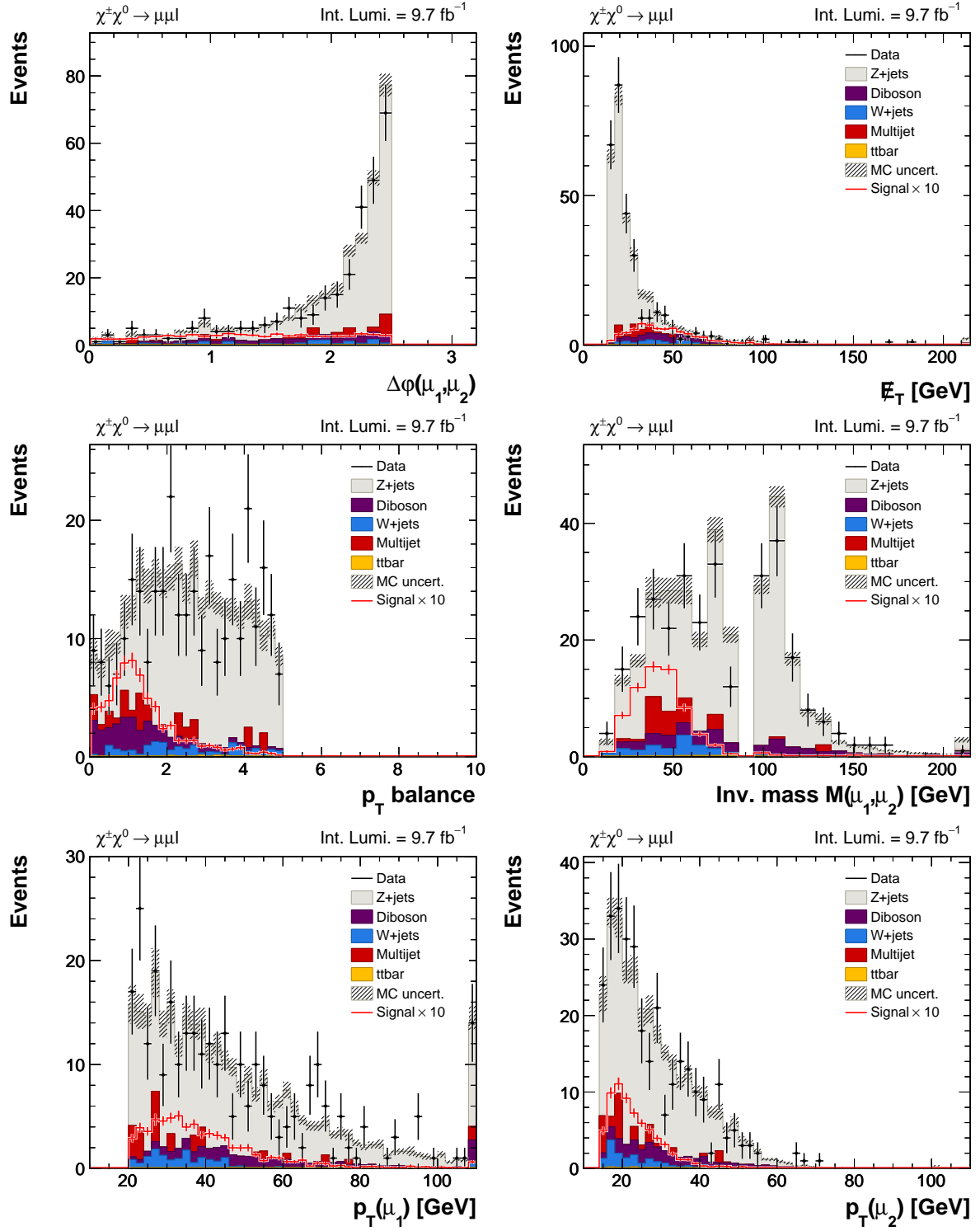
Figure 5.35. $\mu\mu\ell$ channel, after cut 3: $p_{\text{T}}\text{Balance} < 5.0$ 

Figure 5.36. $\mu\mu\ell$ channel, after cut 4: $80 \text{ GeV} < M_{\ell\ell} < 100 \text{ GeV}$ 

6. Multivariate Analysis

After performing the cutflow, the signal to background ratio has improved, but it is still not sufficient to find an excess or set exclusion limits by looking at the event yields alone. The situation cannot be improved much more by further cuts. Instead we apply a multivariate analysis (MVA). The general idea is that multiple input variables get combined into a single output that tells whether an event is rather signal or background-like. The distribution of this output variable should have a very good separation of signal and background.

Different variables in a sample can be correlated. Usually, it is desirable to choose maximally uncorrelated variables, for cut-based as well as multivariate analyses, so that their power of separation is based on independent characteristics. However, if the correlation is different in two subsamples, e.g. signal and background events, it is possible to separate the samples (Figure 6.1).

In the simplest case, a cut is performed on the output variable, and events that do not pass this cut are simply discarded¹. This procedure can be understood as a special case of a cut-based analysis. A regular cutflow is a series of unconditional, independent cuts (Figure 6.2 a)). One can improve on this by using cuts that depend on several variables, such as triangular cuts (Figure 6.2 b)). A better solution combines multiple variables in a nontrivial way, selecting mostly signal-like events with little background (Figure 6.2 c)). A cut on the MVA output corresponds to such a nontrivial cut in input-variable space.

In detail, let the input variables be x_i . One event is given by the collection of all variables, $\mathbf{x} = (x_1, \dots, x_n)$. For a given data sample, each variable has a distribution of x_i . The normalized distribution of one variable is $f(x_i)$, of N variables it is $f(\mathbf{x})$. These can be considered probability density functions: picking a random event from the distribution, as would be measured by the experiment, and a signal or background hypothesis, the probability to find a certain event \mathbf{x} is $f(\mathbf{x}|s)$ or $f(\mathbf{x}|b)$, respectively. In other words, $f(x_i|s)$ and $f(x_i|b)$ are the normalized histograms of the variable x_i . A multivariate technique takes the input variables \mathbf{x} and produces an output variable, or classifier, $y(\mathbf{x})$. This output variable has its own distributions for signal and background, $p(y|s)$ and $p(y|b)$.

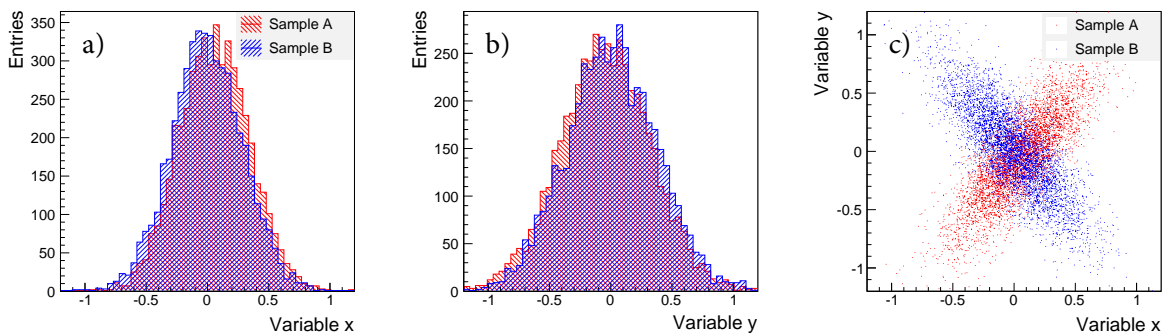


Figure 6.1. Two variables, x and y , are each insufficient to separate samples A and B (a) and b)). Furthermore, x and y are strongly (anti-)correlated. Still, it is beneficial to combine both variables, since their correlation is different in both samples (c)).

¹For the actual calculation of limits, we do not cut, but use all the information in the distribution (see chapter 7).

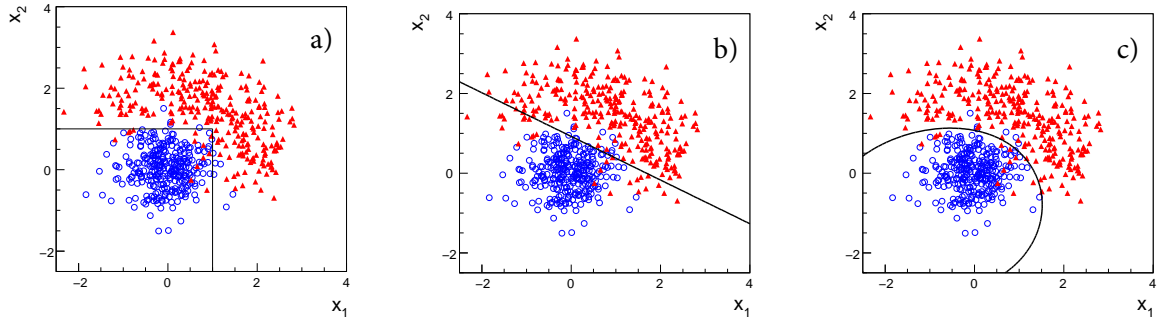


Figure 6.2. Different types of cuts on a two-dimensional distribution: a) combination of two individual cuts, b) triangular cut, on linear combination of both variables, c) cut on non-linear combination of input variables. From [55].

One can place certain cuts on either the input variables or the classifier. The fraction of signal (background) events passing the cut is called the signal (background) efficiency $\varepsilon_{s(b)}$:

$$\varepsilon_s = P(\text{pass cut}|s) = \int_A f(x|s)dx = \int_{-\infty}^{y_{\text{cut}}} p(y|s)dy. \quad (6.1)$$

Here the area of integration A includes all regions that are retained by cuts. The final equality is for the case of a single cut on the output classifier $y(\mathbf{x}) < y_{\text{cut}}$. An analogous equation holds for the background efficiency.

Now, the question is how to choose the best cut to separate signal and background. An optimal construction is given by the Neyman-Pearson lemma. For this, we define the likelihood ratio as:

$$\lambda(\mathbf{x}) = \frac{f(\mathbf{x}|s)}{f(\mathbf{x}|b)}. \quad (6.2)$$

Next, choose the acceptance region A such that $\lambda(\mathbf{x})$ is greater than some constant c everywhere inside the region, and less than c outside of it. Then A gives the highest signal efficiency for a given background efficiency (determined by c).

In practice, we do not know the functional form of $f(\mathbf{x}|s)$ and $f(\mathbf{x}|b)$. We do have a data model (in form of MC and reweighted data events), and could use multi-dimensional histograms for the probability densities, but this becomes very unwieldy for more than a few variables. Instead, we will use boosted decision trees (BDTs) in the following, with the BDT output as a test statistic to distinguish signal and background.

6.1. Boosted Decision Trees (BDTs)

A decision tree is made of a series of yes/no decisions, here cuts on input variables, as shown in Figure 6.3. For a given event, one follows the decision tree starting at the top node moving downwards, until an end node (leaf) is reached. This leaf is associated with an output value that tells how background- or signal-like an event is.

If a cut on the output value is placed, such that only certain leaves lead to acceptance of an event, a BDT is similar to a cutflow-based analysis. The difference is that a simple cutflow only selects a single N -dimensional hypercube out of the input variable space, whereas a single decision tree plus cut may select a union of multiple hypercubes. In practice, as in this analysis, a multitude of decision trees will be used (a

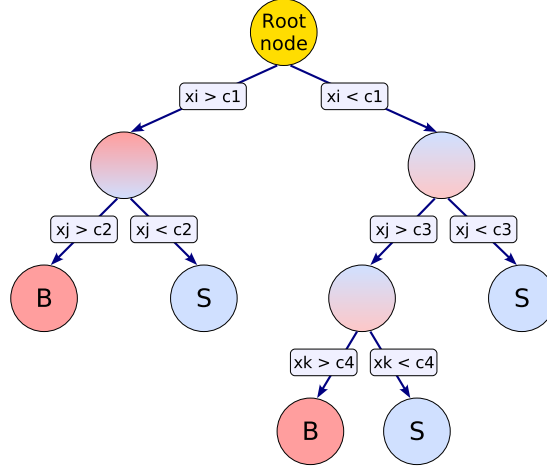


Figure 6.3. Sketch of a simple decision tree. For each event, a series of conditions are considered. If the event fails the condition ($x_i > c_1$), the left branch is taken, otherwise the right branch. Depending on the branch taken, a new condition is posed, or a leaf node is reached. In the latter case, the event is classified as either signal (S) or background (B). From [56].

“forest”), and their (appropriately weighted) average output will be used as a classifier. Instead of putting a cut on the classifier, it is possible and useful to inspect the distribution of the output variable.

The benefits of (boosted) decision trees are:

- They are straightforward to interpret as a series of simple cuts. Even in the case of a large forest, it is possible to investigate which variables are used more frequently, and which add more separation power.
- They are robust with respect to the addition of input variables. Additional variables that do not contribute much appear rarely in the decision trees, and do no damage.

The main disadvantages are:

- Decision trees are susceptible to statistical fluctuations in the training samples. Fluctuations of the training sample’s distributions away from the expectation are an unavoidable problem for all MVAs (as the expectation cannot be known), but can be remedied by higher statistics. The special problem with decision trees is that very minor differences in the training stage may cause very large changes in the tree, as a different first cut may be chosen. This is largely remedied by the use of boosting, however, and with proper settings BDTs offer comparable stability to other techniques.
- While BDTs generally have a very good separation power, other methods such as neural networks or support vector machines may produce superior results after appropriate tuning [56].

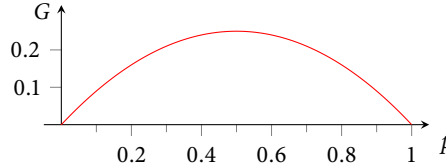
6.1.1. Training

The process of determining optimal branching conditions for a decision tree is called training. One starts with a sample of N training events, $\mathbf{x}_1 \dots \mathbf{x}_N$. Each event has n input variables, $\mathbf{x}_j = \{x^1, \dots, x^n\}$, and one true class, either signal ($y_j = +1$) or background ($y_j = -1$). Furthermore each event is given a weight, initially $w_j = 1$, which is later used in the boosting procedure.

For a given selection, the signal fraction or purity p is given by the fraction of selected events in the signal class:

$$p = \frac{N_{\text{sig.}}}{N_{\text{total}}} \Big|_{\text{sel.}} = \frac{\sum_{j \in \text{sig.}} w_j}{\sum_j w_j} \Big|_{\text{sel.}} \quad (6.3)$$

A high signal fraction ($p \approx 1$) is desirable in a selection, since it implies that it separates both classes well (assuming the signal fraction was less before the selection). However, a low signal fraction ($p \approx 0$) is equivalent when it comes to separation power. To describe the separation attained by a cut, the Gini index G is used:

$$G = p(1 - p) \quad (6.4)$$


To train a decision tree, one starts with the distributions of all variables x^i , and finds the variable that provides the best separation power from a single cut. The separation power of a cut that splits an original sample a into two subsamples b and c is quantified by the change in Gini coefficient:

$$\Delta G = W_a G_a - W_b G_b - W_c G_c \quad (6.5)$$

where W_b is the sum of weights in the b sample,

$$W_b = \sum_{j \in b} w_j$$

The found cut splits the training sample into two subsamples, each optimally enriched in either signal or background. This cut is noted as a node in the tree, and the algorithm is continued on each of the subsamples, until a stopping criterion is reached. The output value for leaf nodes is either +1 or -1, depending on whether it is a predominantly signal or background sample.

6.1.2. Forests and Boosting

So far, one tree has been trained. Although this tree provides optimal separation for the training sample, it is still a simple combination of linear cuts. To achieve better separation, multiple different trees are trained, and the weighted average of their outputs taken as a classifier. The collection of decision trees is called a forest. For the training of the individual trees, a process called boosting is used. Events which are misclassified in an earlier iteration are given a higher weight in later training steps, such that they are taken into account properly.

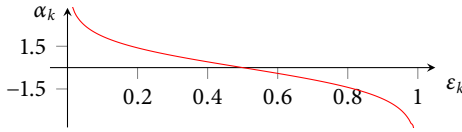
The boosting procedure starts by training a tree as described above. In the first iteration, all weights are set to one:

$$\sum_{j=1}^N w_j^{(1)} \quad (6.6)$$

where the index (1) denotes the first iteration. Tree number k assigns an output value $f_{(k)}(\mathbf{x}_j) = \pm 1$ to each event. This results in a certain misclassification rate ε_1 , which is defined as the sum of weights for all events where the tree assigns a different class than the true class y_j :

$$\varepsilon_k = \sum_{j=1}^N w_j^{(k)} I(f_k(\mathbf{x}_j) \neq y_j) \quad (6.7)$$

Here, I is a function that is 1 if its Boolean argument is true, and 0 otherwise. Now the tree is given a score α_k depending on the error rate. The score function is chosen such that it is positive as long as the error rate is below 50%, which is better than random:

$$\alpha_k = \ln \frac{1 - \varepsilon_k}{\varepsilon_k} \quad (6.8)$$


For the next training step, the weights are updated according to

$$w_i^{(k+1)} = w_i^{(k)} \frac{\exp(-\alpha_k f_k(\mathbf{x}_i) y_i / 2)}{Z_k}, \quad (6.9)$$

where Z_k is a normalization constant to keep the sum of weights equal to one. If an event was misclassified, $f_k(\mathbf{x}_i)$ and y_i have different signs, and the exponent in equation (6.9) is positive, which leads to an increased weight for the event. If the event was correctly classified, the weight decreases in the next iteration.

The algorithm stops after a certain number K of trees are created. From the individual tree's outputs and error rates, a combined classifier is computed:

$$y(\mathbf{x}) = \sum_{k=1}^K \alpha_k f_k(\mathbf{x}) \quad (6.10)$$

This weighted average defines the output of the boosted decision tree for each event. For a large number of iterations K , the BDT will eventually correctly classify every event in the training sample, however it will not necessarily perform as well on statistically independent samples. It might become trained on random fluctuations of the training sample, instead of genuine features of the data. To prevent this “overtraining”, one has to take care in choosing the stopping criterion K . To check whether overtraining has occurred, a second test sample besides the training sample is chosen, and the BDT output distributions for test and training samples are compared. This is done for signal and background events separately. The difference between test and training distributions is quantified using a Kolmogorov-Smirnov test. If the distributions are found to be compatible with each other, it increases confidence that no overtraining has occurred.

6.2. Input variables

For the input to the BDT, we would like to use variables that have power to discriminate between signal and background. Variables which are less correlated to each other are preferred since their pieces of information are more independent. When there are correlations, they should be different in background and signal samples, since MVAs can exploit these differences (Section 6). Of course, the variables have to be well-modeled, and finally they should have not been target of a correction that fixes the background distribution to data, such as the unclustered energy after the UE reweighting (Section 5.6.7).

There are a number of possible variables that are considered: properties of the individual leptons such as transverse momenta, event properties like \cancel{E}_T , and topological variables such as angles and transverse masses. A set of 28 candidate variables has been investigated for inclusion, and is listed in the following:

p_{T1}, p_{T2}, p_{T3}	Transverse momentum of the first or second lepton, or the selected track.
$\varphi_1, \varphi_2, \varphi_3$	Azimuthal angle of the first or second lepton, or the selected track.
ptBalance	Transverse momentum balance, see (5.5)

$\Delta\varphi(\ell_1, \ell_2)$	Azimuthal angle between the two leptons
$\Delta R(\ell_1, \ell_2)$	Angular distance between the two leptons, $\Delta R = \sqrt{\Delta\varphi^2 + \Delta\eta_{\text{det}}^2}$
\cancel{E}_T	Missing transverse energy. Signal events are expected to have MET from LSPs and neutrinos.
$\cancel{E}_T^{\text{special}}$	Special \cancel{E}_T , a variation of missing transverse energy designed to distinguish signal from the $Z + \text{Jets}$ background. A lower value is given to events where $\vec{\cancel{E}}_T$ is close to the nearest jet or lepton. If $\delta\varphi$ is the angle in the transverse plane between $\vec{\cancel{E}}_T$ and the nearest lepton or jet, then the special \cancel{E}_T is defined by:

$$\cancel{E}_T^{\text{special}} = \begin{cases} \cancel{E}_T & \text{if } \delta\varphi > 90^\circ \\ \cancel{E}_T \times \sin \delta\varphi & \text{otherwise} \end{cases} \quad (6.11)$$

$\Delta\varphi(\ell_1, \ell)$	Azimuthal angle between the first lepton and the track
$\Delta\varphi(\ell_2, \ell)$	Azimuthal angle between the second lepton and the track
$\min(\Delta\varphi(\vec{\cancel{E}}_T, \ell_{1,2}))$	Azimuthal angle between vectorial missing transverse energy, and the first or second lepton (whatever is smaller)
$M_T(\ell_1, \vec{\cancel{E}}_T)$	Transverse masses between the first or second lepton and missing transverse energy $\vec{\cancel{E}}_T$ or selected track trk . The transverse mass is a variation of invariant mass using only information in the transverse plane. It was first used at the UA1 experiment in the measurement of the W Boson mass. It is defined as
$M_T(\ell_2, \vec{\cancel{E}}_T)$	
$M_T(\ell_1, trk)$	
$M_T(\ell_2, trk)$	

$$M_T^2 = m_1^2 + m_2^2 + 2(E_{T1}E_{T2} - \vec{p}_{T1} \cdot \vec{p}_{T2}) . \quad (6.12)$$

In case the particles are massless or of negligible mass ($m_{1,2} \approx 0$), this can be simplified to:

$$M_T^2 = 2E_{T,1}E_{T,2}(1 - \cos \phi) \quad (6.13)$$

If one of the decay products is invisible, such as the neutrino in the W decay, or the LSP in the decay $\tilde{e}^- \rightarrow e^- + \tilde{\chi}_1^0$, then the expression becomes:

$$M_T^2(\ell_1, \vec{\cancel{E}}_T) = 2p_{T1} \cancel{E}_T \left(1 - \cos \phi(\vec{p}_{T1}, \vec{\cancel{E}}_T)\right) \quad (6.14)$$

Since $M_T < M$, the invariant mass can be determined by the endpoint of the transverse mass distribution.

$\min(M_T(\ell_{1,2}, \vec{\cancel{E}}_T))$	The transverse mass between $\vec{\cancel{E}}_T$ and the first or second lepton, whatever is smaller.
$MT2$	Stransverse mass [57]. It is similar to the transverse mass, in that it allows one to determine an invariant mass from events with limited information ($\vec{\cancel{E}}_T$ and only transverse quantities). The difference to M_T is that one wants to reconstruct the mass of a <i>pair</i> of particles, for example $\tilde{\chi}_1^\pm$ and $\tilde{\chi}_2^0$. Each particle decays into visible particles (e, μ) as well as invisible particles ($\nu, \tilde{\chi}_1^0$). Another difference to M_T is that the invisible particles can be massive. This introduces the mass of the invisible particles as a parameter χ , which must be specified or guessed.

A closed formula for $MT2$ cannot be given, instead it is calculated by a minimization procedure. A deviation is sketched in the following. Assuming one of the produced particles decays as $\tilde{\chi}_1^- \rightarrow e^- + \tilde{\chi}_1^0$. Writing $\vec{p}_T = \vec{p}_{T,e}$ and $\vec{q}_T = \vec{p}_{T,\tilde{\chi}_1^0}$ for the transverse momenta of the decay products, (6.12) becomes:

$$M_T^2(\vec{p}_T, \vec{q}_T, m_{\tilde{\chi}_1^0}) = m_e^2 + m_{\tilde{\chi}_1^0}^2 + 2(E_{T,e}E_{T,\tilde{\chi}_1^0} - \vec{p}_T \cdot \vec{q}_T)$$

This gives a lower bound on the mass of the intermediate particle (the chargino). Since there are two such particles of same mass, the lower bound on their mass becomes:

$$M_{\tilde{\chi}_1^\pm} \geq \max \left\{ M_T(\vec{p}_T^{(1)}, \vec{q}_T^{(1)}, m_{\tilde{\chi}_1^0}), M_T(\vec{p}_T^{(2)}, \vec{q}_T^{(2)}, m_{\tilde{\chi}_1^0}) \right\}$$

with (1) and (2) denoting the decay products of the first and second intermediates. However, the momenta of the invisible particles are not known, only their sum: the missing transverse momentum of the event. Thus, one has to consider all possible splittings of $\vec{p}_T = \vec{q}_T^{(1)} + \vec{q}_T^{(2)}$, and take the minimum:

$$M_{\tilde{\chi}_1^\pm} \geq \min_{\vec{q}_T^{(1)} + \vec{q}_T^{(2)} = \vec{p}_T} \left[\max \left\{ M_T(\vec{p}_T^{(1)}, \vec{q}_T^{(1)}, \chi), M_T(\vec{p}_T^{(2)}, \vec{q}_T^{(2)}, \chi) \right\} \right]$$

The mass of the neutralino is also not known. To illustrate that it is a parameter to $MT2$, it is conventionally denoted as χ . Since we do not wish to use $MT2$ to determine the chargino mass from the distribution's edge, but rather as a variable to distinguish signal from background, we are free to insert different values for χ . In this case, we have chosen $\chi = 0$, which is the limit of light LSPs.

N_{jets}	The number of jets in the event. Jets are JCCB jets with a cone radius of $\Delta R < 0.5$ and a minimum p_T after correction of 20 GeV.
H_T	The scalar sum of the p_T of all jets.
$\cancel{E}_T \times p_{T3}$	Product of missing transverse energy and track transverse momentum.
Scalar \cancel{E}_T	Scalar sum of transverse energies in an event.
$M(\ell_1, \ell_2)$	Invariant mass between the two leptons.
$M(\ell_1, \ell_2, \text{trk})$	Invariant mass between the two leptons and the charged track.
$M(\ell_1, \ell_2, \cancel{E}_T)$	Invariant mass between the two leptons and the missing transverse energy vector.

While it is a feature of BDTs to be able to deal with a large number of inputs, it is advisable to restrict the set of variables to a smaller list. One reason is that, when the number of events for training is limited, BDTs can become overtrained if used with too many variables (“curse of dimensionality”). Furthermore, tools to debug the BDT behavior, such as linear correlation coefficient plots and parallel coordinate plots are easier to interpret with a limited number of variables. It was found in this analysis that the discriminating power of the BDT did not improve notably when using more than fourteen variables.

The full set of 28 variables is reduced to a more manageable list by removing those that do not contribute significantly to the BDT output, or that contain redundant information. For this, first BDTs were trained including all candidate variables, and a ranking of variable importance was created. The importance is

Rank	Variable	Importance	Rank	Variable	Importance
1.	$M(e, e)$	8.61%	15.	$M(e, e, \cancel{E}_T)$	3.20%
2.	$M(e, e, \text{trk})$	6.78%	16.	$\max \Delta\varphi(e_{1,2}, \cancel{E}_T)$	2.93%
3.	$\eta_{\text{det}}(\text{trk})$	5.98%	17.	p_{T2}	2.84%
4.	$\Delta R(e, e)$	5.67%	18.	\cancel{E}_T	2.70%
5.	$\eta_{\text{det}}(e_1)$	5.48%	19.	$\min M_T(e_{1,2}, \cancel{E}_T)$	2.64%
6.	ptBalance	5.21%	20.	$\cancel{E}_T \times p_T(\text{trk})$	2.59%
7.	$\eta_{\text{det}}(e_2)$	4.99%	21.	$\Delta\varphi(e_2, \cancel{E}_T)$	2.56%
8.	$M_T(e_1, \text{trk})$	3.90%	22.	$M_T(e_2, \cancel{E}_T)$	2.37%
9.	MT2	3.64%	23.	Special \cancel{E}_T	2.34%
10.	$p_T(\text{trk})$	3.58%	24.	h_T	2.29%
11.	$\Delta\varphi(e_1, \cancel{E}_T)$	3.52%	25.	$\min \Delta\varphi(e_{1,2}, \cancel{E}_T)$	2.24%
12.	$M_T(e_2, \text{trk})$	3.51%	26.	$M_T(e_1, \cancel{E}_T)$	2.21%
13.	$\Delta\varphi(e, e)$	3.51%	27.	$N \text{ Jets}$	0.79%
14.	p_{T1}	3.27%	28.	Scalar \cancel{E}_T	0.68%

Table 6.1. Example ranking of all candidate variables as reported by TMVA, obtained from RunIIa, $ee\ell$ channel, using the signal point mSUGRA $m_0 = 100 \text{ GeV}$, $m_{12} = 240 \text{ GeV}$, $\tan\beta = 3$, $\mu > 0$, $A_0 = 0$.

Variable	Variable
p_{T1}	$\Delta\varphi(e, e)$
p_{T2}	\cancel{E}_T
$\eta_{\text{det}}(e_1)$	$\min M_T(e_{1,2}, \cancel{E}_T)$
$\eta_{\text{det}}(e_2)$	$M_T(e_1, \text{trk})$
$\eta_{\text{det}}(\text{trk})$	$N \text{ Jets}$
$M(e, e)$	MT2
$M(e, e, \text{trk})$	ptBalance

Table 6.2. Variables used as input for the BDTs.

calculated by counting how often a variable is used to make decision tree branchings, weighted by the square of the separation gain, and the number of events at the branching. The order of variable importance is fairly consistent over different channels, epochs, and signal points, although small differences occur. A typical ranking is given in Table 6.1. It should be noted that the ranking is not stable with respect to the set of variables, and the removal of one variable might cause the ranking to change entirely.

Beyond the rankings, the linear correlation between each pair of variables was considered. The correlation matrices for background and a typical signal are shown in Figures A.19 and A.20. After removing some weaker variables, 14 were chosen as inputs for the BDT (Figure 6.2). Distributions of the BDT input variables for the three channels, all epochs merged, can be seen in the appendix (Section A.2).

The BDT output distribution for four signal points ($ee\ell$ channel, all epochs merged) is shown in Figure 6.6. The same is shown for the $e\mu\ell$ channel in Figure A.17 and for the $\mu\mu\ell$ channel in Figure A.18 in the appendix.

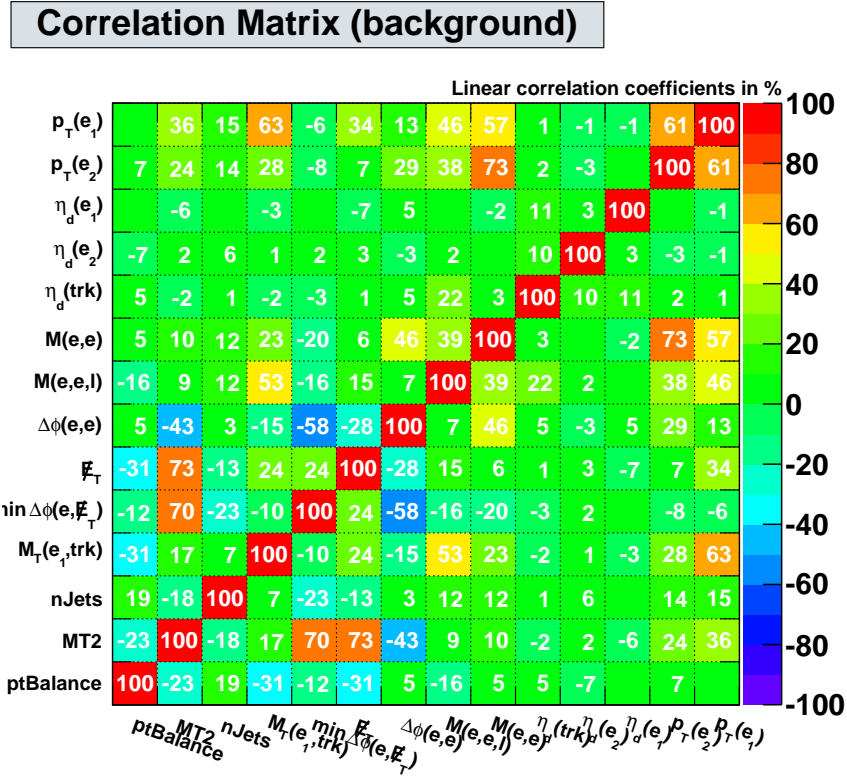


Figure 6.4. Linear correlation coefficients for all pairs of BDT input variables, for the background samples, $ee\ell$ channel, RunIIa epoch. For all candidate variables, see Figure A.19 in the appendix.

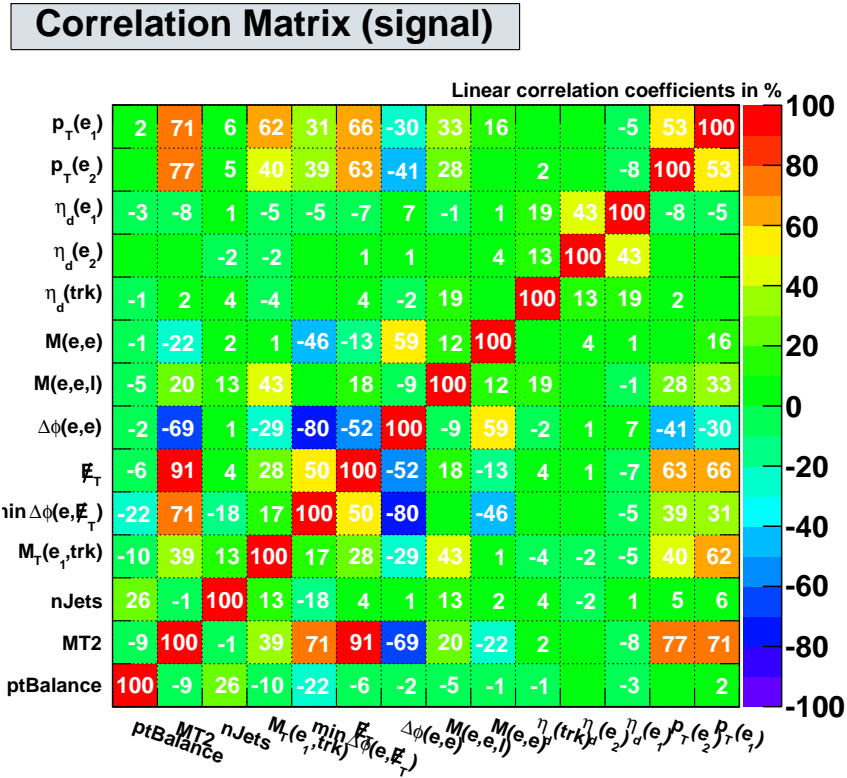


Figure 6.5. Linear correlation coefficients for all pairs of BDT input variables, for a typical signal sample, $ee\ell$ channel, RunIIa epoch. The signal point is mSUGRA $m_0 = 100$ GeV, $m_{12} = 240$ GeV, $\tan\beta = 3$, $\mu > 0$, $A_0 = 0$. For all candidate variables, see Figure A.20 in the appendix.

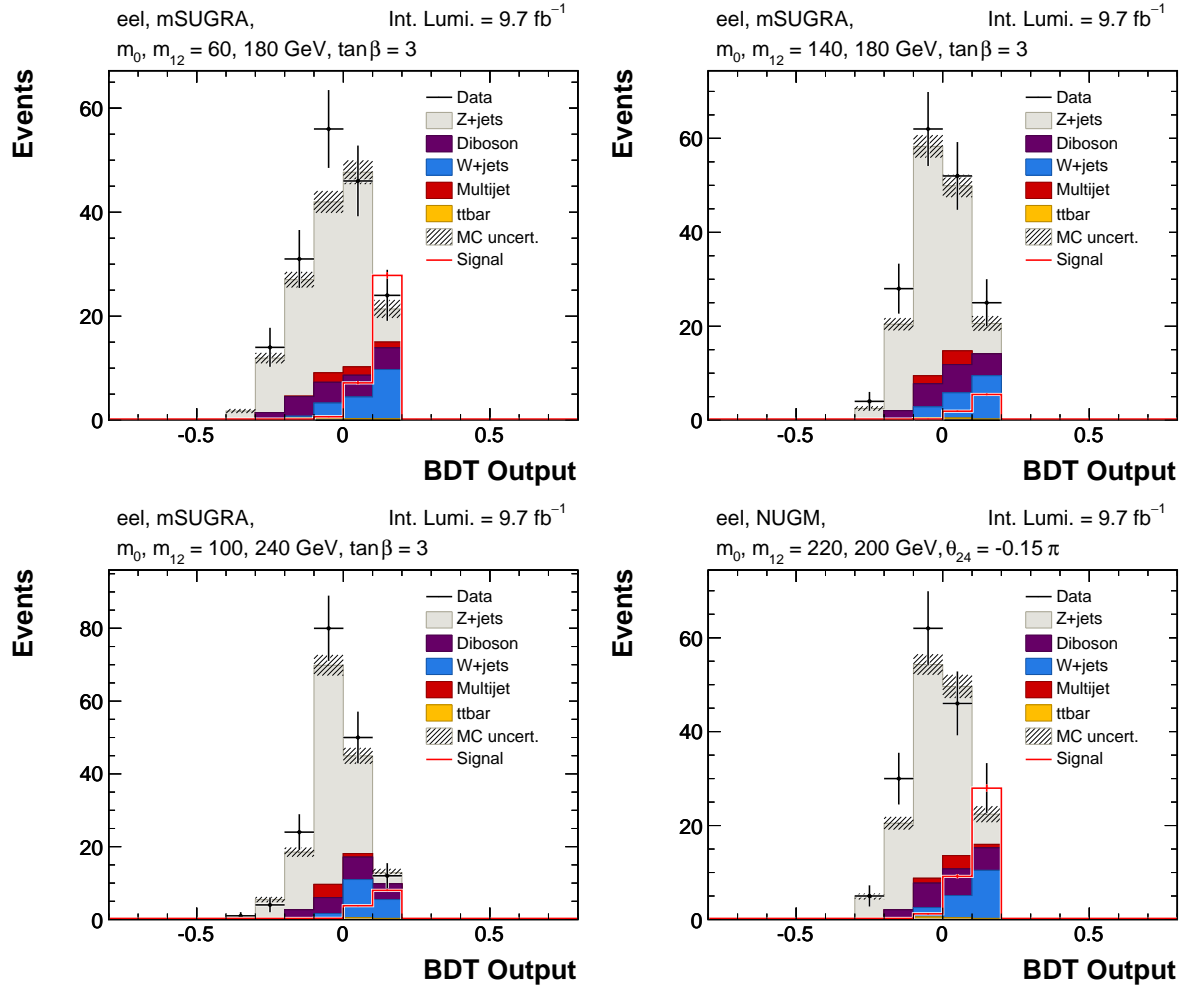


Figure 6.6. Output of the BDT for four signal points, $ee\ell$ channel. All three epochs have been merged. For the mSUGRA points, $\tan\beta = 3$, for NUGM $\tan\beta = 10$, and for all points $\text{sgn } \mu = +1$ and $A_0 = 0$. For the $e\mu\ell$ and $\mu\mu\ell$ channel, see Figures A.17 and A.18 in the appendix.

7. Limit Setting & Results

The final step of the analysis is the interpretation of the BDT outputs. The task is to find out whether the observed number of events (or BDT output distribution) is consistent with the standard model, or if there is an excess. If it is consistent, upper limits on the cross section of supersymmetric particles can be set. Given enough sensitivity, these limits can fall below the predicted cross sections, and one can set bounds on model parameters.

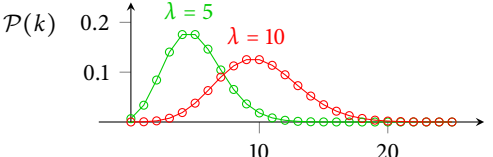
7.1. Statistical methods

In the following, we will consider two hypotheses:

- The null hypothesis H_0 is that there is no signal, only the SM background (b).
- The test (or signal) hypothesis H_1 is that there is the standard model background, plus the signal ($s + b$).

Each hypothesis comes with a set of probability densities (pdfs) for every variable (p_{T1} , \cancel{E}_T , BDT output, and so on). These are sampled by the background and background plus signal histograms. If the experiment is performed once, and a set of N events are observed, these are expected to be distributed according to either the b or the $s + b$ pdfs, depending on which hypothesis is true.

Now instead of one experiment, consider an ensemble of experimental runs. Each run has a different total number of events N , and each of the two hypotheses b and $s + b$ has a different distribution for N . These give the likelihood functions $p(N|s)$ and $p(N|s + b)$, respectively. Since we are dealing with a counting experiment, N will be Poisson-distributed:

$$\mathcal{P}(k, \lambda) = \frac{\lambda^k e^{-\lambda}}{k!} \quad (7.1)$$


Here, λ is the expectation value, $\mathcal{P}(k, \lambda)$ is the probability to count $k \in \mathbb{N}$ events. The standard deviation of a Poisson distribution is $\sigma = \sqrt{\lambda}$.

This treatment of the likelihood as Poissonian only includes statistical uncertainties. Systematics can be treated similarly, using nuisance parameters. In this formalism, the systematic is treated just like an physical addition to the (signal or background) model, with an additional parameter η that is not known precisely. Consider a systematic uncertainty that affects the final number of events N . We can give a probability density for this deviation, depending on the nuisance parameter, $p(N|H, \eta)$ (here, H is either s or $s + b$). Typically a Gaussian uncertainty is used, which is determined by its expectation value and standard deviation. A systematic of $\pm 5\%$ means that, for an ensemble of many experiments, we expect the number of events to follow a Gaussian distribution with a standard deviation of $0.05N$, centered¹ around the old expectation value N (ignoring statistical uncertainties and other systematics here).

¹In a set of actual experiments it might be that the systematic consistently shifts N in one direction. However, this is not known a priori, so we must assume it is randomly distributed. In this sense, the systematic uncertainty parametrizes our ignorance.

The nuisance parameter η itself is not known, but assumed to be distributed according to a prior pdf $\pi(\eta)$. Since the true value of η is not known, it must be integrated out to yield a probability density for N :

$$p(N|H) = \int p(N|H, \eta) \pi(\eta) d\eta$$

The integration is reminiscent of the calculation of an expectation value, with the difference that we now have obtained an expected probability density. This handling of uncertainties on the nuisance parameters is a Bayesian approach, in contrast to the otherwise frequentist treatment [58].

In the case of multiple systematics, this pdf has to be folded with the Poisson distribution of the statistical uncertainty and all other systematics to determine the total likelihood function $p(N|b, \hat{\theta})$ or $p(N|s+b, \hat{\theta})$.

Now that we have the distributions $p(N|s+b, \hat{\theta})$ and $p(N|b, \hat{\theta})$, we can formulate the likelihood ratio as a test statistic (see section (6.2)):

$$Q = \frac{p(N|s+b, \hat{\theta})}{p(N|b, \hat{\theta})} = \frac{\mathcal{P}(N, \lambda_{s+b})}{\mathcal{P}(N, \lambda_b)}, \quad (7.2)$$

where the second equality is the case of a simple Poissonian likelihood (no systematics). Often, the negative log likelihood ratio (NLLR, or just LLR) is chosen as a test statistic. The logarithm simplifies the expression, since the likelihood is typically a product of several distributions. The LLR is given by:

$$LLR = -2 \ln Q = -2 \ln \left(\frac{p(\text{data}|s+b, \hat{\theta})}{p(\text{data}|b, \hat{\theta})} \right) \quad (7.3)$$

In this analysis, we do not just perform a classical “counting experiment” where a certain total number N of events is observed, but rather use the complete information of the BDT output distribution to calculate limits. This is done by splitting the BDT distribution into bins, calculating the likelihood ratio for each bin, and then multiplying them to determine the combined likelihood ratio:

$$Q = \prod_{i=0}^{N_{\text{bins}}} \frac{p(N_i|s+b, \hat{\theta})}{p(N_i|b, \hat{\theta})} \quad \text{or} \quad LLR = -2 \sum_{i=0}^{N_{\text{bins}}} \frac{p(N_i|s+b, \hat{\theta})}{p(N_i|b, \hat{\theta})}$$

Now, pseudoexperiments are performed for the background, and signal+background hypotheses. In a pseudoexperiment, for each bin i , a new N_i is chosen at random from the likelihood distributions $p(N_i|s+b, \hat{\theta})$ and $p(N_i|b, \hat{\theta})$. These samplings of the likelihood distributions are called prior predictive ensembles. Then, the test statistic (the LLR) is calculated. This gives us distributions of expected LLR values if the b or the $s+b$ hypotheses were true. These are compared to the actually observed LLR, determined from data. (Figure 7.1). Using these distributions, one can try to determine whether the data agrees better with the background-only or the signal+background hypothesis, if the two distributions are sufficiently separated. The confidence level CL of a hypothesis is defined as the integrated probability to find an outcome more extreme than the observed one. In Figure 7.1, we consider two confidence levels: CL_{S+B} is the probability to get a LLR value higher than the one observed (more background-like), given that the $s+b$ hypothesis is true. $1 - CL_B$ is the probability to find an LLR lower than observed (more signal+background-like), if the background hypothesis was true.

We can use the CL_{S+B} confidence level to set exclusions. For this, one chooses the LLR value where $CL_{S+B} < \alpha = 5\%$ as a cut. If the observed LLR value is more background-like than the cutoff, one says the signal+background hypothesis is excluded at $1 - \alpha = 95\%$ CL. This strategy has the effect that in only 5% of analyses where the $s+b$ hypothesis was true, we would erroneously exclude it². However, the CL_{S+B} confidence level is a bad choice in the case of a downward fluctuation in data. If the observed data is much

²Error of the first kind - rejecting the hypothesis under test, although it is true.

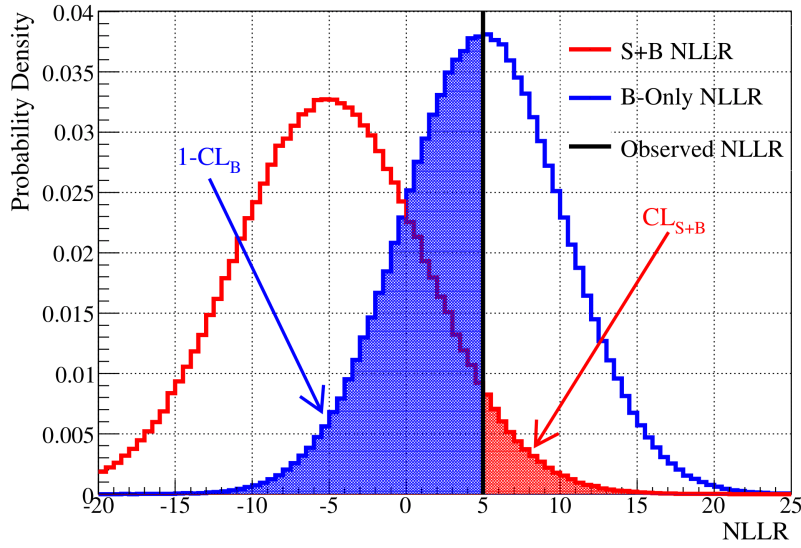


Figure 7.1. Example of log likelihood ratio (NLLR) distributions for the $s + b$ and b only prior predictive ensembles, compared to an observed NLLR. From [58].

below even the background expectation (and thus in conflict also with the background only hypothesis), CL_{S+B} gives an exclusion, although this is likely to be due to a bad background model or too low statistics. The alternative to the CL_{S+B} confidence level that is used in this thesis is the modified frequentist CL_S :

$$CL_S = \frac{CL_{S+B}}{CL_B} \quad (7.4)$$

In the pathological case of a too background-like downward fluctuation, where CL_{S+B} becomes very small, CL_B in the denominator becomes small, too, thus allowing an exclusion.

Instead of just knowing whether a given signal point is excluded or not, we would like to have a measure of how far from an exclusion we are. We would like to know for a given point, which cross section above the predicted one we could exclude. To determine these cross section limits, the signal prediction is scaled up for each point until such a signal is excluded. We can then report that a signal at x times the predicted (SUSY) cross section is excluded. When $x < 1$, this point is excluded with the predicted cross section. In the following, we will present cross section limits not in terms of x times predicted cross section, but as absolute cross section times branching ratio $\sigma \times BR$ in picobarns. In these plots, the signal prediction ($x = 1$) is shown as a red line. When the observed limit falls below this line, the point is excluded.

7.1.1. Two-dimensional limits

Where the considered model depends on two parameters ($m_0, m_{1/2}$), it is interesting to plot the limits as an excluded area in the two-dimensional plane. In this thesis, this is done for two cases, mSUGRA with $\tan \beta = 3, A_0 = 0, \text{sgn } \mu = +1$, and NUGM with $\tan \beta = 10, A_0 = 0, \text{sgn } \mu = +1$ and $\theta_{24} = -0.15\pi$. There are several techniques for creating these plots. Since we have a fairly limited number of points in the ($m_0, m_{1/2}$) plane, we have chosen to interpolate between these points with a smooth function.

The most general function of two parameters of order two is given by

$$f(x, y) = ax^2 + bx + c + dy^2 + ey + fxy \quad (7.5)$$

with the six constants a, b, c, d, e, f . This is fitted to the logarithm of the expected cross section limit (and expected limit $\pm 1\sigma$, and observed limit). It is found that this function gives a reasonable fit to the discrete

Flat Systematic	Effect	Comments
Normalization	10%	
Object ID efficiency		
Electron	2.5 %	$e\bar{e}l$ and $e\mu l$ channels
Muon	4.0 %	$\mu\mu l$ and $e\mu l$ channels
Tracks	4.0 %	
Trigger	5.0 %	
Cross Section		
Z + Jets	6%	
W + Jets	6%	
Diboson	7%	
$t\bar{t}$	10%	
Signal	4%	
PDF	2.5%	
Multijet estim.	30%	Only QCD multijet bkg.
Shape Systematic	Avg. Effect	Comments
Jet energy scale (JES)	+0.32% / -8.32%	
Jet energy resolution (RES)	+8.46% / -8.36%	
Jet shifting (JSSR)	$\pm 0.38\%$	
Jet ID	$\pm 0.04\%$	
Z p_T reweighting (VJets)	+0.03% / -0.08%	
Vertex confirmation	$\pm 0.01\%$	
EM smearing	+8.39% / -8.36%	$e\bar{e}l$ and $e\mu l$ channels
EM scaling	+0.10% / -0.05%	$e\bar{e}l$ and $e\mu l$ channels
Z p_T / $\cos\beta_1$ reweighting	$\pm 4.67\%$	
Unclustered energy reweighting	$\pm 4.66\%$	
Electron p_T reweighting	$\pm 4.99\%$	only $e\bar{e}l$ channel
Electron likelihood reweighting	$\pm 0.77\%$	only $e\bar{e}l$ channel

Table 7.1. Overview of all sources of systematic uncertainty included. For the shape systematics, the average effect per bin of the output distribution is cited.

limits (Figures A.21 and A.22). In the case of mSUGRA, the parameter space covers the two-body and three-body decay regions, which have different kinematics, and different signal efficiencies. For this reason, the two regions are fitted independently here. The results of the 2D fits are shown in Figures 7.5 and 7.9. It should be noted that these plots are for illustrative purposes due to the interpolation. The authoritative limits are shown in the one-dimensional plots, and in the tables in the appendix.

7.2. Systematics

The sources of systematic uncertainty considered are listed in Table 7.1. Some systematics are included as “flat” systematics which only affect the overall background normalization, and some are “shape” systematics whose value may differ from bin to bin of the BDT output distribution.

7.2.1. Trigger

In the DØ Monte Carlo generation, the trigger is not simulated. Instead, reweightings are applied to MC to achieve the correct efficiencies and turn-on curves. The uncertainty of the scale factors involved leads to a systematic uncertainty of 5%.

7.2.2. Object ID

There are several uncertainties associated with the identification of objects such as electrons, muons, and tracks, that are treated as flat systematics.

Electron ID The electron ID systematic is a result of uncertainties of the EM ID efficiency, and statistical uncertainties in the parametrizations used. A flat systematic uncertainty of 2.5% is applied, as determined by studies of the EM ID group [59]. This is applied to all MC samples in channels containing electrons.

Muon ID Similarly, the uncertainty on the muon ID efficiency amounts to a flat systematic of 4% [60].

Track ID For the identification of the additional track, a flat systematic of 4% is assumed.

7.2.3. Cross Sections

The systematic uncertainty on the Z + jets cross section is 4%, on the W + jets and diboson cross sections 6%, and on the $t\bar{t}$ cross section 7%. The uncertainty on the signal cross section is 4%. These are mainly a result of uncertainties in the parton density functions (PDF), and due to the uncertainty of the NLO cross sections.

7.2.4. Multijet Estimation

The uncertainty of the multijet modeling is estimated to be 30%. Note that no multijet events passes the final selection in the $ee\ell$ and $\mu\mu\ell$ channels.

7.2.5. Jets

Although no jets are demanded in the event selection, variation of jet-related parameters can potentially have an effect on the results. The number of jets, but also the missing transverse energy of an event, and related variables depend on these parameters. Systematics are considered for a variation of the jet energy scale (JES), jet energy resolution (RES), the jet smearing, shifting and removal process (JSSR), and the jet ID efficiency. Also, the effect of vertex confirmation is considered for RunIIB.

7.2.6. $Z p_T / \cos \beta_1$ Reweighting

The effect of the custom $Z p_T$ Reweighting (Section 5.6.4) is considered by rerunning the analysis without it.

7.2.7. EM Smearing and Scaling

For channels with electrons ($ee\ell$ and $e\mu\ell$), there are two shape uncertainties included for the smearing and the energy scale of electrons.

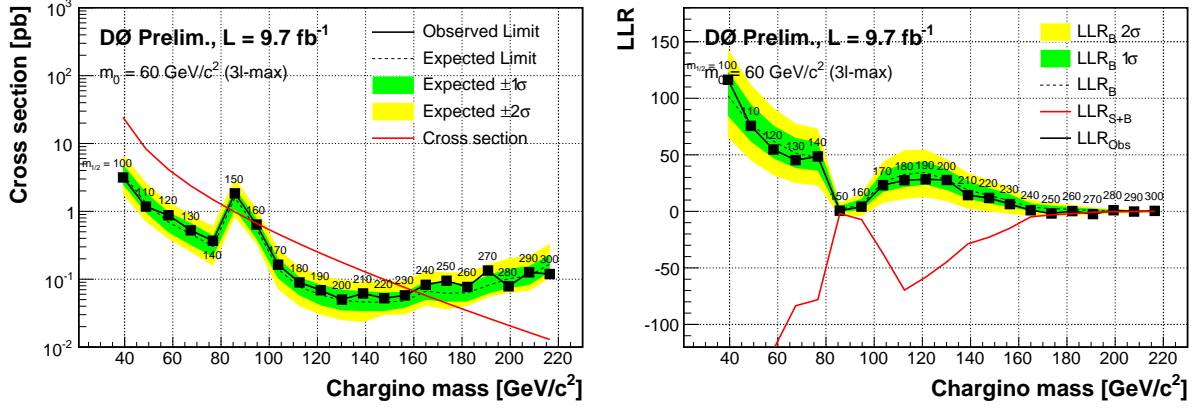


Figure 7.2. Limits for the “3 ℓ -max” mSUGRA scenario, where $m_0 = 60$ GeV, $\tan \beta = 3$, $A_0 = 0$ GeV and $\text{sgn } \mu = +1$. The numbers next to the points are values of $m_{1/2}$ in GeV. Left: expected and observed cross section limits, right: log-likelihood ratio for the background-only and signal plus background hypotheses, and observed LLR.

7.3. mSUGRA Limits

In the following, the cross section limits and log-likelihood ratios for the mSUGRA scenario will be presented. Figure 7.2 shows the limits for the “3 ℓ -max” scenario, which is characterized by a high branching ratio into three light leptons. This plot follows a vertical in the $(m_0, m_{1/2})$ plane. The unified gaugino mass $m_{1/2}$ is varied, while the other variables are fixed to $m_0 = 60$ GeV, $\tan \beta = 3$, $A_0 = 0$ GeV and $\text{sgn } \mu = +1$. Chargino masses up to 160 GeV are excluded, which corresponds to a value for $m_{1/2} = 235$ GeV, with exception of a window from $m(\tilde{\chi}_1^\pm) = 85 \dots 95$ GeV where $m(\tilde{\ell}) \approx m(\tilde{\chi}_2^0)$.

In Figure 7.3, limits on the chargino mass are shown for the “heavy sleptons” scenario, with $m_0 = 170$ GeV, $\tan \beta = 3$, $A_0 = 0$ GeV and $\text{sgn } \mu = +1$. These points mostly lie in the three-body decay region, where $m(\tilde{\ell}) > m(\tilde{\chi}_2^0)$. In this case, no points could be excluded.

The case of varied m_0 is displayed in Figure 7.4, where the other parameters are set to $m_{1/2} = 180$ GeV, $\tan \beta = 3$, $A_0 = 0$ GeV and $\text{sgn } \mu = +1$. Here, values of m_0 up to 115 GeV are excluded, except for the region $m_0 = 75 \dots 85$ GeV. Additionally, the point at $m_0 = 130$ GeV is excluded.

These limits are combined in Figure 7.5, which shows the expected and observed limits in the $(m_0, m_{1/2})$ plane. The black, dashed curve shows the extrapolated expected limit, while the blue, stroked curve shows the observed limit. Note that some points close to the outside of the boundary are excluded, while some points inside are not. One reason is that points close to the boundary have a limit of $\approx 1 \times \sigma$. Statistical fluctuations can affect whether such a point falls below the exclusion limit or not, especially since each point uses a unique BDT, and the observed BDT distribution, not only the signal expectation, varies from point to point. The other reason is that the fitted function might not represent all structure in the parameter space correctly.

All expected and observed limits are tabulated in the appendix, Tables A.4 to 2.19 for $\tan \beta = 3$, and Table A.9 for $\tan \beta > 3$. Figures A.23–A.25 in the appendix show limits on $\tan \beta$, for three points in the $m_0, m_{1/2}$ plane. However, there is no sensitivity for either point.

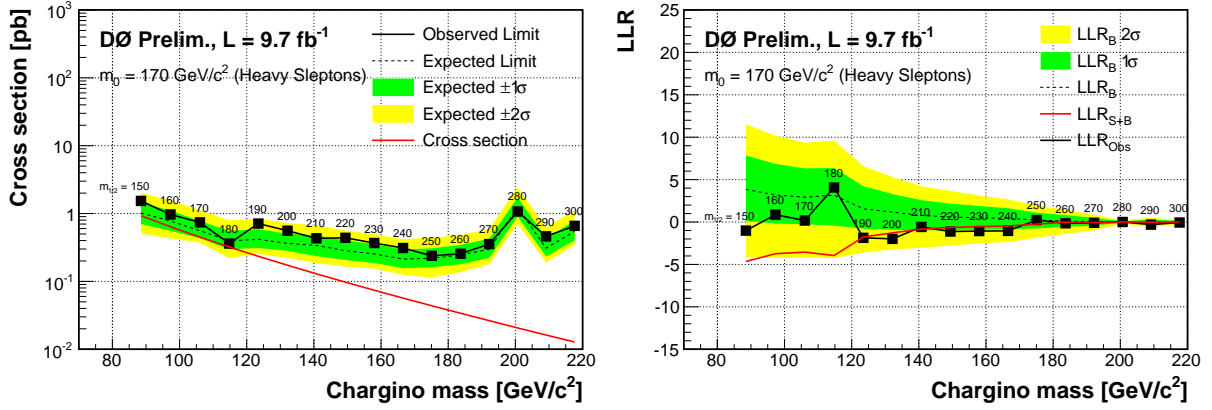


Figure 7.3. Limits for the “heavy sleptons” mSUGRA scenario, in which $m_0 = 170 \text{ GeV}$, $\tan \beta = 3$, $A_0 = 0 \text{ GeV}$ and $\text{sgn } \mu = +1$. The numbers next to the points are values of $m_{1/2}$ in GeV. Left: cross section limits, right: log-likelihood ratio.

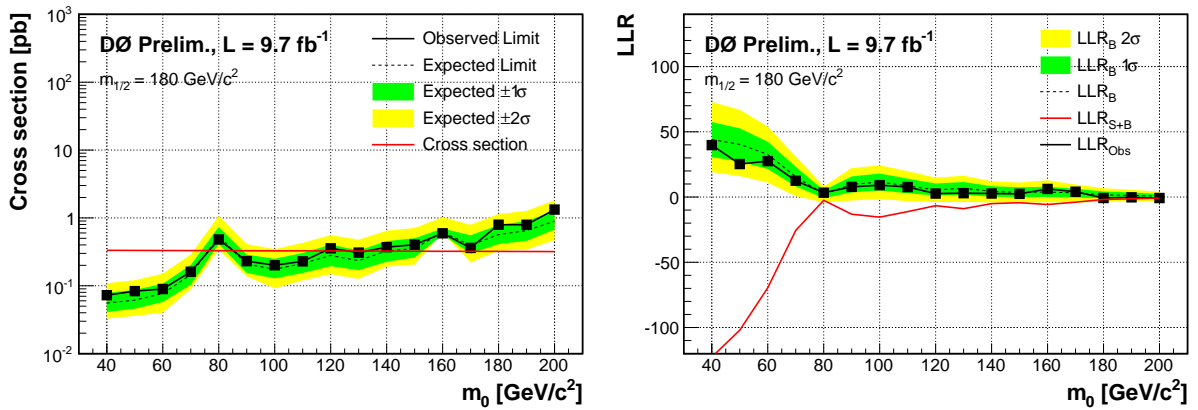


Figure 7.4. Limits on mSUGRA parameters, where $m_{1/2} = 180 \text{ GeV}$, $\tan \beta = 3$, $A_0 = 0 \text{ GeV}$ and $\text{sgn } \mu = +1$. Left: cross section limits, right: log-likelihood ratio.

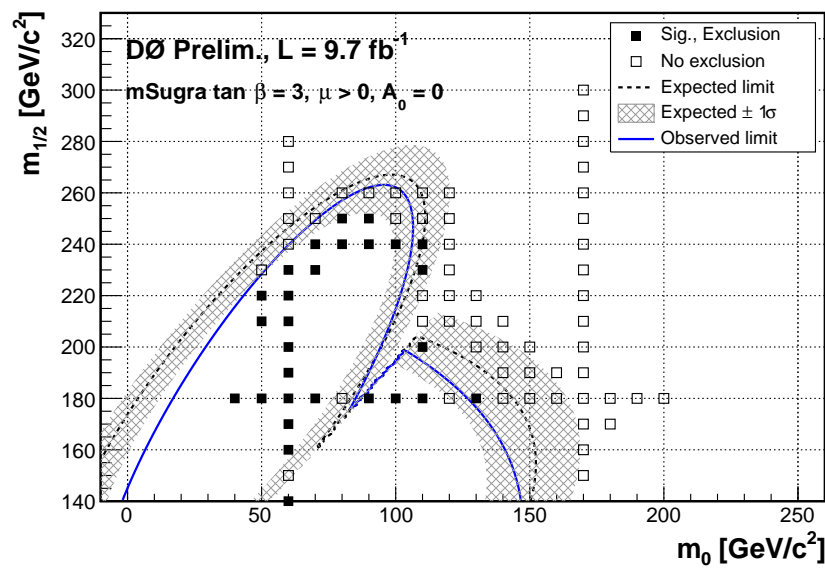


Figure 7.5. Limits on mSUGRA parameters in the $(m_0, m_{1/2})$ plane, where $\tan \beta = 3$, $A_0 = 0$ GeV and $\text{sgn } \mu = +1$. The blue stroked curve shows the extrapolated region for the observed exclusion, the dashed black line shows the expected exclusion, with $\pm 1\sigma$ interval.

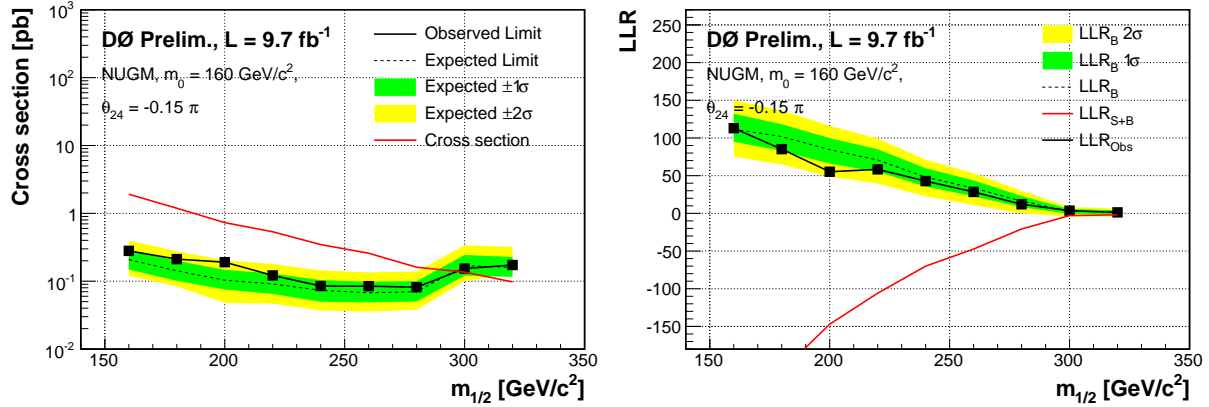


Figure 7.6. Limits for the NUGM scenario with $m_0 = 160 \text{ GeV}$, $\theta_{24} = -0.15\pi$, $\tan \beta = 10$, $A_0 = 0 \text{ GeV}$ and $\text{sgn } \mu = +1$. Left: expected and observed cross section limits, right: log-likelihood ratio for background-only and signal plus background hypotheses, and observed LLR.

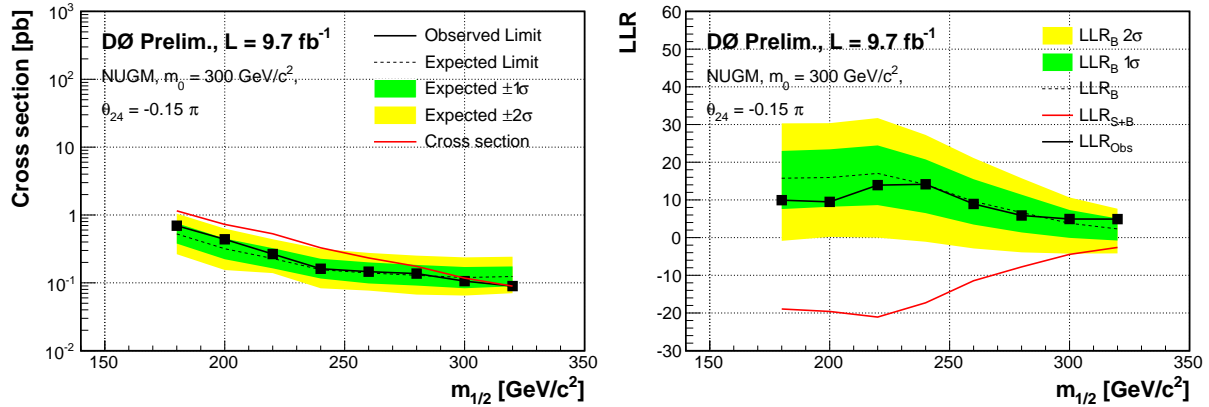


Figure 7.7. Limits for the NUGM scenario with $m_0 = 300 \text{ GeV}$, $\theta_{24} = -0.15\pi$, $\tan \beta = 10$, $A_0 = 0 \text{ GeV}$ and $\text{sgn } \mu = +1$. Left: expected and observed cross section limits, right: log-likelihood ratio for background-only and signal plus background hypotheses, and observed LLR.

7.4. NUGM Limits

Limits were also set on parameters for the non-universal gaugino masses scenario. In Figure 7.6, m_0 is fixed to 160 GeV , while $m_{1/2}$ is varied. The other parameters are set to $\tan \beta = 10$, $A_0 = 0 \text{ GeV}$, $\text{sgn } \mu = +1$, and $\theta_{24} = -0.15\pi$. Masses are excluded up to $m_{1/2} = 295 \text{ GeV}$. For the case of $m_0 = 300 \text{ GeV}$ (Figure 7.7), the limit is $m_{1/2} = 320 \text{ GeV}$. Following a horizontal line in the $(m_0, m_{1/2})$ plane, m_0 is varied, while $m_{1/2} = 260 \text{ GeV}$ in Figure 7.8. In this case, all considered points have been excluded, ranging up to $m_0 = 320 \text{ GeV}$. Figure 7.9 shows these limits in the two-dimensional plane, including fitted extrapolations of expected and observed limits.

Figure 7.10 shows the cross section limits and LLR values for the θ_{24} scan. Over a large part of the parameter space, there is no sensitivity, since M_1 and M_2 are large there, and so are the chargino and neutralino masses. Some points in the vicinity of $\theta_{24} = -0.15\pi$ and $\theta_{24} = 0.06\pi$ have been excluded, though. A possible improvement would be to generate more points near the excluded values, in order to determine the boundaries of exclusion.

A listing of all expected and observed limits can be found in Tables A.7 and A.8 in the appendix.

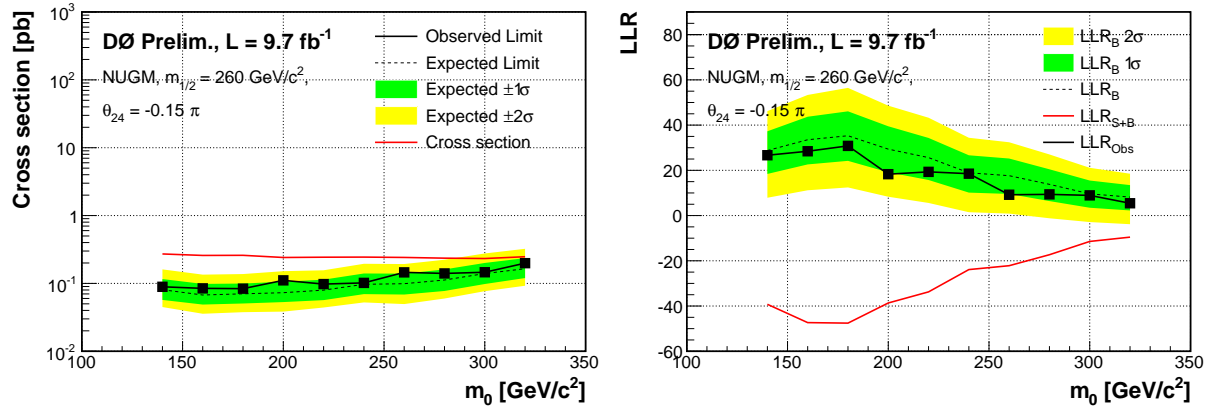


Figure 7.8. Limits for the NUGM scenario with $m_{1/2} = 260 \text{ GeV}$, $\theta_{24} = -0.15\pi$, $\tan \beta = 10$, $A_0 = 0 \text{ GeV}$ and $\text{sgn } \mu = +1$. Left: expected and observed cross section limits, right: log-likelihood ratio for background-only and signal plus background hypotheses, and observed LLR.

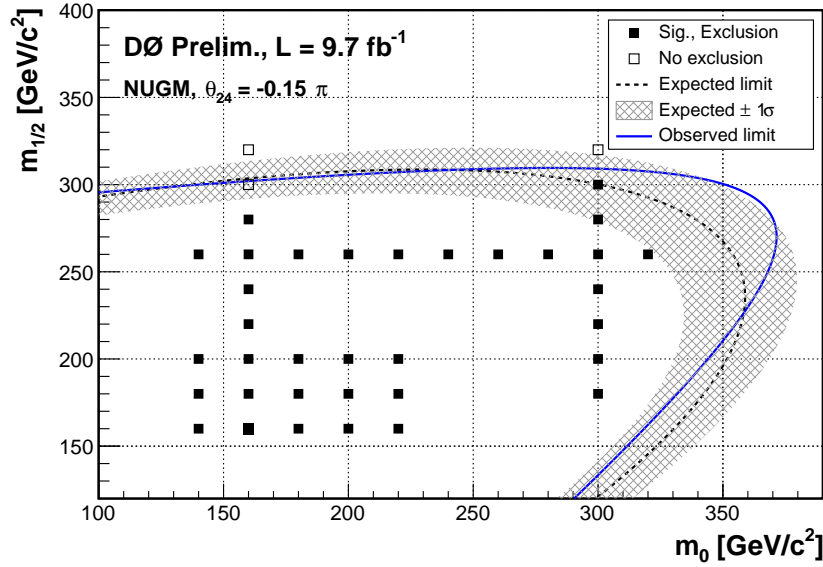


Figure 7.9. Limits on NUGM parameters in the $(m_0, m_{1/2})$ plane, for $\theta_{24} = -0.15\pi$. Other parameters are set to $\tan \beta = 10$, $A_0 = 0 \text{ GeV}$ and $\text{sgn } \mu = +1$.

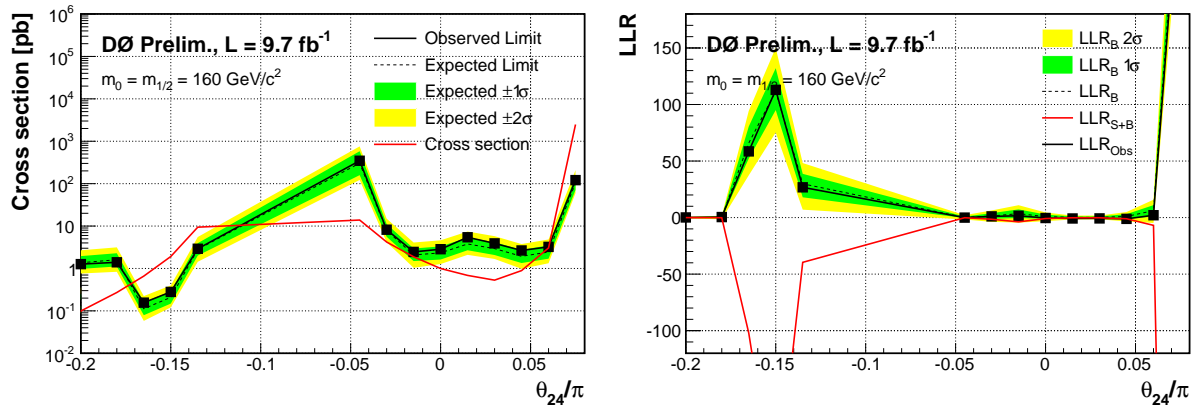


Figure 7.10. Limits for the NUGM scenario with $m_0 = m_{1/2} = 160 \text{ GeV}$, $\tan \beta = 10$, $A_0 = 0 \text{ GeV}$ and $\text{sgn } \mu = +1$. Outside of the displayed region, no values of θ_{24} are excluded. Left: expected and observed cross section limits, right: log-likelihood ratio for background-only and signal plus background hypotheses, and observed LLR.

8. Summary & Outlook

A search for supersymmetry in the trilepton final state has been performed on the full dataset of the DØ experiment. To increase acceptance, only two identified leptons were demanded, plus one isolated charged track. The analysis was split into three channels, $ee\ell$, $e\mu\ell$ and $\mu\mu\ell$. Backgrounds including Z + jets, W + jets, Diboson (WW , WZ , ZZ) and $t\bar{t}$ pair production were modeled using Monte Carlo, the multijet background was estimated by a data-driven method. Comprehensive corrections have been applied to the MC to achieve an accurate background modeling. A set of cuts was then applied to increase the signal to background ratio. The resulting samples were used in a multivariate analysis using boosted decision trees. From a set of candidate variables, the best performing ones were selected and used to train the BDTs. The BDT output distributions were then used to set limits on the cross section for various signal hypotheses. Where the limits fall below the predicted cross section, parts of the parameter space were excluded. Notably, for the mSUGRA model, in the limit of low m_0 , chargino masses up to 160 GeV were excluded at 95% CL, with exception of a window from 85 to 95 GeV. New limits were set in the $(m_0, m_{1/2})$ plane, improving on the previous DØ results.

Limits were also set for a scenario of non-universal gaugino masses, with $\theta_{24} = -0.15\pi$ and $\tan\beta = 10$. For $m_0 = 160$ GeV, values of $m_{1/2}$ up to 295 GeV were excluded, for $m_0 = 300$ GeV the limit is $m_{1/2} < 320$ GeV. In the $(m_0, m_{1/2})$ plane, the area up to $m_0, m_{1/2} \approx 300$ GeV is excluded at 95% CL.

8.1. Further improvements

There are a few opportunities for improvement of the analysis. If the systematic uncertainties were reduced, an exclusion in the “heavy sleptons” scenario ($m_0 = 160$ GeV) seems possible. One candidate is the multijet background, which has a rather large uncertainty of 30% and mainly affects the $e\mu\ell$ channel. The first step would be to determine the uncertainty more accurately. This could be done by performing pseudoexperiments: the parameters a and b in the QCD multijet reweightings are varied randomly according to their uncertainties, then the total number of events N_{QCD} passing the selection is considered. From the distribution of N_{QCD} from all pseudoexperiments, the systematic uncertainty can be determined. Once the uncertainty is calculated, it can be improved by revising the fit function or loosening cuts to add further statistics.

Another option would be the inclusion of final states with tau leptons. Leptonically decaying taus are implicitly included, however one could also explicitly identify hadronically decaying taus. These have the benefit that the branching ratio into tau leptons is often enhanced in supersymmetric models, especially at higher values of $\tan\beta$.

The analysis could also be improved by including more signal points, especially near the exclusion boundaries, as well as in the θ_{24} scan. The interpolation in the $(m_0, m_{1/2})$ plane could also be improved by using a more physics-informed fit function. Essentially, the limits are a function of cross section, branching ratio, and signal efficiency. The first two are known from simulations, and one could model signal efficiency as a function of particle masses and mass differences. We considered that there are different kinematic regions with different signal efficiencies in mSUGRA, by splitting the $(m_0, m_{1/2})$ plane into two regions. This simple method already gave good results and reproduced the well-known limit shape with the gap at $m(\tilde{\ell}) \approx m(\tilde{\chi}_2^0)$.

8.2. Outlook

However, there is only so much that could be done with 2 TeV data. In new phenomena searches, often nothing can compensate for energy (\sqrt{s}). Currently, the unique machine to conduct direct searches for supersymmetric particles is the Large Hadron Collider (LHC). In 2015 it will begin its second run at a center of mass energy of 13 TeV. We have reason to believe that if supersymmetry exists as a fundamental symmetry, and if it is the solution to the hierarchy problem, then it will be found at the LHC. Once it is found, the more challenging task begins - finding out which kind of supersymmetry is realized and trying to determine the theory's parameters. This is also known as the inverse problem. Due to the long decay chains prominent in many models, it is not as simple as searching for a bump. Special kinematic variables, such as MT_2 , provide a handle on supersymmetric masses. Also, in principle it should be possible to see thresholds in invariant mass variables, when the necessary mass is reached to produce a supersymmetric particle. However, these distributions can be washed out due to the characteristics of hadron collisions.

A very interesting venue to analyze the spectrum of supersymmetric particles would be a lepton collider. Currently in planning is the International Linear Collider (ILC), which is to be built in the Kitakami mountains, Japan. The ILC will initially have an e^+e^- center of mass energy of 500 GeV, with the option of an upgrade to 1 TeV. The benefit of an electron collider is the clean initial state, with a well-known center-of-mass. It is not necessary to restrict oneself to transverse quantities such as p_T or \cancel{E}_T , but one can use the whole kinematics of an events. The center-of-mass energy of the collisions is tunable, making it easy to find particle production thresholds. Additionally, the final states are cleaner than those in a hadron collider due to the lack of proton collision remnants and underlying events.

If supersymmetry is not found however, this will be a major theoretical challenge. One will have to reconsider other theories beyond the standard model to deal with the hierarchy problem, such as extra dimensions. If searches for these also turn up negative, one would face the possibility of a “great desert” with no new physics above the energy scale of the standard model. In this case, we might have to rethink some of our assumptions about fundamental physics that lead us to the hierarchy problem. Either way, the near future promises to be an exciting time in high energy physics.

A. Appendix

A.1. Samples and Event Selection

A.1.1. RunII Skims

In the following, the event tags required for the EMinclusive, EMMU and 2MUhighpt skims are listed.

Tag	Requirements
1EM2JET	EM cluster with id = 10 or 11, $E_T > 20$ GeV, $\chi^2_{\text{HMx8}} < 75$ Matched track with $p_T > 7$ GeV and $\Delta\phi < 0.1$ 3 jets with $E_T > 8$ GeV
1EMLOOSE	EM cluster with id = 10 or 11, $E_T > 20$ GeV
2EM	2 EM clusters with id = 10 or 11, $E_T > 7$ GeV
EM1TRK	EM cluster with id = 10 or 11, $E_T > 8$ GeV Matched track with $p_T > 5$ GeV and $\Delta\phi < 0.2$
JES_B	EM cluster with id = 10 or 11, $E_T > 4$ GeV at least on electron trigger fired

Table A.1. Event tags required for EMinclusive skim.

Tag	Requirements
2MU1TRK	two loose muons, one of which matched to track with $p_T > 15$ GeV
2MUhighpt	two loose muons, each matched to track with $p_T > 10$ GeV
MU2TRKhighpt	one loose muons matched to track with $p_T > 15$ GeV one additional track with $p_T > 15$ GeV

Table A.2. Event tags required for 2MUhighpt skim.

Tag	Requirements
EMMU	EM cluster with id = 10 or 11, $E_T > 20$ GeV loose muon with $p_T > 5$ GeV

Table A.3. Event requirements for EMMU skim.

A.1.2. Luminosity Reweighting

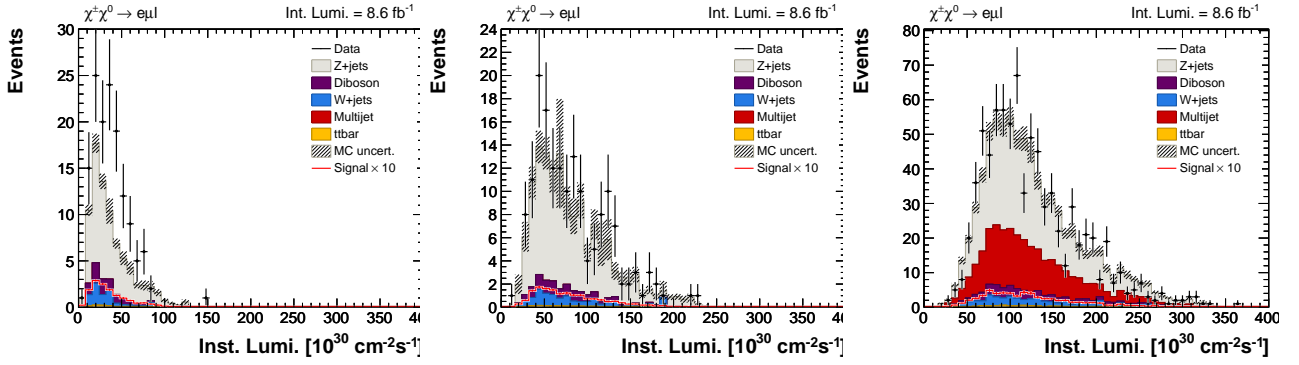


Figure A.1. Instantaneous luminosity \mathcal{L} after application of all corrections, $e\mu\ell$ channel, for RunIIa, RunIIb-1, and RunIIb-234. The luminosity reweighting is described in Section 5.6.1.

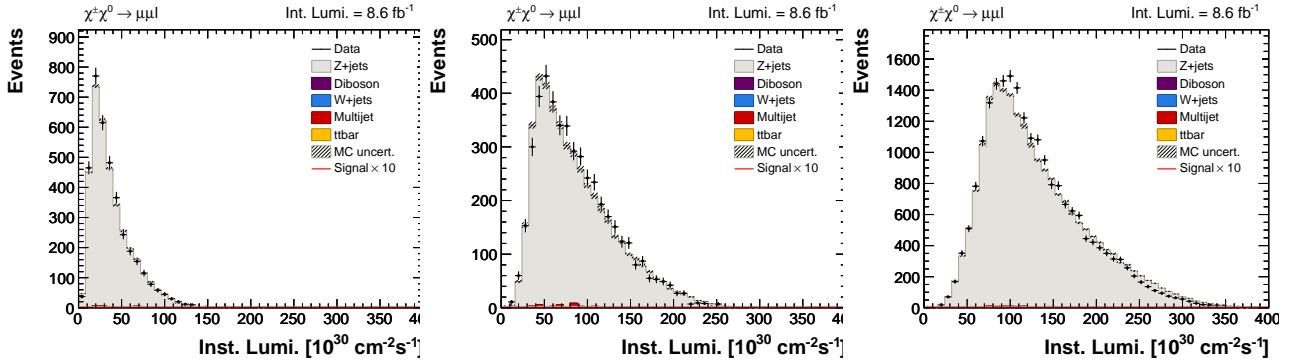


Figure A.2. Instantaneous luminosity \mathcal{L} after application of all corrections, $\mu\mu\ell$ channel, for RunIIa, RunIIb-1, and RunIIb-234. The luminosity reweighting is described in Section 5.6.1.

A.1.3. Beam Reweighting

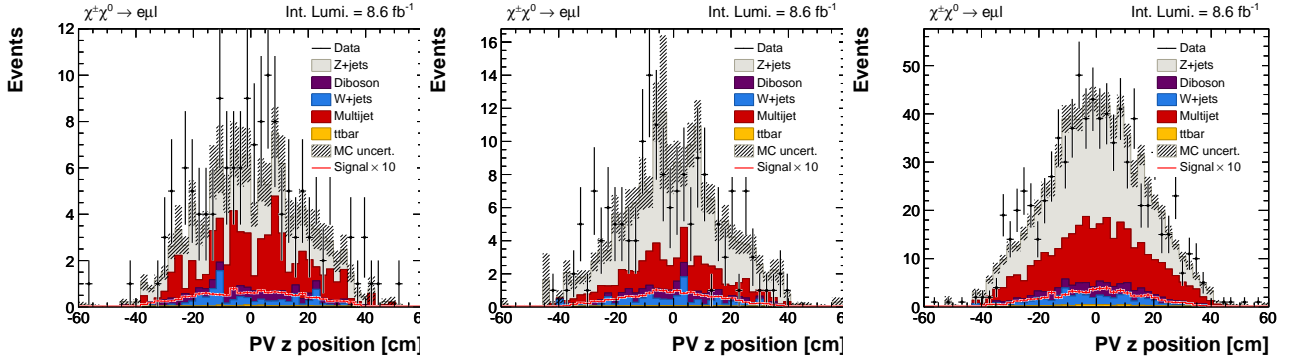


Figure A.3. z coordinate of the primary vertex for the $e\mu\ell$ channel. After application of all corrections, for RunIIa, RunIIb-1, and RunIIb-234.

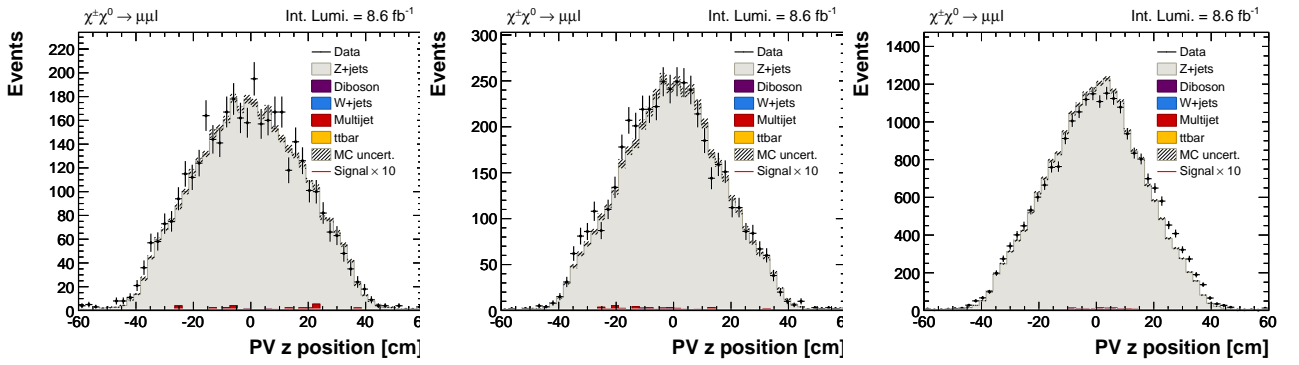


Figure A.4. z coordinate of the primary vertex for the $\mu\ell$ channel. After application of all corrections, for RunIIa, RunIIb-1, and RunIIb-234.

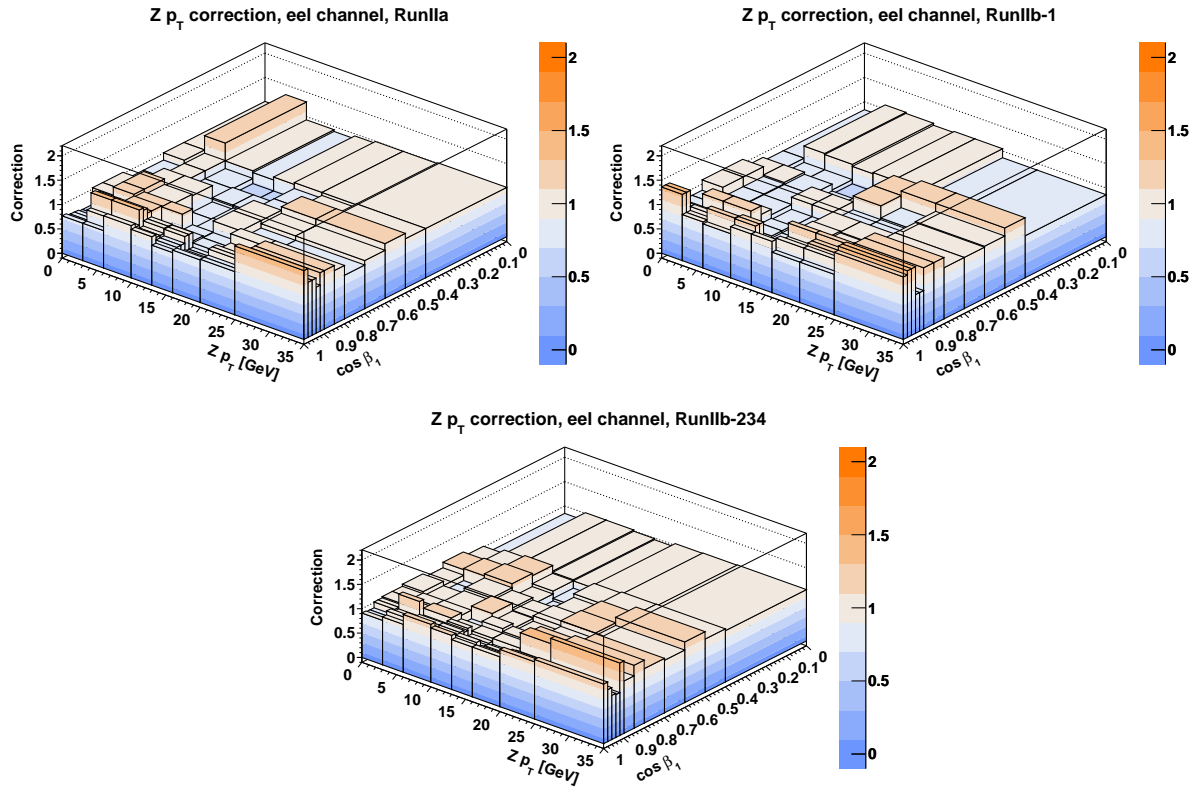
A.1.4. $Z p_T$ Reweighting

Figure A.5. Scale factors for the additional $Z p_T / \cos \beta_1$ reweighting (Section 5.6.4), for the ee channel, RunIIa, RunIIb-1 and RunIIb-234 periods.

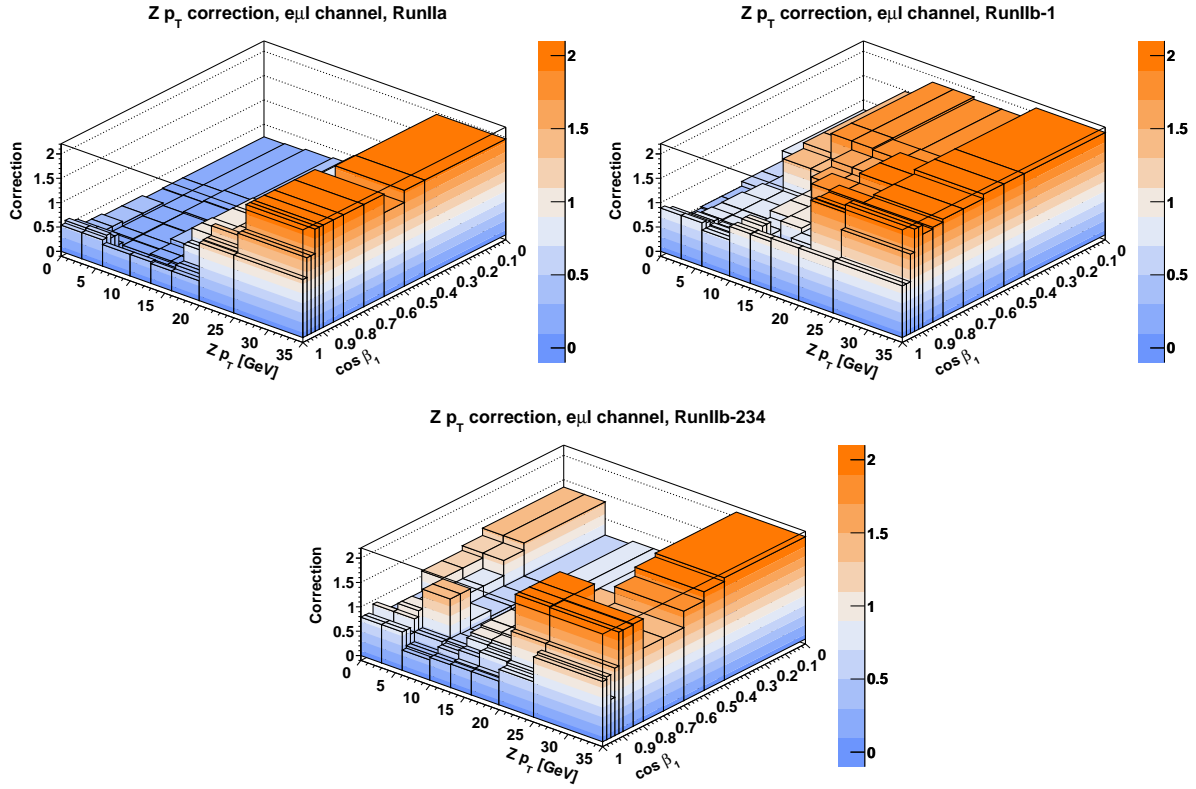


Figure A.6. Scale factors for the additional $Z p_T / \cos \beta_1$ reweighting (Section 5.6.4), for the em channel, RunIIa, RunIIb-1 and RunIIb-234 periods.

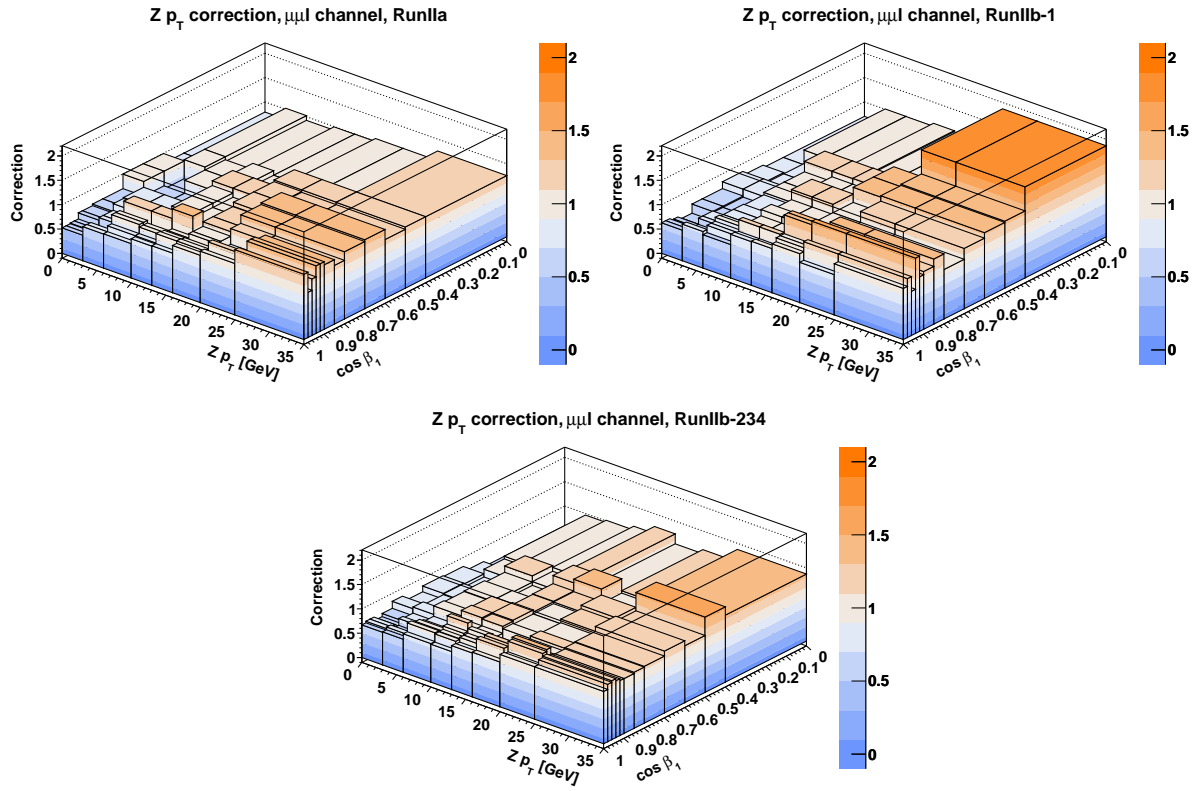


Figure A.7. Scale factors for the additional $Z p_T / \cos \beta_1$ reweighting (Section 5.6.4), for the mm channel, RunIIa, RunIIb-1 and RunIIb-234 periods.

A.1.5. QCD Multijet reweighting functions

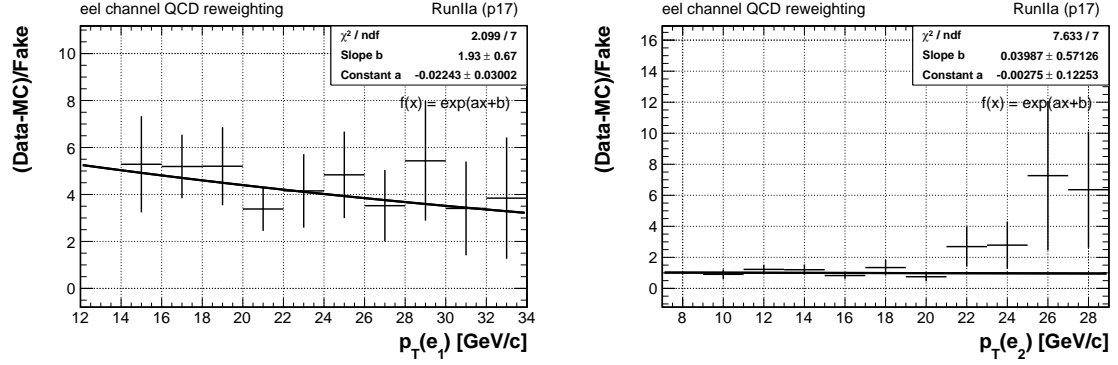


Figure A.8. QCD multijet reweighting functions, eel channel, p17 period. The first reweighting (left) is dependent on the leading electron p_T , the second on the next-to-leading electron p_T .

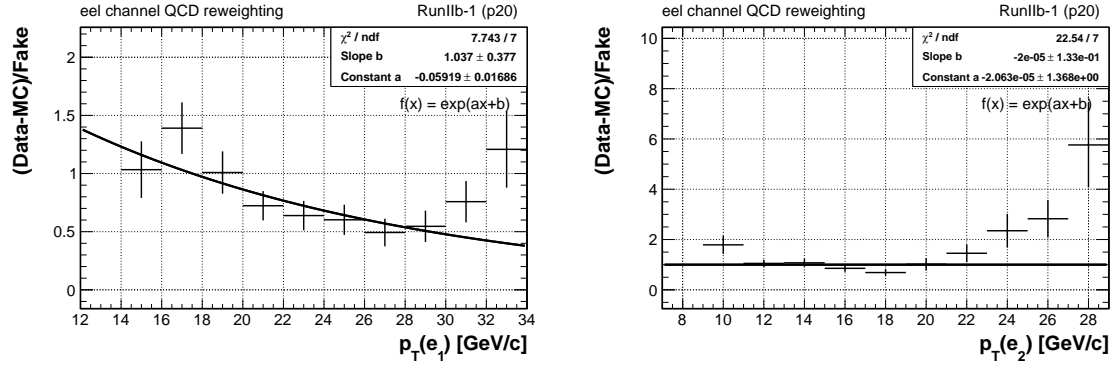


Figure A.9. QCD multijet reweighting functions, eel channel, p20 period. The first reweighting (left) is dependent on the leading electron p_T , the second on the next-to-leading electron p_T .

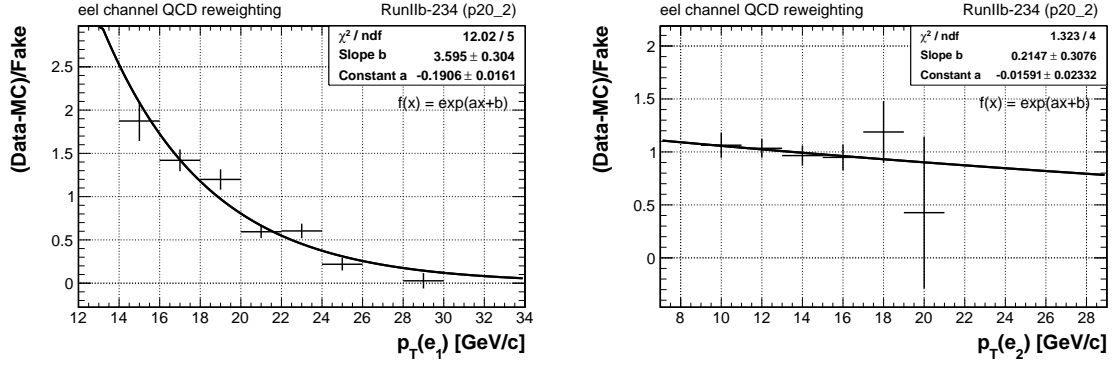


Figure A.10. QCD multijet reweighting functions, $e\ell\ell$ channel, p20_2 period. The first reweighting (left) is dependent on the leading electron p_T , the second on the next-to-leading electron p_T .

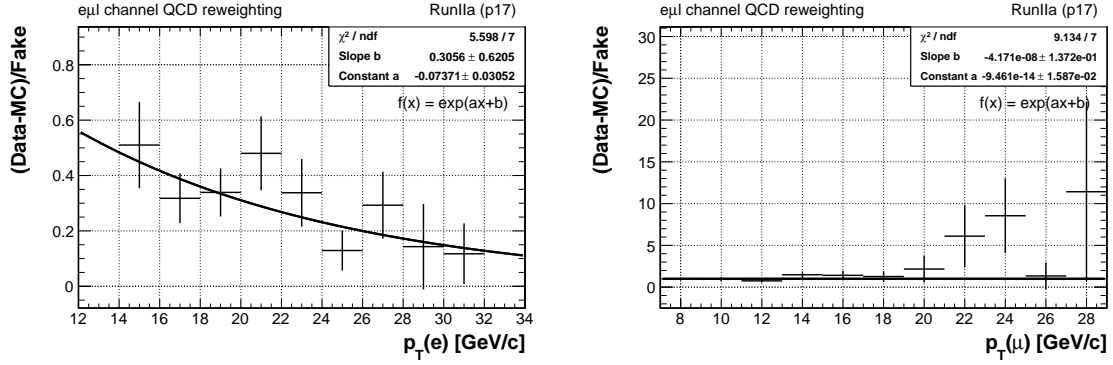


Figure A.11. QCD multijet reweighting functions, $e\mu\ell$ channel, p20 period. The first reweighting (left) is dependent on the electron p_T , the second on the muon p_T .

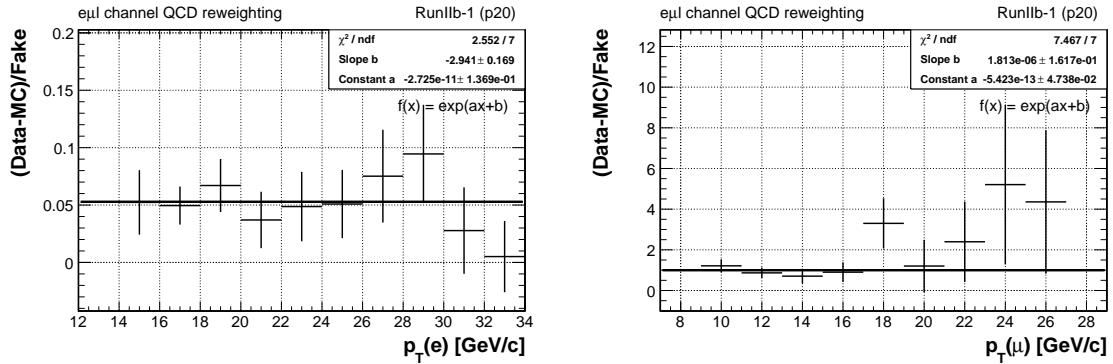


Figure A.12. QCD multijet reweighting functions, $e\mu\ell$ channel, p20 period. The first reweighting (left) is dependent on the electron p_T , the second on the muon p_T .

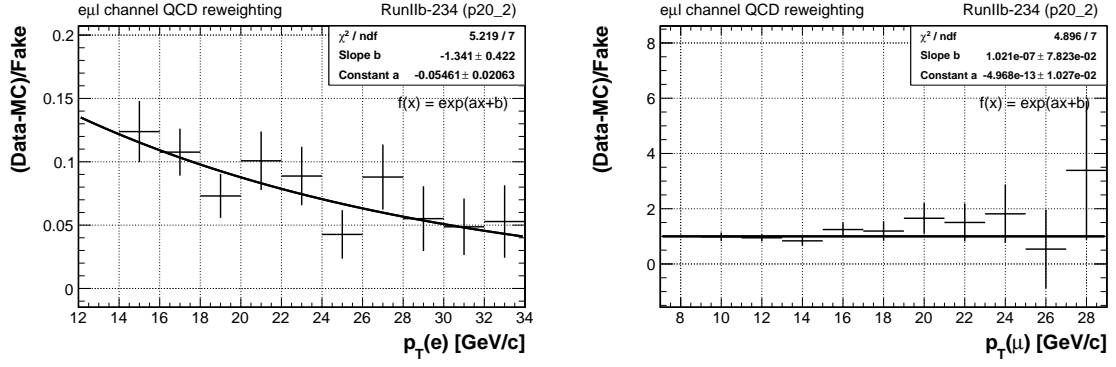


Figure A.13. QCD multijet reweighting functions, $e\mu l$ channel, p20_2 period. The first reweighting (left) is dependent on the electron p_T , the second on the muon p_T .

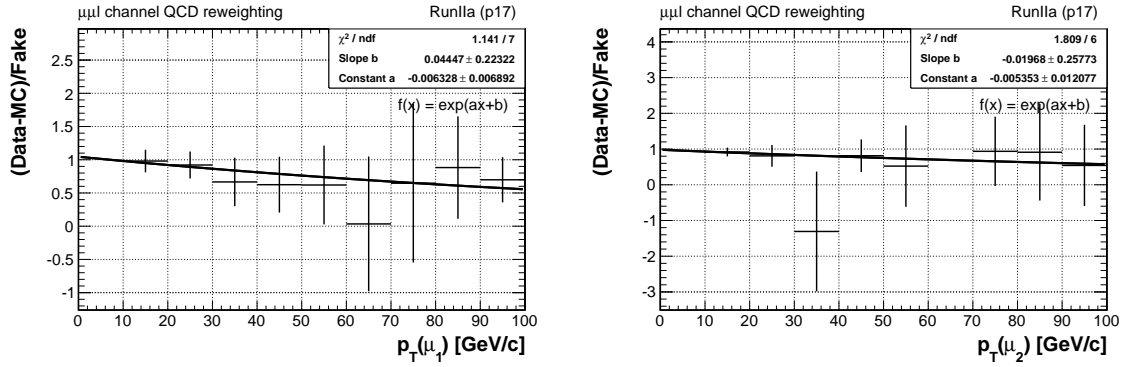


Figure A.14. QCD multijet reweighting functions, $\mu\mu l$ channel, p17 period. The first reweighting (left) is dependent on the leading muon p_T , the second on the next-to-leading muon p_T .

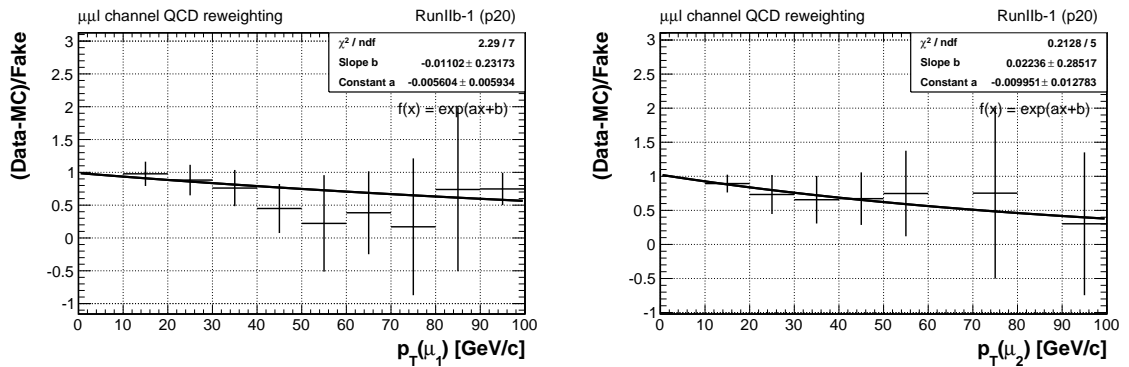


Figure A.15. QCD multijet reweighting functions, $\mu\mu l$ channel, p20 period. The first reweighting (left) is dependent on the leading muon p_T , the second on the next-to-leading muon p_T .

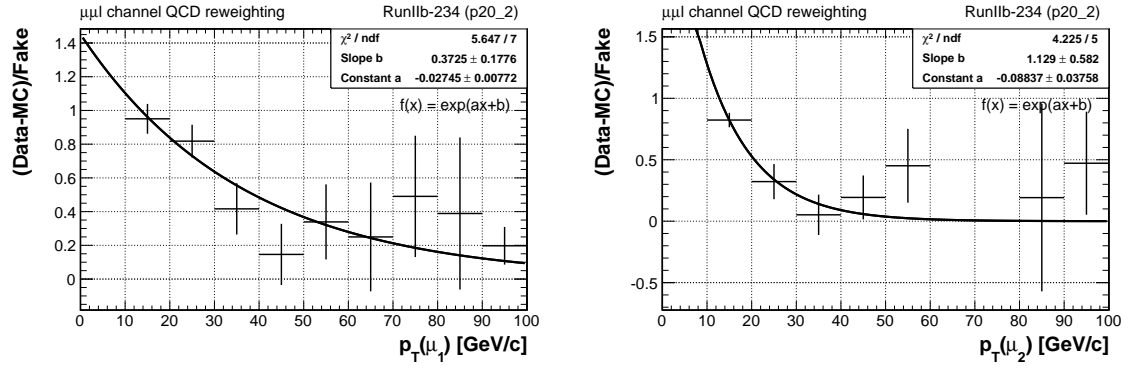
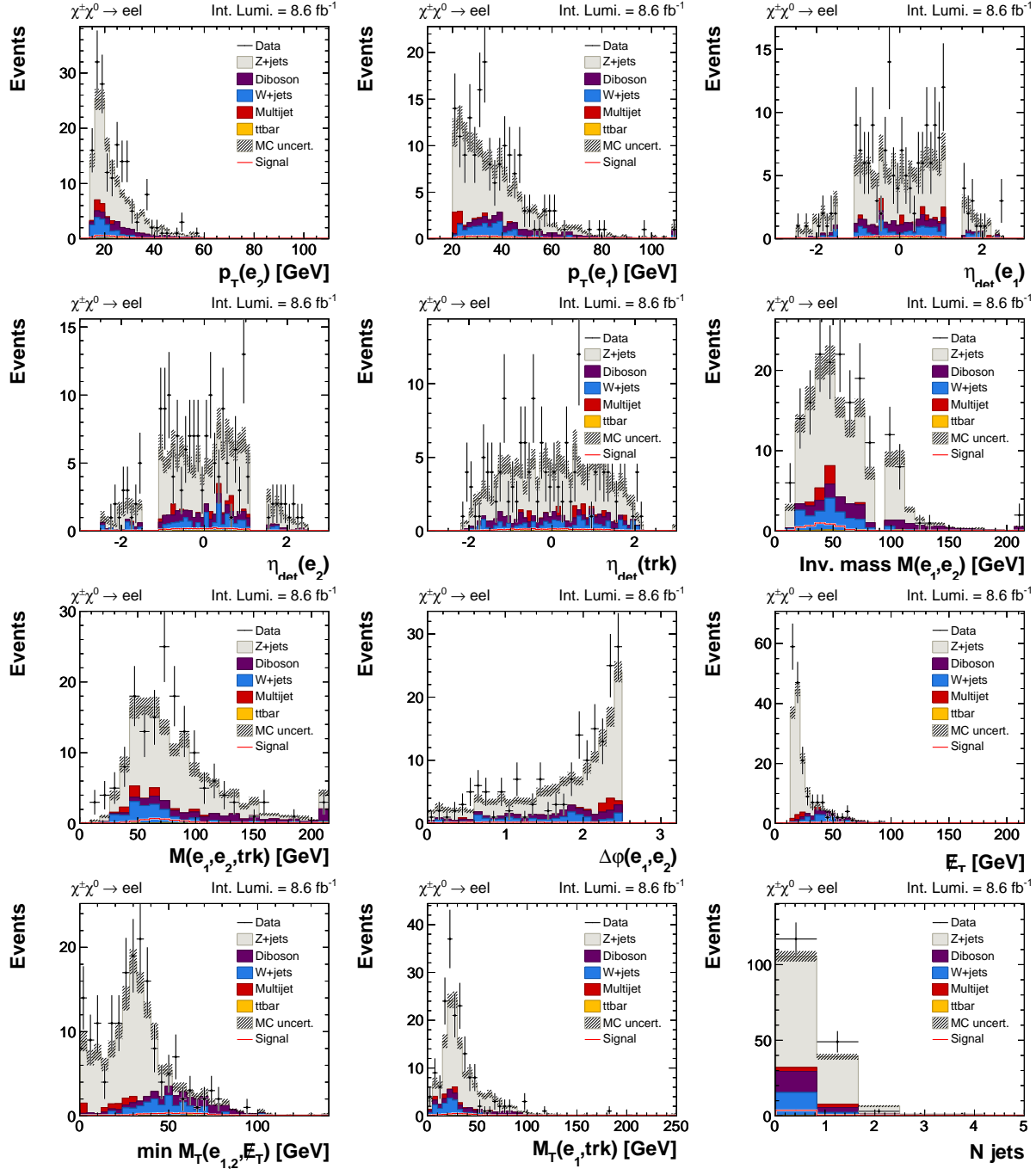


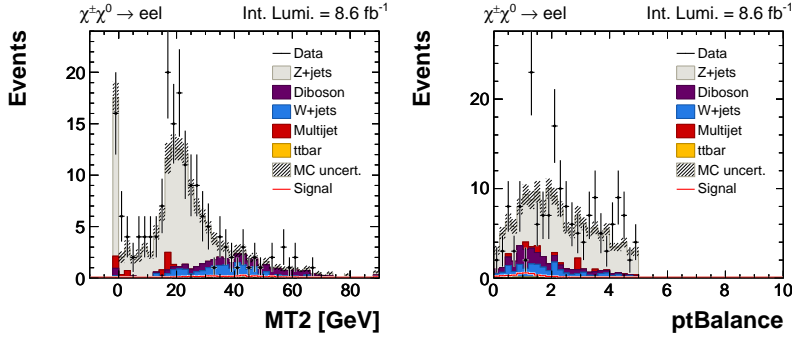
Figure A.16. QCD multijet reweighting functions, $\mu\mu\ell$ channel, p20_2 period. The first reweighting (left) is dependent on the leading muon p_T , the second on the next-to-leading muon p_T .

A.2. BDT inputs

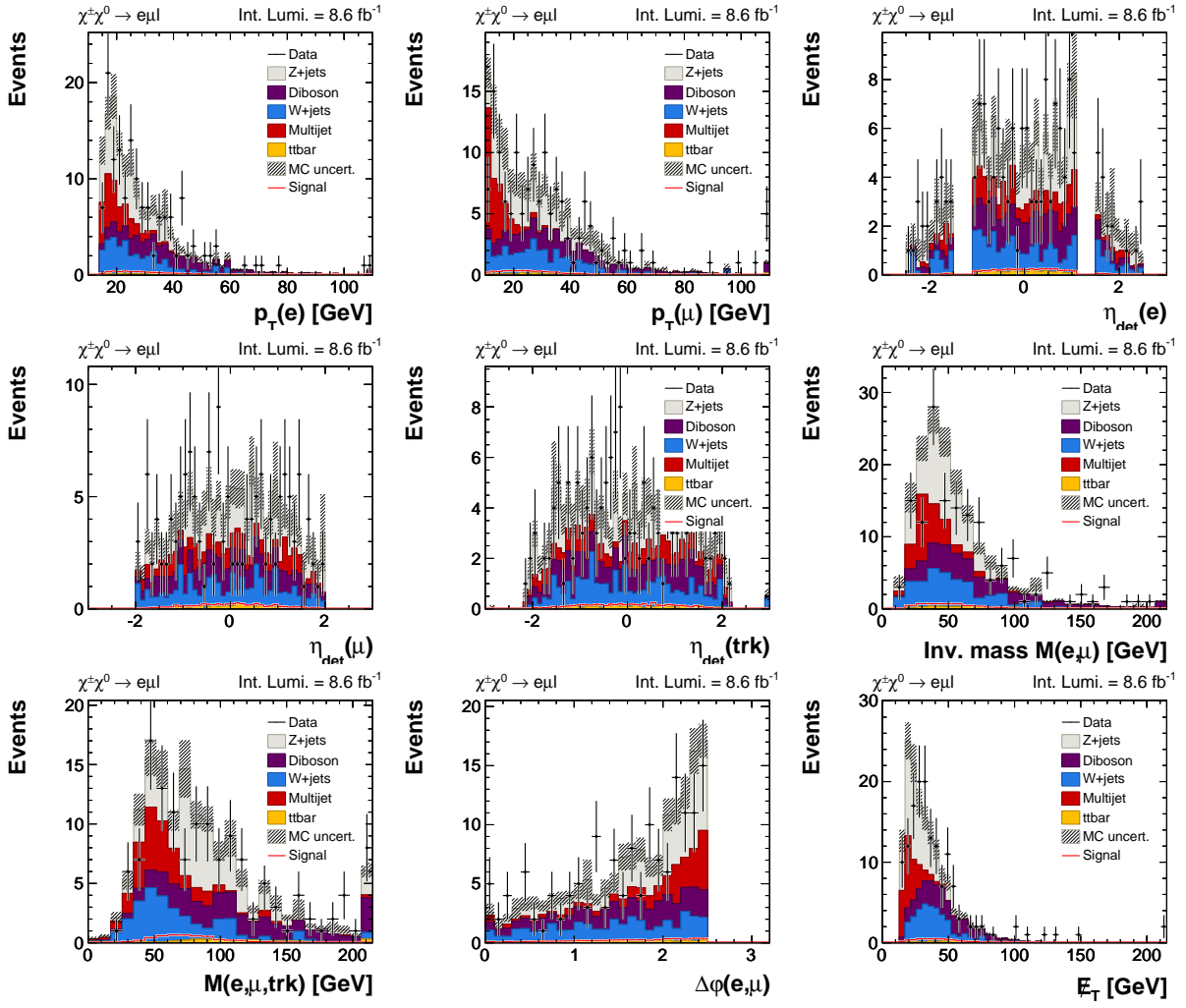
In the following, the input distributions to the BDTs will be shown. For all plots, the signal shown is mSUGRA with $m_0 = 100$ GeV, $m_{1/2} = 240$ GeV, $\tan\beta = 3$, $A_0 = 0$ GeV and $\text{sgn}\mu = +1$.

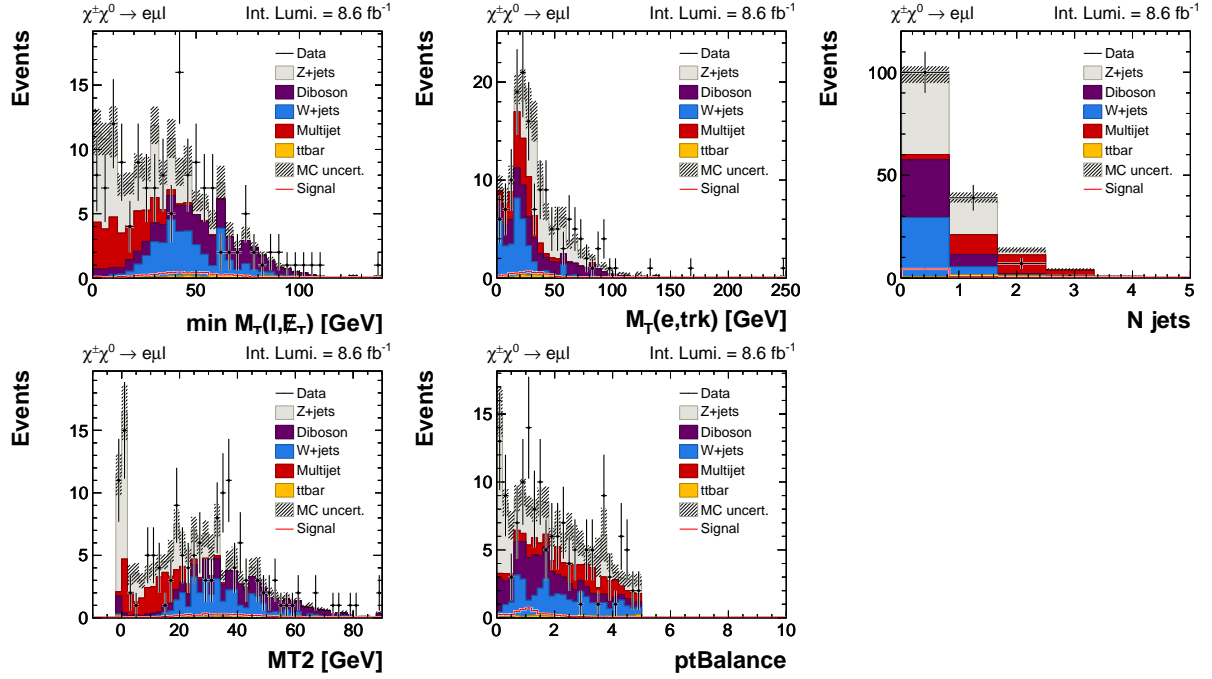
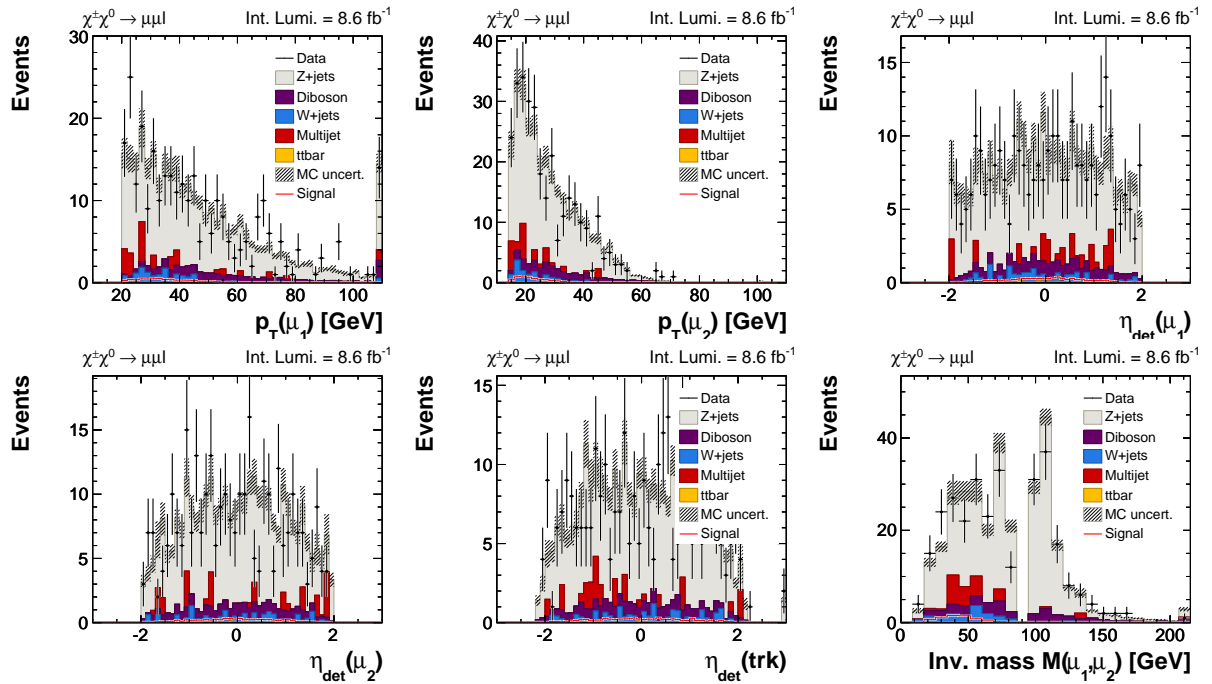
A.2.1. $ee\ell$ channel

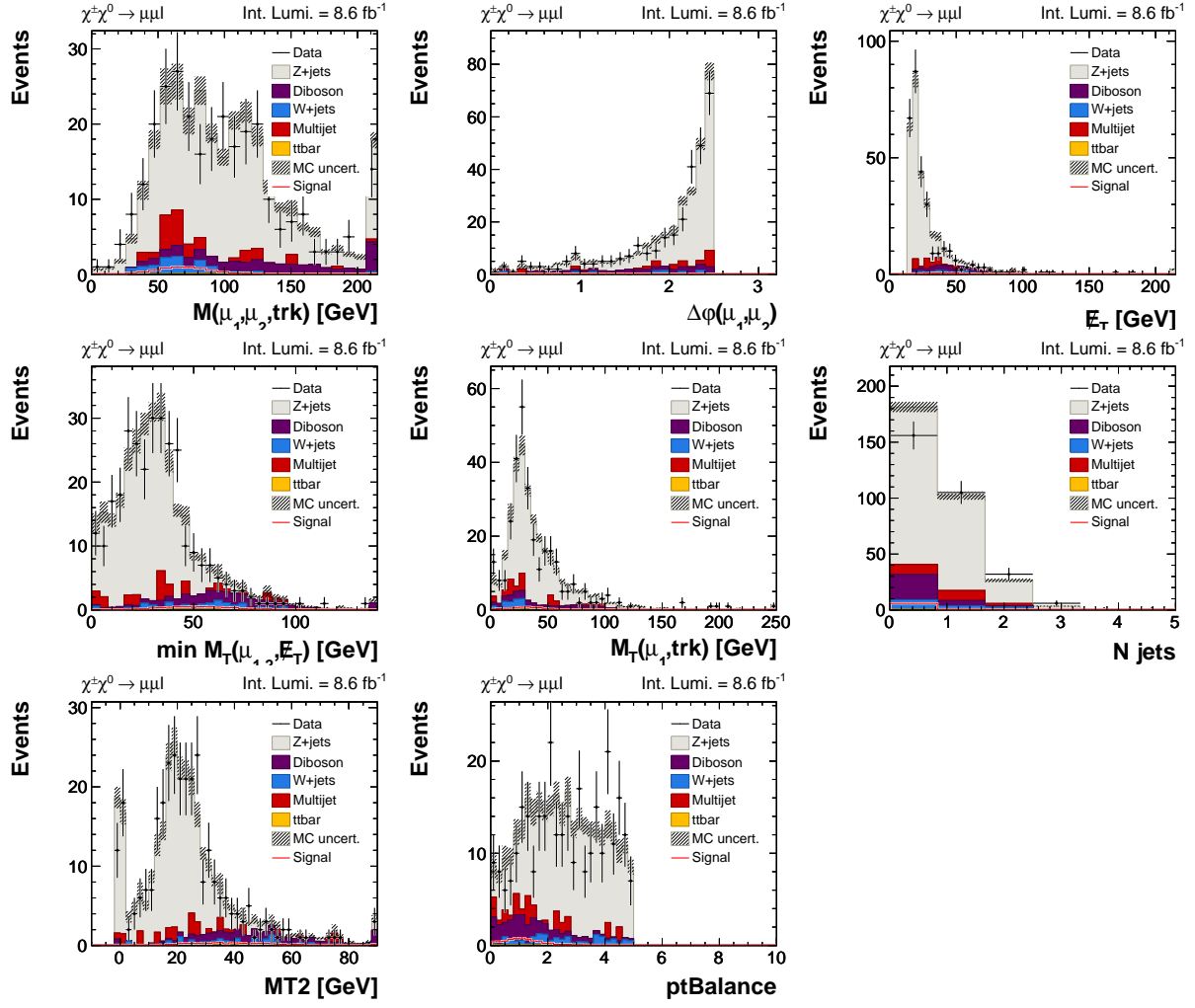




A.2.2. $e\mu\ell$ channel



A.2.3. $\mu\mu l$ channel



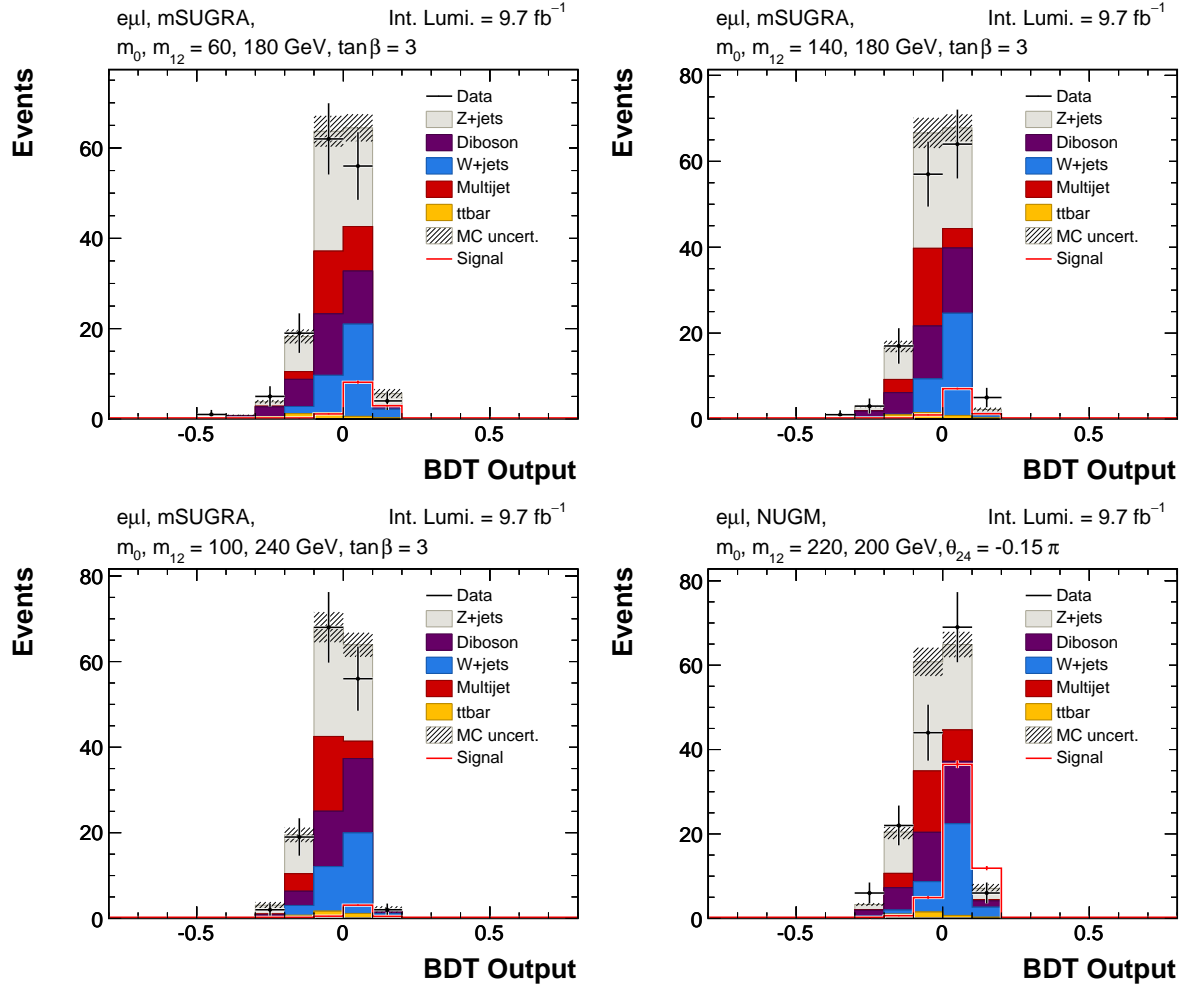


Figure A.17. Output of the BDT for four signal points, $e\mu\ell$ channel. All three epochs have been merged. For the mSUGRA points, $\tan\beta = 3$, for NUGM $\tan\beta = 10$, and for all points $\text{sgn } \mu = +1$ and $A_0 = 0$.

A.3. BDT Outputs

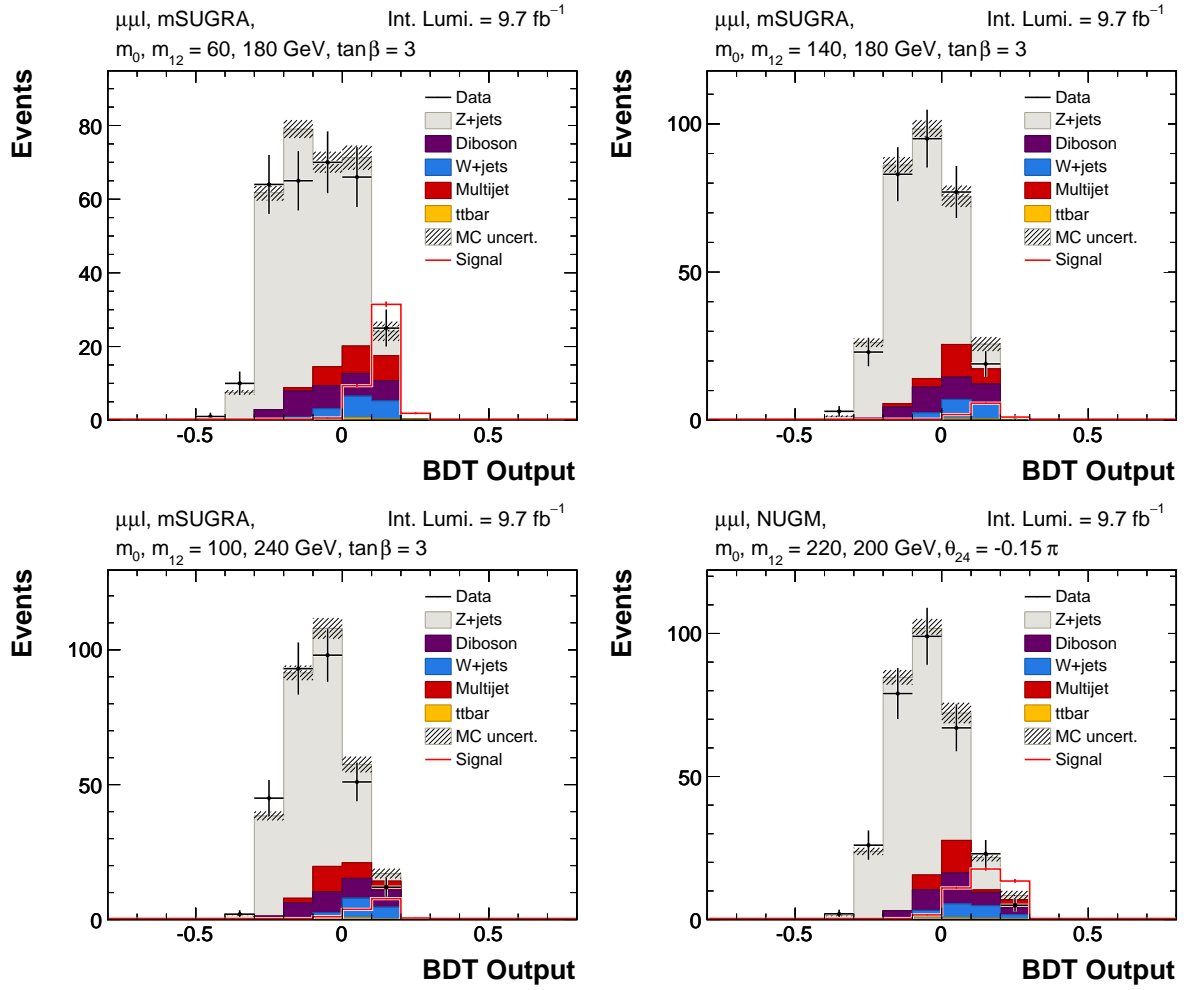


Figure A.18. Output of the BDT for four signal points, $\mu\mu\ell$ channel. All three epochs have been merged. For the mSUGRA points, $\tan\beta = 3$, for NUGM $\tan\beta = 10$, and for all points $\text{sgn}\mu = +1$ and $A_0 = 0$.

A.4. BDT Plots

Correlation Matrix (background)

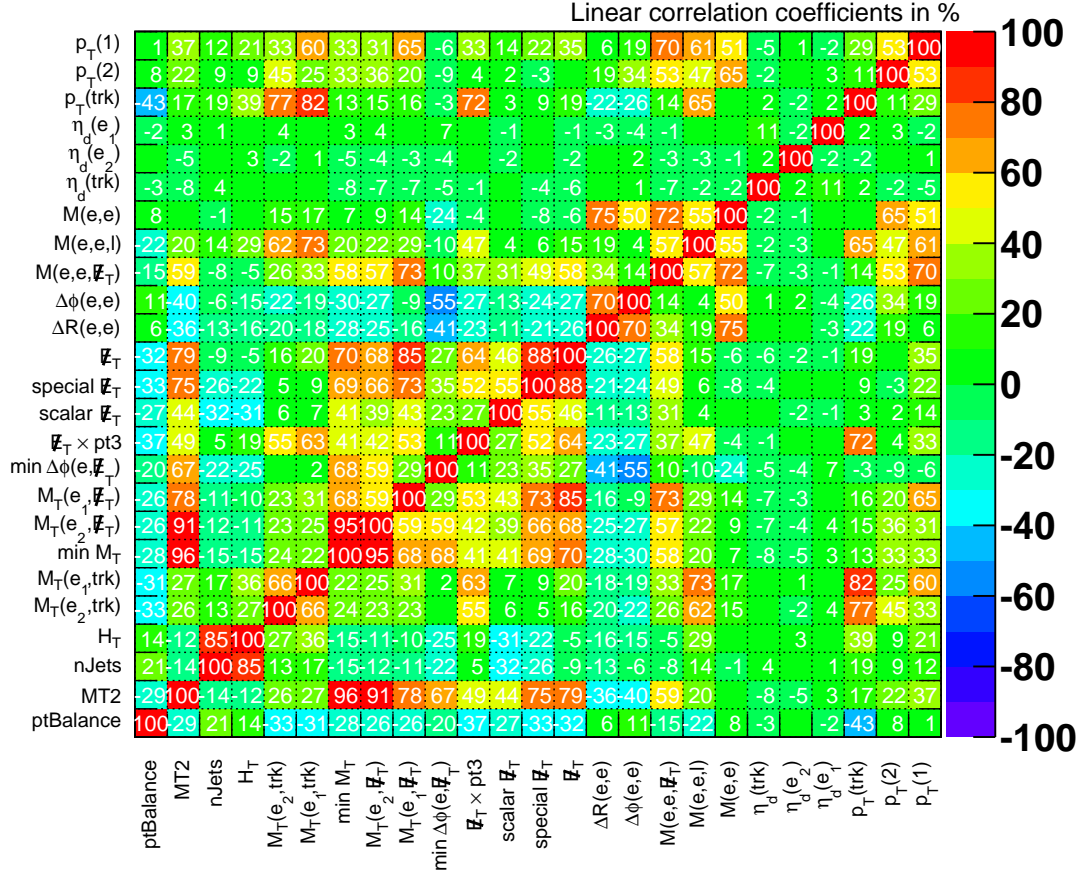


Figure A.19. Linear correlation coefficients for all pairs of candidate variables, for the background samples, $e\bar{e}l$ channel, RunIIa epoch.

A.5. Limits

A.5.1. $\tan\beta$ scan

m_0 [GeV]	$m_{1/2}$ [GeV]	σ_{NLO} [pb]	$BR(3\ell)$	$m(\tilde{\chi}_1^0)$ [GeV]	$m(\tilde{\chi}_2^0)$ [GeV]	$m(\tilde{\chi}_1^\pm)$ [GeV]	$m(\tilde{\ell})$ [GeV]	Exp. Limit	Obs. Limit
40	180	0.333	0.240	63.0	115.5	112.3	86.3	0.17	0.22
50	180	0.332	0.243	63.1	115.6	112.4	91.4	0.18	0.25
50	210	0.132	0.229	76.9	140.9	138.8	99.6	0.40	0.44
50	220	0.099	0.236	81.5	149.4	147.6	102.5	0.70	0.69
50	230	0.075	0.264	86.0	157.8	156.2	105.4	1.11	1.34
60	70	0.240	0.078	2.7	34.1	9.9	75.8	145.74	210.70
60	80	0.062	0.116	4.9	39.9	19.9	77.1	121.07	122.17
60	90	1.490	0.149	12.3	46.1	29.7	78.6	9.27	12.46
60	100	24.200	0.171	19.3	52.8	39.4	80.2	0.14	0.13
60	110	8.330	0.183	25.8	59.8	48.8	81.9	0.16	0.14
60	120	4.130	0.191	31.9	67.1	58.2	83.8	0.17	0.21
60	130	2.380	0.203	37.7	74.8	67.4	85.8	0.19	0.22
60	140	1.490	0.221	43.2	82.7	76.6	87.9	0.20	0.25
60	150	0.978	0.338	48.4	90.8	85.7	90.1	1.62	1.88
60	160	0.665	0.294	53.4	99.0	94.7	92.4	0.84	0.96
60	170	0.464	0.253	58.3	107.3	103.7	94.8	0.30	0.35
60	180	0.331	0.244	63.1	115.7	112.6	97.2	0.23	0.27
60	190	0.240	0.240	67.8	124.1	121.4	99.8	0.24	0.29
60	200	0.177	0.238	72.4	132.5	130.2	102.3	0.28	0.28
60	210	0.132	0.236	77.0	141.0	138.9	105.0	0.35	0.47
60	220	0.099	0.234	81.5	149.5	147.7	107.7	0.46	0.53
60	230	0.075	0.226	86.0	157.9	156.3	110.5	0.64	0.77
60	240	0.058	0.236	90.4	166.3	165.0	113.3	1.15	1.44
60	250	0.044	0.253	94.9	174.8	173.6	116.2	1.40	2.14
60	260	0.034	0.235	99.3	183.3	182.2	119.1	1.83	2.24
60	270	0.027	0.200	103.7	191.7	190.8	122.1	3.03	5.03
60	280	0.021	0.168	108.1	200.2	199.3	125.0	4.87	3.76
60	290	0.016	0.142	112.5	208.6	207.8	128.1	6.86	7.70
60	300	0.013	0.110	116.9	217.1	216.4	131.1	12.94	9.24
70	180	0.330	0.251	63.2	115.8	112.7	103.7	0.44	0.49

Table A.4. Signal points generated for the mSUGRA scenario, including masses of the lightest two neutralinos, the lightest chargino, and the lightest slepton. Expected and observed limits are limits on N times the SUSY cross section, at 95% CL. A point is excluded if the observed limit is below 1.0. For all points, $\tan \beta = 3$, $A_0 = 0$ and $\text{sgn } \mu = +1$. Part 1/3.

m_0 [GeV]	$m_{1/2}$ [GeV]	σ_{NLO} [pb]	$BR(3\ell)$	$m(\tilde{\chi}_1^0)$ [GeV]	$m(\tilde{\chi}_2^0)$ [GeV]	$m(\tilde{\chi}_1^\pm)$ [GeV]	$m(\tilde{\ell})$ [GeV]	Exp. Limit	Obs. Limit
70	240	0.057	0.228	90.5	166.4	165.1	118.9	0.67	0.89
70	250	0.044	0.198	95.0	174.9	173.7	121.7	0.91	1.03
80	180	0.329	0.283	63.2	115.9	112.9	110.7	1.65	1.46
80	240	0.057	0.226	90.6	166.6	165.2	125.1	0.65	0.81
80	250	0.044	0.221	94.9	175.0	173.8	127.7	0.86	0.83
80	260	0.034	0.214	99.4	183.5	182.4	130.3	1.18	1.82
90	180	0.328	0.180	63.3	116.1	113.0	118.1	0.64	0.70
90	240	0.057	0.224	90.6	166.7	165.3	131.7	0.64	0.75
90	250	0.044	0.218	95.0	175.1	173.9	134.2	0.82	0.86
90	260	0.034	0.210	99.5	183.6	182.5	136.7	1.20	1.41
100	180	0.327	0.141	63.4	116.2	113.2	125.9	0.54	0.61
100	240	0.057	0.221	90.6	166.8	165.4	138.8	0.67	0.71
100	250	0.044	0.215	95.1	175.2	174.0	141.1	0.76	1.10
100	260	0.034	0.205	99.5	183.7	182.6	143.5	1.18	1.43
110	180	0.327	0.117	63.4	116.4	113.4	134.0	0.65	0.70
110	200	0.175	0.137	72.7	133.2	130.9	137.7	0.91	0.91
110	210	0.130	0.251	77.3	141.6	139.6	139.7	5.61	5.96
110	220	0.098	0.233	81.8	150.0	148.3	141.8	1.81	1.75
110	230	0.074	0.224	86.2	158.5	157.0	143.9	0.86	0.95
110	240	0.057	0.219	90.7	166.9	165.6	146.1	0.75	0.64
110	250	0.044	0.211	95.1	175.4	174.2	148.3	0.99	1.19
110	260	0.034	0.199	99.5	183.8	182.7	150.7	1.38	1.44
120	180	0.326	0.099	63.5	116.5	113.6	142.3	0.86	1.09
120	210	0.130	0.120	77.3	141.7	139.8	147.7	1.20	1.37
120	220	0.098	0.085	81.9	150.2	148.5	149.7	2.47	3.17
120	230	0.074	0.221	86.3	158.6	157.1	151.7	2.65	4.43
120	240	0.057	0.213	90.8	167.1	165.7	153.8	1.22	1.69
120	250	0.044	0.204	95.2	175.5	174.3	155.9	0.91	1.15
120	260	0.034	0.192	99.6	183.9	182.9	158.1	1.47	2.26
130	180	0.325	0.085	63.6	116.7	113.8	150.8	0.72	0.95

Table A.5. Signal points generated for the mSUGRA scenario, continued. Expected and observed limits are limits on N times the SUSY cross section, at 95% CL. A point is excluded if the observed limit is below 1.0. For all points, $\tan \beta = 3$, $A_0 = 0$ and $\text{sgn } \mu = +1$. Part 2/3.

m_0 [GeV]	$m_{1/2}$ [GeV]	σ_{NLO} [pb]	$BR(3\ell)$	$m(\tilde{\chi}_1^0)$ [GeV]	$m(\tilde{\chi}_2^0)$ [GeV]	$m(\tilde{\chi}_1^\pm)$ [GeV]	$m(\tilde{\ell})$ [GeV]	Exp. Limit	Obs. Limit
130	200	0.174	0.093	72.9	133.5	131.3	154.2	1.20	2.17
130	210	0.130	0.097	77.4	141.9	140.0	155.9	1.37	2.09
130	220	0.098	0.104	81.9	150.3	148.6	157.8	1.57	2.25
140	180	0.324	0.074	63.7	116.9	114.0	159.5	1.01	1.14
140	190	0.236	0.076	68.4	125.3	122.8	161.0	1.17	1.66
140	200	0.174	0.079	73.0	133.7	131.5	162.7	1.41	2.07
140	210	0.130	0.082	77.4	142.1	140.2	164.4	1.65	2.01
150	180	0.323	0.063	63.8	117.1	114.3	168.3	1.09	1.25
150	190	0.235	0.066	68.5	125.5	123.0	169.8	1.27	1.34
150	200	0.173	0.068	73.0	133.8	131.7	171.3	1.69	1.87
160	180	0.322	0.053	63.9	117.3	114.5	177.3	1.92	1.84
160	190	0.235	0.056	68.5	125.6	123.2	178.7	1.55	2.09
170	150	0.929	0.037	49.7	92.8	88.5	182.7	1.10	1.65
170	160	0.638	0.039	54.5	101.0	97.3	183.8	1.22	1.52
170	170	0.449	0.042	59.3	109.2	106.1	185.0	1.24	1.65
170	180	0.322	0.045	64.0	117.5	114.8	186.3	1.23	1.12
170	190	0.234	0.047	68.6	125.9	123.5	187.7	1.78	3.04
170	200	0.173	0.050	73.1	134.2	132.1	189.1	2.10	3.22
170	210	0.129	0.052	77.7	142.6	140.8	190.5	2.62	3.34
170	220	0.097	0.053	82.2	151.0	149.4	192.0	2.91	4.50
170	230	0.074	0.054	86.6	159.4	158.0	193.6	3.43	4.96
170	240	0.057	0.053	91.0	167.8	166.6	195.2	3.76	5.47
170	250	0.044	0.051	95.5	176.2	175.1	196.9	5.02	5.45
170	260	0.034	0.046	99.9	184.7	183.7	198.7	7.22	7.55
170	270	0.026	0.037	104.3	193.1	192.2	200.5	11.28	13.44
170	280	0.021	0.033	108.7	201.5	200.7	202.3	59.99	51.98
170	290	0.016	0.062	113.0	209.9	209.1	204.2	19.08	28.45
170	300	0.013	0.011	117.4	218.3	217.6	206.1	42.71	51.45
180	170	0.447	0.034	59.4	109.5	106.4	194.2	1.42	2.23
180	180	0.321	0.037	64.1	117.7	115.0	195.5	1.77	2.47
190	180	0.320	0.030	64.2	118.0	115.3	204.7	2.03	2.48
200	180	0.319	0.024	64.3	118.2	115.6	214.0	2.81	4.16

Table A.6. Signal points generated for the mSUGRA scenario, continued. Expected and observed limits are limits on N times the SUSY cross section, at 95% CL. A point is excluded if the observed limit is below 1.0. For all points, $\tan\beta = 3$, $A_0 = 0$ and $\text{sgn}\mu = +1$. Part 3/3.

m_0 [GeV]	$m_{1/2}$ [GeV]	θ_{24}	σ_{NLO} [pb]	$BR(3\ell)$	$m(\tilde{\chi}_1^0)$ [GeV]	$m(\tilde{\chi}_2^0)$ [GeV]	$m(\tilde{\chi}_1^\pm)$ [GeV]	$m(\tilde{\ell})$ [GeV]	Exp. Limit	Obs. Limit
140	160	-0.15π	1.864	0.120	24.5	71.5	71.4	147.4	0.11	0.14
140	180	-0.15π	1.154	0.119	28.0	80.2	80.2	147.6	0.12	0.19
140	200	-0.15π	0.729	0.114	31.5	89.0	89.1	147.9	0.15	0.27
160	160	-0.15π	1.915	0.124	24.6	71.5	71.5	166.5	0.11	0.15
160	180	-0.15π	1.191	0.130	28.0	80.3	80.3	166.7	0.12	0.18
160	200	-0.15π	0.730	0.131	31.5	89.1	89.2	167.0	0.14	0.26
180	160	-0.15π	2.056	0.117	24.6	71.6	71.5	185.8	0.11	0.12
180	180	-0.15π	1.259	0.128	28.1	80.4	80.4	186.0	0.13	0.16
180	200	-0.15π	0.773	0.134	31.5	89.2	89.3	186.3	0.15	0.25
200	160	-0.15π	1.660	0.104	24.6	71.7	71.6	205.2	0.17	0.26
200	180	-0.15π	1.144	0.118	28.1	80.5	80.5	205.4	0.15	0.22
200	200	-0.15π	0.741	0.128	31.6	89.3	89.4	205.7	0.16	0.30
220	160	-0.15π	1.826	0.090	24.6	71.8	71.7	224.7	0.20	0.24
220	180	-0.15π	1.210	0.105	28.1	80.6	80.6	224.9	0.16	0.22
220	200	-0.15π	0.727	0.118	31.6	89.4	89.4	225.2	0.19	0.34
160	220	-0.15π	0.535	0.128	35.0	97.9	98.0	167.3	0.17	0.23
160	240	-0.15π	0.347	0.123	38.5	106.8	106.9	167.6	0.21	0.24
160	260	-0.15π	0.258	0.114	42.0	115.6	115.9	168.0	0.26	0.33
160	280	-0.15π	0.161	0.100	45.6	124.4	124.7	168.3	0.44	0.51
160	300	-0.15π	0.136	0.086	49.1	133.3	133.6	168.7	1.24	1.13
160	320	-0.15π	0.098	0.070	52.6	142.1	142.5	169.1	1.64	1.77
140	260	-0.15π	0.272	0.080	42.0	115.5	115.7	148.9	0.30	0.33
180	260	-0.15π	0.259	0.130	42.1	115.7	116.0	187.2	0.27	0.32
200	260	-0.15π	0.241	0.134	42.1	115.8	116.0	206.5	0.30	0.46
220	260	-0.15π	0.243	0.130	42.1	115.9	116.1	226.0	0.33	0.40
240	260	-0.15π	0.244	0.122	42.2	116.0	116.2	245.5	0.40	0.42
260	260	-0.15π	0.241	0.112	42.2	116.1	116.3	265.1	0.41	0.60
280	260	-0.15π	0.236	0.101	42.2	116.2	116.4	284.7	0.48	0.60
300	260	-0.15π	0.233	0.091	42.2	116.2	116.5	304.4	0.60	0.63
320	260	-0.15π	0.247	0.081	42.3	116.3	116.5	324.1	0.67	0.80
300	180	-0.15π	1.151	0.053	28.2	80.9	80.8	303.5	0.46	0.60
300	200	-0.15π	0.727	0.067	31.7	89.7	89.7	303.7	0.44	0.60
300	220	-0.15π	0.529	0.078	35.2	98.5	98.6	303.9	0.43	0.50
300	240	-0.15π	0.328	0.087	38.7	107.4	107.5	304.2	0.48	0.49
300	280	-0.15π	0.175	0.084	45.8	125.1	125.4	304.7	0.74	0.78
300	300	-0.15π	0.117	0.083	49.3	134.0	134.3	304.9	1.02	0.90
300	320	-0.15π	0.089	0.080	52.8	142.9	143.3	305.2	1.39	1.00

Table A.7. Signal points generated for the NUGM scenario, including sparticle masses. Expected and observed limits are limits on N times the SUSY cross section, at 95% CL. A point is excluded if the observed limit is below 1.0. For all points, $\tan\beta = 10$, $A_0 = 0$ and $\text{sgn}\mu = +1$. Part 1/2.

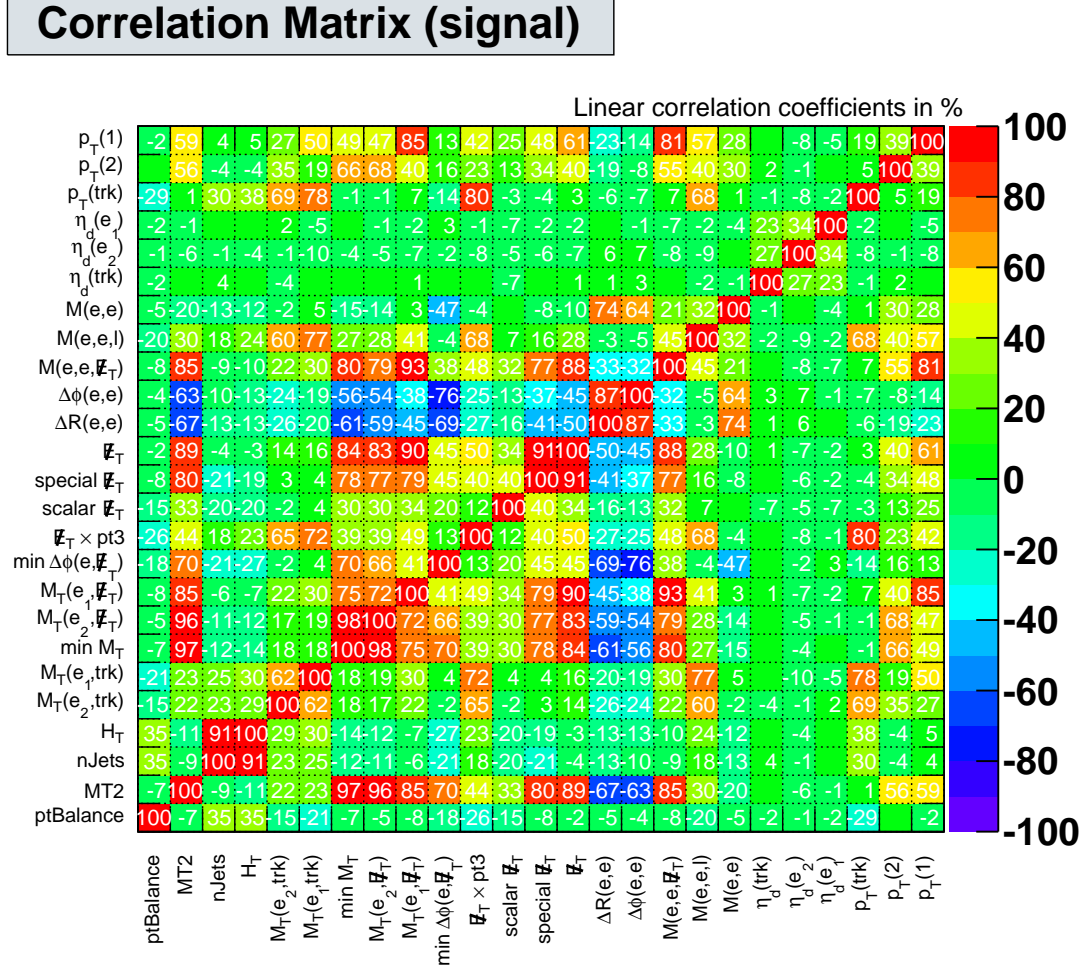


Figure A.20. Linear correlation coefficients for all pairs of candidate variables, for a typical signal sample, $ee\ell$ channel, RunIIa epoch. The signal point is mSUGRA $m_0 = 170$ GeV, $m_{12} = 170$ GeV, $\tan \beta = 10$, $\mu > 0$, $A_0 = 0$.

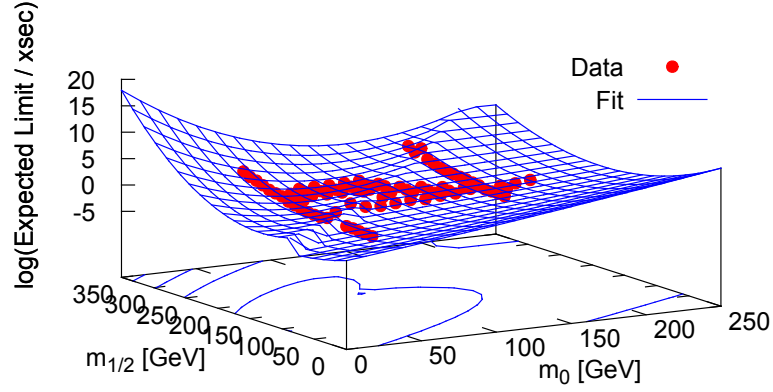


Figure A.21. Fit of a smooth function to the expected limit for the mSUGRA ($m_0, m_{1/2}$) plane. The vertical axis shows the logarithm of the expected limit in multiples of the SUSY cross section.

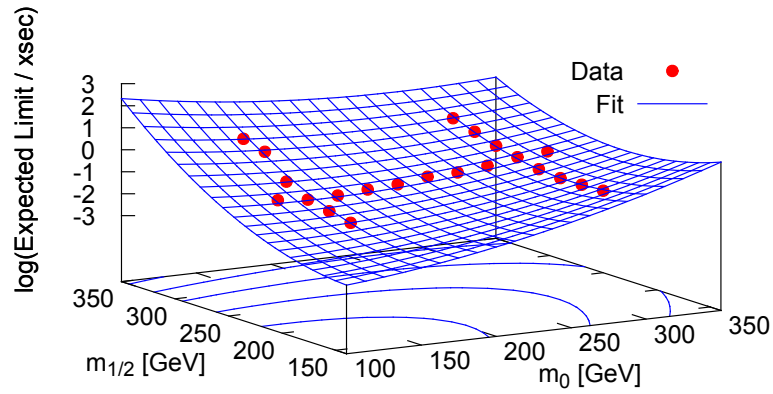


Figure A.22. Fit of a smooth function to the expected limit for the NUGM model. The vertical axis shows the logarithm of the expected limit in multiples of the SUSY cross section.

m_0 [GeV]	$m_{1/2}$ [GeV]	θ_{24}	σ_{NLO} [pb]	$BR(3\ell)$	$m(\tilde{\chi}_1^0)$ [GeV]	$m(\tilde{\chi}_2^0)$ [GeV]	$m(\tilde{\chi}_1^\pm)$ [GeV]	$m(\tilde{\ell})$ [GeV]	Exp. Limit	Obs. Limit
160	160	-0.67π	4.786	0.019	39.0	71.4	54.1	183.7	5.04	4.76
160	160	-0.65π	0.129	0.029	79.3	133.8	120.1	182.8	5.20	5.07
160	160	-0.60π	0.009	0.031	84.5	207.0	201.9	180.3	36.26	32.22
160	160	-0.40π	0.000	0.040	46.7	318.2	317.3	167.8	418.49	388.55
160	160	-0.30π	0.003	0.044	18.7	243.7	243.7	164.2	68.63	58.10
160	160	-0.20π	0.099	0.040	10.5	133.3	133.3	164.7	13.73	12.75
160	160	-0.18π	0.271	0.085	16.2	108.9	108.9	165.3	5.93	5.16
160	160	-0.16π	0.661	0.119	20.4	90.3	90.3	165.8	0.17	0.24
160	160	-0.13π	9.413	0.114	28.7	52.6	52.5	167.2	0.30	0.31
160	160	-0.04π	13.860	0.060	48.5	60.7	58.9	172.7	21.94	25.01
160	160	-0.03π	4.204	0.037	52.4	76.2	75.1	173.7	1.88	1.95
160	160	-0.01π	1.884	0.027	55.4	90.8	89.7	174.7	1.11	1.30
160	160	0.01π	0.686	0.006	59.6	112.3	109.6	176.7	5.51	7.94
160	160	0.03π	0.530	0.007	60.0	115.4	110.5	177.7	5.54	7.36
160	160	0.04π	0.890	0.011	57.5	110.9	100.5	178.6	2.17	2.99
160	160	0.06π	3.045	0.019	46.9	100.8	76.6	179.6	0.80	1.06
160	160	0.07π	2484.000	0.018	8.4	51.0	21.5	180.4	0.04	0.05

Table A.8. Signal points generated for the NUGM scenario, including sparticle masses, continued. Expected and observed limits are limits on N times the SUSY cross section, at 95% CL. A point is excluded if the observed limit is below 1.0. For all points, $\tan \beta = 10$, $A_0 = 0$ and $\text{sgn } \mu = +1$. Part 2/2.

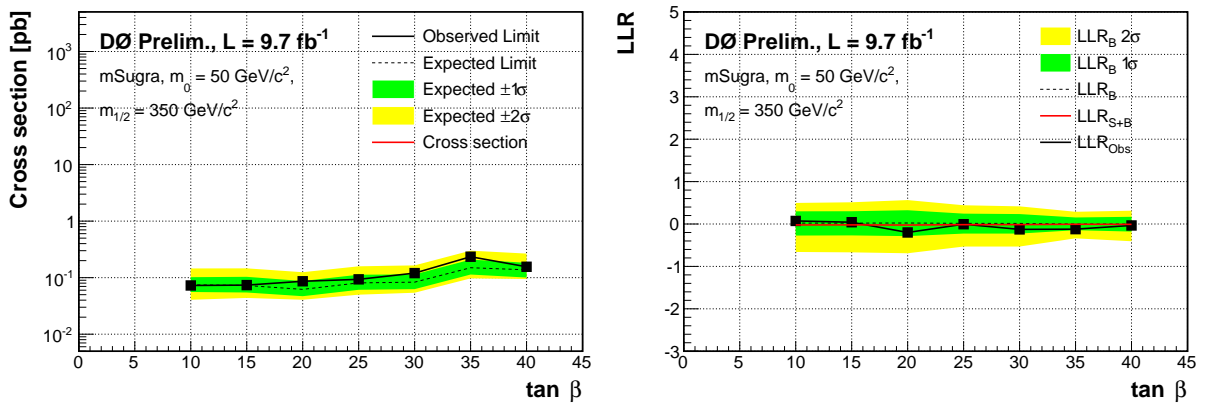


Figure A.23. Cross section limits and LLR for the $\tan \beta$ scan in the mSUGRA scenario. Here $m_0 = 50$ GeV, $m_{1/2} = 350$ GeV, $A_0 = 0$ GeV and $\text{sgn } \mu = +1$.

m_0 [GeV]	$m_{1/2}$ [GeV]	$\tan \beta$	σ_{NLO} [pb]	$BR(3\ell)$	$m(\tilde{\chi}_1^0)$ [GeV]	$m(\tilde{\chi}_2^0)$ [GeV]	$m(\tilde{\chi}_1^\pm)$ [GeV]	$m(\tilde{\ell})$ [GeV]	Exp. Limit	Obs. Limit
170	230	5	0.071	0.032	87.4	159.8	158.8	194.3	5.47	7.18
170	230	7	0.068	0.025	88.0	160.7	160.1	194.5	7.12	8.98
170	230	9	0.066	0.022	88.5	161.5	161.2	194.6	10.67	11.88
170	230	10	0.065	0.022	88.6	161.9	161.6	194.6	12.21	10.57
170	230	11	0.064	0.021	88.7	162.2	161.9	194.7	12.51	11.41
170	230	12	0.064	0.021	88.9	162.4	162.2	194.7	12.51	15.01
170	230	13	0.063	0.021	89.0	162.6	162.5	194.7	13.33	14.16
170	230	15	0.062	0.021	89.1	163.0	162.9	194.7	14.00	21.47
170	230	20	0.061	0.024	89.4	163.7	163.7	194.8	14.56	18.09
170	230	25	0.060	0.040	89.6	164.1	164.1	194.8	112.52	166.57
170	230	30	0.059	0.043	89.6	164.4	164.4	194.8	17.86	20.47
170	230	35	0.059	0.044	89.8	164.6	164.7	194.9	14.96	17.99
170	230	40	0.058	0.044	89.9	164.8	164.8	194.9	56.04	46.29
230	230	10	0.066	0.004	88.9	162.4	162.1	248.6	40.22	40.75
230	230	15	0.063	0.005	89.4	163.4	163.4	248.7	39.86	34.27
230	230	20	0.062	0.006	89.7	164.1	164.1	248.7	33.53	32.55
230	230	25	0.061	0.007	89.8	164.5	164.6	248.8	39.43	33.21
230	230	30	0.060	0.010	89.9	164.8	164.9	248.8	40.64	45.37
230	230	35	0.060	0.015	90.0	165.0	165.2	248.8	33.27	32.25
230	230	40	0.059	0.025	90.1	165.3	165.4	248.8	33.03	29.95

Table A.9. Signal points for the $\tan \beta$ scan in the mSUGRA scenario. Expected and observed limits are limits on N times the SUSY cross section, at 95% CL. A point is excluded if the observed limit is below 1.0. For all points, $A_0 = 0$ and $\text{sgn } \mu = +1$.

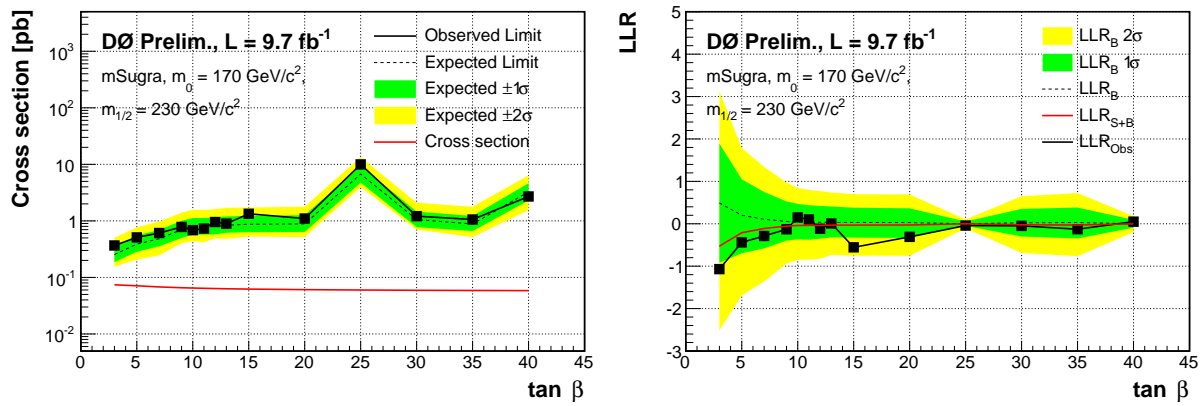


Figure A.24. Cross section limits and LLR for the $\tan \beta$ scan in the mSUGRA scenario. Here $m_0 = 170$ GeV, $m_{1/2} = 230$ GeV, $A_0 = 0$ GeV and $\text{sgn } \mu = +1$.

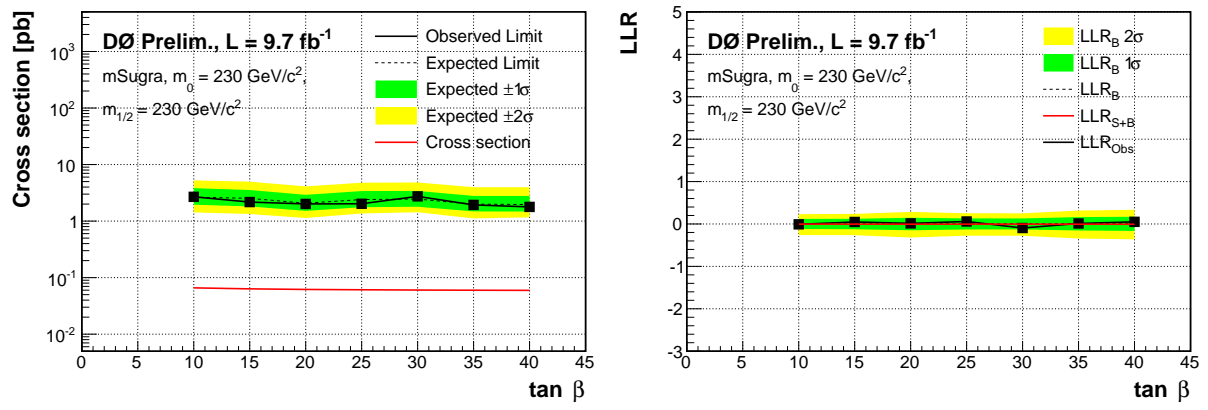


Figure A.25. Cross section limits and LLR for the $\tan \beta$ scan in the mSUGRA scenario. Here $m_0 = 230 \text{ GeV}$, $m_{1/2} = 230 \text{ GeV}$, $A_0 = 0 \text{ GeV}$ and $\text{sgn } \mu = +1$.

List of Figures

2.1.	Sketch of the Higgs potential showing spontaneous symmetry breaking.	8
2.2.	Renormalization of the scalar mass.	10
2.3.	Running couplings in the standard model and the MSSM	10
2.4.	Rotation curve of the NGC3198 galaxy, from Doppler shift measurements of the 21.1 cm hydrogen line	14
2.5.	Running of the SUSY parameters in the CMSSM, from [19].	17
2.6.	Schematic plot of different regions in the (c)MSSM, from [20].	17
2.7.	Resolution of the hierarchy problem by supersymmetry	19
2.8.	Dependence of the absolute gaugino mass parameters $ M_i $ on θ_{24}	20
2.9.	Co-production of charginos $\tilde{\chi}_1^\pm$ and neutralinos $\tilde{\chi}_2^0$	21
2.10.	Leptonic decays of the chargino $\tilde{\chi}_1^\pm$	21
2.11.	Leptonic decays of the second-lightest neutralino $\tilde{\chi}_2^0$	21
2.12.	Varying the value of m_0	23
2.13.	Varying the value of $m_{1/2}$	23
2.14.	Varying the value of $\tan \beta$	24
2.15.	Varying the value of θ_{24}	24
2.16.	Varying the value of A_0	25
2.17.	Varying the value of the top quark mass	25
2.18.	mSUGRA limits set by previous $D\bar{O}$ searches for charginos and neutralinos with 2.7 fb^{-1} [26]	26
2.19.	Exploration of the mSUGRA $(m_0, m_{1/2})$ plane	26
2.20.	Same as above but with $\tan \beta = 10$ and $\theta_{24} = -0.15\pi$ (non-universal gaugino masses).	26
2.21.	Summary of ATLAS searches in the $(m_0, m_{1/2})$ plane of the mSUGRA/CMSSM model.	27
2.22.	Summary of ATLAS limits in searches for gluino pair production (Gtt simplified models).	28
2.23.	ATLAS limits depending on the mass of the lightest stop \tilde{t}_1 and the lightest neutralino $\tilde{\chi}_1^0$	29
2.24.	Overview of limits ATLAS limits from searches for stop pair production	29
2.25.	Electron / photon vertex diagram, and a first-order vertex correction	31
2.26.	Possible corrections to the muon's magnetic moment	31
2.27.	Decay of a B_s meson into two muons via a standard model process ("penguin" diagram)	33
2.28.	Possible decay of a B_s meson into two muons via SUSY particles	33
3.1.	Plan of the Fermilab accelerator complex during Run II of the Tevatron	36
3.2.	Schematic overview of the $D\bar{O}$ detector, from [38].	37
3.3.	Schematics of the tracking system (SMT and CFT), solenoid, and central preshower detector	38
3.4.	Rendering of the silicon microstrip tracker, showing barrels and discs. From [38].	38
3.5.	Cross sectional view of an SMT barrel.	38
3.6.	Side view of one quadrant of the $D\bar{O}$ calorimeter	40
3.7.	Contributions to the energy loss of electrons and positrons in lead	40
3.8.	Location of the central (CPS) and forward preshower detectors (FPS) and the intercryostat detector (ICD). From [38].	41
3.9.	Schematic drawing of two calorimeter unit cells. From [38].	42
3.10.	Overview of the drift tubes in the muon system. From [38].	44

3.11. Overview of the scintillators in the muon system. From [38].	44
3.12. Sketch of the DØ luminosity monitor, from [38]	45
3.13. Overview of the three level trigger system, from [38].	46
3.14. Detector systems considered in the level 1 and level 2 triggers	47
4.1. Illustration of $\tan \lambda$	50
4.2. Transverse projection of a track.	50
4.3. Parametrization of tracks using intersections with geometric surfaces, from [42]. The track is red and the surface is shown in brown.	50
4.4. Illustration of the Histogramming Track Finder	51
4.5. Illustration of chord length and sagitta	52
4.6. Track momentum uncertainty due to multiple scattering, adapted from [42]	53
4.7. Schematic of jet evolution in a detector	57
4.8. Infrared and collinear safety of jet algorithms. Images from [47].	58
5.1. Integrated luminosity of the five epochs of RunII.	63
5.2. Signal MC points for the mSUGRA scenario, in the $(m_0, m_{1/2})$ plane	64
5.3. Signal MC points generated with non-universal gaugino masses (NUGM), in the $(m_0, m_{1/2})$ plane.	64
5.4. Instantaneous luminosity \mathcal{L} after application of all corrections, $ee\ell$ channel	69
5.5. z coordinate of the primary vertex for the $ee\ell$ channel, after application of all corrections	70
5.6. Reconstructed Z boson p_T , before application of additional $Z p_T / \cos \beta_1$ reweighting	71
5.7. Distribution of $\cos \beta_1$, before application of additional $Z p_T / \cos \beta_1$ reweighting	71
5.8. Scale factors for the additional $Z p_T / \cos \beta_1$ reweighting, for the ee channel, RunIIa period. Plots for the other epochs can be found in Figure A.5 of the appendix.	71
5.9. Reconstructed Z boson p_T , after application of additional $Z p_T / \cos \beta_1$ reweighting	72
5.10. Distribution of $\cos \beta_1$, after application of additional $Z p_T / \cos \beta_1$ reweighting	72
5.11. p_T dependent electron scale factors for RunIIb-1 (p20), CC region (left) and EC region (right). The scale factor is fitted with the function $f(x) = a + d \operatorname{erf}((x - b)/c)$	73
5.12. p_T dependent electron scale factors for RunIIb-2,3,4 (p20_2)	73
5.13. Unclustered energy before and after unclustered energy reweighting, $ee\ell$ channel, p17 period.	74
5.14. Unclustered energy before and after unclustered energy reweighting, $ee\ell$ channel, p20 period.	74
5.15. Unclustered energy before and after unclustered energy reweighting, $ee\ell$ channel, p20_2 period.	74
5.16. MET before and after unclustered energy reweighting, $ee\ell$ channel, p17 period.	75
5.17. MET before and after unclustered energy reweighting, $ee\ell$ channel, p20 period.	75
5.18. MET before and after unclustered energy reweighting, $ee\ell$ channel, p20_2 period.	75
5.19. 3D electron likelihood reweighting, for the $ee\ell$ channel, p17 period. From left to right: $\eta_{\text{det}} = -1.5 \dots -1.1$, $\eta_{\text{det}} = -1.1 \dots 1.1$, and $\eta_{\text{det}} = 1.1 \dots 1.5$	76
5.20. 3D electron likelihood reweighting, for the $ee\ell$ channel, p20 period. From left to right: $\eta_{\text{det}} = -1.5 \dots -1.1$, $\eta_{\text{det}} = -1.1 \dots 1.1$, and $\eta_{\text{det}} = 1.1 \dots 1.5$	76
5.21. 3D electron likelihood reweighting, for the $ee\ell$ channel, p20_2 period. From left to right: $\eta_{\text{det}} = -1.5 \dots -1.1$, $\eta_{\text{det}} = -1.1 \dots 1.1$, and $\eta_{\text{det}} = 1.1 \dots 1.5$	76
5.22. QCD multijet reweighting functions, $e\mu\ell$ channel, p20_2 period. The first reweighting (left) is dependent on the electron p_T , the second on the muon p_T . For other channels and epochs, see the appendix (Section A.1.5).	78
5.23. $ee\ell$ channel, preselection	81

5.24. $e\ell\ell$ channel, after cut 1: $\Delta\phi(e, \mu) < 2.5$	82
5.25. $e\ell\ell$ channel, after cut 2: $\cancel{E}_T > 15$ GeV	83
5.26. $e\ell\ell$ channel, after cut 3: $\text{ptBalance} < 5.0$	84
5.27. $e\ell\ell$ channel, after cut 4: $80 \text{ GeV} < M_{\ell\ell} < 100 \text{ GeV}$	85
5.28. $e\mu\ell$ channel, preselection	86
5.29. $e\mu\ell$ channel, after cut 1: $\Delta\phi(e, \mu) < 2.5$	87
5.30. $e\mu\ell$ channel, after cut 2: $\cancel{E}_T > 15$ GeV	88
5.31. $e\mu\ell$ channel, after cut 3: $\text{ptBalance} < 5.0$	89
5.32. $\mu\mu\ell$ channel, preselection	90
5.33. $\mu\mu\ell$ channel, after cut 1: $\Delta\phi(e, \mu) < 2.5$	91
5.34. $\mu\mu\ell$ channel, after cut 2: $\cancel{E}_T > 15$ GeV	92
5.35. $\mu\mu\ell$ channel, after cut 3: $\text{ptBalance} < 5.0$	93
5.36. $\mu\mu\ell$ channel, after cut 4: $80 \text{ GeV} < M_{\ell\ell} < 100 \text{ GeV}$	94
6.1. Two variables, each insufficient to separate two samples, correlated differently in each sample	95
6.2. Different types of cuts on a two-dimensional distribution	96
6.3. Sketch of a simple decision tree.	97
6.4. Linear correlation coefficients for all pairs of BDT input variables, for the background samples	103
6.5. Linear correlation coefficients for all pairs of BDT input variables, for a typical signal sample	104
6.6. Output of the BDT for four signal points, $e\ell\ell$ channel	105
7.1. Example of log likelihood ratio (NLLR) distributions for the $s+b$ and b only prior predictive ensembles, compared to an observed NLLR. From [58].	109
7.2. Limits for the “ 3ℓ -max” mSUGRA scenario, where $m_0 = 60$ GeV, $\tan\beta = 3$, $A_0 = 0$ GeV and $\text{sgn}\mu = +1$	112
7.3. Limits for the “heavy sleptons” mSUGRA scenario, in which $m_0 = 170$ GeV, $\tan\beta = 3$, $A_0 = 0$ GeV and $\text{sgn}\mu = +1$	113
7.4. Limits on mSUGRA parameters, where $m_{1/2} = 180$ GeV, $\tan\beta = 3$, $A_0 = 0$ GeV and $\text{sgn}\mu = +1$. Left: cross section limits, right: log-likelihood ratio.	113
7.5. Limits on mSUGRA parameters in the $(m_0, m_{1/2})$ plane, where $\tan\beta = 3$, $A_0 = 0$ GeV and $\text{sgn}\mu = +1$. The blue stroked curve shows the extrapolated region for the observed exclusion, the dashed black line shows the expected exclusion, with $\pm 1\sigma$ interval.	114
7.6. Limits for the NUGM scenario with $m_0 = 160$ GeV, $\theta_{24} = -0.15\pi$, $\tan\beta = 10$, $A_0 = 0$ GeV and $\text{sgn}\mu = +1$. Left: expected and observed cross section limits, right: log-likelihood ratio for background-only and signal plus background hypotheses, and observed LLR.	115
7.7. Limits for the NUGM scenario with $m_0 = 300$ GeV, $\theta_{24} = -0.15\pi$, $\tan\beta = 10$, $A_0 = 0$ GeV and $\text{sgn}\mu = +1$. Left: expected and observed cross section limits, right: log-likelihood ratio for background-only and signal plus background hypotheses, and observed LLR.	115
7.8. Limits for the NUGM scenario with $m_{1/2} = 260$ GeV, $\theta_{24} = -0.15\pi$, $\tan\beta = 10$, $A_0 = 0$ GeV and $\text{sgn}\mu = +1$. Left: expected and observed cross section limits, right: log-likelihood ratio for background-only and signal plus background hypotheses, and observed LLR.	116
7.9. Limits on NUGM parameters in the $(m_0, m_{1/2})$ plane, for $\theta_{24} = -0.15\pi$. Other parameters are set to $\tan\beta = 10$, $A_0 = 0$ GeV and $\text{sgn}\mu = +1$	116
7.10. Limits for the NUGM scenario with $m_0 = m_{1/2} = 160$ GeV, $\tan\beta = 10$, $A_0 = 0$ GeV and $\text{sgn}\mu = +1$. Outside of the displayed region, no values of θ_{24} are excluded. Left: expected and observed cross section limits, right: log-likelihood ratio for background-only and signal plus background hypotheses, and observed LLR.	117

A.1.	Instantaneous luminosity \mathcal{L} after application of all corrections, $e\mu\ell$ channel, for RunIIa, RunIIb-1, and RunIIb-234. The luminosity reweighting is described in Section 5.6.1. . . .	122
A.2.	Instantaneous luminosity \mathcal{L} after application of all corrections, $\mu\mu\ell$ channel, for RunIIa, RunIIb-1, and RunIIb-234. The luminosity reweighting is described in Section 5.6.1. . . .	122
A.3.	z coordinate of the primary vertex for the $e\mu\ell$ channel. After application of all corrections, for RunIIa, RunIIb-1, and RunIIb-234.	123
A.4.	z coordinate of the primary vertex for the $\mu\ell$ channel. After application of all corrections, for RunIIa, RunIIb-1, and RunIIb-234.	123
A.5.	Scale factors for the additional $Z p_T / \cos \beta_1$ reweighting (Section 5.6.4), for the ee channel, RunIIa, RunIIb-1 and RunIIb-234 periods.	124
A.6.	Scale factors for the additional $Z p_T / \cos \beta_1$ reweighting (Section 5.6.4), for the em channel, RunIIa, RunIIb-1 and RunIIb-234 periods.	125
A.7.	Scale factors for the additional $Z p_T / \cos \beta_1$ reweighting (Section 5.6.4), for the mm channel, RunIIa, RunIIb-1 and RunIIb-234 periods.	126
A.8.	QCD multijet reweighting functions, $ee\ell$ channel, p17 period. The first reweighting (left) is dependent on the leading electron p_T , the second on the next-to-leading electron p_T . .	127
A.9.	QCD multijet reweighting functions, $ee\ell$ channel, p20 period. The first reweighting (left) is dependent on the leading electron p_T , the second on the next-to-leading electron p_T . .	127
A.10.	QCD multijet reweighting functions, $ee\ell$ channel, p20_2 period. The first reweighting (left) is dependent on the leading electron p_T , the second on the next-to-leading electron p_T . .	128
A.11.	QCD multijet reweighting functions, $e\mu\ell$ channel, p20 period. The first reweighting (left) is dependent on the electron p_T , the second on the muon p_T	128
A.12.	QCD multijet reweighting functions, $e\mu\ell$ channel, p20 period. The first reweighting (left) is dependent on the electron p_T , the second on the muon p_T	128
A.13.	QCD multijet reweighting functions, $e\mu\ell$ channel, p20_2 period. The first reweighting (left) is dependent on the electron p_T , the second on the muon p_T	129
A.14.	QCD multijet reweighting functions, $\mu\mu\ell$ channel, p17 period. The first reweighting (left) is dependent on the leading muon p_T , the second on the next-to-leading muon p_T	129
A.15.	QCD multijet reweighting functions, $\mu\mu\ell$ channel, p20 period. The first reweighting (left) is dependent on the leading muon p_T , the second on the next-to-leading muon p_T	129
A.16.	QCD multijet reweighting functions, $\mu\mu\ell$ channel, p20_2 period. The first reweighting (left) is dependent on the leading muon p_T , the second on the next-to-leading muon p_T . .	130
A.17.	Output of the BDT for four signal points, $e\mu\ell$ channel	135
A.18.	Output of the BDT for four signal points, $\mu\mu\ell$ channel	136
A.19.	Linear correlation coefficients for all pairs of candidate variables, for the background samples, $ee\ell$ channel, RunIIa epoch.	137
A.20.	Linear correlation coefficients for all pairs of candidate variables, for a typical signal sample, $ee\ell$ channel, RunIIa epoch. The signal point is mSUGRA $m_0 = 170$ GeV, $m_{12} = 170$ GeV, $\tan \beta = 10$, $\mu > 0$, $A_0 = 0$	142
A.21.	Fit of a smooth function to the expected limit for the mSUGRA ($m_0, m_{1/2}$) plane. The vertical axis shows the logarithm of the expected limit in multiples of the SUSY cross section.	143
A.22.	Fit of a smooth function to the expected limit for the NUGM model. The vertical axis shows the logarithm of the expected limit in multiples of the SUSY cross section.	143
A.23.	Cross section limits and LLR for the $\tan \beta$ scan in the mSUGRA scenario. Here $m_0 = 50$ GeV, $m_{01/2} = 350$ GeV, $A_0 = 0$ GeV and $\text{sgn } \mu = +1$	144
A.24.	Cross section limits and LLR for the $\tan \beta$ scan in the mSUGRA scenario. Here $m_0 = 170$ GeV, $m_{1/2} = 230$ GeV, $A_0 = 0$ GeV and $\text{sgn } \mu = +1$	145

A.25. Cross section limits and LLR for the $\tan\beta$ scan in the mSUGRA scenario. Here $m_0 =$ 230 GeV, $m_{1/2} = 230$ GeV, $A_0 = 0$ GeV and $\text{sgn}\,\mu = +1$	146
--	-----

Bibliography

- [1] The ATLAS Collaboration, G. Aad et al., *Observation of a new particle in the search for the Standard Model Higgs boson with the ATLAS detector at the LHC*, Phys.Lett. **B716** (2012), pp. 1–29
The CMS Collaboration, S. Chatrchyan et al., *Observation of a new boson at a mass of 125 GeV with the CMS experiment at the LHC*, Phys.Lett. **B716** (2012), pp. 30–61.
- [2] B. de Wit and J. Smith, *Field Theory in Particle Physics, Volume 1*, North Holland (Aug. 1986), ISBN: 978-0444869999.
- [3] F. Halzen and A. D. Martin, *Quarks and Leptons* (1985), ISBN: 978-0471887416.
- [4] The Particle Data Group, J. Beringer et al., *Review of Particle Physics*, Phys. Rev. D **86** (1 July 2012), p. 010001.
- [5] D. I. Kazakov, *Beyond the standard model (in search of supersymmetry)* (2000), arXiv: hep-ph/0012288.
- [6] L. Randall and R. Sundrum, *Large Mass Hierarchy from a Small Extra Dimension*, Phys. Rev. Lett. **83** (17 Oct. 1999), pp. 3370–3373.
- [7] E. Farhi and L. Susskind, *Technicolour*, Physics Reports **74.3** (1981), pp. 277–321.
- [8] The ATLAS Collaboration, G. Aad et al., *Search for contact interactions and large extra dimensions in dilepton events from pp collisions at $\sqrt{s} = 7$ TeV with the ATLAS detector*, Phys.Rev. **D87** (2013), p. 015010
The ATLAS Collaboration, G. Aad et al., *Search for Extra Dimensions in diphoton events using proton-proton collisions recorded at $\sqrt{s} = 7$ TeV with the ATLAS detector at the LHC*, New J.Phys. **15** (2013), p. 043007
The ATLAS Collaboration, G. Aad et al., *Search for dark matter candidates and large extra dimensions in events with a photon and missing transverse momentum in pp collision data at $\sqrt{s} = 7$ TeV with the ATLAS detector*, Phys.Rev.Lett. **110** (2013), p. 011802
The ATLAS Collaboration, G. Aad et al., *Search for dark matter candidates and large extra dimensions in events with a jet and missing transverse momentum with the ATLAS detector*, JHEP **1304** (2013), p. 075.
- [9] H. Georgi and S. L. Glashow, *Unity of All Elementary-Particle Forces*, Phys. Rev. Lett. **32** (8 Feb. 1974), pp. 438–441.
- [10] J. Baez and J. Huerta, *The Algebra of Grand Unified Theories*, Bull. Amer. Math. Soc. **47** (2010), pp. 483–552.
- [11] E. Witten, *Quest for Unification* (2002), arXiv: hep-ph/0207124.
- [12] The SNO Collaboration, S. Ahmed et al., *Constraints on nucleon decay via ‘invisible’ modes from the Sudbury Neutrino Observatory*, Phys. Rev. Lett. **92** (2004), p. 102004.
- [13] G. Hinshaw et al., *Nine-year Wilkinson Microwave Anisotropy Probe (WMAP) Observations: Cosmological Parameter Results*, ApJS **208**, 19 (Oct. 2013), p. 19.

- [14] T. S. van Albada et al., *Distribution of dark matter in the spiral galaxy NGC 3198*, Astrophysical Journal, Part 1 **295** (Aug. 1985), pp. 305–313, issn: 0004-637X.
- [15] S. Dimopoulos and H. Georgi, *Softly broken supersymmetry and SU(5)*, Nuclear Physics B **193.1** (1981), pp. 150–162, issn: 0550-3213.
- [16] M. Byrne, C. F. Kolda, and P. Regan, *Bounds on charged, stable superpartners from cosmic ray production*, Phys.Rev. **D66** (2002), p. 075007.
- [17] P. C. McGuire and P. J. Steinhardt, *Cracking open the window for strongly interacting massive particles as the halo dark matter* (2001), arXiv: astro-ph/0105567.
- [18] G. Bertone, ed., *Particle dark matter. Observations, models and searches.*, Cambridge University Press (2010), ISBN: 978-0-521-76368-4.
- [19] S. P. Martin, *A Supersymmetry Primer* (1997), arXiv: hep-ph/9709356.
- [20] M. Battaglia, I. Hinchliffe, and D. Tovey, *Cold dark matter and the LHC*, J.Phys. **G30** (2004), R217–R244.
- [21] J. E. Younkin, *Topics in Supersymmetry*, PhD thesis, Northern Illinois University, United States (2012).
- [22] R. Barbieri and G. F. Giudice, *Upper bounds on supersymmetric particle masses*, Nuclear Physics B **306** (Aug. 1988), pp. 63–76.
- [23] J. E. Younkin and S. P. Martin, *Non-universal gaugino masses, the supersymmetric little hierarchy problem, and dark matter*, Phys.Rev. **D85** (2012), p. 055028.
- [24] Tevatron Electroweak Working Group and DØ and CDF collaborations, *Combination of CDF and DO results on the mass of the top quark using up to 9.7 fb^{-1} at the Tevatron* (2014), arXiv: hep-ex/1407.2682.
- [25] The ATLAS, CDF, CMS and DØ Collaborations, *First combination of Tevatron and LHC measurements of the top-quark mass* (2014), arXiv: hep-ex/1403.4427.
- [26] The D0 Collaboration, V. M. Abazov et al., *Search for associated production of charginos and neutralinos in the trilepton final state using 2.3 fb^{-1} of data*, Phys. Lett. **B680** (2009), pp. 34–43.
- [27] The ATLAS collaboration, *Summary plots from the ATLAS Supersymmetry physics group* (Mar. 21, 2014), URL: https://atlas.web.cern.ch/Atlas/GROUPS/PHYSICS/CombinedSummaryPlots/SUSY/index.html#ATLAS_SUSY_MSUGRA.
- [28] The ATLAS Collaboration, G. Aad et al., *Search for new phenomena using final states with large jet multiplicities and missing transverse momentum with ATLAS in 20 fb^{-1} of $\sqrt{s} = 8\text{ TeV}$ proton-proton collisions*, ATLAS-CONF-2013-054, CERN, Geneva (May 2013).
- [29] G. Aad et al., *Search for strong production of supersymmetric particles in final states with missing transverse momentum and at least three b-jets using 20.1 fb^{-1} of pp collisions at $\sqrt{s} = 8\text{ TeV}$ with the ATLAS Detector*, ATLAS-CONF-2013-061, CERN, Geneva (June 2013).
- [30] G. Aad et al., *Search for supersymmetry using events with three leptons, multiple jets, and missing transverse momentum in 13.0 fb^{-1} of pp collisions with the ATLAS detector at $\sqrt{s} = 8\text{ TeV}$* , ATLAS-CONF-2012-151, CERN, Geneva (Nov. 2012).
- [31] G. Aad et al., *Search for strongly produced superpartners in final states with two same sign leptons with the ATLAS detector using 21 fb^{-1} of proton-proton collisions at $\sqrt{s} = 8\text{ TeV}$* , ATLAS-CONF-2013-007, CERN, Geneva (Mar. 2013).

-
- [32] The ATLAS Collaboration, *Search for direct production of the top squark in the all-hadronic $t\bar{t} + E_T^{\text{miss}}$ final state in 21 fb^{-1} of pp -collisions at $\sqrt{s} = 8\text{ TeV}$ with the ATLAS detector*, tech. rep. ATLAS-CONF-2013-024, CERN, Geneva (Mar. 2013).
 - [33] G. Aad et al., *Search for direct production of charginos and neutralinos in events with three leptons and missing transverse momentum in 21 fb^{-1} of pp collisions at $\sqrt{s} = 8\text{ TeV}$ with the ATLAS detector*, ATLAS-CONF-2013-035, CERN, Geneva (Mar. 2013).
 - [34] The Muon (g-2) Collaboration, G. W. Bennett et al., *Final report of the E821 muon anomalous magnetic moment measurement at BNL*, Phys. Rev. D **73** (Apr. 2006), p. 072003.
 - [35] The New (g-2) Collaboration, F. Gray, *Measuring the muon's anomalous magnetic moment to 0.14 ppm*, J.Phys.Conf.Ser. **312** (2011), p. 102006.
 - [36] The LHCb Collaboration, R. Aaij et al., *First Evidence for the Decay $B_s^0 \rightarrow \mu^+ \mu^-$* , Phys.Rev.Lett. **110** (2013), p. 021801.
 - [37] D. E. Johnson, *Instrumentation Requirements for the Fermilab Main Injector*, Beams-doc 77 v1, Fermilab (Nov. 2002).
 - [38] The DØ Collaboration, V. M. Abazov et al., *The Upgraded DØ Detector*, Nucl. Instrum. Meth. **A565** (2006), pp. 463–537.
 - [39] The D0 Collaboration, J. Ellison, *The D0 Detector Upgrade and Physics Program* (2000), DØ-Note 3830, arXiv: hep-ex/0101048.
 - [40] The Particle Data Group, C. Amsler et al., *Review of particle physics*, Phys. Lett. **B667** (2008).
 - [41] The DØ Collaboration, S. Abachi et al., *Beam tests of the DØ uranium liquid argon end calorimeters*, Nucl. Instrum. Meth. **A324** (1993), pp. 53–76.
 - [42] G. Hesketh, *Central Track Extrapolation Through the DØ Detector*, DØ-Note 4079 (Jan. 2003).
 - [43] A. Khanov, *HTF: histogramming method for finding tracks. The algorithm description.*, DØ-Note 3778 (Sept. 2000).
 - [44] R. Gluckstern, *Uncertainties in track momentum and direction, due to multiple scattering and measurement errors*, Nucl.Instrum.Meth. **24** (1963), pp. 381–389.
 - [45] K. Kleinknecht, *Detektoren für Teilchenstrahlung*, Teubner Studienbücher, Teubner Stuttgart (1984).
 - [46] A. Schwartzman and C. Tully, *Primary Vertex Reconstruction by Means of Adaptive Vertex Fitting*, DØ-Note 4918 (2005).
 - [47] G. C. Blazey et al., *Run II jet physics* (2000), arXiv: hep-ex/0005012.
 - [48] L. Sawyer and A. L. Stone, *Missing ET Reconstruction: Variable and Methods*, DØ-Note 3957 (July 2003).
 - [49] T. Sjostrand et al., *Pythia 6.3 physics and manual* (2003), arXiv: hep-ph/0308153.
 - [50] M. Shamim and T. Bolton, *Generator Level Reweighting of p_T of Z Boson*, DØ-Note 5565 (Jan. 2008).
 - [51] X. Bu et al., *Search for Standard Model Higgs Boson with Same Flavour Opposite Charge Dileptons and Missing Transverse Energy using Boosted Decision Trees for 8.1 fb^{-1} of $p\bar{p}$ Collisions at $\sqrt{s} = 1.96\text{ TeV}$* , DØ-Note 6175 (Feb. 2011).
 - [52] G. Hesketh, *W p_T Re-weighting for Alpgen and Pythia*, DØ-Note 5786 (Oct. 2008).
 - [53] A. Faure et al., *Search for Standard Model Higgs Boson with Same Flavour Opposite Charge Dileptons and Missing Transverse Energy using Boosted Decision Trees for 8.6 fb^{-1} of $p\bar{p}$ Collisions at $\sqrt{s} = 1.96\text{ TeV}$* , DØ-Note 6288 (Aug. 2012).
-

- [54] X. Bu et al., *Electron Identification for Summer 2010*, DØ-Note 6116 (Sept. 2010).
- [55] G. Cowan, *Topics in statistical data analysis for high-energy physics* (Dec. 2010), arXiv: physics . data-an/1012.3589.
- [56] A. Hoecker et al., *TMVA - Toolkit for Multivariate Data Analysis* (Mar. 2007), eprint: physics/0703039.
- [57] C. Lester and D. Summers, *Measuring masses of semiinvisibly decaying particles pair produced at hadron colliders*, Phys.Lett. **B463** (1999), pp. 99–103
A. Barr, C. Lester, and P. Stephens, *$m(T2)$: The Truth behind the glamour*, J.Phys. **G29** (2003), pp. 2343–2363.
- [58] W. Fisher, *Collie: A Confidence Level Limit Evaluator*, DØ-Note 5595 (June 9, 2009).
- [59] O. Atramentov et al., *Electron and Photon Identification with p20 data*, DØ-Note 5761 (Sept. 2008).
- [60] S. Cho et al., *Muon ID Certification for p20 data*, DØ-Note 5824 (Dec. 2008).

Acknowledgments

Someone once said, particle physics analyses are like sausages: you don't want to know how they are made. Well, now I know, and I wouldn't have made it so far without the support of many people. First of all, I'd like to thank my advisor, Carsten Hensel for his support from near and far, and also for his incredible patience with me. I'd like to thank Arnulf Quadt for his continued support, even when things got complicated. I've got to thank Jörn Grosse-Knetter for agreeing to assess my thesis, and also Ariane Frey, Wolfram Kollatschny and Steffen Schumann for being my examiners. Many thanks to Yvonne Peters and Björn Penning for their friendship, for valuable discussions and for helping me out with DØ stuff, and thanks to Erik Gerwick for checking my theory writing. My gratitude goes to Mandy Rominsky and Mike Eads for starting this analysis with me and for creating the basis on which this work is built. Also, I have to thank all the many other people in the DØ collaboration whose code and work I have been using and have benefited from. In the best time I have been standing on shoulders of giants, in other times I at least had some interesting coding riddles to ponder about. I have to thank Tibor Kurca for helping me generate my Monte Carlo so quickly. I'd like to thank my colleagues and friends, including but not limited to Jens, Jörn, Elisabeth, Tobias, Lars, Johannes, Lara and Olaf for many entertaining coffee breaks, occasional Schnitzel and Bier outings, and more. I'd like to thank Frauke for always standing by my side sympathetically even as I was descending into thesis madness. Finally, my deepest thanks go out to my family for supporting and believing in me, and setting me on the way to achieve all that I have so far.

Curriculum Vitae

Personal Information

Name: Jason Dhia Mansour
Address: Weender Landstr. 81
37075 Göttingen
Germany
Email: jd.mansour@gmail.com
Born: November 9, 1984 in Washington, D.C., USA
Nationality: USA



Education

since Oct. 2010 PhD student at the Georg-August University of Göttingen, under supervision of Prof. Carsten Hensel
April 2011 – Sep. 2011 Research stay at Fermilab, Batavia, USA for my PhD thesis
Aug. 2010 Received Diplom of Physics with grade “sehr gut” in Göttingen
Title of the thesis: “Search for the Associated Production of Charginos and Neutralinos in the Like-sign Dimuon Final State with the DØ Experiment”
Feb. 2009 – Mar. 2010 Research stay at Fermilab for my Diploma thesis
Summer 2008 Sommer student at DESY Zeuthen in the ATLAS top group
March 2007 Holiday School on Gravitational Physics, Albert-Einstein-Institute in Potsdam
2003 – 2010 Studies of physics at the University of Göttingen
1994 – 2003 Städtisches Gymnasium Barntrup

Language Skills

Fluent in English and German

Publications

V. M. Abazov et al. [D0 Collaboration], “Search for universal extra dimensions in $p\bar{p}$ collisions,” Phys. Rev. Lett. 108, 131802 (2012) [arXiv:1112.4092 [hep-ex]]

Jason Mansour, “Search for Universal Extra Dimensions with the D0 Experiment”, Proceedings of the DPF-2011 Conference, Providence, RI, August 8-13, 2011 [arXiv:1110.2991 [hep-ex]]